GDAŃSK UNIVERSITY OF TECHNOLOGY

The author of the doctoral dissertation: **Jagoda Ewa Budnik**
Scientific discipline: **Materials engineering**

DOCTORAL DISSERTATION

Title of doctoral dissertation: **Structure, defect chemistry, and charge transport in mixed ionic-electronic conducting perovskites based on $Ba(Ce,Zr,Y)O_{3-\delta}$ and $Sr(Fe,Co)O_{3-\delta}$**

Title of doctoral dissertation (in Polish): **Struktura, chemia defektów i transport ładunku w perowskitach wykazujących mieszane przewodnictwo jonowo-elektronowe opartych na $Ba(Ce,Zr,Y)O_{3-\delta}$ i $Sr(Fe,Co)O_{3-\delta}$**

Supervisor *signature*
Prof. Ph.D., D.Sc., Eng. Maria Gazda
Auxiliary supervisor *signature*
Ph.D., Eng. Tadeusz Miruszewski

Gdańsk, year 2026

GDAŃSK UNIVERSITY OF TECHNOLOGY

STATEMENT

The author of the doctoral dissertation: **Jagoda Ewa Budnik**

I, the undersigned, declare that I am aware that in accordance with the provisions of Art. 27 (1) and (2) of the Act of 4th February 1994 on Copyright and Related Rights (Journal of Laws of 2021, item 1062), the university may use my doctoral dissertation entitled:
Structure, defect chemistry, and charge transport in mixed ionic-electronic conducting perovskites based on $Ba(Ce,Zr,Y)O_{3-\delta}$ and $Sr(Fe,Co)O_{3-\delta}$
for scientific or didactic purposes.[1]

Gdańsk, 20.02.2026 .....

signature of the PhD student

Aware of criminal liability for violations of the Act of 4th February 1994 on Copyright and Related Rights and disciplinary actions set out in the Law on Higher Education and Science(Journal of Laws 2021, item 478), as well as civil liability, I declare, that the submitted doctoral dissertation is my own work.

I declare, that the submitted doctoral dissertation is my own work performed under and in cooperation with the supervision of Prof. Ph.D., D.Sc., Eng. Maria Gazda and the auxiliary supervision of Ph.D., Eng. Tadeusz Miruszewski.

This submitted doctoral dissertation has never before been the basis of an official procedure associated with the awarding of a PhD degree.

All the information contained in the above thesis which is derived from written and electronic sources is documented in a list of relevant literature in accordance with Art. 34 of the Copyright and Related Rights Act.

I confirm that this doctoral dissertation is identical to the attached electronic version.

Gdańsk, 20.02.2026 .....

signature of the PhD student

I, the undersigned, agree to include an electronic version of the above doctoral dissertation in the open, institutional, digital repository of Gdańsk University of Technology.

Gdańsk, 20.02.2026 .....

signature of the PhD student

[1] Art 27. 1. Educational institutions and entities referred to in art. 7 sec. 1 points 1, 2 and 4–8 of the Act of 20 July 2018 – Law on Higher Education and Science, may use the disseminated works in the original and in translation for the purposes of illustrating the content provided for didactic purposes or in order to conduct research activities, and to reproduce for this purpose disseminated minor works or fragments of larger works.

2. If the works are made available to the public in such a way that everyone can have access to them at the place and time selected by them, as referred to in para. 1, is allowed only for a limited group of people learning, teaching or conducting research, identified by the entities listed in paragraph 1.

GDAŃSK UNIVERSITY OF TECHNOLOGY

DESCRIPTION OF DOCTORAL DISSERTATION

The Author of the doctoral dissertation: Jagoda Ewa Budnik

Title of doctoral dissertation: Structure, defect chemistry, and charge transport in mixed ionic-electronic conducting perovskites based on $Ba(Ce,Zr,Y)O_{3-\delta}$ and $Sr(Fe,Co)O_{3-\delta}$

Title of doctoral dissertation in Polish: Struktura, chemia defektów i transport ładunku w perowskitach wykazujących mieszane przewodnictwo jonowo-elektronowe opartych na $Ba(Ce,Zr,Y)O_{3-\delta}$ i $Sr(Fe,Co)O_{3-\delta}$

Language of doctoral dissertation: English

Supervisor: Prof. Ph.D., D.Sc., Eng. Maria Gazda

Auxiliary supervisor: Ph.D., Eng. Tadeusz Miruszewski

Date of doctoral defense:

Keywords of doctoral dissertation in Polish: perowskity, uwodnienie, chemia defektów, dyfuzja w ciele stałym, wymiana powierzchniowa, tlenki trójprzewodzące

Keywords of doctoral dissertation in English: perovskites, water uptake, defect chemistry, diffusion in solids, surface exchange, triple-conducting oxides

Summary of doctoral dissertation in Polish:
Celem niniejszej pracy było zbadanie zależności między składem chemicznym, strukturą krystaliczną a transportem ładunku w perowskitowych tlenkach wykazujących mieszane przewodnictwo jonowo-elektronowe. Analizowano dwie grupy materiałów: $BaCe_{0,6}Zr_{0,2}Y_{0,2-x}M_xO_{3-\delta}$ (BCZYM, M = Tb, Pr, Fe), wykazujące wysoką przewodność protonową i jonów tlenu; oraz $SrFe_{1-x}Co_xO_{3-\delta}$ (SFC) charakteryzujące się dominującą przewodnością elektronową. Synteza w fazie stałej umożliwiła uzyskanie materiałów o wysokiej symetrii, a dodatek NiO zapewnił jednofazowość i wysoką gęstość próbek. W BCZYM, podstawienie Tb zwiększyło całkowitą przewodność elektryczną oraz ruchliwość protonów i wakansów tlenowych, Pr również podwyższało ruchliwości nośników jonowych, natomiast podstawienie Fe prowadziło do obniżenia przewodności i ruchliwości nośników. W SFC kobalt stabilizował wakanse tlenowe, przy zachowywaniu wysokiej symetrii struktury materiałów, a przewodnictwo elektryczne zależało głównie od ruchliwości dziur elektronowych. Obecność pary wodnej zwiększała przewodnictwo jonowe i protonowe w BCZYM oraz modyfikowała właściwości transportowe i wymianę powierzchniową tlenu w SFC, co podkreśla istotną rolę defektów protonowych w mechanizmach transportu zachodzących w mieszanych przewodnikach jonowo-elektronowych.

Summary of doctoral dissertation in English:
The aim of this dissertation was to investigate the relationships between chemical composition, crystal structure, and charge transport in perovskite oxides exhibiting mixed ionic-electronic conductivity. Two groups of materials were studied: $BaCe_{0.6}Zr_{0.2}Y_{0.2-x}M_xO_{3-\delta}$ (BCZYM, M = Tb, Pr, Fe), exhibiting high proton and oxygen-ionic conductivity, and $SrFe_{1-x}Co_xO_{3-\delta}$ (SFC), with predominantly electronic conductivity. Solid-state synthesis enabled obtaining materials of high symmetry, while the addition of NiO sintering aid ensured phase purity and densification of samples. In BCZYM, Tb substitution enhanced total electrical conductivity and mobilities of protons and oxygen vacancies, Pr also improved mobilities of both ionic carriers, whereas the substitution of Fe decreased the conductivity and carrier mobility. In SFC, Co stabilised oxygen vacancies while preserving high structural symmetry. The electrical conductivity of SFC materials was mainly governed by electron-hole mobility. Water vapour increased oxygen-ionic and introduced proton conductivity in BCZYM. It also influenced transport of electronic and ionic charge carriers, as well as oxygen surface exchange in SFC, highlighting the significant role of proton defects in transport mechanisms in mixed ionic-electronic conductors.

Acknowledgments

The completion of this dissertation would not have been possible without the contributions of many people, who shared their knowledge with me, inspired me, and provided support in my daily work.

First of all, I would like to express my deepest gratitude to my supervisor, ***Prof. Ph.D., Eng. Maria Gazda****, for her academic guidance and unwavering commitment to ensuring the high quality of both my own work and our joint projects. Her scientific expertise, as well as her remarkable attention to linguistic precision, have been an invaluable resource from which I have tried to learn as much as possible during several years of our close collaboration.*

I am also grateful to my auxiliary supervisor, ***Ph.D., Eng. Tadeusz Miruszewski****, for his openness to new ideas and numerous discussions that often went beyond the main focus of our research. His insights and boundless imagination have repeatedly broadened my horizons.*

I would like to thank the entire ***Protons in Solids group*** *and my colleagues from the* ***Institute of Nanotechnology and Materials Engineering****, with whom I had the pleasure of working – for sharing their extensive experience and for the collaboration in contributing to the advancement of our scientific field.*
Special thanks go to ***M.Sc. Eng. Joanna Pośpiech****,* ***M.Sc. Eng. Daria Balcerzak****, and* ***M.Sc. Eng. Arkadiusz Dawczak*** *for creating a welcoming and cheerful atmosphere in our "coop", so lively that sometimes it was almost impossible to focus on work.*

I am grateful to ***Ph.D., Eng. Piotr Okoczuk*** *for drawing me out of the everyday whirlwind with scientific – and other – discussions that often extended far beyond my usual areas of interest.*

I would also like to thank ***Ph.D., Eng. Mikołaj Chlipała*** *and* ***Ph.D., Eng. Daniel Jaworski*** *for assisting me in the decision to start my PhD and for supporting me during the initial stages of this journey.*

I owe special thanks to my family: ***Mom*** *and* ***Dad*** *– for their unwavering certainty in the success of the challenge I undertook;* ***grandma Ela*** *and* ***Emila*** *– for reminding me that life beyond work exists;* ***grandpa Michał*** *and* ***aunt Marysia*** *– for cheering me on at every step of my academic path; and* ***aunt Kinia*** *– for discovering in me the spark of a scientist when I was young and for nurturing the scientific curiosity she undoubtedly helped ignite.*
I am also grateful to my ***brother Mateusz****, as well as* ***Wiktor****,* ***Agata****, and* ***Kacper*** *– for believing in my abilities, even when I myself began to doubt them.*

This journey would not have been possible without my friend, ***M.Sc. Eng. Dominika Krzyszczyk****, who over the course of my PhD ensured I did not get lost in the chaos of work and helped me maintain perspective – both regarding my responsibilities and myself.*
Equally invaluable during this time were my oldest friends: ***Wiktoria Ossowska****,* ***B.Eng. Izabela Balewska****,* ***M.Sc. Eng. Jakub Jeziorski****, and* ***M.Sc. Thomas Asensi.***

Finally, I would like to thank ***Ph.D., Eng. Robert Kozioł*** *and express my special gratitude for being my rock and for standing by me through all the highs and lows I have experienced over the past years. Your support and optimism have been a source of stability and strength in moments when I needed them most.*

Podziękowania

Realizacja niniejszej pracy doktorskiej nie byłaby możliwa bez udziału wielu osób, które dzieliły się ze mną swoją wiedzą, inspirowały mnie i towarzyszyły mi w codziennej pracy.

W pierwszej kolejności chciałabym podziękować mojej promotor, ***prof. dr. inż. Marii Gaździe****, za wsparcie merytoryczne oraz pełne zaangażowanie w zapewnianiu wysokiej jakości moich oraz naszych wspólnych prac. Jej autorytet naukowy, ale również niezwykła dbałość o precyzję językową, stanowiły nieocenioną wartość, z której starałam się czerpać jak najwięcej w trakcie kilku lat naszej bliskiej współpracy.*

Za otwartość na nowe pomysły oraz liczne, często wykraczające poza pierwotnie obrany nurt tematyczny, dyskusje dziękuję mojemu promotorowi pomocniczemu, ***dr. inż. Tadeuszowi Miruszewskiemu****, który wielokrotnie poszerzał moje horyzonty, dzieląc się swoją wiedzą i inspirując nieskrępowaną wyobraźnią.*

Dziękuję całemu ***zakładowi Protons in Solids*** *oraz kolegom z* ***Instytutu Nanotechnologii i Inżynierii Materiałowej****, z którymi miałam przyjemność współpracować – za dzielenie się swoim bogatym doświadczeniem oraz owocną współpracę przy tworzeniu nowych wkładów w rozwój naszej dyscypliny naukowej.*
Za wprowadzanie zdrowej atmosfery i tak dobrego humoru w naszym „kurniku", że aż czasem trudno było skupić się na pracy, pragnę podziękować ***mgr. inż. Joannie Pośpiech****,* ***mgr. inż. Darii Balcerzak*** *i* ***mgr. inż. Arkadiuszowi Dawczakowi****.*

Dziękuję również ***dr. inż. Piotrowi Okoczukowi*** *za wyciąganie mnie z wiru codzienności naukowymi – i nie tylko – dyskusjami poszerzającymi moje dotychczasowe obszary zainteresowań.*

Za pomoc w podjęciu decyzji o rozpoczęciu doktoratu oraz za wsparcie na początku tej drogi chciałabym podziękować ***dr. inż. Mikołajowi Chlipale*** *i* ***dr. inż. Danielowi Jaworskiemu****.*

Chciałabym również podziękować mojej rodzinie: ***Mamie*** *i* ***Tacie*** *– za niesłabnącą pewność powodzenia podjętego przeze mnie wyzwania,* ***babci Eli*** *i* ***Emili*** *– za przypominanie mi, że życie poza pracą istnieje,* ***dziadkowi Michałowi*** *i* ***cioci Marysi*** *– za kibicowanie mi na każdym kroku mojej akademickiej drogi, oraz* ***cioci Kini*** *– za odkrycie we mnie w młodości iskierki ścisłowca i pielęgnowanie naukowego płomienia, który niewątpliwe pomogła rozpalić.*
Dziękuję również mojemu ***bratu Mateuszowi****, oraz* ***Wiktorowi****,* ***Agacie*** *i* ***Kacprowi*** *– za wiarę w moje możliwości, nawet kiedy ja zaczynałam w nie wątpić.*

Przeżycie tej przygody nie byłoby możliwe bez mojej przyjaciółki, ***mgr. inż. Dominiki Krzyszczyk****, która przez ostatnie lata nie pozwalała mi się zagubić w chaosie pracy oraz pomagała mi zachować zdrowy dystans – zarówno do obowiązków, jak i do samej siebie.*
Nieocenieni w tym czasie byli również moi najstarsi przyjaciele: ***Wiktoria Ossowska****,* ***inż. Izabela Balewska****,* ***mgr inż. Jakub Jeziorski*** *oraz* ***M.Sc. Thomas Asensi****.*

Na koniec chciałabym podziękować ***dr. inż. Robertowi Koziołowi*** *i wyrazić szczególną wdzięczność za bycie moją opoką oraz towarzyszenie mi we wszystkich wzlotach i upadkach, których doświadczałam w ciągu ostatnich lat. Twoje wsparcie i optymizm były dla mnie źródłem stabilności i siły w chwilach, gdy najbardziej ich potrzebowałam.*

This research was supported by the National Science Centre of Poland under grant no. 2021/41/N/ST5/03437. X-ray absorption spectroscopy measurements were performed at the National Synchrotron Radiation Centre SOLARIS, supported by the Ministry of Science and Higher Education of Poland under contract no. 1/SOL/2021/2.

List of publications

Articles forming the basis of this dissertation:

1. **Budnik, J.**; Mielewczyk-Gryń, A.; Gazda, M.; Miruszewski, T. Water Uptake Kinetics and Electrical Transport in $BaCe_{0.6}Zr_{0.2}Y_{0.1}M_{0.1}O_{3-\delta}$ (M = Tb, Pr, Fe) Protonic Conductors. *J. Mater. Chem. A Mater.* **2023**, *11* (25), 13389–13398. https://doi.org/10.1039/D2TA07236J.

2. **Budnik, J.**; Mielewczyk-Gryń, A.; Gazda, M.; Miruszewski, T. Influence of Iron Content on Water Uptake and Charge Transport in $BaCe_{0.6}Zr_{0.2}Y_{0.2-x}Fe_xO_{3-\delta}$ Triple-Conducting Oxides. *J. Mater. Chem. A Mater.* **2024**, *12* (24), 14569–14582. https://doi.org/10.1039/D3TA06917F.

3. **Budnik, J.;** Gazda, M.; Maximenko, A.; Mielewczyk-Gryń, A.; Pośpiech, J.; Wachowski, S.; Witkowska, A.; Miruszewski, T. $Sr(Fe,Co)O_{3-\delta}$ Mixed Conductors: How Cobalt Drives Oxygen Vacancy Formation. *Chemistry of Materials* **2025**, *37* (21), 8822–8834. https://doi.org/10.1021/acs.chemmater.5c01904.

4. **Budnik, J.;** Gazda, M.; Miruszewski, T. Electrical and Thermoelectric Transport of $SrFe_{1-x}Co_xO_{3-\delta}$ Mixed-Conducting Perovskites. *Solid State Sci.* **2026**, *173*, 108174. https://doi.org/10.1016/j.solidstatesciences.2025.108174.

Other publications:

1. Czudec, M. M.; Jaworski, D.; **Budnik, J.**; Mielewczyk-Gryń, A.; Subramani, T.; Gazda, M.; Navrotsky, A.; Miruszewski, T. Thermoelectric and Electrical Properties of Triple-Conducting Multicomponent Oxides Based on Substituted Barium Cerate-Zirconate. *Dalton Transactions* **2024**, *54* (5), 1994–2004. https://doi.org/10.1039/d4dt01992j.

2. Kuc, K.; Czudec, M.; Jaworski, D.; **Budnik, J.**; Mielewczyk-Gryń, A.; Gazda, M.; Miruszewski, T. Thermoelectric and Electrical Transport Properties of Mixed-Conducting Multicomponent Oxides Based on $Ba(Zr,Ce)O_{3-\delta}$. *Journal of Physics and Chemistry of Solids* **2025**, *197*. https://doi.org/10.1016/j.jpcs.2024.112416.

Table of contents

Abstract

In this work, the relationships between chemical composition, crystal structure, and electrical transport properties in two distinct perovskite systems: $BaCe_{0.6}Zr_{0.2}Y_{0.2-x}M_xO_{3-\delta}$ compounds with mixed-valence metal substituents (BCZYM, where M = Tb, Pr, Fe) and the $SrFe_{1-x}Co_xO_{3-\delta}$ series (SFC, where x = 0, 0.2, 0.4, 0.6, 0.8); were investigated. The BCZYM materials demonstrate significant oxygen-ionic conductivity with high concentrations of mobile oxygen vacancies, enabling the incorporation of a substantial number of protons in humidified atmospheres. Proton defects contribute considerably to the total electrical conductivity. The SFC materials exhibit mixed ionic-electronic conducting behaviour with a predominant concentration of electronic charge carriers. In both material groups, the electronic transport in air is characterised by a p-type conduction mechanism.

Solid-state reactive synthesis enabled the fabrication of perovskite materials exhibiting high symmetry across all compositions. The addition of nickel oxide was confirmed to be crucial for achieving phase purity and densification of samples.

The defect chemistry analysis via iodometric titration and thermogravimetric analysis revealed that oxygen-vacancy concentrations systematically decreased with iron content in $BaCe_{0.6}Zr_{0.2}Y_{0.2-x}Fe_xO_{3-\delta}$ compositions. $BaCe_{0.6}Zr_{0.2}Y_{0.1}Tb_{0.1}O_{3-\delta}$ exhibited the highest vacancy concentration within the $BaCe_{0.6}Zr_{0.2}Y_{0.1}M_{0.1}O_{3-\delta}$ group. Proton incorporation in BCZYM materials at 300 °C proceeded predominantly via hydration reaction, with proton concentrations strongly depending on the oxygen nonstoichiometry. The dependencies of proton uptake efficiency on average cation electronegativity and A-B site electronegativity differences were confirmed.

Electrical transport measurements established thermally activated conduction behaviour across all compositions. Water vapour enhanced total electrical conductivity in all BCZYM samples through proton incorporation, with terbium substitution leading to the highest total electrical conductivity and the lowest activation energies for conduction in dry and wet air.

Electrical conductivity relaxation experiments revealed both single-fold and two-fold stoichiometry relaxation kinetics during hydration/dehydration processes in BCZYM materials. Hydration kinetics proceeded more rapidly with reduced activation energies compared to dehydration. In the case of oxidation/reduction processes, water vapour influenced oxygen incorporation and reduced the associated activation energies. In the case of reduction, these effects were composition-dependent.

The evaluation of ionic carriers' mobilities demonstrated that iron incorporation systematically reduced oxygen-vacancy mobility in BCZYM, while the lanthanide substitutions

enhanced it. $BaCe_{0.6}Zr_{0.2}Y_{0.1}Tb_{0.1}O_{3-\delta}$ and $BaCe_{0.6}Zr_{0.2}Y_{0.1}Pr_{0.1}O_{3-\delta}$ achieved the highest proton mobilities, exceeding the mobility in the $BaCe_{0.6}Zr_{0.2}Y_{0.2}O_{3-\delta}$ reference composition.

In the case of the SFC group, X-ray absorption spectroscopy studies revealed distinct oxidation state behaviours with varying cobalt content, with iron maintaining relatively stable 3.2+ oxidation state and cobalt exhibiting oxidation state of 2.9−3.0+. Cobalt acted as an oxygen vacancy stabilising centre, controlling the covalency of the transition metal-oxygen bond. Iron coordination environments varied between octahedral and lower-coordination geometries.

The SFC series also demonstrated p-type conduction via small-polaron hopping, achieving maximum conductivity of 177 S/cm for $SrFe_{0.6}Co_{0.4}O_{3-\delta}$ at approximately 500 °C. Thermoelectric measurements confirmed that the variations in electron-hole mobility, rather than carrier concentration changes, primarily governed the observed conductivity trends.

The influence of water on transport properties of $SrFe_{0.6}Co_{0.4}O_{3-\delta}$ was also investigated. The presence of water vapour led to reduced chemical surface exchange coefficients for both oxidation and reduction processes, limiting the surface reactions involving oxygen. Conversely, chemical diffusion coefficients for oxidation increased in wet conditions, indicating enhanced bulk oxygen transport. The total electrical conductivity measured in wet air remained lower across the entire temperature range, which was attributed primarily to a decreased mobility of electron holes. Below 650 °C, electron-hole concentrations were slightly higher in wet air. The reduced electron-hole mobilities in water vapour suggest possible structural distortions due to proton defect presence, which may also contribute to the observed enhanced chemical diffusion of oxygen in the bulk material.

The research presented in this dissertation was supported by the National Science Centre Poland under the PRELUDIUM project entitled “Influence of crystal structure on thermodynamics of proton transport in perovskite materials” (grant number 2021/41/N/ST5/03437).

Streszczenie

W niniejszej rozprawie zbadano zależności pomiędzy składem chemicznym, strukturą krystaliczną i właściwościami transportu elektrycznego w dwóch grupach materiałów perowskitowych: związkach $BaCe_{0,6}Zr_{0,2}Y_{0,2-x}M_xO_{3-\delta}$ z podstawnikami metali o zmiennej wartościowości (BCZYM, gdzie M = Tb, Pr, Fe) oraz serii $SrFe_{1-x}Co_xO_{3-\delta}$ (SFC, gdzie x = 0; 0,2; 0,4; 0,6; 0,8). Materiały BCZYM charakteryzują się mieszanym przewodnictwem jonowo-elektronowym, przy znacznym udziale przewodnictwa jonów tlenu dzięki wysokiej koncentracji wakansów tlenowych. Posiadają one zdolność tworzenia defektów protonowych w atmosferach mokrych, przy czym protony wnoszą istotny wkład do całkowitej przewodności elektrycznej BCZYM. Materiały SFC również wykazują mieszane przewodnictwo jonowo-elektronowe, przy czym koncentracja nośników elektronowych jest w nich dominująca.

Synteza w stanie stałym umożliwiła otrzymanie materiałów perowskitowych o wysokiej symetrii dla wszystkich składów, a dodatek NiO okazał się istotny dla uzyskania czystości fazowej oraz zagęszczenia próbek.

Analiza chemii defektów wykazała systematyczny spadek koncentracji wakansów tlenowych wraz ze wzrostem zawartości żelaza w $BaCe_{0,6}Zr_{0,2}Y_{0,2-x}Fe_xO_{3-\delta}$. Najwyższą koncentrację wakansów w grupie $BaCe_{0,6}Zr_{0,2}Y_{0,1}M_{0,1}O_{3-\delta}$ zaobserwowano dla $BaCe_{0,6}Zr_{0,2}Y_{0,1}Tb_{0,1}O_{3-\delta}$. Wprowadzenie protonów w 300 °C przebiegało głównie poprzez reakcję uwodnienia i silnie zależało od niestechiometrii tlenowej w związkach BCZYM. Zaobserwowano również zależność wydajności uwodnienia od średniej elektroujemności kationów i różnic elektroujemności pomiędzy kationami w pozycjach A i B sieci krystalicznej.

Badania właściwości elektrycznych wykazały aktywowany termicznie charakter przewodnictwa elektrycznego. Obecność pary wodnej zwiększała całkowitą przewodność elektryczną we wszystkich próbkach BCZYM, co wiązało się z wprowadzeniem protonów do struktury. Materiał podstawiany terbem wykazywał najwyższą całkowitą przewodność elektryczną i najniższe energie aktywacji w suchym i wilgotnym powietrzu spośród wszystkich badanych materiałów BCZYM.

Badania metodą relaksacji przewodnictwa elektrycznego potwierdziły występowanie zarówno jedno-, jak i dwustopniowej kinetyki relaksacji stechiometrii podczas procesów uwodnienia i odwodnienia, przy czym uwodnienie zachodziło szybciej i przy niższych energiach aktywacji. Obecność pary wodnej wpływała również na procesy utleniania/redukcji, ułatwiając wprowadzenie tlenu i obniżając energie aktywacji dla dyfuzji i wymiany powierzchniowej. Dla redukcji, efekty te były zależne od składu.

Analiza ruchliwości nośników jonowych wykazała, że Fe obniżało ruchliwość wakansów tlenowych w BCZYM, podczas gdy podstawienia lantanowców ją podwyższały. Składy $BaCe_{0,6}Zr_{0,2}Y_{0,1}Tb_{0,1}O_{3-\delta}$ oraz $BaCe_{0,6}Zr_{0,2}Y_{0,1}Pr_{0,1}O_{3-\delta}$ odznaczały się również najwyższą ruchliwością protonów, przewyższając ruchliwość protonów w materiale referencyjnym $BaCe_{0,6}Zr_{0,2}Y_{0,2}O_{3-\delta}$.

W przypadku grupy SFC, badania absorpcji promieniowania rentgenowskiego ujawniły różne zachowania stopni utlenienia: żelazo utrzymywało stabilny stopień utlenienia ok. 3.2+, natomiast kobalt przyjmował wartości 2.9−3.0+, pełniąc rolę centrum stabilizującego wakanse tlenowe i wpływając na kowalencyjność wiązań między metalem przejściowym a tlenem. Lokalna struktura wokół Fe zmieniała się pomiędzy geometrią oktaedryczną i niższymi koordynacjami, a udział wielościanów o obniżonej koordynacji rósł wraz z zawartością Co i lokalizował się głównie przy powierzchni materiałów.

Seria SFC również wykazywała przewodnictwo typu p poprzez mechanizm hoppingu małych polaronów, osiągając maksymalną przewodność 177 S/cm dla $SrFe_{0,6}Co_{0,4}O_{3-\delta}$ w ok. 500 °C. Pomiary termoelektryczne potwierdziły, że obserwowane trendy przewodnictwa wynikają głównie ze zmian ruchliwości dziur elektronowych, a nie zmian koncentracji nośników.

Zbadano również wpływ wody na właściwości transportowe $SrFe_{0,6}Co_{0,4}O_{3-\delta}$. Obecność pary wodnej prowadziła do obniżenia współczynników wymiany powierzchniowej tlenu zarówno dla procesów utleniania, jak i redukcji, ograniczając kinetykę reakcji powierzchniowych. Jednocześnie współczynniki dyfuzji chemicznej dla utleniania wzrosły w mokrej atmosferze, co wskazuje na poprawę transportu tlenu w objętości materiału. Całkowita przewodność elektryczna w atmosferze wilgotnej była jednak niższa w całym zakresie badanych temperatur, głównie z powodu zmniejszonej ruchliwości dziur elektronowych. Poniżej 650 °C koncentracja dziur elektronowych była nieco wyższa, co sugeruje, że obecność protonów mogła powodować lokalne deformacje strukturalne, wspomagające dyfuzję tlenu w objętości.

Badania prezentowane w niniejszej pracy zostały sfinansowane przez Narodowe Centrum Nauki w ramach projektu PRELUDIUM pt. „Wpływ struktury krystalicznej na termodynamikę transportu protonowego w materiałach perowskitowych” (nr grantu 2021/41/N/ST5/03437).

List of acronyms and symbols

Acronyms

AC	Alternating Current
AFC	Alkaline Fuel Cell
BCZY622	$BaCe_{0.6}Zr_{0.2}Y_{0.2}O_{3-\delta}$
BCZYFe2	$BaCe_{0.6}Zr_{0.2}Y_{0.18}Fe_{0.02}O_{3-\delta}$
BCZYFe5	$BaCe_{0.6}Zr_{0.2}Y_{0.15}Fe_{0.05}O_{3-\delta}$
BCZYFe10	$BaCe_{0.6}Zr_{0.2}Y_{0.1}Fe_{0.1}O_{3-\delta}$
BCZYM	$BaCe_{0.6}Zr_{0.2}Y_{0.2}M_xO_{3-\delta}$ (M = Tb, Pr, Fe)
BCZYPr	$BaCe_{0.6}Zr_{0.2}Y_{0.1}Pr_{0.1}O_{3-\delta}$
BCZYTb	$BaCe_{0.6}Zr_{0.2}Y_{0.1}Tb_{0.1}O_{3-\delta}$
BR	Branching Ratio
CPE	Constant Phase Element
DAFC	Direct Alcohol Fuel Cell
DC	Direct Current
ECR	Electrical Conductivity Relaxation
EIS	Electrochemical Impedance Spectroscopy
EXAFS	Extended X-Ray Absorption Fine Structure
FT	Fourier Transform
FY	Fluorescence Yield
GOF	Goodness Of Fit
HS	High Spin
IS	Intermediate Spin
IT-SOFC	Intermediate-Temperature Solid Oxide Fuel Cell
K-V	Kröger–Vink
LS	Low Spin
MCFC	Molten Carbonate Fuel Cell

MIEC	Mixed Ionic-Electronic Conductor
ORR	Oxygen Reduction Reaction
PAFC	Phosphoric Acid Fuel Cell
PCEC	Proton Ceramic Electrolysis Cell
PCFC	Proton Ceramic Fuel Cell
PEC	Protonic Electrochemical Cell
PEMFC	Proton Exchange Membrane Fuel Cell
PSC	Perovskite Solar Cells
SCO	$SrCoO_{3-\delta}$
SFC	$SrFe_{1-x}Co_xO_{3-\delta}$
SFO	$SrFeO_{3-\delta}$
SOEC	Solid Oxide Electrolysis Cell
SOFC	Solid Oxide Fuel Cell
SSRS	Solid-State Reactive Synthesis
TCO	Triple-Conducting Oxide
TEC	Thermal Expansion Coefficient
TEY	Total Electron Yield
TG	Thermogravimetry
TM	Transition Metal
TPB	Triple-Phase Boundary
XAFS	X-Ray Absorption Fine Structure
XANES	X-Ray Absorption Near Edge Structure
XAS	X-Ray Absorption Spectroscopy
XRD	X-Ray Diffractometry
YSZ	Yttria-Stabilised Zirconia

Symbols

$[i]$	molar concentration of *i*
a, b, c, α, β, γ	unit cell parameters
a_i	activity of species *i*
A_i''	interstitial anion (double ionised)
c_i	concentration of species *i*
D	diffusion coefficient
D_{chem}	chemical diffusion coefficient
D_i	self-diffusion coefficient of species *i*
δ	oxygen nonstoichiometry
ΔG	change in Gibbs free energy
ΔH	change in enthalpy
ΔS	change in entropy
ΔS_{config}	change in configurational entropy
ΔS_{vibr}	change in vibrational entropy
ΔV	thermovoltage
e	elementary charge
e'	electron
E_g	energy band gap
E_a	activation energy
γ	thermodynamic factor
$h^\bullet$	electron hole
$\hbar$	reduced Planck constant
$\chi(E)$	EXAFS function
χ_i	electronegativity of *i*
j_i	electrical current density transported by species *i*
k	photoelectron wavenumber
k_B	Boltzmann constant

k_{chem}	chemical surface exchange coefficient
K_X	equilibrium constant of reaction *X*
K_X'	reduced equilibrium constant of reaction *X*
L	Biot number
λ	wavelength
m_e	mass of electron
$M_i^{\bullet\bullet}$	interstitial metal (double ionised)
μ	absorption coefficient
μ_i	chemical potential of species *i*
n_d	number of defects
n_i	number of species *i* in the system
$OH_O^{\bullet}$	proton defect
OS_i	average oxidation state of *i*
p	concentration of electron holes
p_{H_2O}	partial pressure of water
p_{O_2}	partial pressure of oxygen
r_i	radius of ion *i*
R	resistance
R_{exp}	expected residual in Rietveld refinement
R_p	profile residual in Rietveld refinement
R_{wp}	weighted profile residual in Rietveld refinement
ρ_X	density of *X*
S	Seebeck coefficient
σ	electrical conductivity
σ_{el}	electronic conductivity
σ_i	partial conductivity of species *i*
σ_{ionic}	ionic conductivity

σ_{total}	total electrical conductivity
t	time
T	temperature
t_G	Goldschmidt tolerance factor
t_i	transference number of i
T_D	Debye temperature
T_{max}	temperature corresponding to the electrical conductivity maximum
θ	angle of X-ray incidence (in XRD)
u_i	mobility of charge carrier i
$u_{OH_O^{\bullet},max}$	upper limit for proton mobility
$u_{v_O^{\bullet\bullet},diff}$	mobility of oxygen vacancies established based on the diffusion data
$u_{v_O^{\bullet\bullet},\sigma_O}$	mobility of oxygen vacancies established based on the partial conductivity data
$v_A^{\bullet\bullet}$	anion vacancy (double ionised)
v_M''	metal vacancy (double ionised)

1. Introduction and motivation

In recent decades, awareness concerning the detrimental impact of human activities on the environment, primarily through the release of greenhouse gases, has increased. Furthermore, the rising global energy demand contributes to the depletion of fossil fuel supplies, underscoring the pressing need for alternative energy production solutions. Therefore, advancing sustainable and efficient energy technologies has emerged as a fundamental priority. Renewable energy sources, including wind, hydro, and solar power, offer a viable solution because they generate no greenhouse gas emissions or other pollutants. Nonetheless, their relatively low efficiency and high costs remain a substantial challenge. A potential alternative is the use of electrochemical devices, such as fuel cells, for energy production.

Various types of fuel cells exist, primarily categorised by their operating temperature and the specific kind of electrolyte employed. The schematic overview of the types of fuel cells with the corresponding operation temperatures is presented in **Figure 1.1**. Solid oxide fuel cell (SOFC) is one of the fuel cell types closest to commercialisation and/or already commercialised. Additionally, electrochemical devices such as solid oxide electrolysis cells (SOECs) enable the opposite process – converting electrical energy into chemical energy, which can also serve as a reliable method for energy storage. Nonetheless, the technologies discussed may present long-term stability issues, primarily related to the high temperatures required for the efficient operation of such devices.

Figure 1.1. Schematic overview of the types of fuel cells with the corresponding typical operation temperatures: direct alcohol fuel cell (DAFC), proton exchange membrane fuel cell (PEMFC), alkaline fuel cell (AFC), phosphoric acid fuel cell (PAFC), protonic ceramic fuel cell (PCFC), molten carbonate fuel cell (MCFC), and solid oxide fuel cell (SOFC) with oxygen-ion conducting electrolytes. The illustration was prepared based on information provided by Samsudin et al. and Zhang et al.[1,2]

A potential successor to the solid oxide electrochemical cell technology may involve electrochemical cells based on a proton-conducting electrolyte. Proton ceramic fuel cells (PCFCs) and proton ceramic electrolysis cells (PCECs) can operate efficiently at intermediate temperatures, eliminating the problems associated with long-term stability and degradation related to SOFCs/SOECs functioning at very high temperatures. They also present a set of advantages over these technologies, including the ability of PCFCs to directly use as fuel not only hydrogen but also hydrocarbons.

PCFCs closely correspond to SOFCs regarding the operating principles and main components of the device. The primary difference between the two lies in the electrolyte, which conducts protons in the case of PCFCs, whereas SOFCs employ oxygen-ionic conductors. This distinction results in lower operating temperatures of PCFCs compared to standard SOFCs, owing to the lower activation energies associated with proton conductivity compared to oxide-ionic conductivity.[3] Furthermore, in PCFCs, the main product of fuel cell operation, water, is generated on the cathode (positrode) side, as opposed to SOFCs, where the production of water occurs on the anode (negatrode), leading to the dilution of fuel in the latter. This results in enhanced fuel utilisation in PCFCs, a higher Nernst potential and improved performance in comparison to SOFCs.[4] A schematic representation of protonic and conventional solid oxide fuel cells fed with hydrogen, as well as their electrolyser counterparts, is shown in **Figure 1.2**.

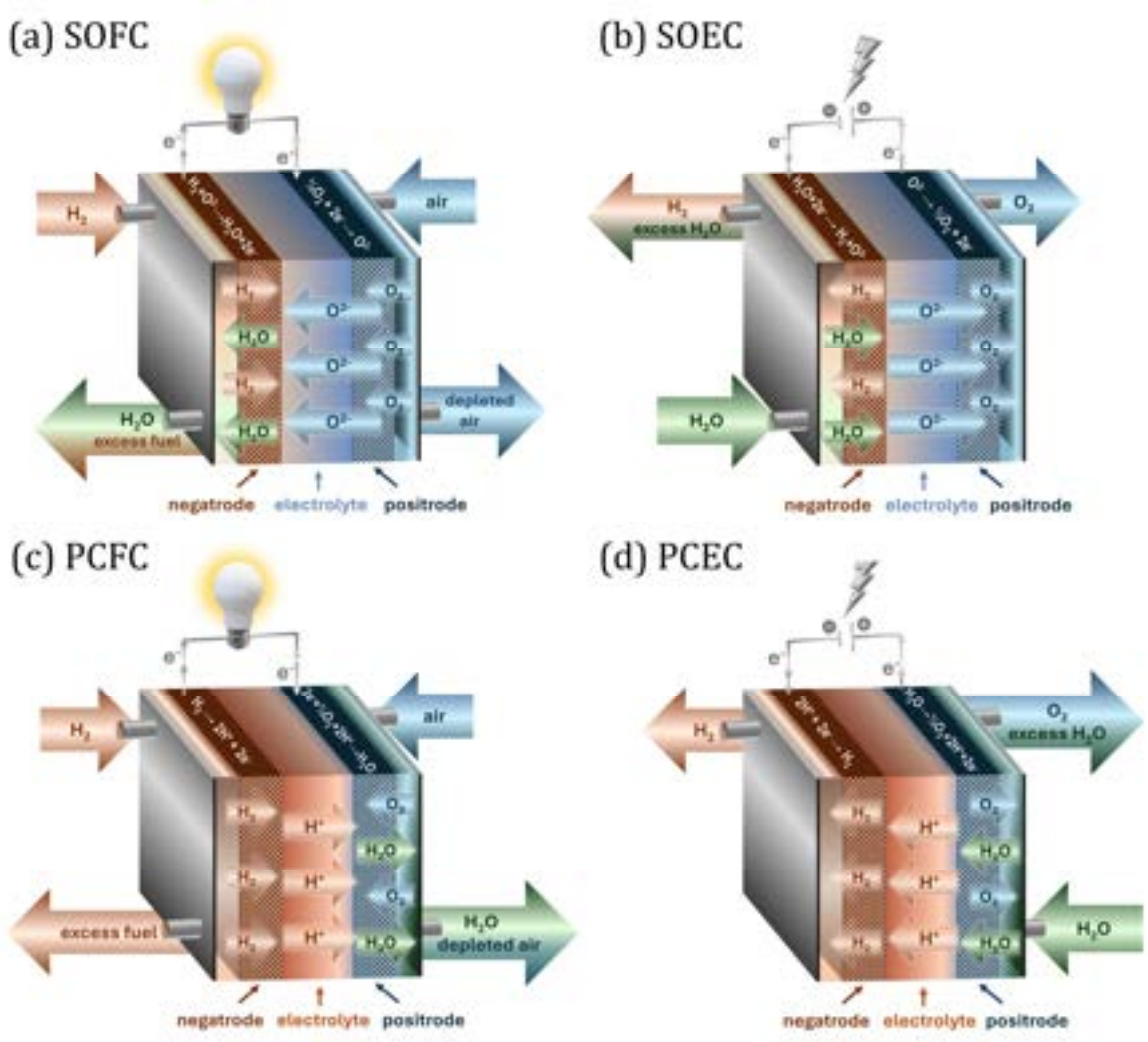

Figure 1.2. A schematic representation of different types of electrochemical cells with solid oxide electrolyte: conventional solid oxide fuel (a) and solid oxide electrolysis cell (b) with oxygen-ion conducting electrolytes, protonic ceramic fuel cell (c) and protonic ceramic electrolysis cell (d). The arrows signify the flow of gases and ionic species in various components of the cells. The electrochemical reactions on each electrode are shown on their top.

Another advantage of PCFCs is their higher tolerance to H_2S, CO, SO_2, and CO_2, allowing for the direct use of hydrocarbons without the need for prior fuel reforming. This results in considerably reduced emissions when compared to traditional methods utilising these fuels.[5] Consequently, since PCFCs can operate efficiently without the necessity of being hydrogen-fed, it allows them to avoid the challenges associated with hydrogen storage and transportation. In conclusion, compared to conventional solid oxide electrochemical cells, their protonic counterparts may offer several benefits, including longer device lifespans, reduced degradation, and decreased costs.[6,7] Moreover, the electrolysis in PCEC produces dry hydrogen since the incoming water is supplied on the positrode side of the device. In contrast, the hydrogen produced via SOECs requires additional drying afterwards.

The primary challenge in advancing fuel cell technology lies in the design and fabrication of appropriate materials for the elements of the device, particularly positrodes. The positrodes for fuel cells with solid oxide as an electrolyte need to fulfil several requirements, including high electronic conductivity, thermal expansion coefficient (TEC) that aligns with the TEC of the electrolyte, and a high specific surface area with active sites available for fast oxygen exchange reaction, facilitating an efficient oxygen reduction reaction (ORR). Moreover, because the water is produced on the positrode side of PCFCs, it must remain stable in high partial pressures of water (p_{H_2O}). Furthermore, the activity of the positrode can be improved by expanding the active area beyond the triple-phase boundary (TPB) region. One of the most promising groups of materials for this application is triple-conducting oxides (TCOs). TCOs are a class of ceramics that can conduct three types of mobile charge carriers: oxygen ions, electrons or electron holes, and protons. It may be a composite material, created by integrating a conventional mixed ionic-electronic conductor (MIEC) with a proton-conducting oxide, thereby expanding the cathode active area by introducing new TPBs at the interfaces of these phases.[8] An alternative approach involves employing a single-phase TCO that facilitates the conduction of the three mobile charge carriers within one material. However, due to the complex nature of the diffusion and electrical transport mechanisms associated with the conductivity of three types of charge carriers occurring in TCOs, a comprehensive description of these phenomena is essential. Nevertheless, the employment of TCO as a positrode material enables the active surface area to expand into the entire surface of the positrode, which leads to a tremendous enhancement of the electrocatalytic activity.[9] The schematic illustration of the transport paths of chemical species travelling to the electrochemically active sites in three types of materials employed as a positrode in PCFC is shown in **Figure 1.3**.

The properties of mixed proton conductors are complex and depend on several interconnected factors. The design of positrode materials frequently involves a compromise

between electronic and proton conductivity, which, when combined with other required properties such as chemical stability, catalytic activity, and mechanical compatibility with the electrolyte, makes it difficult.[10]

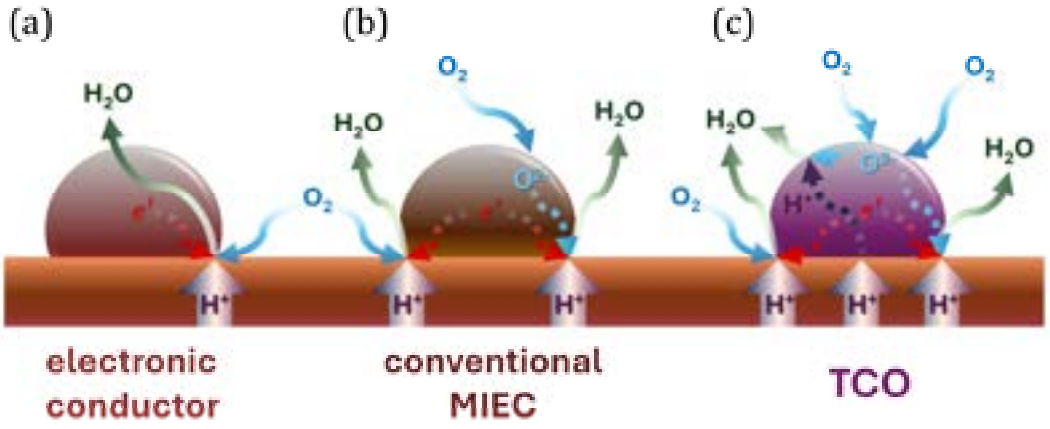

Figure 1.3. Schematic illustration of the chemical species moving to the electrochemically active sites in three different types of positrode materials in contact with an electrolyte (orange bar) in PCFC: electronic conductor (a), mixed oxygen-ionic - electronic conductor (b), and triple-conducting oxide (c). The dotted arrows signify the species moving within the positrode material.

Taking into account the potential advantages of mixed ionic-electronic conductors and triple-conducting oxides in protonic and solid oxide cells, among other electrochemical devices, a detailed understanding of the fundamental processes governing their transport properties is essential. The performance of positrode materials is determined not only by their electrical conductivity but also by the interplay between crystal structure, defect chemistry, and the mobility of different charge carriers under operating conditions. In particular, the water vapour and the resulting presence of proton defects can significantly modify both bulk transport and surface exchange processes. Therefore, systematic studies of relationships between composition, structure and transport properties in mixed-conducting perovskite oxides are vital to provide a reliable basis for the selection of materials for applications in energy conversion and other electrochemical processes.

1.1. Main objectives and theses

The aim of this work is to advance understanding of charge transport in mixed-conducting perovskites, with particular focus on the roles of chemical composition, structural properties, and defect chemistry. This work contributes to extensive research on mixed ionic-electronic conducting materials, including triple-conducting oxides, by providing detailed insights into the mechanisms governing ionic and electronic transport. The findings presented in this dissertation are expected to support the development and assessment of new perovskite materials for electrochemical applications.

The materials studied in this work are mixed ionic-electronic conductors belonging to the perovskite family, with the following compositions:

1) **$BaCe_{0.6}Zr_{0.2}Y_{0.2-x}M_xO_{3-\delta}$ compounds** substituted with mixed-valence metals (BCZYM, where M = Tb, Pr, Fe), which possess a high concentration of mobile oxygen vacancies, enabling a significant oxygen-ionic conductivity.
2) **$SrFe_{1-x}Co_xO_{3-\delta}$ series** (SFC), which exhibit mixed ionic-electronic conductivity with a predominance of electronic charge carriers.

The research presented in this work was based on the following scientific theses:

I. The type and amount of substituents control defect concentrations and transport properties in the following ways:
   a. mixed-valence metal substituents (Fe, Tb, or Pr) may improve partial electronic conductivity in BCZYM,
   b. Co stabilises oxygen vacancies in $SrFe_{1-x}Co_xO_{3-\delta}$ without reducing the symmetry of the crystal structure.

II. The addition of NiO as a sintering aid can simplify the solid-state synthesis and densification of single-phase materials.

III. Proton defects affect the transport of other charge carriers in mixed-conducting oxides.

To verify the theses listed above, the following tasks were carried out:

I. Synthesis of single-phase BCZYM and SFC groups of materials.

II. Characterisation of the crystal structure, including long-range order and local distortions, using X-ray diffraction and X-ray absorption spectroscopy.

III. Evaluation of the average oxidation states of transition-metal cations and their coordination environments using X-ray absorption spectroscopy.

IV. Determination of the concentration of mobile charge carriers, using iodometric titration, X-ray absorption spectroscopy, thermogravimetric analysis, and thermoelectric measurements.

V. Investigation of the electrical properties of BCZYM materials:
   a. Influence of water vapour on the total electrical conductivity,
   b. Partial electronic, oxygen-ionic, and protonic electrical conductivity,
   c. Mobilities of oxygen vacancies and protons.

VI. Investigation of the electrical properties of SFC materials:
   a. Influence of NiO sintering aid,
   b. Concentration and mobility of electron holes,

c. Influence of water vapour on the transport properties.

VII. Analysis of the oxygen and proton transport kinetics with the electrical conductivity relaxation method.

VIII. Analysis of the results in relation to the composition, defect chemistry and structural features of materials.

This dissertation is organised into five main chapters, as well as conclusions, literature, appendix, and lists of acronyms, symbols, figures and tables. The introduction, including the **motivation, objectives and theses** of the dissertation, is presented in **Chapter 1**. **Chapter 2 provides the theoretical background**, covering the fundamental aspects of perovskite materials, defect chemistry, diffusion mechanisms, oxygen-ionic and mixed ionic-electronic transport, and the concept of triple-conducting oxides. **Chapter 3 introduces the two groups of materials investigated** in this work: $BaCe_{0.6}Zr_{0.2}Y_{0.2-x}M_xO_{3-\delta}$ (M = Tb, Pr, Fe) and $SrFe_{1-x}Co_xO_{3-\delta}$. Their structural characteristics, defect chemistry and transport features are summarised to clarify the context for the experimental studies. **Chapter 4 describes the research methodology**, including the sample fabrication methods (solid-state synthesis and coprecipitation) and the characterisation techniques used: X-ray diffraction, X-ray absorption spectroscopy, thermogravimetry, iodometric titration, DC and AC electrical measurements, electrical conductivity relaxation and thermoelectric measurements. **The obtained results are presented in Chapter 5**, which is divided into two sections corresponding to the two material groups. Each section discusses the structural properties, defect chemistry, transport behaviour, and diffusion processes occurring in the studied materials. The results are summarised in **Conclusions**. The final part of the dissertation contains the lists of literature sources, figures, tables and an extensive appendix with supplementary results and details regarding the experimental methodology.

2. Theoretical background

2.1. Perovskite materials

Perovskites can be characterised by the general chemical formula ABX_3, where A and B are cations, while X is an anion. They are a broad class of materials exhibiting diverse properties, owing to their ability to contain different cations and anions on the A, B, and X sublattices. This translates into a wide variety of applications, such as catalysis[11], electrochemical energy storage and production, photovoltaics, supercapacitors[12], magnetic devices, and piezoelectrics[13]. Some of the most attention-grabbing applications of perovskites include electrodes for SOFCs and PCFCs, exhibiting high oxygen reduction activity and proton conductivity;[14,15] ferroelectric memories, employing ferroelectricity and antiferromagnetism for data storage;[16] and perovskite solar cells (PSCs), exhibiting a high efficiency of light harvesting, owing to the tunability of the optical band gaps of the utilised perovskite materials.[17,18]

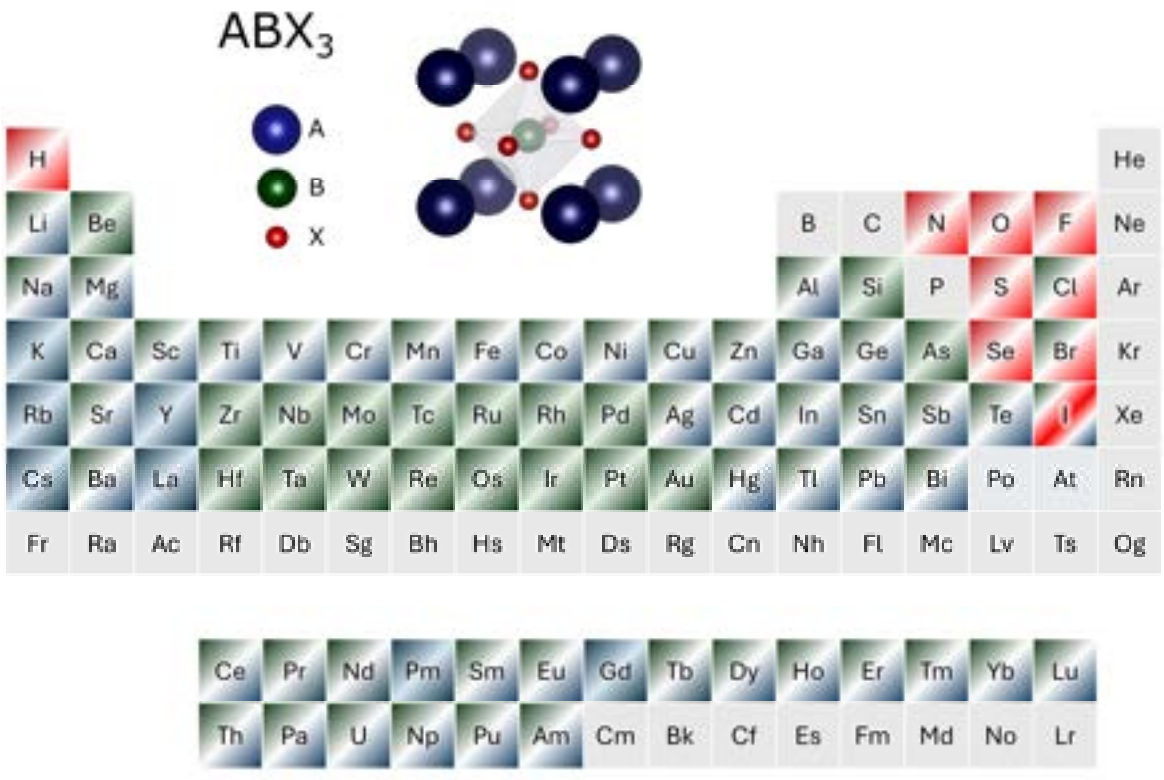

Figure 2.1. An overview of possible cations in A (blue), B (green), and X (red) sublattices of the perovskite structure for the elements of the periodic table. The illustration was prepared based on the works on Gibin et al.[19], Bhalla et al.[20], Aïssa et al.[21], and Tao et al.[17]

The elements reported to be able to occupy particular sublattices in the ABX_3 structure are shown in **Figure 2.1**. Depending on the elements and the external conditions such as temperature, pressure and partial pressure of oxygen, perovskite materials have different crystal structures, ranging from simple cubic (shown in **Figure 2.2**) to structures

of lower symmetry. The chemical composition and the crystal structure influence the properties and stability of the material. Owing to an enormous number of possible combinations of A, B, and X elements, as well as the modifications of the crystal structure, it is possible to achieve a wide range of carefully tailored features, such as mechanical, electrical, optical, and thermal properties, suitable for a chosen application.

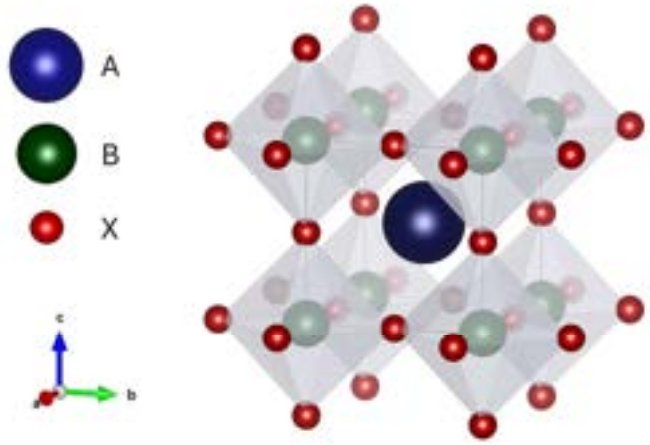

Figure 2.2. A unit cell of cubic perovskite ($Pm\bar{3}m$ space group). The illustration was prepared using Vesta software.[22]

In the ideal cubic perovskite unit cell (**Figure 2.2**) with a $Pm\bar{3}m$ space group, the large A cation resides in a 12-fold coordination (cuboctahedral) site, while the smaller B-site cation occupies BX_6 octahedra, with each octahedron sharing corners with six identical neighbouring octahedra. The perovskite structure may be predicted according to the value of the Goldschmidt tolerance factor,[23] which can be calculated as:

$$t_G = \frac{r_A + r_X}{\sqrt{2}(r_B + r_X)}, \tag{2.1}$$

where r_A, r_B, and r_X are the average radii of the A, B, and X ions, respectively. If t_G is close to 1 ($0.9 < t_G < 1$), the structure will assume cubic symmetry. The cubic structure might also be seen at lower t values, such as $0.75 < t_G < 1.0$. If the tolerance factor deviates from unity, some octahedra tilting or deformation can be expected. For small t_G values, the symmetry is reduced to orthorhombic, rhombohedral, tetragonal, monoclinic, and triclinic, while for $t_G > 1$, the structure can be hexagonal.[24] The rotation of octahedra can result in a tilt pattern corresponding to an orthorhombic symmetry in which the A cations possess lower coordination than in the ideal cubic structure. This may lead to a decrease in the mobility of ionic carriers. Furthermore, Jahn-Teller distortions can deform the BX_6 octahedra by elongating and compressing them in perpendicular axes, resulting in orthorhombic or tetragonal crystal structures. However, such distortions generally require the presence of Jahn-Teller active ions, such as Mn or Cu.[25,26] Another factor that can influence the symmetry

of the perovskite unit cell is oxygen deficiency. In the case of a significant deviation from the ideal oxygen stoichiometry, vacancy ordering can occur, leading to the formation of new crystal structures with lower symmetry, such as brownmillerites, described by the formula $A_2B_2O_5$. Brownmillerites can be imagined as structures composed of two alternating perovskite layers of tetrahedral and octahedral symmetry. Oxides exhibiting such structures can be beneficial in terms of ionic conductivity, e.g. for the application in electrochemical devices such as fuel cells operating at intermediate temperatures.[27,28]

Aside from the most prevalent ABX_3 perovskite materials, other, more complex perovskite structures, such as double- and layered perovskites, can also be obtained. The double perovskite structure is characterised by the B sites occupied by two distinct cations (denoted as B and B') in an ordered, alternated way. This doubles the unit cell, which can be described with the chemical formula $A_2BB'X_6$. This particular arrangement of B cations determines their transport and magnetic properties, such as antiferromagnetism.[29] Despite the concerns over their stability, double perovskites can find many applications, e.g. in photovoltaics, reaching high power conversion efficiencies without containing lead in their composition.[30,31] Furthermore, these materials exhibit potential in electrochemical applications, serving as catalysts for the oxygen evolution reaction.[32]

On the other hand, layered perovskites consist of parallel, ordered layers of atoms separated by spacer motifs. They can be divided into three families: Ruddlesden-Popper phases, Dion-Jacobson phases, and Aurivillius phases. The layered structures facilitate anisotropic conductivity and can improve ionic transport, which is beneficial for solid oxide fuel cells and photocatalytic water splitting.[33] Nonetheless, this study will focus on oxides exhibiting the ABX_3 perovskite structure, meaning the mentioned complex structures will not be explored further.

2.2. Defect chemistry of crystalline solids

The properties of solids, particularly their stability, electrical, mechanical, and thermal properties, are influenced by the defects in their structure. Defects in crystalline materials can be categorised by their dimensionality into point defects (0D), line defects (1D), plane defects (2D), and volume defects (3D). Each defect and its concentration can affect material characteristics.

In ionic solids, especially ionic conductors, point defects determine the transport properties of the material, influencing the concentration and mobility of the ionic charge carriers. There are several types of point defects possible to occur in crystalline solids. To describe the defects and the reactions of defect formation, the Kröger-Vink (K-V) notation can be employed. K-V notation specifies the standard adopted in the field of defect chemistry,

describing the charge of the defect and its position in comparison to the neutral charge and the position of the considered species in an ideal crystal. An example of a defect presented in a Kröger-Vink notation can be written as:

$$A_C^B, \tag{2.2}$$

where B is the charge of the defect, calculated in relation to the charge of the position C it occupies, and A is the type of a chemical species (or its lack) it represents. A can be an atom of the host material or an atom not initially present in the host material (a dopant or a substituent), a vacancy, an electron or an electron hole. It can also represent an atom or ion in an interstitial position. In K-V notation, the charge of the defect is calculated as the difference between the charge of the species occupying the considered lattice site and the charge of this site in the ideal crystal. Therefore, if the defect possesses a charge higher than the original atom, the charge is presented as a dot or dots (•). If the charge of a defect is lower, the symbol of the negative charge (′) is used. If the charges are equal, the "X" sign is used.

There are multiple variations of the point defect that can be present in ionic crystals, such as vacancies, interstitial atoms, dopants/substituents, Frenkel (and anti-Frenkel) defects, Schottky (and anti-Schottky) defects, proton defects, and localised electronic defects. Depending on the composition of the material, its symmetry, and external conditions such as temperature and partial pressure of oxygen or water, different defects can dominate. The summary of structural point defects in an ionic solid with an example reaction of formation and an impact of its presence on the crystal is presented in **Table 2.1**. The illustration of each defect in a crystal lattice is shown in **Figure 2.3**. A vacancy represents a vacant position in the crystal lattice site, which causes a lattice deformation in its proximity and reduces the density of the crystal. An interstitial atom is an atom of the host material or some foreign atom occupying a position between the lattice sites of an ideal crystal. Its presence also leads to some lattice distortion; however, it increases the density of the crystal. A substituent is a foreign atom (not present in an ideal host material) occupying a site or interstitial position. Depending on their size and charge, they can deform the crystal lattice differently. Moreover, if the ionic radius and charge of this atom are similar to those of an atom of the host material occupying this position, a solid solution can be formed. However, if the charge of the substituent differs from that associated with the site it occupies, its presence can lead to an emergence of additional electronic or other point defects. If the substituent is of lower valency, it can be considered an acceptor, while if its valency is higher, a donor. An acceptor in oxide can introduce oxygen vacancies ($v_O^{\bullet\bullet}$) and electron holes

($h^{\bullet}$), whereas a donor can introduce electrons (e') or lead to the formation of metal vacancies (v_M'').

A Frenkel defect is formed when a cation leaves its lattice site and localises in an interstitial position. As a result, a pair of defects emerges: cation vacancy (v_M'') and a cation in an interstitial position ($M_i^{\bullet\bullet}$). This defect type dominates in materials in which the cations are much smaller than the anions. The opposite situation, in which an anion leaves its site and occupies an interstitial position, is called an anti-Frenkel defect.

Table 2.1. Structural point defects in a hypothetical MO oxide, with their corresponding example reaction of formation, reduced equilibrium constant, and the impact they have on the crystal.

Type of defect	Reaction of formation	Equilibrium constant	Impact on the material
(oxygen) vacancy	$O_O^X = \frac{1}{2}O_2 + \boldsymbol{v_O^{\bullet\bullet}} + 2e'$	$K'_{red} = [v_O^{\bullet\bullet}]n^2 {p_{O2}}^{\frac{1}{2}}$	• decrease in density • increase in ionic conductivity
interstitial (oxygen) ion	$\frac{1}{2}O_2 = \boldsymbol{O_i''} + 2h^{\bullet}$	$K'_{ox} = [O_i'']p^2 {p_{O2}}^{-\frac{1}{2}}$	• increase in density
substituent (donor)	$Mh_2O_3 = 2\boldsymbol{Mh_M^{\bullet}} + 2O_O^X + 2e' + \frac{1}{2}O_2$	-	• increase in electronic conductivity • possible influence on ionic conductivity
Frenkel defect	$M_M^X + v_i^X = \boldsymbol{M_i^{\bullet\bullet}} + \boldsymbol{v_M''}$	$K'_F = [M_i^{\bullet\bullet}][v_M'']$	• possible influence on electronic and ionic conductivity[34,35]
anti-Frenkel defect	$A_A^X + v_i^X = \boldsymbol{A_i''} + \boldsymbol{v_A^{\bullet\bullet}}$	$K'_{AF} = [A_i'']{[v_A^{\bullet\bullet}]}$	• increase in electronic hopping conductivity[36] • possible influence on thermal properties[37]
Schottky defect	$M_M^X + A_A^X = M_M^X + A_A^X + \boldsymbol{v_M''} + \boldsymbol{v_A^{\bullet\bullet}}$	$K'_S = [v_M'']{[v_A^{\bullet\bullet}]}$	• decrease in density • reduction in thermal conductivity[37] • influence on structural stability and ionic transport[38]
anti-Schottky defect	$M_M^X + A_A^X = \boldsymbol{M_i^{\bullet\bullet}} + \boldsymbol{A_i''}$	$K'_{AS} = [A_i'']{[M_i^{\bullet\bullet}]}$	• increase in density • influence on mechanical properties[39]
proton	$H_2O_{(g)} + O_O^X + v_O^{\bullet\bullet} = 2\boldsymbol{OH_O^{\bullet}}$	$K'_{OH} = [OH_O^{\bullet}]^2[v_O^{\bullet\bullet}]^{-1}{p_{H2O}}^{-1}$	• introducing proton conductivity

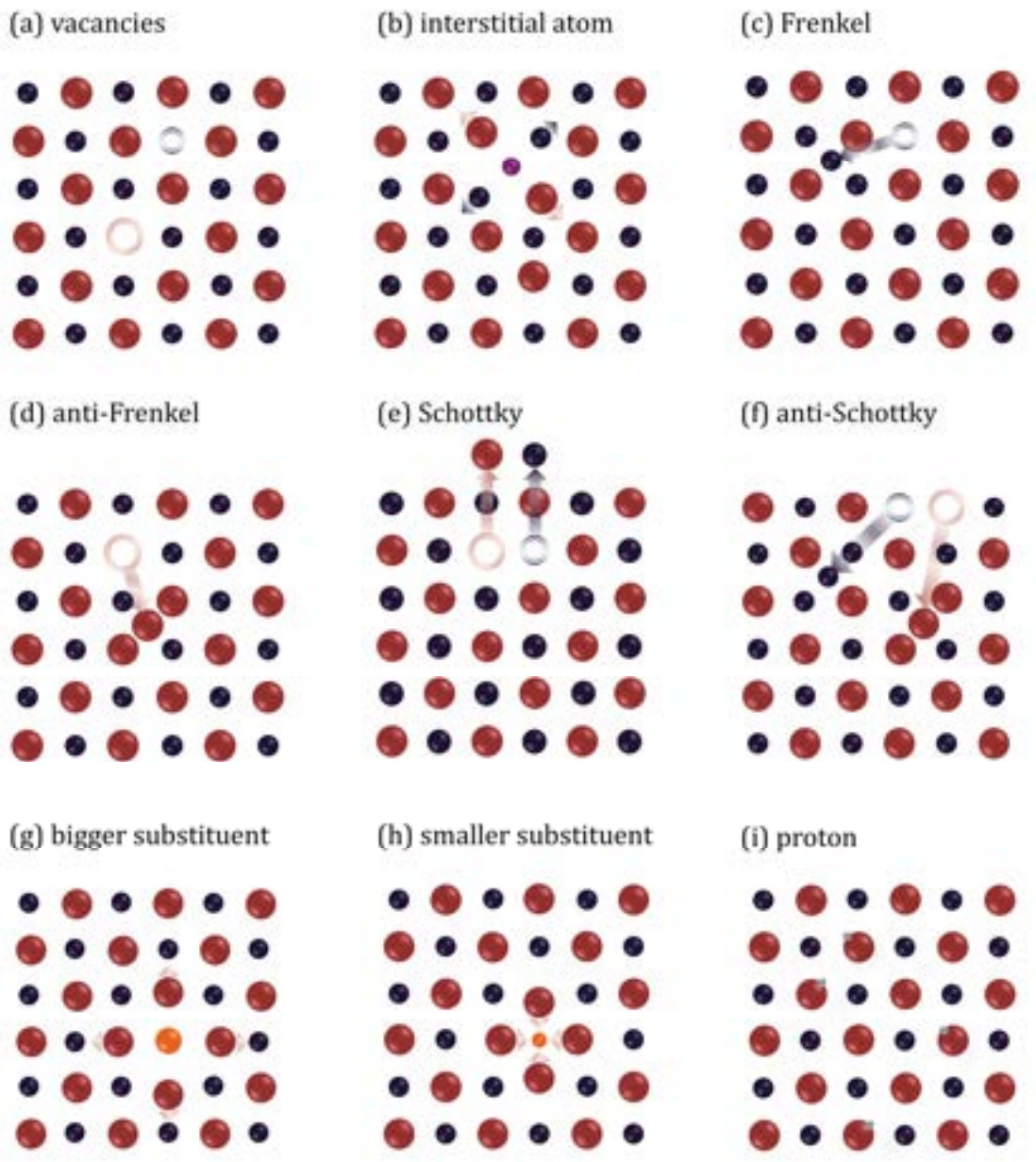

Figure 2.3. Illustration of point defects occurring in ionic crystals: cation and anion vacancies (a), a foreign atom in an interstitial position (b), Frenkel defect (c), anti-Frenkel defect (d), Schottky defect, anti-Schottky defect (f), cation substituent bigger (g) and smaller (h) than the host atom in a lattice position, and proton defects (i). The red atom signifies an anion, and the dark blue atom signifies a cation. Arrows indicate the direction of atom movement.

A Schottky defect is created when both cation and anion leave their lattice sites and settle on the surface of the material, which results in the formation of a defect pair consisting of a cation vacancy (v_M'') and an anion vacancy ($v_A^{\bullet\bullet}$). In the case of the compounds of stoichiometries other than MO, a Schottky defect is not a pair of cation and anion vacancies but consists of a different number of vacancies. It is prevalent in close-packed crystals made of cations and anions of similar ionic radii. An anti-Schottky defect represents an opposite scenario, in which cation and anion leave their sites and move to the interstitial positions (creating $M_i^{\bullet\bullet}$ and A_i'', respectively).

A proton defect represents a hydrogen atom covalently bonded with an oxygen atom in a crystal lattice. In the case of inorganic oxides, hydrogen is not a constituent of a compound. The presence of proton defects inside the material requires exposing the oxide to a humidified atmosphere. The water can react with the material, which incorporates protons through hydration or hydrogenation reactions. The proton defects will be discussed in detail in the subsequent chapters.

The material properties dependent on the intrinsic point defects are determined by their concentration, which is governed by thermodynamics. The equilibrium state corresponds to a minimum of Gibbs free energy of the system, which can be defined as:

$$\Delta G = \Delta H_{system} - T\Delta S_{system}, \tag{2.3}$$

where ΔG represents a change in the Gibbs free energy of the system, ΔH_{system} is a change in enthalpy, T is a temperature, and ΔS_{system} is a change in entropy in the system resulting from the formation of considered defects. The defect concentration at a certain temperature and pressure corresponds to the equilibrium conditions. Entropy can be divided into vibrational and configurational entropy, which corresponds to the formation of new defects. Hence, a more detailed representation of ΔG can be written as:

$$\Delta G = n_d(\Delta H - T\Delta S_{vibr}) - T\Delta S_{config}, \tag{2.4}$$

where ΔH and ΔS_{vibr} is the enthalpy and vibrational entropy associated with the formation of one defect, respectively, ΔS_{config} is the configurational entropy, and n_d is the number of defects created. The change in vibrational entropy can be defined as the difference between the frequency of vibration of atoms in the proximity of the created defect (υ') and the vibration frequency of the same atoms in an ideal crystal (υ). It can be written as:

$$\Delta S_{vibr} = X_{at} k_B \, ln(\upsilon/\upsilon'), \tag{2.5}$$

where X_{at} denotes the number of the affected atoms around the defect and k_B is the Boltzmann constant. Depending on the defect type, the influence of the vibrational entropy can be different, since the change in the vibration frequency caused by the defect can be either positive (e.g. for interstitial atoms) or negative (e.g. for vacancies). The configurational entropy can be expressed using the formula:

$$\Delta S_{config} = k_B \, ln \, W, \tag{2.6}$$

where W represents a probability that can be defined through the number of combinations in which a number n_d of defects can occupy the $N + n_d$ sites, where N is the number of lattice sites in a crystal. The thermodynamic probability W can be written as:

$$W = \frac{(N + n_d)!}{N!\, n_d!}. \tag{2.7}$$

Since the numbers of lattice sites and defects are very large in real crystals, Stirling's approximation can be employed to simplify equations (2.6) and (2.7):

$$\Delta S_{config} = k_B \left(N \ln \frac{N + n_d}{N} + n_d \ln \frac{N + n_d}{n_d} \right), \tag{2.8}$$

which shows the scaling of configurational entropy with the crystal size (N). However, ΔS_{config} is not proportional to the number of defects n_d.

The curves representing the dependence of enthalpy and both entropies and the resulting Gibbs free energy on the defect concentration are shown in **Figure 2.4**. The creation of new defects increases the total enthalpy of the system, but at the same time, the entropy part of the equation (2.3) decreases, since the formation of defects increases the entropy of the system. The equilibrium will be reached when the sum of both contributions reaches a minimum. Therefore, the defect formation will take place in the material spontaneously until the number of defects reaches the equilibrium n_{eq}, associated with the minimum of Gibbs free energy ΔG_{min} for given conditions. The defects will always be present in any crystal above 0 K.

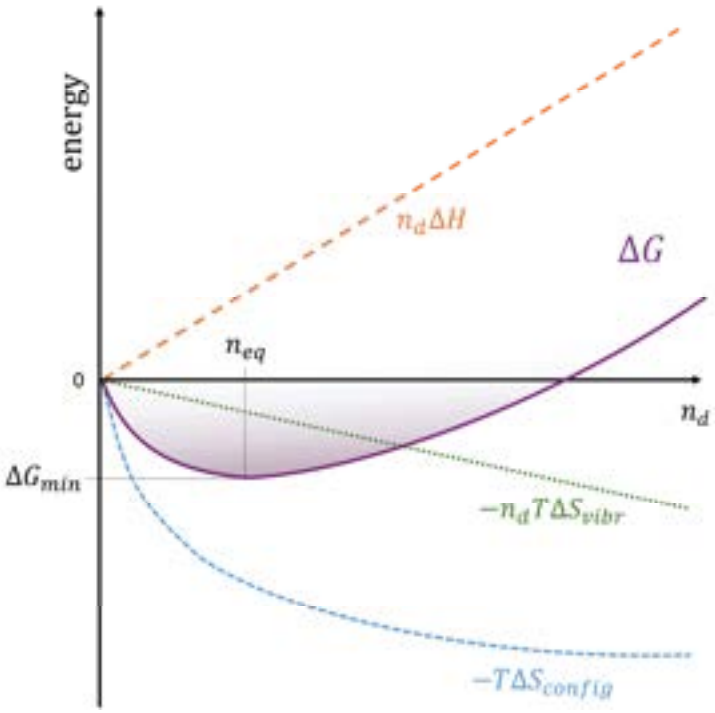

Figure 2.4. The enthalpy of formation, configurational and vibrational entropy, and Gibbs free energy, as a function of number of defects n_d. ΔG_{min} and n_{eq} signify the values of Gibbs free energy and number of defects corresponding to the thermodynamic equilibrium.

In order to determine the equilibrium concentration of a defect, one needs to find a minimum to equation (2.4). By setting its derivative with respect to n_d equal to zero, the equilibrium number of defects n_{eq} for given conditions can be established:

$$n_{eq} \approx N \cdot exp(-\Delta H/k_B T) \cdot exp(\Delta S_{vibr}), \tag{2.9}$$

hence, the number of intrinsic defects at a certain temperature depends on the enthalpy and vibrational entropy associated with the formation of those defects.

The concentration of extrinsic point defects in a crystal, which form as a result of introducing substituents or changing the stoichiometry, can be described similarly to species in a solution, where the concentration is determined by the activities of each chemical species taking part in the reaction of the defect formation. For a reaction written as:

$$aA + bB \leftrightarrows cC + dD, \tag{2.10}$$

where A and B are the reagents, C and D are the products of the reaction, while a, b, c, and d are the chemical reaction coefficients, controlling the concentrations of species in equilibrium; the change in Gibbs free energy associated with that reaction can be expressed using the chemical potential of each species taking part in the reaction – as a difference between the contributions related to products and reactants:

$$\Delta G = \Delta n_C \mu_C + \Delta n_D \mu_D - (\Delta n_A \mu_A + \Delta n_B \mu_B), \tag{2.11}$$

where μ_A, μ_B, μ_C, and μ_D represent the chemical potentials corresponding to A, B, C, and D, respectively, while Δn_A, Δn_B, Δn_C, and Δn_D signify the change in the number of each species in the system. The chemical potential of a species depends on a temperature and can be written in terms of its activity as:

$$\mu_i = \mu_i^0 + k_B T \, ln \, a_i, \tag{2.12}$$

where μ_i^0 is the chemical potential of species i at standard conditions, a_i is an activity of this species. Therefore, the change of the Gibbs free energy can be expressed as:

$$\Delta G = \Delta G^0 + k_B T \, ln \left(\frac{a_C^c a_D^d}{a_A^a a_B^b} \right), \tag{2.13}$$

where ΔG^0 signifies the change of Gibbs free energy in standard conditions. Owing to the low number of defects in comparison to the total number of atoms constituting the crystal, the activities of species in most materials can be approximated by using a molar fraction for each species i. In an equilibrium state, when the change of Gibbs free energy is equal to 0, the formula describing ΔG^0 can be simplified to:

$$\Delta G^0 = -k_B T \, ln \, K, \tag{2.14}$$

where K is called an equilibrium constant. Since Gibbs free energy can be defined through enthalpy and entropy, the equilibrium constant can be expressed in terms of standard enthalpy and standard (vibrational) entropy as:

$$K = K^0 \cdot exp\left(-\frac{\Delta H^0}{k_B T}\right) = exp\left(\frac{\Delta S^0_{vibr}}{k_B}\right) \cdot exp\left(-\frac{\Delta H^0}{k_B T}\right). \quad (2.15)$$

K is constant at a given temperature and pressure, hence one can also use reduced equilibrium constants, which omit the other constant parameters. The equations of reduced equilibrium constants corresponding to the example equations of point defect formation reactions for various point defects are presented in **Table 2.1**.

Aside from the point defects, there are also defects of higher dimensionality. The line (1D) defects represent dislocations, including edge dislocations, screw dislocations, and a combination of the two. Dislocations alter the order of neighbouring crystallographic planes, resulting in the contraction/expansion of the crystal lattice in its proximity. Since their ability to move through the material facilitates plastic deformation, the presence of dislocations directly influences the mechanical properties of the material, including ductility and mechanical strength.

Another class of defects in crystalline materials is plane (2D) defects, e.g., surfaces, phase interfaces, grain boundaries, and stacking faults. A phase boundary represents an interface between two distinct crystalline phases. They can be coherent when the atoms of the neighbouring phases are correlated and bonded, noncoherent when there is no bonding between the atoms of different phases, or semi-coherent when only some of the atoms are bonded. Another type of plane defect is a grain boundary, representing an interface between two crystallites/grains of a varied crystallographic orientation. Grain boundaries can significantly influence the diffusion and electrical properties of the polycrystalline material. The diffusion of species along a 1D or 2D defect occurs more rapidly than the diffusion across the crystal lattice; hence, the plane (and line) defects create easy diffusion paths in the ceramic.

A volume defect is another category of defect in a crystalline solid. They can include pores, which are small regions inside the material without any atoms, or inclusions, representing regions made of foreign phases inside the host crystal.

Aside from structural defects, electronic defects in a crystal can also exist, including electrons and electron holes. They can be localised on a specific atom or delocalised. The localised electronic defects are created when the metal in the crystal changes its oxidation state. Such electronic defects can propagate through the material through hopping between localised states. On the other hand, a delocalised electronic defect is not bound to any atom but propagates occupying the states in the conduction band or the valence band (for electrons

and holes, respectively). This results in a higher mobility associated with these charge carriers. A formation of intrinsic electronic defects can be written as:

$$0 = e' + h^{\bullet}, \tag{2.16}$$

with the corresponding reduced equilibrium constant:

$$K_i' = [e'][h^{\bullet}]. \tag{2.17}$$

The concentration of mobile electrons depends on the temperature, since the excitation requires thermal energy. It also depends on the ionisation energy ΔH_i, which, in the case of intrinsic generation, is defined by the energy band gap E_g of the material:

$$[e'] = [h^{\bullet}] = (K_i')^{\frac{1}{2}} \sim exp\left(\frac{-\Delta H_i}{2k_B T}\right) = exp\left(\frac{-E_g}{2k_B T}\right). \tag{2.18}$$

Localised and delocalised electronic defects are responsible for the electronic conductivity.

2.3. Diffusion in ionic solids

Since ionic conductivity depends on the mobility of mobile ions, which are determined by their diffusion coefficient, the transport properties of ionic solids are strictly related to the diffusion phenomena. Furthermore, the diffusion in solids facilitates the chemical reactions and microstructural changes. Diffusion in polycrystalline solids occurs as a lattice diffusion through point defects such as vacancies or interstitial ions. It can also proceed through the dislocations, grain boundaries, or any surfaces, which constitute fast diffusion paths. This type of diffusion typically occurs more rapidly than lattice diffusion. The effectiveness and contributions of various types of diffusion are primarily determined by temperature and the microstructure of the material.

2.3.1. Mechanisms of diffusion

The lattice diffusion occurs through the movement of point defects. There are a few mechanisms of such diffusion: vacancy, interstitial, and interstitialcy mechanisms, and some more complex ones, such as crowdion and ring mechanisms. The diffusion of defect clusters is also observed in oxides with high nonstoichiometry. The illustrations depicting the lattice-diffusion mechanisms for the movement of individual point defects are shown in **Figure 2.5**.

The vacancy mechanism involves an atom at a lattice site moving into the vacancy next to it, filling it and leaving the empty site behind. It can also be perceived as a movement of vacancies in the opposite direction. The interstitial mechanism involves an atom moving from one interstitial site to another nearby. It leads to a significant lattice distortion, which makes it probable only in the case of a smaller atom diffusing between the larger atoms occupying the crystal lattice. For instance, such a scenario can be observed in metals,

when atoms of light elements (e.g., hydrogen, carbon, nitrogen) diffuse through the lattice. It can also occur in some oxides, especially those exhibiting fluorite, brownmillerite and perovskite crystal structures. The interstitialcy mechanism also involves the movement of an atom in an interstitial position. The interstitial atom pushes one of the nearest atoms occupying the lattice site, causing it to move into another interstitial position, while the first atom takes its place in the lattice site. The direction of the movement of the second atom into a new interstitial position can be the same as the jump causing the push (collinear) or different (noncollinear). The crowdion mechanism of diffusion is also a type of interstitialcy mechanism, in which the additional atom is put inside a line of other atoms, causing a crowded packing of atoms displaced from their equilibrium positions in this region. The movement of such a defect occurs along the line. This form of diffusion can take place in elemental solids. Another mechanism of diffusion is ring diffusion, in which a group of atoms forms a circle ("ring") and rotates within it by exchanging positions. It does not require any defects to be included in such a movement. Ring diffusion can occur in metals; however, it is less prevalent than vacancy or interstitial mechanisms.

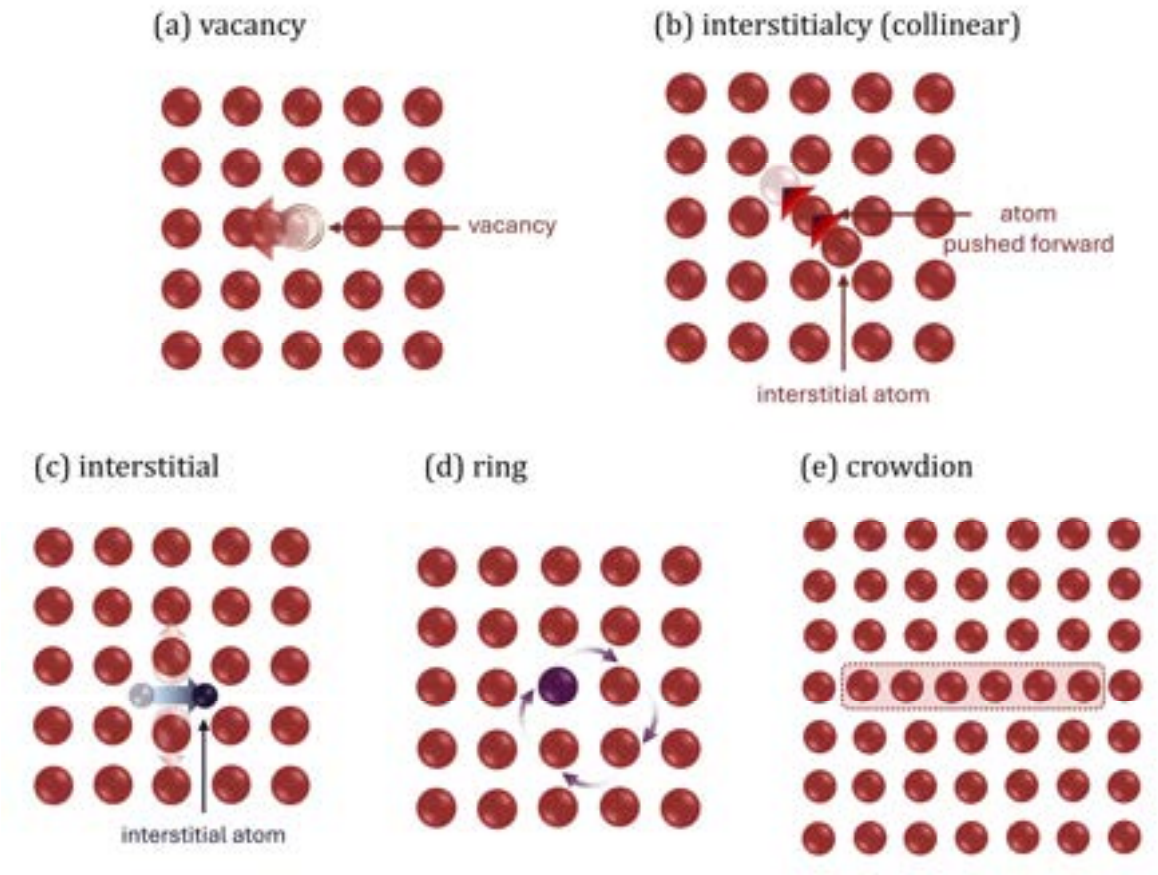

Figure 2.5. Illustrations depicting various mechanisms of diffusion in crystalline solids: vacancy (a), interstitialcy (b), interstitial (c), ring (d), and crowdion (e) mechanisms.

2.3.2. Mechanisms of proton diffusion

The diffusion of protons may proceed in a solid according to one of two mechanisms: the vehicular or Grotthuss mechanism. An illustration of both mechanisms is shown in **Figure 2.6**. The vehicular mechanism involves the movement of a proton bound to oxygen, moving together as a pair through the lattice. Therefore, it consists of the movement of an oxygen ion – via vacancy or interstitial mechanism; however, the activation energy of such diffusion is lower than the one corresponding to the diffusion of the oxygen ion itself. This stems from the fact that the radius of the hydroxide ion is smaller than the oxygen ion (100 pm vs 140 pm). This type of proton diffusion mechanism can be observed, e.g. in hydrochloric acid or Nafion.[40,41]

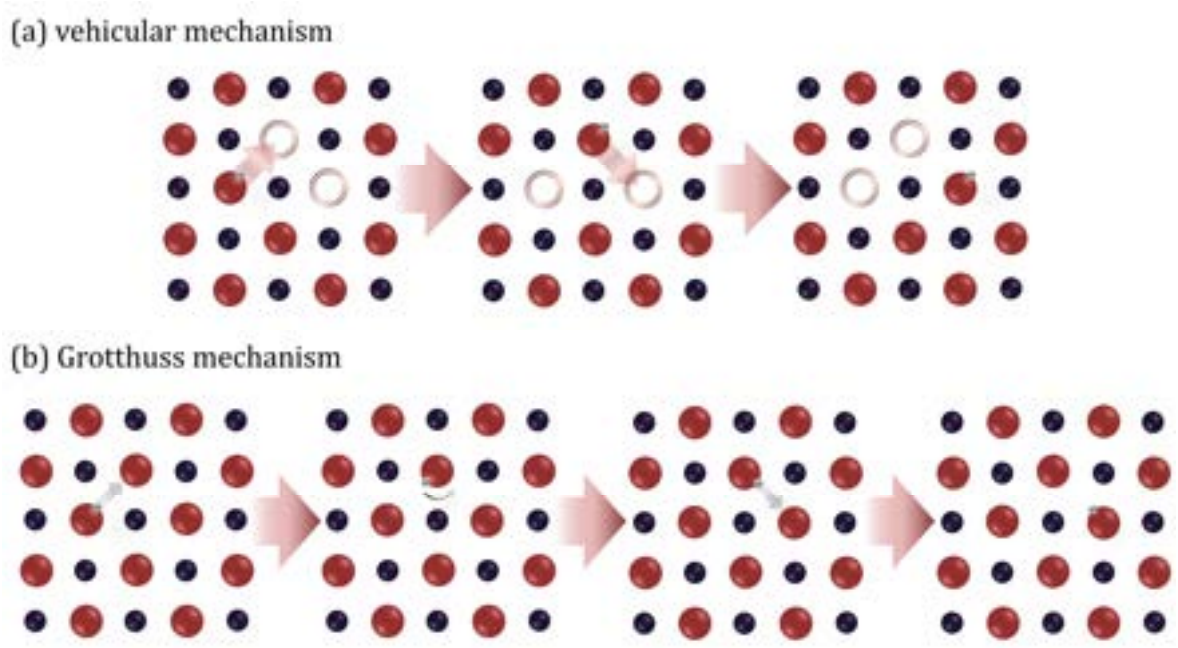

Figure 2.6. Schematic illustration of proton transport via vehicular (a) and Grotthuss (b) mechanisms.

A different scenario can be found in metal oxides, including perovskites, in which the Grotthuss mechanism is responsible for the proton movement through the material. In this case, a proton is also bound to oxygen, yet proton transport occurs via hopping between adjacent oxygen ions.[42] Such a mechanism can be divided into two steps: rotation of the proton around the oxygen ion (preparing for the jump), which sets the direction according to the smallest distance to the next oxygen ion, and the jump itself. The activation energy of the rotation is considerably smaller compared to the one related to the jump (≤ 0.1 eV vs $0.1 - 0.5$ eV) and the reorientation step is faster than the transfer between the oxygen atoms ($\tau_{rotation} \sim 10^{-12}$ s vs $\tau_{jump} \sim 10^{-11}$ s).[43,44] Therefore, the jump can be considered a limiting step for the efficiency of the process. The dynamics of the proton transport depends

on the distances between the neighbouring sites available for hopping and their number. The simulated paths for proton movement between the oxygen atoms within one octahedron and between the octahedra of the cubic perovskite are presented in **Figure 2.7**. Since protons jump between oxygen ions in the same or nearby BO_6 octahedra, the proton mobility is affected by the O–O distance. Furthermore, in the case of predominantly ionic mixed conductors, perovskites closest to the ideal cubic structure generally exhibit the highest proton mobility.[45]

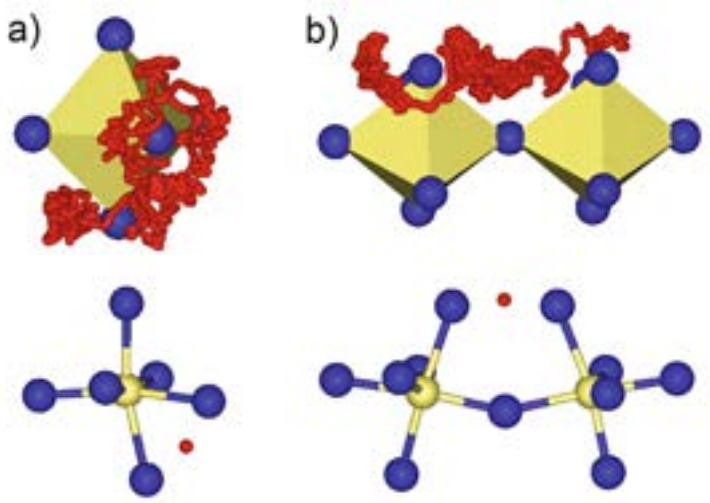

Figure 2.7. Graphical illustration of numerical results of the proton transfer simulations between the oxygen ions within the same octahedron (a) and between the adjacent octahedra (b). The red pattern signifies the trace of the proton movement around and between the oxygen ions. The intra-octahedron transfer (a) involves a distortion of the octahedron, while the inter-octahedra transfer requires octahedra tilting to facilitate the effective transfer.[46]

2.3.3. The dependence of diffusion on temperature and oxygen partial pressure

The oxygen diffusion in oxides, particularly oxygen-deficient ones, most often occurs via the vacancy mechanism. In this mechanism, the oxygen ion can make a successful jump only if the neighbouring site is not occupied. The number of successful jumps per unit of time (Γ) can be written as:

$$\Gamma = N_d \omega Z, \tag{2.19}$$

where N_d represent the oxygen vacancy molar fraction, and Z is the number of adjacent sites that the oxygen atom can occupy. Vacancy molar fraction $[v_O^{\bullet\bullet}]$ at temperature T can be expressed as:

$$N_d = [v_O^{\bullet\bullet}] = exp\left(\frac{\Delta S_d}{x k_B}\right) \cdot exp\left(-\frac{\Delta H_d}{x k_B T}\right), \tag{2.20}$$

where $\frac{\Delta H_d}{x}$ and $\frac{\Delta S_d}{x}$ are the enthalpy and entropy changes related to the defect (vacancy) formation. The x parameter depends on the reaction of the defect formation. This equation

shows that with increasing temperature the concentration of vacancies increases, leading to increased Γ. Moreover, in the case of oxygen vacancies in an oxide, the concentration of defects depends on the oxygen partial pressure in the atmosphere surrounding the material. Additionally, if the oxide can undergo hydration, the vacancy concentration will also depend on the partial pressure of water, since some oxygen vacancies can take part in the reaction with water, facilitating the process of proton incorporation into the material.

The jumping of an atom between the sites involves overcoming the energy barrier related to the lattice distortion, which corresponds to the energy required for the appropriate displacement of neighbouring atoms. The height of the energy barrier ΔH_m determines the attempt frequency ω:

$$\omega = \upsilon \, exp\left(\frac{\Delta S_m}{k_B}\right) \cdot exp\left(-\frac{\Delta H_m}{k_B T}\right), \tag{2.21}$$

where ΔH_m and ΔS_m are the migration enthalpy and entropy. At the same time, υ represents the vibration frequency (typically considered to be equivalent to Debye frequency).

As can be seen, the diffusion coefficient is strongly dependent on temperature. However, there are terms that are non- or weakly temperature dependent, particularly those related to entropy, crystal structure (including interatomic distances and symmetry), and the Debye frequency. Therefore, the diffusion coefficient can be written as:

$$D = D_0 \cdot exp\left(-\frac{Q}{k_B T}\right), \tag{2.22}$$

where D_0 is the preexponential factor, independent of temperature, and Q is the total activation energy. Q consists of the enthalpy of formation of the defect involved in diffusion (energy required to create one oxygen vacancy in the case of the oxygen diffusion via vacancy mechanism in metal oxides) and the enthalpy of mobility (energy needed to overcome the potential barrier during the jump between the equilibrium positions). In the case of the oxygen diffusion in metal oxides with oxygen deficiency at low partial pressures of oxygen, the concentration of vacancies can be expressed using an equation implementing the equilibrium constant:

$$[v_O^{\bullet\bullet}] = \left(\tfrac{1}{4} K_{v_O^{\bullet\bullet}}\right)^{1/3} p_{O_2}^{-1/6} = \left(\tfrac{1}{4}\right)^{1/3} exp\left(\frac{\Delta S_{v_O^{\bullet\bullet}}}{3k_B}\right) \cdot exp\left(-\frac{\Delta H_{v_O^{\bullet\bullet}}}{3k_B T}\right) p_{O_2}^{-1/6}, \tag{2.23}$$

where $\Delta H_{v_O^{\bullet\bullet}}$ and $\Delta S_{v_O^{\bullet\bullet}}$ denote the enthalpy and entropy related to the formation of an oxygen vacancy and $K_{v_O^{\bullet\bullet}}$ is the equilibrium constant corresponding to the vacancy formation reaction.[47] This indicates that the diffusion coefficient for such transport of oxygen ions decreases with increasing oxygen partial pressure. In this case, the preexponential factor D_0 can be written as:

$$D_0 = \alpha a_0^2 \upsilon \cdot exp \frac{\frac{\Delta S_{v_O^{\cdot\cdot}}}{3} + \Delta S_m}{k_B}, \tag{2.24}$$

and the activation energy can be expressed as:

$$Q = \frac{\Delta H_{v_O^{\cdot\cdot}}}{3} + \Delta H_m. \tag{2.25}$$

If the concentration of oxygen vacancies is defined by the concentration of an acceptor substituent $[A_M{}']$, there are no terms related to the formation of the vacancies in (2.25), since in this case their concentration does not depend on the temperature nor oxygen partial pressure:

$$D = \alpha a_0^2 \upsilon \cdot [A_M{}'] \cdot exp\left(\frac{\Delta S_m}{k_B}\right) \cdot exp\left(-\frac{\Delta H_m}{k_B T}\right), \tag{2.26}$$

which means that the diffusion in such a scenario is limited only by the mobility of the oxygen vacancies.

In the case of interstitial diffusion of solute, such as protons in oxides, moving via the Grotthuss mechanism, the diffusion coefficient does not depend on the concentration of the moving species (for the solute conditions). Therefore, the activation energy for such diffusion corresponds solely to the activation energy of mobility:

$$D = D_0 \cdot exp\left(-\frac{\Delta H_m}{k_B T}\right). \tag{2.27}$$

2.3.4. Chemical diffusion

The diffusion coefficients described in chapter **2.3.3** can be considered "self-diffusion" coefficients, which signifies that the diffusion phenomena concerned the independent transport of individual species within the crystal. Such movement can be chaotic (random diffusion) or induced by the potential gradient and can be directly related to the mobility of the diffusing species u_i using the Nernst-Einstein relation:

$$D_i = \frac{u_i}{Z_i e} k_B T, \tag{2.28}$$

where D_i denotes the self-diffusion coefficient of species i, while $Z_i e$ represents its charge. The direct measurement of D_i is difficult and requires the distinction between the diffusion response of various atoms moving in the system. A more convenient approach might be to employ the chemical diffusion coefficients, which describe the cumulative effect of ambipolar diffusion. The ambipolar diffusion assumes the correlated movement of species in the presence of a potential gradient, e.g. during the oxygen ion transport in mixed ionic-

electronic conductors. The chemical diffusion coefficient D_{chem} can be related to the self-diffusion coefficient via relation:

$$D_{chem} = \gamma \cdot D_i, \tag{2.29}$$

where γ denotes the Wagner thermodynamic factor, which can be expressed as:

$$\gamma = \frac{1}{Z_i} \frac{\partial \, ln \, a_i}{\partial \, ln \, c_i}. \tag{2.30}$$

where a_i denotes the activity of species i, while c_i represents its concentration. If the considered species is an oxygen ion in a mixed ionic-electronic conducting perovskite, Z_i assumes the value of 2. The thermodynamic factor depends on both temperature and oxygen partial pressure.

The diffusion phenomena can be investigated using the transient methods of diffusion measurements, such as electrical conductivity relaxation (ECR). In this method, the process occurring at the surface of the material is described as a flow of particles from regions of higher to lower concentration within the sample. The ECR method enables the determination of two parameters: the chemical diffusion coefficient D_{chem} and chemical surface exchange coefficient k_{chem}. These parameters can be related by the equation:

$$D_{chem} \left(\frac{dc}{dx}\right)_{bulk} = k_{chem} \left(\frac{dc}{dt}\right)_{interface}. \tag{2.31}$$

In the case of oxidation/reduction experiments, the k_{chem} parameter provides information about the material's ability to incorporate and release the oxygen ions, which is determined by the oxygen-vacancy concentration on the surface of the material, constituting the active absorption centres. k_{chem} allows for assessment of the material in terms of its ability to efficiently undergo oxygen reactions on the surface, which is crucial for its application as an electrode in electrochemical devices.

2.4. Ionic and mixed ionic-electronic conductivity

The electrical current density (j_i) transported by species i can be expressed using the Ohm law as:

$$j_i = Z_i e \cdot u_i \cdot c_i \cdot E, \tag{2.32}$$

where E represents the electrical field, $Z_i e$ denotes the charge of species i, while u_i and c_i their mobility and concentration, respectively. By grouping the species-related coefficients of the equation above, a new parameter describing the partial conductivity associated with species i can be introduced:

$$\sigma_i = Z_i e \cdot u_i \cdot c_i. \tag{2.33}$$

The total electrical conductivity of the material able to conduct more than one type of charged species, such as mixed ionic-electronic conductors, can be expressed as a sum of the partial conductivities for each mobile carrier i:

$$\sigma_{total} = \sum_{i} \sigma_i. \tag{2.34}$$

The contribution of the conductivity of species i, expressed as a transference number of i, is defined as the ratio of the conductivity related to those species to the total conductivity:

$$t_i = \frac{\sigma_i}{\sigma_{total}}. \tag{2.35}$$

Therefore, the sum of the transference numbers of all the species contributing to the electrical conductivity is equal to 1. The total electrical conductivity can also be described as a sum of the electronic and ionic conductivities:

$$\sigma_{total} = \sigma_{el} + \sigma_{ionic}. \tag{2.36}$$

Electronic conductivity is related to the transport of electrons and electron holes, while ionic conductivity describes the movement of ionic species such as cations, anions, and protons. The relative contribution of electronic and ionic conductivities to the total conductivity may depend on temperature, partial pressure of oxygen, and partial pressure of water, in the case of proton conductors. Due to a much higher mobility of electronic charge carriers compared to ionic species, even if the concentration of ionic carriers is much higher than that of electrons/electron holes, the oxide can still be a predominantly electronic conductor. However, the transport of ions in ceramic materials often constitutes a significant or at least nonnegligible contribution to the total conductivity of those materials.

In ionic and mixed conductors, diffusion and electrical conduction are interrelated. The movement of charged ionic species can be driven both by a concentration gradient and the electrical potential gradient, leading to a directional diffusion of those species.

Figure 2.8 illustrates the diffusion of an atom in a one-dimensional lattice in two scenarios: without (a) and with (b) an electrical potential gradient. In the latter scenario, the height of the energy barrier between the adjacent sites is lower in one direction and higher in the other, resulting in a disproportion of the probability of the atom movement in those directions. The net flux density of carriers in one direction is related to the difference in the jump frequencies in two directions.

Since the mobility of ionic species and their diffusion coefficient are related (eq. (2.28)), the ionic conductivity is strictly dependent on the diffusion properties for the considered ionic carrier and can be expressed as:

$$\sigma_i = (Z_i e)^2 c_i \frac{D_i}{k_B T}. \tag{2.37}$$

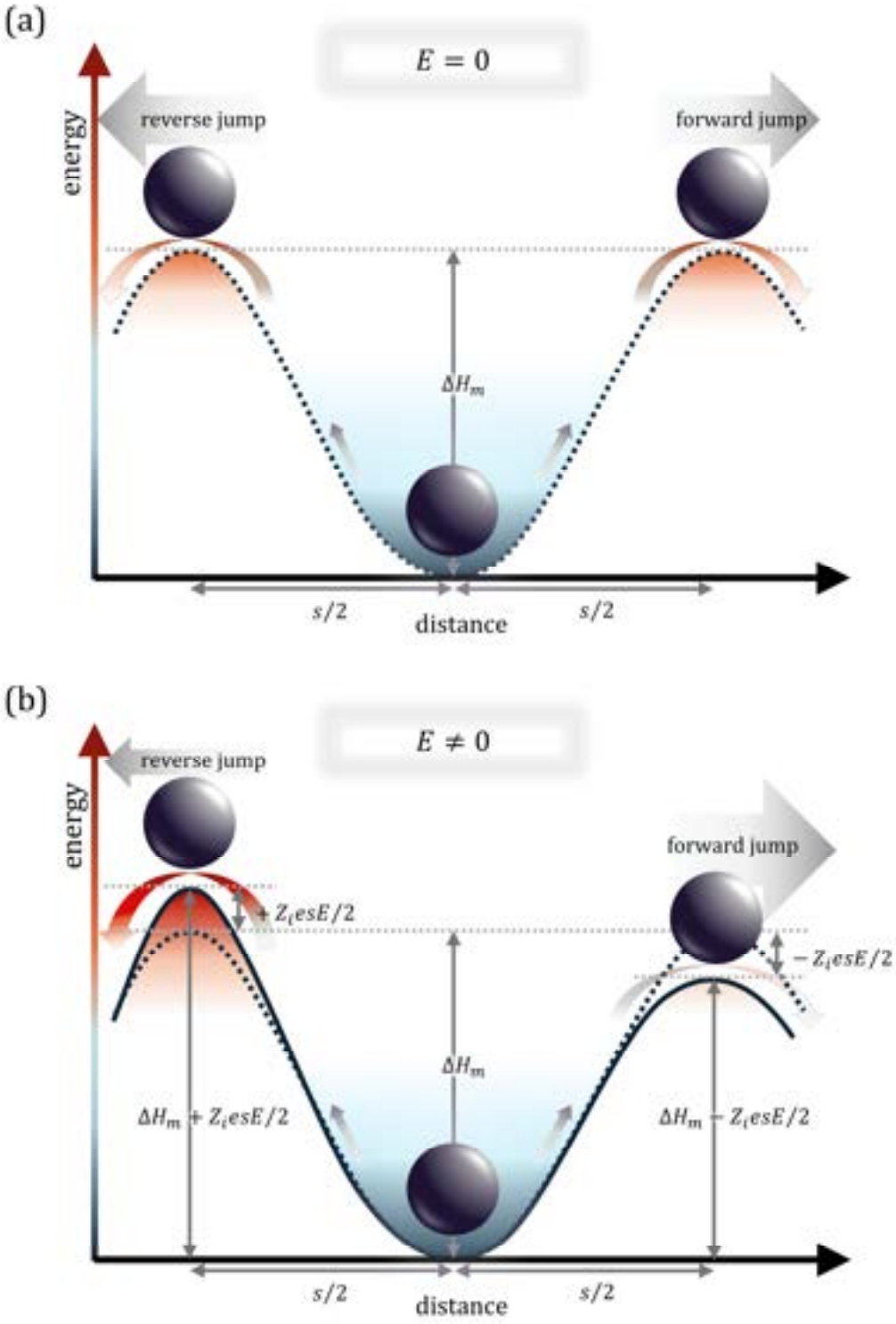

Figure 2.8. An illustration of an atom residing in a site in a 1D crystal lattice and the energy barriers between the adjacent sites. Scenario (a) represents a situation where there is no electrical field present and the energy barrier ΔH_m is the same in both directions. Scenario (b) represents a situation with an electrical field applied and the energy barriers altered, leading to a varying probability of the atom jumping in two directions. Distance s denotes the distance between the adjacent sites for the considered atom.

The electronic conductivity of most oxides is thermally activated. The energy band gap determines the concentration of electronic carriers excited at a specific temperature via an intrinsic excitation mechanism while the energy levels introduced by point defects and their concentration determine the extrinsically excited carriers. Due to the partially ionic nature of bonds in oxides, electrons and holes can be considered localised on the crystal lattice sites. Such quasiparticles of electronic defects coupled with the lattice deformation can be described as a polaron, which will be described in more detail later in this chapter. For an intrinsic semiconductor, the electronic conductivity can be expressed as:

$$\sigma_{el} = \sigma_e + \sigma_h = e(u_{e'} + u_{h\bullet})\sqrt{N_C N_V} \cdot exp\left(-E_g/2k_B T\right), \tag{2.38}$$

where σ_e and σ_h are the conductivity of electrons and electron holes, respectively, $u_{e'}$ and $u_{h\bullet}$ are their mobilities, while N_C and N_V are the density of states on the conduction and valence bands, respectively, and E_g is the energy gap. The band energy diagram for the doped semiconducting material is presented in **Figure 2.9**. For the example of an acceptor substituent, at a temperature at which the acceptor level is almost full but the interband excitation may be neglected, the concentration of the electron holes p is equivalent to the concentration of the acceptor itself (N_A):

$$p \approx N_A. \tag{2.39}$$

At lower temperatures, the concentration of electron holes can be expressed as:

$$p = \sqrt{N_V N_A} \cdot exp(-E_{ion}/2k_B T), \tag{2.40}$$

where E_{ion} is the ionisation energy, equivalent to the energy difference between the acceptor level and the top of the valence band.

Most oxides at elevated temperatures are electronic conductors and their conductivity increases with increasing temperature due to the increased concentration of electronic carriers. Nevertheless, their total conductivity is significantly lower than that of a metal. However, some transition metal oxides exhibit a similar "metal-like" behaviour of the conductivity decreasing with increasing temperature, which generally can be associated with the reduction of the mobility of electronic charge carriers.

The mobility of electronic charge carriers depends on the interaction between electrons and the crystal lattice. In nonpolar (covalent) solids, the itinerant electron model can be applied. The mobility of electronic carriers is limited by the scattering on structural defects and thermal vibrations of the ions in crystal lattice. The scattering associated with defects dominates at low temperatures, while the electron-phonon scattering prevails at elevated temperatures.

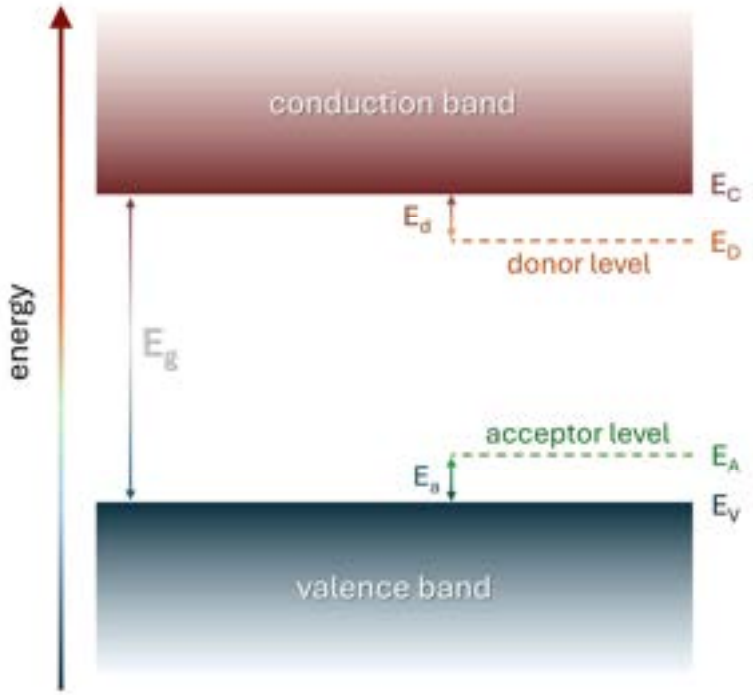

Figure 2.9. Schematic representation of a semiconductor band energy diagram with additional energy levels introduced by a donor and an acceptor.

In the case of ionic solids, such as oxides, electrons polarise the crystal lattice around them, locally distorting the structure and leading to the formation of a polaron. If the interaction between the carrier and the lattice is weak, which takes place in strongly ionic compounds with a large energy gap, it can be considered a large polaron. In materials with stronger interactions between the lattice and electrons/holes, the carriers are more localised, leading to a smaller size associated with those quasiparticles (smaller than a unit cell). At low temperatures ($T < \frac{T_D}{2}$, where T_D is the Debye temperature), small polaron tunnels between the positions in a narrow band, and its mobility is defined by the phonon scattering, which leads to its decrease with increasing temperature. At high temperatures ($T > \frac{T_D}{2}$), small polarons are localised and trapped on specific atoms.[48] In such a scenario, electronic carriers move via a thermally activated hopping mechanism, analogous to the diffusion of ionic charged carriers. Therefore, their mobility can be described through the Nernst-Einstein relation as:

$$u_{small\ polaron} = \frac{e}{k_B T} D = const. T^{-1} \cdot exp\left(-\frac{E_m}{k_B T}\right), \tag{2.41}$$

where E_m denotes the activation energy of hopping, equivalent to the migration enthalpy for this carrier. The exponential temperature dependence enables the distinguishing of this mechanism from the others. Analogous to the diffusion transport of ions, the mobility of small polarons depends on the crystal structure of the system and the local geometry around the ions, which determine the distances between the atoms and the energy of migration E_m.

The conductivity of materials exhibiting the ionic and/or small-polaron conductance can be expressed using the Arrhenius relation as:

$$\sigma = \sigma_0 T^{-1} \cdot exp\left(-\frac{E_a}{k_B T}\right), \tag{2.42}$$

where E_a denotes the activation energy for conduction, consisting of the energy of migration and the energy required for the excitation of the electronic carrier or the formation of a defect. σ_0 is very weakly dependent on temperature and, in MIEC oxides, it is defined by the crystal structure of the material, its defect chemistry, and the oxygen nonstoichiometry.

MIEC materials can be divided into categories based on the relative contributions of ionic and electronic charge carrier concentrations. Materials with a predominant concentration of electronic charge carriers, such as calcium-substituted chromate lanthanide, exhibit high electronic conductivity; hence, they can be applied in SOFCs as interconnectors.[49] The mixed conductors can also exhibit comparable concentrations of electrons/holes and mobile ionic carriers. In the case of this group, the transference numbers for electronic and ionic carriers can be comparable or differ by one order of magnitude, which requires the mobilities of those species to be similar. Such properties are shown by ceria in oxygen partial pressures below 10^{-19} atm., at which the formation of appropriate amounts of oxygen vacancies and electrons enables the condition $n = 2[v_O^{\bullet\bullet}]$ to be met.[50] The third group of MIEC materials exhibits a much higher concentration of mobile ionic carriers than electronic defects, which is generally found in highly ordered structures. This is typically associated with predominantly ionic conductivity ($t_{ionic} \approx 1$), which makes these materials perfect candidates for electrolytes for application in fuel cells with solid oxide electrolyte.

The characteristics of a material and its association with one of the aforementioned groups depend on the conditions, such as temperature and the partial pressures of oxygen and, in the case of a material undergoing water uptake, the partial pressure of water. Each MIEC material exhibits distinct regions of differing properties depending on the atmosphere. The schematic representation of a p_{O_2} dependence of carrier concentration (Brouwer plot) for a simple MIEC of a wide energy gap is shown in **Figure 2.10**. The concentrations of ionic charge carriers in an oxide depend on its defect chemistry. Therefore, they are influenced by the presence of ionised point defects and homovalent impurities/substituents, as well as the oxygen nonstoichiometry of the compound. The predominant types of defects depend on the atmosphere. Additionally, doping the material with a heterovalent substituent can change the dominant types of point defects in each p_{O_2} region and influence the concentrations of charge carriers.

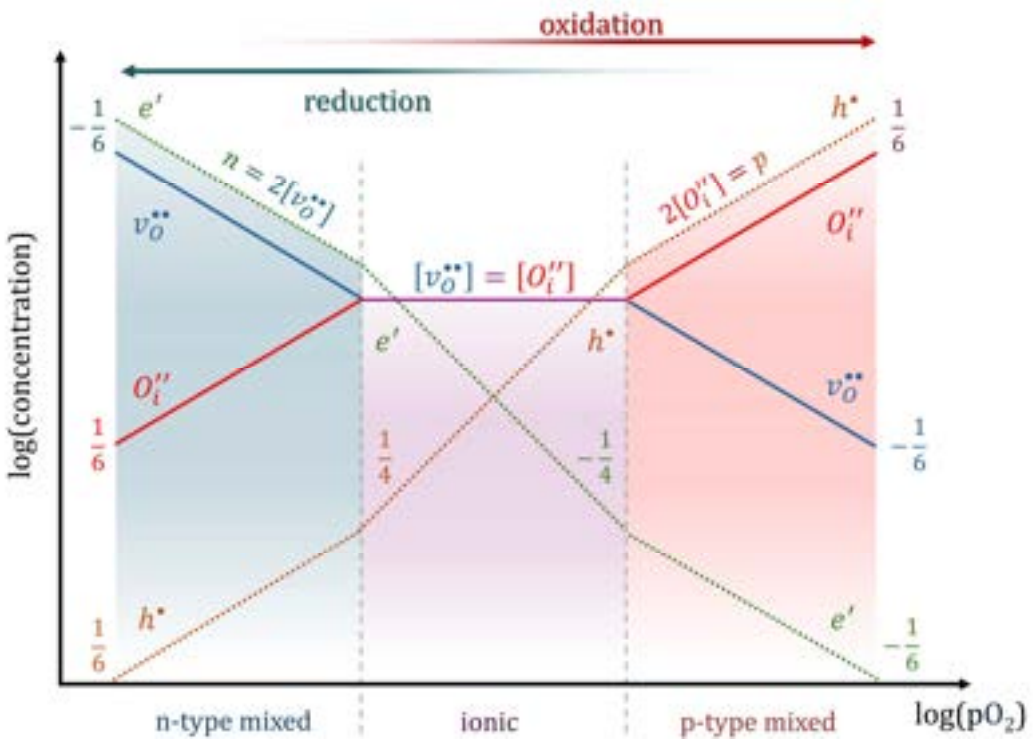

Figure 2.10. The Brouwer plot of MIEC of a wide band gap, showing p_{O_2} dependencies of the concentration of oxygen vacancies, oxygen in interstitial positions, electrons, and electron holes. The p_{O_2} range was divided into three regions, depending on the type of disorder they exhibit (predominant defects present): n-type mixed in the lowest p_{O_2}, stoichiometric (here ionic) in the intermediate p_{O_2} range, and p-type mixed in the highest p_{O_2}. The fractions included signify the exponent for the dependence of concentration on p_{O_2}.

2.4.1. Triple-conducting oxides

Aside from the most common mixed ionic-electronic conducting oxides with mobile oxygen vacancies and electrons or electron holes, there can be distinguished a group of MIEC materials exhibiting an additional type of ionic conductivity – proton conductivity. In triple-conducting oxides (TCOs) three types of mobile charge carriers are present: electrons or electron holes, oxygen vacancies, and protons. A traditional MIEC or an oxygen-ion conducting oxide can become a triple-conducting material via exposure to a humid atmosphere. The TCO material may be either a single-phase material or a composite. They demonstrate considerable potential for diverse electrochemical applications, such as electrode materials in protonic ceramic fuel cells (PCFCs)[51,52], electrolysers (PCECs)[53], and membrane reactors[54]. Therefore, TCOs present a significant opportunity for developing cutting-edge electrochemical devices, paving the way for progress in energy conversion and storage technologies.

Since protons are not native to the lattices of ceramic oxides, proton conduction in those materials requires the incorporation of protons into a structure in the form of positively charged hydroxide defects. There are two possible processes of proton

incorporation into oxide materials: (1) hydration reaction, which is a dissociative absorption of water by the acid-base reaction:

$$v_O^{\bullet\bullet} + O_O^x + H_2O \rightleftharpoons 2OH_O^{\bullet}, \tag{2.43}$$

and (2) hydrogenation reaction, which is a combination of reduction and hydration reactions:

$$2O_O^x + 2h^{\bullet} + H_2O \rightleftharpoons 2OH_O^{\bullet} + \frac{1}{2}O_2. \tag{2.44}$$

The first mechanism prevails in materials with a high oxygen-vacancy concentration ($2[v_O^{\bullet\bullet}]>[h^{\bullet}]$). If proton defect formation occurs via the hydration reaction, two protons are incorporated into the material with the consumption of one vacancy. Because proton mobility is generally higher than that of oxygen vacancies, this scenario typically leads to enhanced total electrical conductivity in a humid atmosphere. The schematic representation of proton incorporation via hydration is shown in **Figure 2.11**. The hydrogenation mechanism of proton incorporation dominates in materials with a high electron-hole concentration ($2[v_O^{\bullet\bullet}]<[h^{\bullet}]$). Two protons are incorporated into the material at the cost of two electron holes. This reaction decreases the total electrical conductivity in a wet atmosphere.

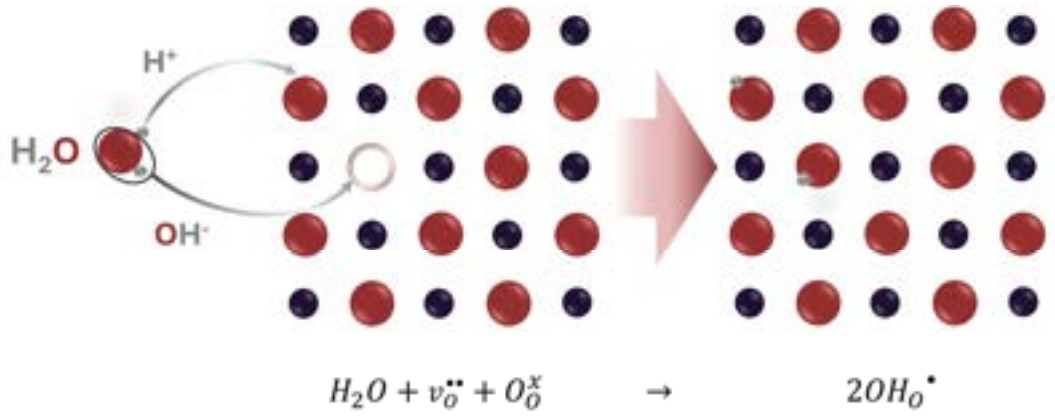

Figure 2.11. Schematic illustration of the proton incorporation into an oxide via the hydration reaction.

The efficiency of the hydration reaction is determined by the standard hydration enthalpy ΔH_{hydr}, which is influenced by the electronegativity of the cations. The electronegativity of the A and B cations defines the ionicity/covalency of the A–O and B–O bonds, which also affect the defect chemistry in ABO_3 materials. ΔH_{hydr} decreases with the decrease in the electronegativity difference between the A and B cations (see **Figure 2.12**), leading to a higher concentration of protons incorporated via this reaction. Furthermore, the lower average electronegativity of the A and B cations may decrease electron transfer from oxygen, resulting in increased oxygen ion basicity. This may lead to increased proton concentration, simultaneously diminishing the mobility of electron holes.[55–57]

The dependence of Gibbs free energy of hydration on the average cation electronegativity is presented in **Figure 2.13**.

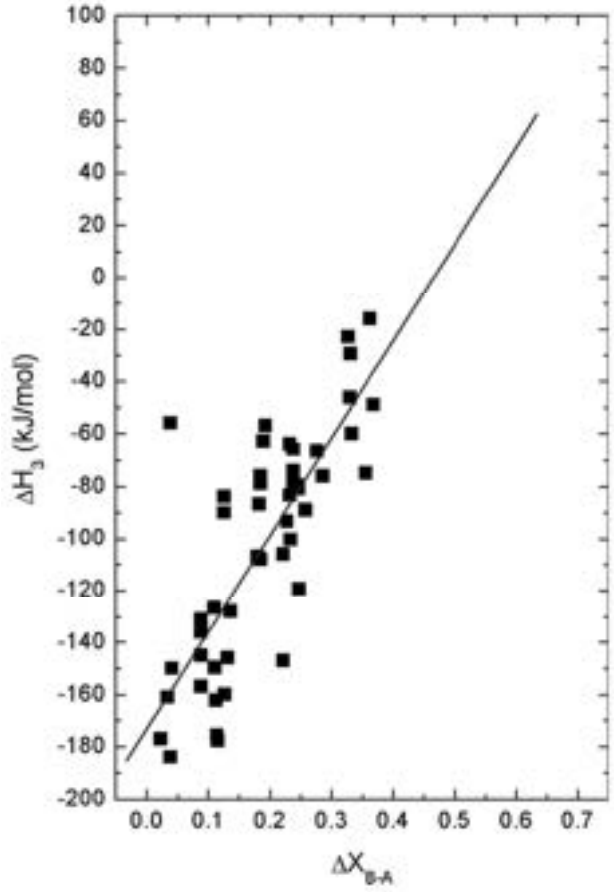

Figure 2.12. Hydration enthalpy as a function of the electronegativity difference between A and B cations in ABO_3 materials.[45]

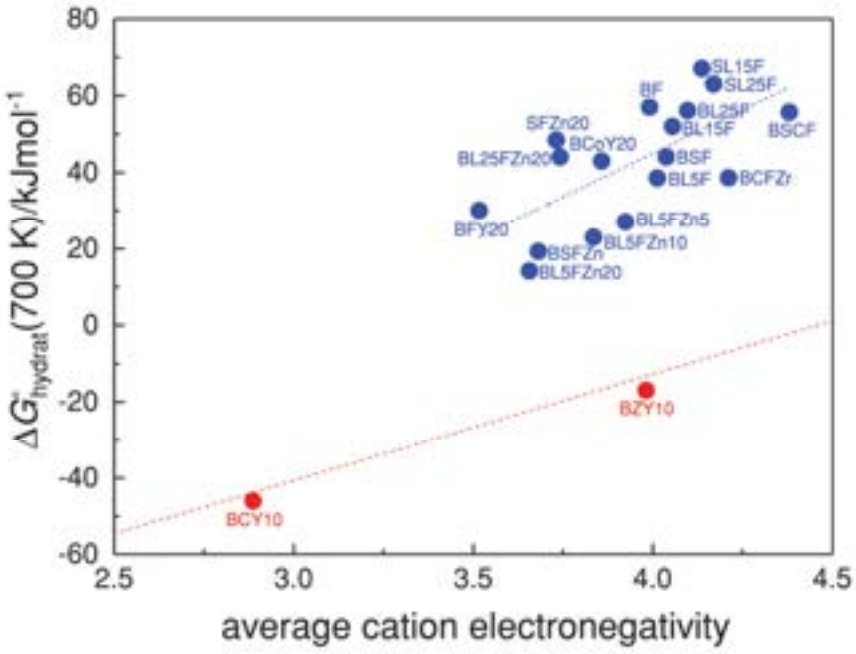

Figure 2.13. Gibbs free energy of hydration at 700 K as a function of the average electronegativity of A and B cations in ABO_3 perovskite materials.[56]

The feasibility of proton uptake can also be influenced by structural distortions and the electronic structure of the oxide. For several perovskite oxides with redox-active transition metals (TM), the buckling of the B–O–B bonds has been linked to charge delocalisation and the degree of covalency of the B–O bonds.[58,59] The relationship between the composition, structural distortions, and electronic structure in (Ba,Sr,La)(Fe,Zn,Y)$O_{3-\delta}$ perovskite materials has been investigated by Raimondi et al. They reported the collective influence of those material features on proton uptake and highlighted the influence of oxygen states on the covalency of Fe–O bonds, for which the charge transfer to transition-metal cations influenced the basicity of oxide ions. Lower covalency of Fe–O bonds correlated with the increase in oxygen ion basicity, which led to the highest proton concentration in the materials exhibiting the most significant structural distortions.[60] Additionally, Raimondi et al. investigated the connection between the buckling of Fe–O–B bonds and the Fe 3*d* – O 2*p* orbital overlap, establishing its positive influence on the proton uptake abilities of (Ba,La)(Fe,Zn,Y)$O_{3-\delta}$ perovskites.[61] Therefore, despite decreasing the ionic conductivity of an oxide, lowering the crystal structure symmetry may have non-obvious consequences in the case of mixed protonic conductors with predominant electronic conductivity.[62] However, the effect of this local distortion on the water uptake may be positive only if the long-range ordering of the crystal preserves a high symmetry (see **Figure 2.14**).

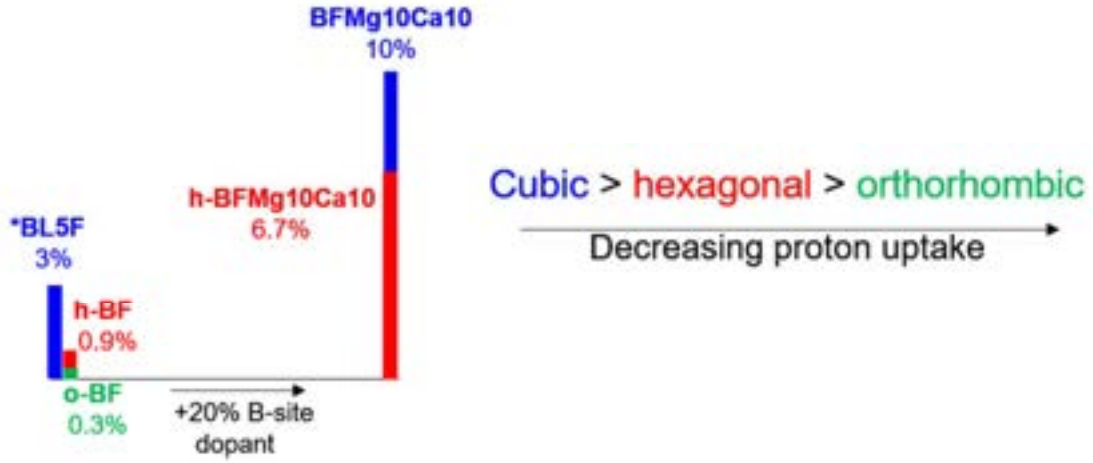

Figure 2.14. Proton uptake at 250 °C in $p_{H_2O} = 16.7$ mbar for perovskite-based oxides of different crystal structure. BL5F, h-BF, o-BF, h-BFMg10Ca10, and BFMg10Ca10 represent cubic $Ba_{0.95}La_{0.05}FeO_{3-\delta}$, hexagonal $BaFeO_{3-\delta}$, orthorhombic $BaFeO_{3-\delta}$, hexagonal $BaFe_{0.8}Mg_{0.1}Ca_{0.1}O_{3-\delta}$, and cubic $BaFe_{0.8}Mg_{0.1}Ca_{0.1}O_{3-\delta}$, respectively. The values shown underneath each material label indicate the molar concentration of protons (in relation to 1 mol of the compound).[63]

Proton transport in ceramics can be studied using relaxation methods, such as ECR, which enable the indirect investigation of the proton mobility by analysing the diffusion of water through a material. In oxygen-ionic conductors with a small electronic conductivity, the diffusion of protons is limited by the slower diffusion of oxygen. Such a process can be described by a single chemical diffusion coefficient, which includes the contributions

of the diffusion of one oxygen ion and two protons. Conversely, in materials with more than two mobile charge carriers the mechanisms related to water diffusion and its kinetics may be more complex.[64] In triple-conducting oxides, the electroneutrality condition must be satisfied within an ensemble of three carriers: protons, oxygen vacancies, and electrons or holes (in low or high p_{O_2}, respectively). Two possible stoichiometry relaxation mechanisms that can occur during the water-uptake process in a triple-conducting oxide are illustrated in **Figure 2.15**. In the so-called single-fold relaxation (**Figure 2.15a**), the concentration of electron holes is low and oxygen vacancies, as the slowest mobile species, limit the overall water diffusion rate. In this case, diffusion occurs in the same way as in the materials with only two mobile charge carriers, in which the concentrations of charged point defects are directly coupled to one another by the electroneutrality condition. Therefore, one chemical diffusion coefficient can be determined due to the coupling between proton and oxygen vacancy. Two-fold relaxation (**Figure 2.15b**) occurs if the concentration of mobile electron holes is sufficiently high. In this case, the electroneutrality condition is satisfied by the changes in the concentration of electronic charge carriers, so fast protons can respond to the gradient of the chemical potential of water, the driving force of proton diffusion, independently of slower oxygen vacancies.[64] Consequently, independent diffusion of protons and oxygen vacancies is possible, which allows the determination of two distinct diffusion coefficients.[65]

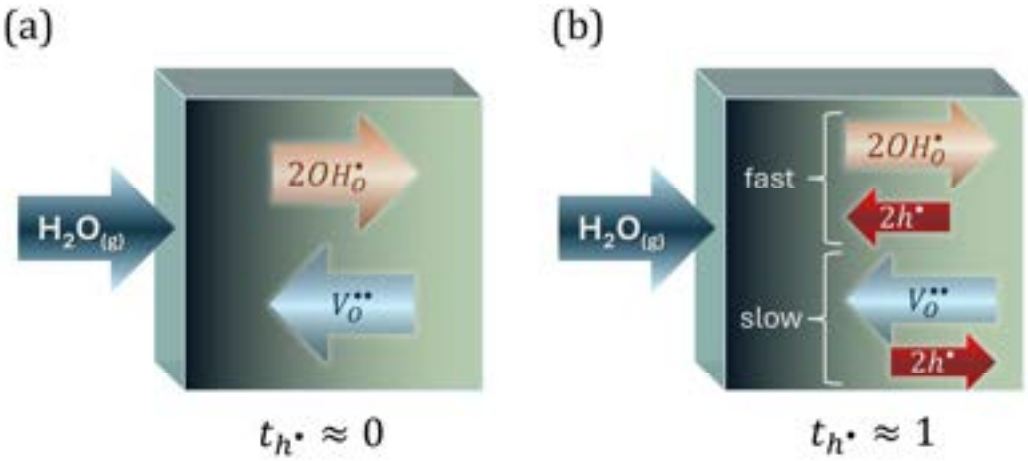

Figure 2.15. Schematic illustration of the flow of protons and oxygen vacancies during the water uptake via single-fold (a) and two-fold (b) stoichiometry relaxation. The specific relaxation process occurring during the proton uptake in a material depends on the transference number of electron holes $t_{h^{\bullet}}$.

The properties of a ceramic, such as the concentration of the mobile species and its catalytic capabilities, can be controlled via the design of material composition. When the B-site cation of the perovskite oxide is substituted with the appropriate type and amount of substituent, the ORR and proton conductivity might be enhanced. Acceptor substituent at the B-site promote hydration by introducing oxygen vacancies and stabilising protons in the structure, thanks to their basicity (low electronegativity). Additionally, if the substituent

has a relatively large ionic radius, the unit cell volume can be expanded, which may increase the mobility of oxygen vacancies. Moreover, the substitution with a mixed-valence metal might enhance the electronic conductivity as well as the capability for redox reactions.[66,67]

The properties of a perfect MIEC for the application as a positrode material in PCFC would be high electronic conductivity to transfer the electrons needed for the oxidation reaction efficiently, and sufficient ionic conductivity, including oxygen-ionic and proton conductivity. A material exhibiting such properties could enable electrochemical reactions on the whole surface of an electrode, leading to its optimal utilisation (see **Figure 1.3**). However, the defects participating in these transport processes rarely exist in a substantial amount at the same time, since the conditions facilitating their formation do not typically overlap. The partial pressure dependencies of the concentrations of oxygen vacancies, protons, and electron holes in an acceptor-doped oxide are shown in **Figure 2.16.** The highest concentration of protons does not occur in conditions where the concentration of electron holes is significant.

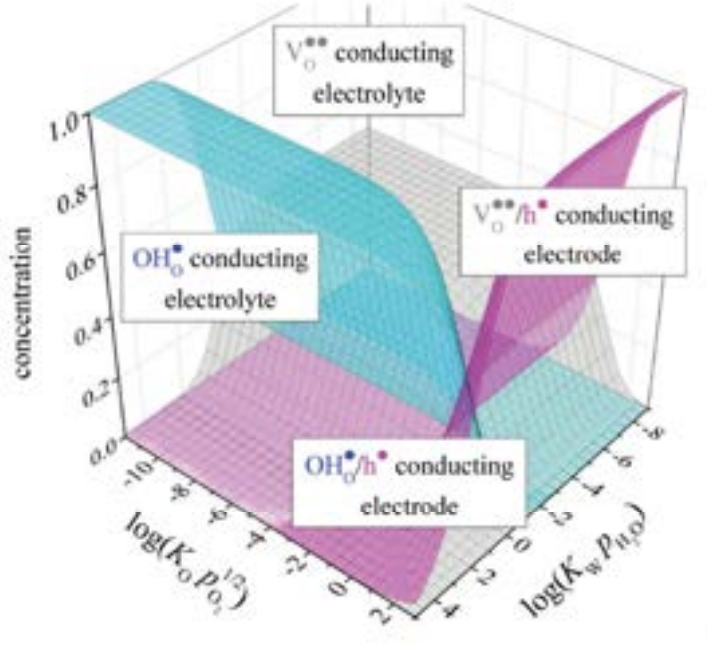

Figure 2.16. The concentrations of oxygen vacancies, protons, and electron holes as a function of oxygen and water partial pressures in an acceptor-doped oxide.[64]

3. Selected materials

The materials studied in this work belong to the $ABO_{3-\delta}$ perovskite family, where A is a 2+ cation, and B assumes an oxidation state between 3+ and 4+. They can be divided into two main groups:

- **$BaCe_{0.6}Zr_{0.2}Y_{0.2-x}M_xO_{3-\delta}$ (BCZYM) compounds with yttrium substituted with mixed-valence elements**
  These materials exhibit a high concentration of oxygen vacancies while maintaining predominant electronic partial conductivity. Their ionic conductivity is high. Thus, these materials can also undergo water uptake in the presence of water vapour, making them TCOs.
- **$SrFe_{1-x}Co_xO_{3-\delta}$ series of compounds (SFC)**
  This group exhibits high partial electronic conductivity ($t_{el} \approx 1$).

3.1. Barium cerate zirconates

3.1.1. $BaCeO_{3-\delta}$ and $BaZrO_{3-\delta}$

Owing to their high proton conductivity and chemical stability, perovskite oxides based on barium, cerium, and zirconium are the most prevalent state-of-the-art proton-conducting oxides.[5] Furthermore, they consist of earth-abundant elements, decreasing the fabrication costs of such materials. Both, barium cerate (BCO) and barium zirconate (BZO) are well-established ionic conductors, exhibiting significant protonic conductivity in water vapour. Alkaline-earth element – barium – occupies the A site of the ABO_3 lattice, and smaller ions of cerium or zirconium (for BCO and BZO, respectively) reside in the B sublattice.

$BaCeO_3$ exhibits an orthorhombic crystal structure ($Pmcn$) at room temperature and transforms into $Imma$ orthorhombic, rhombohedral ($R\bar{3}c$), and finally into the cubic structure ($Pm\bar{3}m$) with increasing temperature.[68,69] It can incorporate a high number of protons into the structure; however, such feasibility for the reaction with water causes its low thermochemical stability in humidified conditions, which leads to the formation of separate phases of cerium oxide and barium hydroxide:[70]

$$BaCeO_3 + H_2O \rightarrow Ba(OH)_2 + CeO_2. \quad (3.1)$$

Moreover, compounds based on this material are not stable in H_2S and CO_2[71], which can be present in biogas fuels used for fuel cell feeding, leading to the decomposition of BCO.[72] On the other hand, $BaZrO_3$ is characterised by higher chemical stability in atmospheres containing those species. However, it possesses a lower ability of proton incorporation

and exhibits high grain-boundary resistance, resulting in a significant drop in the electrical conductivity. Furthermore, obtaining a high density BZO ceramic requires high sintering temperatures. BZO possesses a cubic crystal structure ($Pm\bar{3}m$).[68]

To enhance the structural stability of BCO, cerium can be substituted with more acidic ions, such as titanium[73] or niobium[74]. However, such modifications lead to a decrease in the ionic conductivity of the material.[75] An alternative approach might be the substitution of cerium with zirconium, resulting in the formation of $BaCeO_3$-$BaZrO_3$ solid solution (BCZO), which leads to an improvement in materials stability, at the same time reducing the ionic conductivity to a lesser degree.[72] Barium cerates, zirconates, and their solid solutions are the basis for the commonly used electrolyte materials for proton ceramic cells.

3.1.2. $Ba(Ce,Zr,Y)O_{3-\delta}$

Owing to a small deviation from the ideal cubic structure and a large volume of the unit cell, advantageous for oxygen vacancy and proton mobility, as well as for proton formation through hydration, ABO_3 perovskites exhibit exceptionally high proton conductivities.[44,45] Moreover, partial substitution of B-cations with acceptor elements results in increased oxygen-vacancy concentration, which may improve the proton conductivity in perovskite oxides. In addition to increasing the concentration of oxygen vacancies required for the hydration reaction (equation (2.43)), thus improving water uptake, acceptor substituents can enhance the mobility of protons in the structure.[45] Oversized B-substituents (such as Y^{3+} or Zn^{2+}) can also further increase the proton uptake.[60]

The introduction of acceptor substituents is widely used in the case of barium cerates,[76–80] zirconates,[81–84] and their solid solutions,[85–89] in which the substitution with yttrium and ytterbium is a frequent practice in the design of efficient proton-conducting materials. The acceptor-doped barium cerate-zirconate solid solutions are mixed oxygen ionic-protonic conductors, commonly applied as an electrolyte for PCFCs.[87,90,91] The introduction of oxygen vacancies into such systems via the yttrium substitution proceeds according to the reactions:

$$2Ce_{Ce}{}^{x} + O_O{}^{x} + Y_2O_3 \rightarrow 2Y_{Ce}{}' + v_O{}^{\bullet\bullet} + 2CeO_2, \tag{3.2}$$

and

$$2Zr_{Zr}{}^{x} + O_O{}^{x} + Y_2O_3 \rightarrow 2Y_{Zr}{}' + v_O{}^{\bullet\bullet} + 2ZrO_2, \tag{3.3}$$

for the substitution of cerium and zirconium, respectively.

To obtain a material with appropriate ionic transport properties, water uptake capabilities and a high degree of chemical stability, the proportions of cerate and zirconate and the amount of acceptor must be selected. In this work, the base compound

for the synthesised materials was $BaCe_{0.6}Zr_{0.2}Y_{0.2}O_{3-\delta}$ (BCZY622). Since $Ba(Ce,Y)O_{3-\delta}$ exhibits higher proton conductivity than $Ba(Zr,Y)O_{3-\delta}$ (see **Figure 3.1**), a composition with a predominance of cerium while maintaining sufficient structural and chemical stability provided by zirconium was chosen.

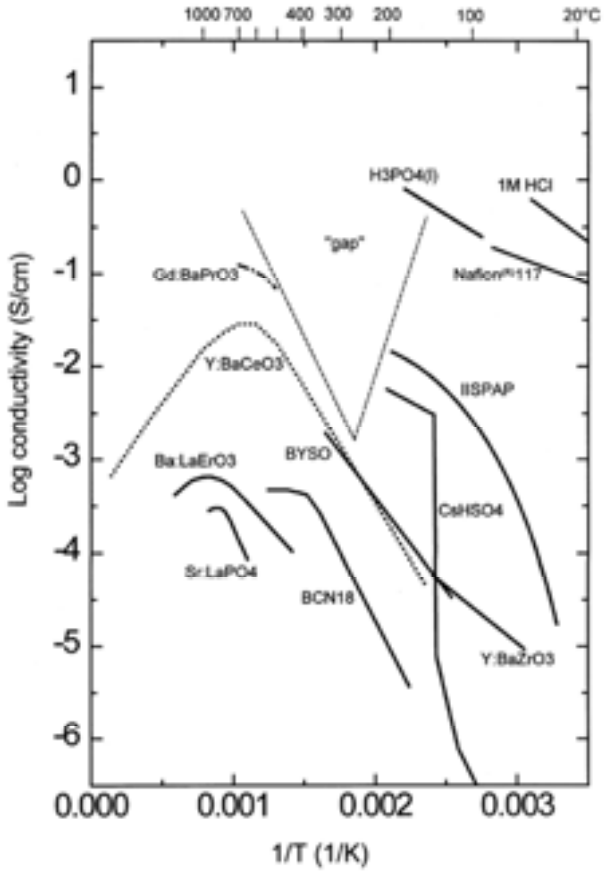

Figure 3.1. Proton conductivity as a function of temperature for various materials, including the substituted barium cerate (Y:BaCeO3) and zirconate (Y:BaZrO3) with 10 mol.% of yttrium in the B-site.[92]

3.1.3. $BaCe_{0.6}Zr_{0.2}Y_{0.2-x}M_xO_{3-\delta}$

To further enhance the transport properties of BCZY materials, mixed-valence cations, such as praseodymium[93,94], cobalt,[95,96] or ruthenium,[97] can be substituted in place of cerium, zirconium, or yttrium, leading to an increase in their electronic conductivity. Since such materials possess three types of mobile charge carriers: oxygen vacancies, protons, as well as electrons or electron holes, they can be considered triple-conducting. Therefore, $Ba(Ce,Zr,Y,M)O_{3-\delta}$, where M is a mixed-valence metal, can be considered as one of the representative groups in the TCO family and regarded as potential materials for the application in positrodes in PCFCs and PCECs.

In this study, yttrium in $BaCe_{0.6}Zr_{0.2}Y_{0.2}O_{3-\delta}$ was substituted by several mixed-valence metals. The materials were investigated with respect to structural properties, defect chemistry, diffusion and surface exchange features, and electrical conductivity. The chosen substituents

were terbium, praseodymium, and iron, incorporated into 10 mol.% of the B-site. To further examine the influence of iron on the BCZY properties, two additional compositions with 2 and 5 mol.% of iron in the B-site were synthesised and studied. Solid solutions of wide and narrow band gap barium-based perovskite oxides (such as barium zirconate and barium ferrite, respectively)[98,99] have been previously studied in terms of an application as positrode materials for PCFC materials.[100,101]

Since only a limited number of studies in the literature have documented the impact of a water vapour-rich atmosphere on the surface exchange of oxygen,[102,103] the selected material group were also analysed in terms of the influence of water vapour on the oxygen diffusion and oxygen surface exchange characteristics. The literature provides different and sometimes conflicting conclusions about the possible effect of the protons' presence on the oxidation and reduction kinetics. This is particularly important as electrochemical devices generally function in a humid environment. Additionally, in the case of TCOs, proton defects influence their electrochemical characteristics. The existing understanding of this influence is insufficient, highlighting the need for further in-depth investigation. Therefore, the research results presented in this dissertation and the conclusions drawn may shed new light on this complex topic.

3.2. Strontium ferrite cobaltites

3.2.1. $SrFeO_{3-\delta}$ and $SrCoO_{3-\delta}$

Strontium ferrite (SFO) is a perovskite material in which oxygen nonstoichiometry greatly influences structural and electrical properties. $SrFeO_{3-\delta}$ ($0 \leq \delta \leq 0.5$) exhibits mixed ionic-electronic conductivity, due to the different oxidation states of iron ions (Fe^{3+} and Fe^{4+}), which makes it a good material for the application as an electrode in SOFCs, sensors, and oxygen membranes.[104] If $\delta = 0$, SFO is a simple cubic perovskite ($Pm\bar{3}m$), in which eight FeO_6 octahedra are located in the unit cell corners and strontium occupies a central position (see **Figure 3.2a**). With increasing oxygen nonstoichiometry, oxygen vacancies can exhibit a long-range ordering, leading to a decrease in the symmetry of the system.[105,106] The possible crystal structures observed for SFO materials of various oxygen nonstoichiometries are shown in **Figure 3.2**.[105,106] The symmetry of the system can also vary with temperature (see **Figure 3.3**).

Depending on the atmosphere, $SrFeO_{3-\delta}$ may exhibit p-type or n-type conductivity. In oxidising atmospheres ($p_{O_2} > 10^{-5}$ atm.), the hole conductivity dominates, while in strongly reducing atmospheres ($p_{O_2} < 10^{-15}$ atm.), the electron conductivity prevails.[107,108] All experiments in this work were conducted in air. Thus, the electron-hole transport was assumed to be the primary contributor to the overall conductivity. In oxidising conditions

(when the oxygen nonstoichiometry $\delta \neq 0$), the hole conduction occurs by an exchange of holes between the Fe^{4+} and Fe^{3+} iron ions via a small-polaron hopping mechanism.[109,110] In general, the concentration of electron holes in SFO is influenced by oxygen nonstoichiometry, therefore affecting its electrical conductivity.[104]

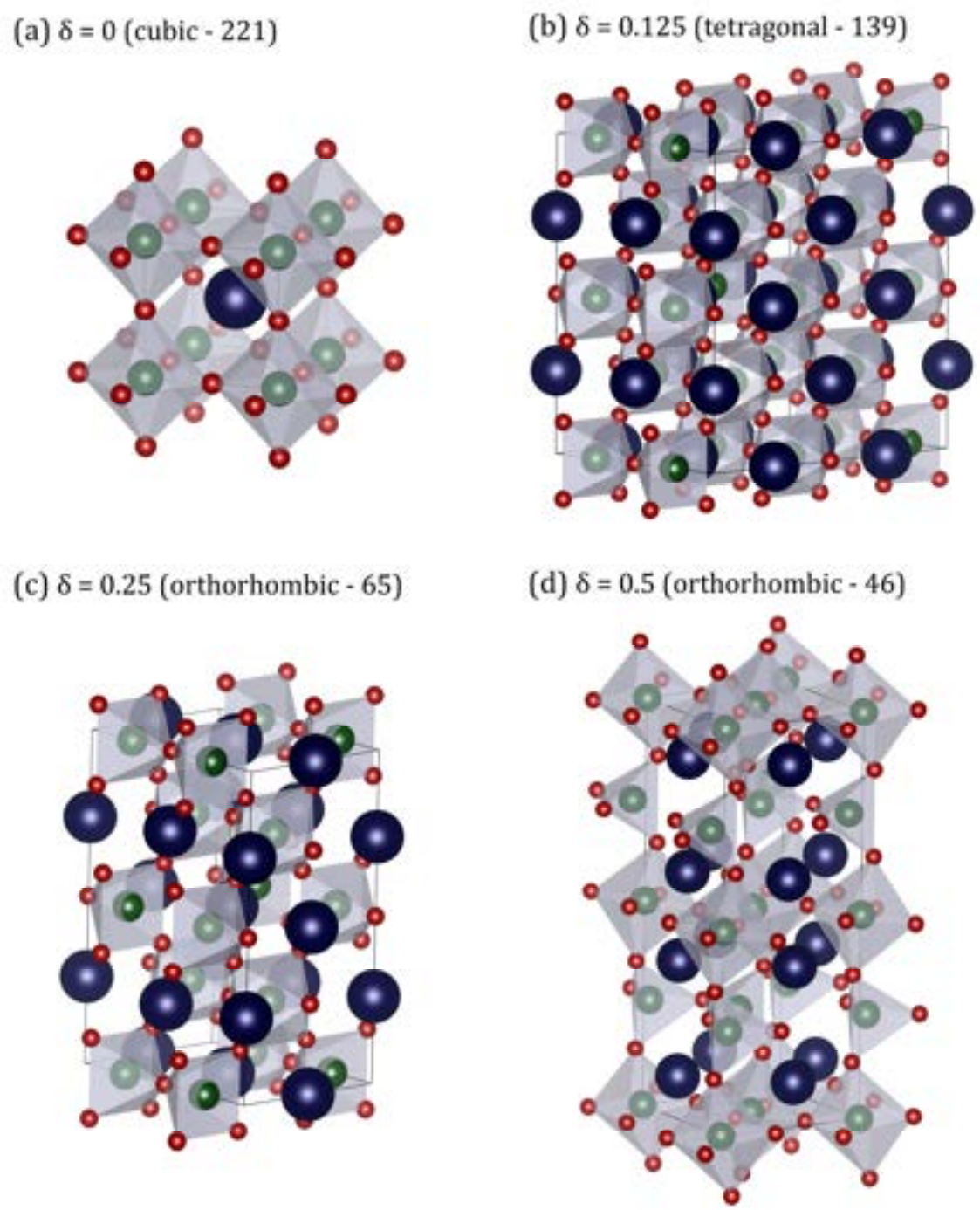

Figure 3.2. Unit cells of $Sr_nFe_nO_{3n-1}$ exhibiting vacancy long-range-ordering, where n=∞ (a), n=8 (b), n=4 (c), and n=2 (d), which correspond to oxygen nonstoichiometry equal to 0, 0.125, 0.25, and 0.5, respectively. The crystal systems with appropriate space group numbers for each unit cell are placed in the brackets. The blue, green, and red spheres represent strontium, iron, and oxygen, respectively.

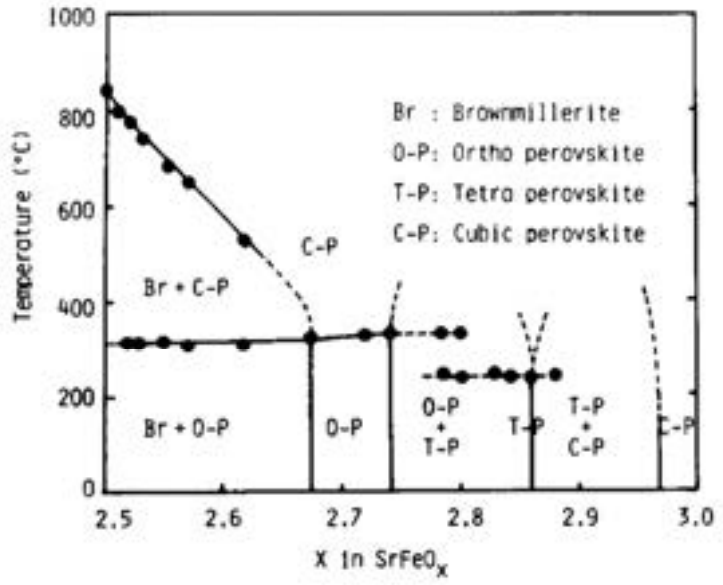

Figure 3.3. Phase diagram of strontium ferrite, exhibiting various crystal structures, dependent on the temperature and oxygen nonstoichiometry.[105]

The transport of oxygen ions in SFO occurs through the vacancy mechanism, wherein oxygen ions migrate to neighbouring vacancies through a hopping process. The ionic conductivity is related to the diffusion rate of oxygen ions, which is affected by the crystal symmetry and the concentration of oxygen vacancies. The ionic conductivity of SFO reaches 0.143 S/cm at 800 °C.[111]

Strontium cobaltite $SrCoO_{3-\delta}$ perovskite (SCO) shows high ionic-electronic conductivity, following the same conduction mechanisms as SFO. What is more, the electrical conductivity and surface exchange kinetics of SCO exceed those of SFO. It also displays exceptionally high mobility of oxygen ions and high catalytic efficiency.[112,113] A drawback of strontium cobaltite is a structural transition at 900 °C. Above 900 °C, the crystal structure of SCO is cubic, while below it transforms into lower symmetry structures (2H-type hexagonal perovskite[114–116] or brownmillerite). Since the high symmetry of a perovskite unit cell promotes high mobility of oxygen vacancies and an optimal overlap between 3*d* orbitals of transition metal and 2*p* orbitals of oxygen, it provides both, high oxygen-ionic and electronic conductivity.[110,117] Therefore, the total electrical conductivity of SCO below the transition temperature is much lower.[118–120] Stabilisation of the cubic perovskite structure at low temperatures may be achieved by substituting cobalt with iron.[121]

3.2.2. $SrFe_{1-x}Co_xO_{3-\delta}$

The solid solution of strontium ferrite and cobaltite – $SrFe_{1-x}Co_xO_{3-\delta}$ (SFC) – might offer a combination of the advantages of SFO and SCO, while reducing their limitations. SFC materials provide the good structural stability of SFO and the rapid surface exchange of oxygen with excellent mixed conductivity of SCO. The crystal structure of $SrFe_{1-x}Co_xO_{3-\delta}$

($x \leq 0.8$) was reported to be cubic at room temperature, which provides favourable conditions for oxygen transport.[119] This might be crucial in terms of applications for these materials since, according to the Wagner formula, both electronic and ionic conductivities determine oxygen permeation flux through the perovskite mixed conductors.[119,122] The conduction mechanism of electron holes in SFC at lower temperatures is a thermally activated p-type small-polaron hopping, so the electron-hole conductivity increases with increasing temperature. After reaching the maximum, the electrical conductivity decreases with increasing temperature. The cobalt content in SFC materials has a significant impact on electrical properties. With increasing cobalt content, the electrical conductivity and oxygen-vacancy concentration were reported to increase, whereas structural stability at low temperatures – to decrease.[123] At 800 °C, the ionic conductivity ranges from ≈ 0.1 S/cm to ≈ 1.2 S/cm for $SrFeO_{3-\delta}$ and $SrFe_{0.67}Co_{0.33}O_{3-\delta}$, respectively.[124,125] Taking into the account the total electrical conductivity ($\sim 10^{-2}$ S/cm), the transference number of oxygen ions in SFC materials varies from 10^{-3} to 10^{-2}, depending on the cobalt content.[126] Moreover, Teraoka et al. investigated the oxygen permeation rate through $SrFe_{0.2}Co_{0.8}O_{3-\delta}$ ceramic membranes, which was two orders of magnitude higher compared to YSZ.[127]

Other perovskites containing iron and cobalt have also been widely investigated for their magnetic properties, in which local disorder at the B-site and spin-lattice interactions have been found to influence lattice parameters and magnetic behaviour. In disordered double perovskites, the anomalies in lattice expansion and phonon modes related to the presence of magnetoelastic coupling and spin-phonon interactions have been reported.[128–130] The theoretical work on $NdSrCoFeO_6$ system by Silva et al. further suggested that mixed-valence states of B cations and the disorder on the B-site may create competing magnetic exchange pathways and frustration, influencing the distribution of oxygen vacancies and the local electronic environment.[131] Furthermore, the investigations of related perovskites show that local ordering or clustering of oxygen vacancies can modify the symmetry of transition-metal sites and alter the electronic structure.[132,133] Although these effects are the most pronounced at low temperatures, associated with magnetic ordering or spin-state transitions, they point to a possible interplay between the distribution of oxygen vacancies, local structural disorder, and electronic properties of Co-/Fe-containing perovskites. Even without the long-range magnetic order, these interactions may affect the mobility and formation of oxygen vacancies.

Although SFC materials possess promising properties for application in various electrochemical devices, the oxygen diffusion and surface-exchange characteristics of this system need further investigation. Moreover, there are no reports on the influence of water vapour on the oxygen diffusion behaviour and electrical transport in those materials.

A comprehensive analysis of the long-range and local structure, as well as an investigation of defect chemistry, electrical, and thermoelectric properties, may provide a new understanding of the SFC system and SFC-related materials. The material series chosen for this purpose was $SrFe_{1-x}Co_xO_{3-\delta}$, where x = 0, 0.2, 0.4, 0.6, 0.8.

4. Research methodology

4.1. Fabrication of samples

4.1.1. Solid-state reactive sintering

The solid-state reactive synthesis (SSRS) method is widely used for fabricating ceramic materials. It is valued for its high efficiency, simplicity, reproducibility, and cost-effectiveness. It facilitates the formation of thermodynamically stable products by promoting chemical reactions between solid-state reactants at temperatures below the melting point of all components.[134] The SSRS method enables simultaneous phase formation, grain growth, and densification.

A key factor affecting the efficiency of the synthesis is the distance between reactant grains and their size, as they determine the diffusion of atoms between phases. To address this, the reactants are ground into a fine powder and pressed into pellets prior to the synthesis. Additionally, the process can be optimised by using additives that lower the synthesis temperature and enhance both the reaction efficiency and sintering.

Another critical parameter influencing the efficiency of SSRS is the temperature at which the synthesis is conducted, as it governs the rate of diffusion within the sample. According to the Tammann rule, the temperature should exceed 2/3 of the melting temperature of at least one of the reagents. This condition promotes the dominance of volume diffusion over surface diffusion at grain boundaries, which is prevalent at lower temperatures.[135] Lattice diffusion plays a crucial role in enabling the reaction to occur throughout the sample volume.

In this study, two material groups, $BaCe_{0.6}Zr_{0.2}Y_{0.2-x}M_xO_{3-\delta}$ (M = Fe, Pr, Tb; x = 0.02, 0.05, 0.1) and $SrFe_{1-x}Co_xO_{3-\delta}$ (x = 0, 0.2, 0.4, 0.6, 0.8), were synthesised using the SSRS method. The synthesis steps are illustrated in **Figure 4.1**. For the BCZYM material group, the stoichiometric amounts of $BaCO_3$ (Sigma Aldrich, 99.9%), CeO_2 (Chempur, 99.99% (REO)), ZrO_2 (Alfa Aesar, 99%), Y_2O_3 (Alfa Aesar, 99.99%(REO)), Fe_2O_3 (Alfa Aesar, 99.9%), Pr_6O_{11} (Chempur, 99.9% (REO)), and Tb_4O_7 (Alfa Aesar 99.9% (REO)) were mixed by manual grinding in an agate mortar, followed by ball-milling with zirconia balls (with ball-to-powder mass ratio 3:1) for 12 cycles at 450 rpm. The milling process was conducted in zirconia bowls filled with isopropyl alcohol. Each milling cycle included 50 minutes of milling and a 10-minute pause, allowing the mixture to cool before the next cycle. After the milling, the suspension was dried and gently ground in a mortar. The resulting fine powder mixture was then calcined in synthetic air for 24 hours at 950 °C, with a heating and cooling rate of 5 °C/min, to decompose the barium carbonate reactant. The powder was subsequently mixed

with 1 wt% NiO (abcr, 99% (metal basis)), ball-milled again for 12 cycles, and uniaxially pressed into pellets using a hydraulic press at 250 MPa. The powders were formed into pellets of two shapes: either 12 mm-diameter cylinders for electrochemical impedance spectroscopy (EIS) measurements or cuboids (18 × 10 mm^2) for electrical conductivity relaxation (ECR) measurements. NiO was used as a sintering aid to ensure high density of BCZYM samples, which is critical for diffusion experiments.[89,91] It was chosen as it is the most effective sintering aid, compared to other additives such as LiF, Al_2O_3, and SnO_2, improving densification and lowering the sintering temperature of BCZY samples.[136] The addition of small amounts of NiO can lead to the formation of BaY_2NiO_5 phase with a low melting point, which, in its liquid form, can facilitate both sintering and grain growth. Furthermore, BaY_2NiO_5 decomposes at temperatures above 1200 °C, resulting in increased oxygen and cation vacancies concentrations, further enhancing sintering kinetics.[137] The last step involved sintering the pellets at 1300 °C for 10 hours, with a heating and cooling rate of 3 °C/min.

Figure 4.1. Schematic representation of the solid-state reaction route used for the synthesis of the $BaCe_{0.6}Zr_{0.2}Y_{0.2-x}M_xO_{3-\delta}$ (M = Fe, Pr, Tb) and $SrFe_{1-x}Co_xO_{3-\delta}$ samples.

To ensure a better clarity for the reader, in the chapter "**Results and discussion**", the $BaCe_{0.6}Zr_{0.2}Y_{0.2-x}M_xO_{3-\delta}$ compounds are referred using shorter labels. The labels (summarised in **Table 4.1**) indicate the additional substituent and its amount used.

Table 4.1. The labels used for each perovskite oxide of $BaCe_{0.6}Zr_{0.2}Y_{0.2-x}M_xO_{3-\delta}$ family investigated in this work.

Complete chemical formula	Label
$BaCe_{0.6}Zr_{0.2}\mathbf{Y_{0.2}}O_{3-\delta}$	BCZY622
$BaCe_{0.6}Zr_{0.2}Y_{0.1}\mathbf{Tb_{0.1}}O_{3-\delta}$	BCZYTb10
$BaCe_{0.6}Zr_{0.2}Y_{0.1}\mathbf{Pr_{0.1}}O_{3-\delta}$	BCZYPr10
$BaCe_{0.6}Zr_{0.2}Y_{0.1}\mathbf{Fe_{0.1}}O_{3-\delta}$	BCZYFe10
$BaCe_{0.6}Zr_{0.2}Y_{0.15}\mathbf{Fe_{0.05}}O_{3-\delta}$	BCZYFe5
$BaCe_{0.6}Zr_{0.2}Y_{0.18}\mathbf{Fe_{0.02}}O_{3-\delta}$	BCZYFe2

For the $SrFe_{1-x}Co_xO_{3-\delta}$ (x = 0, 0.2, 0.4, 0.6, 0.8) materials, SSRS was also employed, using $SrCO_3$ (Chempur, 99.0%), Fe_2O_3 (Alfa Aesar, 99.9%), and Co_3O_4 (Chempur, 99.97%) as initial reagents. The synthesis route analogous to that used for the BCZYM group was employed (see **Figure 4.1**). The first ball-milling process was conducted for 24 cycles at 600 rpm. Calcination was carried out under the same conditions as those for the BCZYM group. After the second ball-milling, the powder was mixed with 1 wt% poly(vinyl butyral-co-vinyl alcohol-co-vinyl-acetate) (PVB) and 1 wt% NiO, and manually ground in isopropyl alcohol. PVB served as a binder, enhancing powder densification during pressing. The dried powder was then pressed into pellets and sintered for 24 hours at 1200 °C for $x \in \langle 0, 0.6\rangle$ or at 1050 °C for $x = 0.8$. Lower sintering temperature for $SrFe_{0.2}Co_{0.8}O_{3-\delta}$ was chosen because of a high content of cobalt oxide, due to its low melting point. To avoid brittleness and cracking of the sintered samples, the pressure used for the formation of pellets was relatively low – 100 MPa. To further reduce the risk of cracking of samples, the 2°/min cooling rate was applied to relax the stresses inside the sample. The relative density of the obtained SFC samples exceeded 92%. The parameters used in the synthesis steps for both material groups are summarised in **Table 4.2**.

Table 4.2. Summary of the parameters used during the preparation and synthesis process of samples.

	$BaCe_{0.6}Zr_{0.2}Y_{0.2-x}M_xO_{3-\delta}$					**$SrFe_{1-x}Co_xO_{3-\delta}$**				
Substituent	M = Fe			M = Pr	M = Tb	x = 0	x = 0.2	x = 0.4	x = 0.6	x = 0.8
	x = 0.02	x = 0.05	x = 0.1	x = 0.1	x = 0.1					
1st milling	450 rpm, 12 h					600 rpm, 24 h				
Calcination	24 h at 950 °C in synthetic air flow (heating/cooling 5 °/min)									
2nd milling	450 rpm, 12 h					600 rpm, 24 h				
Additives	NiO					NiO and PVB				
Pressing	250 MPa					100 MPa				
Sintering	10 h at 1300 °C (heating/cooling 3 °/min)					24 h at 1200 °C (heating 3 °/min, cooling 2 °/min)				24 h at 1050 °C (heating 3 °/min, cooling 2 °/min)

4.1.2. Coprecipitation method

The coprecipitation method is a widely employed wet chemistry technique for synthesising mixed oxides, where the precipitation of soluble components results in the formation of water-insoluble product. Typically, aqueous salt solutions are used and a crystalline phase is formed through the coprecipitation reaction. This synthesis process involves several stages, including nucleation, particle growth, and agglomeration, which can occur simultaneously. The rate at which each stage proceeds, influencing the particle size and distribution, is governed by several factors, such as temperature, pH of the solution, stirring rate, and the rate at which the initial reactant solutions are combined.

The $BaCe_{0.6}Zr_{0.2}Y_{0.2}O_{3-\delta}$ (BCZY622) reference sample was synthesised using the coprecipitation method. Ammonium carbonate ($(NH_3)_2CO_3$) was dissolved in water, and the resulting solution was heated to 60 °C while being stirred magnetically. Stoichiometric amounts of $Ba(NO_3)_2$, $Ce(NO_3)_3$, $Y(NO_3)_3$, and $ZrO(NO_3)_2$ were separately dissolved in water to form individual nitrate solutions, each with a concentration of 1 mol/dm^3. The nitrate solution was then gradually added to the ammonium carbonate solution until a volume ratio of 1:5 was achieved. The solid product was filtered, dried for 24 hours at 80 °C, ground in a mortar, and calcined at 1000 °C for 3 hours. The resulting powder was then ground again with the addition of 1 wt% PVB and 1 wt% NiO, followed by uniaxial pressing at 300 MPa. Finally, the pellets were sintered at 1450 °C for 4 hours. The synthesis steps are illustrated in **Figure 4.2**.

Figure 4.2. Schematic representation of the coprecipitation route used to synthesise the $BaCe_{0.6}Zr_{0.2}Y_{0.2}O_{3-\delta}$ sample.

4.2.Material characterisation techniques

4.2.1. X-ray diffraction

X-ray diffraction (XRD) is an experimental technique employed to investigate the structural properties of crystalline materials. This method relies on the diffraction and subsequent interference of electromagnetic waves scattered by atoms on parallel crystal planes. Waves reflected at the appropriate angle interfere constructively following Bragg's law:

$$n\lambda = 2d\,sin\,\theta, \tag{4.1}$$

where λ denotes the wavelength of the incident radiation, n is the diffraction order, d is the interplanar distance, and θ is the angle of incidence. **Figure 4.3** presents the schematic representation of Bragg's law. The diffraction pattern, which contains information on the angles and intensities of the collected reflections, provides an indirect "image" of the electron density within the crystal. This allows the determination of various structural parameters such as unit cell dimensions, atomic site occupancies, preferred orientation, and strain. Additionally, XRD enables the analysis of the phase composition of the crystalline sample.

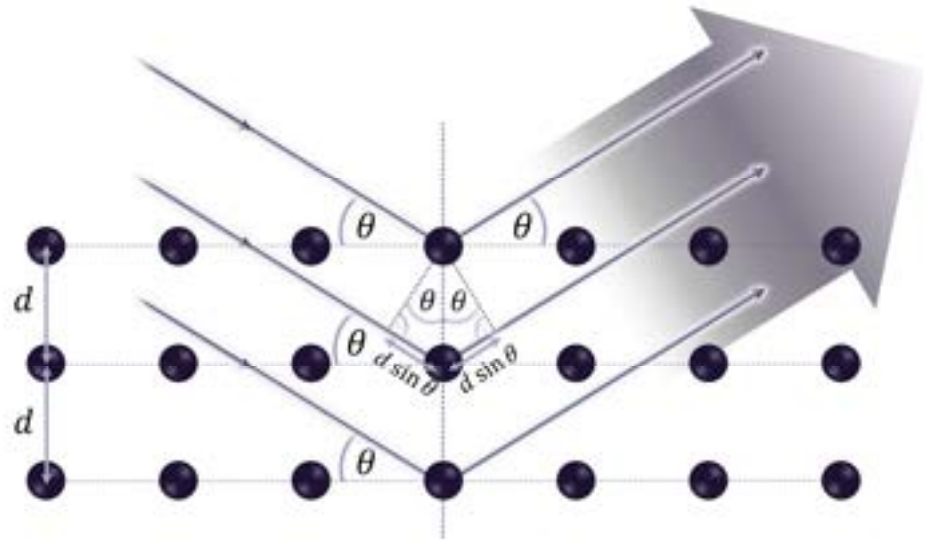

Figure 4.3. Schematic depiction of Bragg's law on the lattice planes.

In this study, the crystal structure and phase composition of the polycrystalline samples were examined using a Phillips X'Pert Pro diffractometer, operating in atmospheric air at room temperature. The diffractometer operates in Bragg-Brentano geometry, which utilises the sample fixed in the horizontal position and the radiation source and detector moving by $-\theta$ and θ, respectively. From the angles of incident radiation that yielded amplification, one can determine the interplanar distances within the examined material, according to equation (4.1). Measurements were performed using CuK_α radiation ($\lambda = 1.541$ Å) under

40 kV and 30 mA settings of the tube and a PIXcel1D detector. The obtained XRD patterns were analysed and refined using HighScore Plus XRD analysis software, employing the Rietveld refinement technique.[138]

The Rietveld refinement method is an analysis technique used to interpret diffraction patterns. The refinement enables the extraction of detailed structural information based on the nonlinear least squares method, where the mathematical model is fitted iteratively to the experimental data by minimising the weighted sum of squared differences between the observed and calculated intensities ($y_{i,obs}$ and $y_{i,calc}$, respectively):[139]

$$\chi^2 = \sum_i w_i \left(y_{i,obs} - y_{i,calc}\right)^2, \tag{4.2}$$

where w_i is the weighting factor and i denotes that the intensity corresponds to $2\theta_i$. The $y_{i,calc}$ intensity is calculated based on the contributions from the fitted structural parameters, as well as the microstructural factors and effects related to the instrument used in the experiment. The refinement is an iterative process that begins with the optimisation of fundamental parameters, such as background, unit cell parameters, scale factors, as well as peak shape and width (parameters of the profile function), and subsequently includes more intricate factors like thermal parameters and site occupancies. After each parameter modification, the diffraction pattern is recalculated, and the deviations from the experimental data are reevaluated.

To assess the quality of the refinement, several metrics can be employed: profile residual R_p (agreement between observed and calculated patterns), weighted profile residual R_{wp} (agreement between observed and calculated patterns scaled by intensity weights w), expected residual R_{exp} (best achievable fit for the analysed dataset), and goodness of fit (GOF); which can be expressed with equations (4.3)-(4.6):[140]

$$R_p = \frac{\sum_i \left|y_{i,obs} - y_{i,calc}\right|}{\sum_i y_{i,obs}}, \tag{4.3}$$

$$R_{wp}^2 = \frac{\sum_i w_i \left(y_{i,obs} - y_{i,calc}\right)^2}{\sum_i w_i \left(y_{i,obs}\right)^2}, \tag{4.4}$$

$$R_{exp}^2 = \frac{N_{fit} - P_{fit}}{\sum_i w_i \left(y_{i,obs}\right)^2}, \tag{4.5}$$

$$GOF = \left(\frac{R_{wp}}{R_{exp}}\right)^2, \tag{4.6}$$

where N_{fit} represents the number of data points used for the fitting, while P_{fit} is the number of fitted parameters used for the calculation of the model pattern.

The unit cell parameters derived from the Rietveld refinement were subsequently used to calculate the theoretical densities of the respective materials. The refinement employed the pseudo-Voigt function as a profile function to model the shape of the diffraction reflexes.

4.2.2. X-ray absorption spectroscopy

X-ray Absorption Spectroscopy (XAS) is an experimental technique enabling the investigation of the electronic structure of the analysed atom present in the sample and the local structure around it. The method facilitates the element-specific X-ray radiation absorption behaviour of an atom when the photon energy exceeds the binding energy of its core-level electrons. Depending on the chemical state of the atom and the local geometry around it, the probability of absorbing radiation of a specific energy varies, giving rise to a characteristic modulation in the absorption spectrum referred to as the X-ray absorption fine structure (XAFS). A comprehensive analysis of these spectra can reveal information about the electronic and atomic structure of the investigated material, such as coordination chemistry, oxidation state, and coordination number of the chosen atom, as well as the interatomic distances between the absorber and its closest neighbours and the presence of structural disorder.

The sample absorbs the X-ray radiation used in the XAS experiments through the photoelectric effect, in which the core-level electron absorbs a photon and transitions to a higher energy level. If the incident photon's energy exceeds the core electron's binding energy, it will be absorbed, and excess energy will be transferred to the photoelectron in the form of its kinetic energy. Consequently, the probability of absorption depends on the energy of the incident photons and the characteristic energy above which absorption rapidly increases (called the absorption edge), a value characteristic of each element due to the unique energy levels of its core electrons. The absorption behaviour of the material can be described by the absorption coefficient μ and it is influenced by the density of the sample ρ, the energy of the X-ray photon E_{ph}, as well as the parameters related purely to absorbing atoms: atomic mass M_{at} and atomic number Z_{at}:[141]

$$\mu \approx \frac{\rho {Z_{at}}^4}{M_{at} {E_{ph}}^3}. \tag{4.7}$$

The probability of absorption can also be defined through a relationship between the intensity of the incident X-ray beam I_0 and the resulting intensity of the transmitted radiation I_t leaving the material. Such a relationship is described by the Beer-Lambert Law:[142]

$$I_t = I_0 e^{-\mu x_t}, \tag{4.8}$$

where x_t is the thickness of the sample.

The XAS experiment involves measuring the absorption coefficient of the material as a function of energy. The XAFS spectrum collected at the K-edge of an atom ($1s$ electron excitation) can be divided into two regions: X-ray absorption near edge structure (XANES) and extended X-ray absorption fine structure (EXAFS), as illustrated in **Figure 4.4**. XANES provides insights into the formal oxidation state and coordination environment of the absorbing atom, distinguishing, for instance, between tetrahedral and octahedral geometries. By comparing the absorption edge energy E_0 to those of reference compounds containing ions of the same element in known oxidation states, the formal oxidation state of the absorber can be determined. On the other hand, EXAFS provides detailed structural information, such as interatomic distances, coordination numbers, and the identity of neighbouring atoms. The measured absorption coefficient of the material can be described as a function of energy as:

$$\mu(E) = \mu_0(E) \cdot [1 + \chi(E)], \tag{4.9}$$

where μ_0 represents the absorption coefficient of an isolated atom, while $\chi(E)$ is the EXAFS function describing the oscillations of the photoelectron interacting with neighbouring atoms. The EXAFS function can be extracted from the XAFS data using the equation:

$$\chi(E) = \frac{\mu(E) - \mu_0(E)}{\Delta\mu_0(E)}, \tag{4.10}$$

where $\Delta\mu_0$ denotes the step change in the absorption at the energy corresponding to the energy edge E_0. These oscillations are typically represented as a function of photoelectron wavenumber k, defined as:

$$k = \sqrt{\frac{2m_e(E - E_0)}{\hbar^2}}, \tag{4.11}$$

where m_e is the mass of an electron. Since the EXAFS oscillations arise from the interaction of the photoelectron emitted from the absorbing atom with the surrounding atoms, the coordination shells of the nearest neighbours are responsible for the occurrence of different frequencies in the $\chi(k)$ function. The influence of the scattering atoms on the EXAFS spectrum can be described by equation:

$$\chi(k) = S_0^2 \sum_i N_j \frac{f_j(k)}{kR_j{}^2} e^{\frac{-2R_j}{\lambda_m(k)}} e^{-2k^2\sigma_j^2} \sin\left(2kR_j + \delta_j(k)\right), \tag{4.12}$$

where S_0 is an amplitude reduction factor, λ_m is the mean free path of the photoelectron, while the other parameters are related to the neighbouring scattering atom j: N_j is the coordination number, R_j is the distance between the absorber and the scatterer, σ_j^2 is the mean square radial displacement, while f_j is the scattering amplitude and δ_j is the phase shift, representing the scattering properties of the atom j.[141]

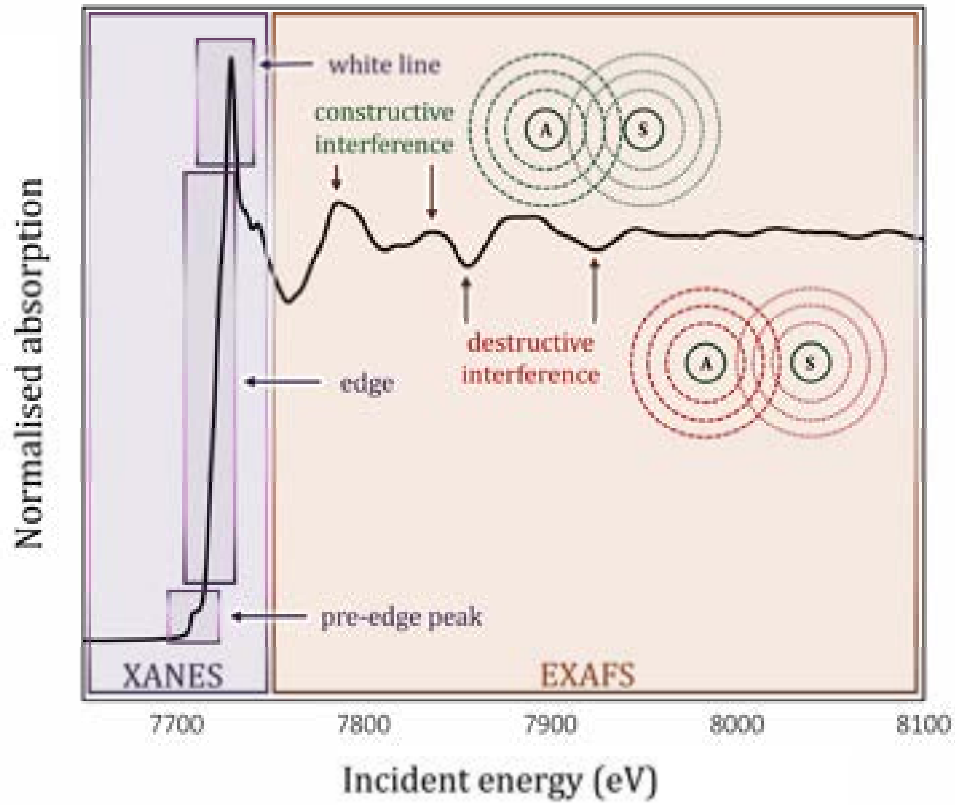

Figure 4.4. Normalised XAS spectrum of Co_3O_4 (recorded at the K-edge of cobalt) with XANES and EXAFS regions outlined, with characteristic features of the spectrum marked. The green diagram illustrates the constructive interference of the photoelectron wave, whereas the red diagram depicts its destructive interference. In these representations, "A" and "S" denote the absorbing and scattering atoms, respectively.

Therefore, EXAFS equation (4.12) allows one to determine the number of neighbouring atoms (coordination number) and the distances to those atoms. The EXAFS data can be transformed from the momentum space into the real space using the Fourier transform (FT), producing an intensity distribution as a function of distances from the atom. The resulting FT-EXAFS plots, which contain contributions from the scattering paths of the photoelectron, can then be fitted using FEFF software with appropriate modelling, enabling the extraction of information about the local structure around the absorbing atom.

In this work, the XAS measurements were conducted in the SOLARIS National Synchrotron Radiation Centre. Spectra at the K-edges of iron (7.112 keV) and cobalt (7.709 keV), as well as the L-edges of barium (5.247 keV), cerium (5.723 keV), terbium (7.514 keV), and praseodymium (5.964 keV), were acquired at the ASTRA beamline. Prior to the experiment, each sample, in fine powder form, was mixed with cellulose.

The powder mixture was then uniaxially pressed into cylindrical pellets, mounted on a plastic holder with a window, and secured with Kapton tape. An illustration depicting the prepared sample setup is shown in **Figure 4.5**. All spectroscopic data collected at the ASTRA beamline were obtained at ambient temperature and pressure in a transmission mode. To ensure a good statistical quality of the acquired spectra, each measurement was repeated 2–3 times, and after an initial evaluation, the spectra were merged into one. Additionally, the spectra were checked and refined regarding errors related to glitches in the source radiation. The data collected at the ASTRA beamline were analysed using Athena software, belonging to the Demeter collection of analytical software.[143] The Fe and Co K-edge spectra were further analysed in the EXAFS range.

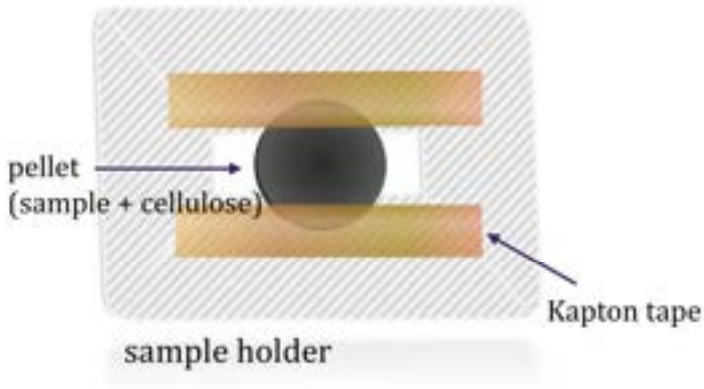

Figure 4.5. Sample prepared for the XAS measurement using the ASTRA beamline in the SOLARIS National Synchrotron Radiation Centre.

The spectra collected at the K-edge of oxygen (532 eV), as well as the L-edges of iron (721 eV) and cobalt (779 eV), were measured at the PIRX beamline of the SOLARIS Centre under high-vacuum conditions. For these measurements, the powdered samples were applied onto the carbon tape mounted on a holder. The illustration of such a setup ready for insertion into the measurement chamber is presented in **Figure 4.6**. The measurements were conducted using the total electron yield (TEY) and fluorescence (FY) detection modes. The spectra collected at the PIRX beamline were normalised and analysed using the PyMca software.[144]

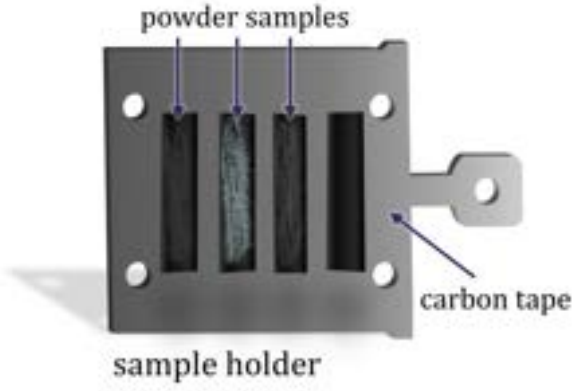

Figure 4.6. Samples prepared for the XAS measurement using the PIRX beamline in the SOLARIS National Synchrotron Radiation Centre.

4.2.3. Density measurements

The density of the samples was determined via the Archimedes method. Using the laboratory scale with the dedicated equipment for this hydrostatic method, with the use of kerosene as the reference liquid of known density ($\rho_{kerosene} = 0.8271$ g/cm^3), it was possible to determine the absolute density of an analysed sample according to the equation:

$$\rho_{abs} = \frac{m_{dry}}{m_{wet-air} - m_{wet-kerosene}} \rho_{kerosene}, \tag{4.13}$$

where m_{dry} is the mass of the dry sample in air, while $m_{wet-air}$ and $m_{wet-kerosene}$ represent the mass of the sample soaked in kerosene in air and submerged in the liquid, respectively.

The relative density ρ_{rel} of the sample was determined as the ratio of the obtained absolute density ρ_{abs} and the theoretical density ρ_{theor}:

$$\rho_{rel} = \frac{\rho_{abs}}{\rho_{theor}} \cdot 100\%. \tag{4.14}$$

The theoretical density was determined using the unit cell parameters obtained through Rietveld refinement of XRD data:

$$\rho_{theor} = \frac{M_{at}}{V_{cell}}, \tag{4.15}$$

where M_{at} represents the total mass of atoms in the unit cell, while V_{cell} denotes the unit cell volume calculated based on the refined parameters obtained from XRD studies.

4.3. Defect chemistry analysis

4.3.1. Iodometric titration

Iodometric titration is a well-established analytical technique for determining the concentration of oxidising species in a solution. It enables the identification of the oxidation states of various elements, particularly those in transition-metal compounds. In the context of perovskite materials, this method allows the determination of the oxidation states of mixed-valence ions constituting the compound.

In this work, the oxidation states of the B-site cations of $ABO_{3-\delta}$ perovskite oxides were determined by iodometric titration. The procedure involved dissolving a small amount of powdered sample ($15 - 20$ mg) and approximately 0.2 g of potassium iodide in $15 - 20$ ml of 2M hydrochloric acid in a flask previously flushed with nitrogen for 30 minutes to create an inert atmosphere. A magnetic stirrer stirred the solution to enhance the dissolution process of oxides.

The B-site cations in the investigated perovskite materials can exist in oxidation states of 4+,3+, and 2+ (e.g., Fe and Co) or 4+ and 3+ (e.g., lanthanides such as Ce, Tb, and Pr). In the former case, the B cations released from the sample are reduced by iodide from their 4+ and 3+ states to the 2+ state, as described by reactions:

$$2B^{3+} + 3I^- \rightarrow 2B^{2+} + I_3^-, \tag{4.16}$$

$$B^{4+} + 3I^- \rightarrow B^{2+} + I_3^-, \tag{4.17}$$

whereas in the latter case, the reduction follows:

$$2B^{4+} + 3I^- \rightarrow 2B^{3+} + I_3^-. \tag{4.18}$$

Once the solid sample was fully dissolved, the liberated iodine was titrated with 0.01M $Na_2S_2O_3$. During this step, iodine reacts with thiosulfate ions according to the reaction:

$$2{S_2O_3}^{2-} + I_3^- \rightarrow {S_4O_6}^{2-} + 3I^-. \tag{4.19}$$

Thiosulfate was added to the solution using a microburet until the solution was decolourised entirely. Near the end of the titration, a starch indicator (1 wt% aqueous solution) was introduced to enhance the visibility of the colour change. Since atmospheric oxygen can oxidise thiosulfate, influencing the result, the entire process was conducted under a protective nitrogen atmosphere.

The amount of iodine ions produced in reactions (4.16)-(4.18) depends solely on the amount of B ions present in the solution in the oxidised form. By knowing the mass of the sample with a defined composition, along with the concentration and volume of sodium thiosulfate used in the titration, it is possible to calculate the mean oxidation state of the B-site cation in the $ABO_{3-\delta}$ oxide. However, if the analysed compound contains multiple mixed-valence ions at the B-site, the iodometric titration does not give information about the oxidation state of each cation occupying this site. Nonetheless, with the appropriate assumptions and constraints, this technique can be employed to evaluate the oxygen nonstoichiometry δ.

For the $BaCe_{0.6}Zr_{0.2}Y_{0.2-x}M_xO_{3-\delta}$ group, the following assumptions were made: the Ba, Zr, and Y cations were considered to exist in fixed 2+, 4+, and 3+ oxidation states, respectively, while Ce (assumed to be 100% in the 4+ state prior to the titration) and M could undergo reduction. Based on these assumptions, the oxygen nonstoichiometry of $BaCe_{0.6}Zr_{0.2}Y_{0.2-x}Fe_xO_{3-\delta}$ was calculated using the following equation:

$$\delta_{BCZYFex} = 0.1 - \frac{x}{2}\left(\frac{C_{Na_2S_2O_3} \cdot V_{Na_2S_2O_3} - 0.6\frac{m}{M}}{x\frac{m}{M}} - 1\right), \tag{4.20}$$

where $C_{Na_2S_2O_3}$ and $V_{Na_2S_2O_3}$ represent the concentration and volume of the sodium thiosulfate solution used for the titration, while m and M are the mass of the dissolved sample and the molar mass of the compound, respectively.

Similar assumptions were applied for $BaCe_{0.6}Zr_{0.2}Y_{0.1}M_{0.1}O_{3-\delta}$, where M = Tb and Pr. However, the analysis differed because of the different reduction pathways for terbium and praseodymium ions (as described by equation (4.18)). The oxygen nonstoichiometry of $BaCe_{0.6}Zr_{0.2}Y_{0.1}Tb_{0.1}O_{3-\delta}$ and $BaCe_{0.6}Zr_{0.2}Y_{0.1}Pr_{0.1}O_{3-\delta}$ was determined as:

$$\delta_{BCZYTb/Pr} = 0.1 - 0.05\left(\frac{C_{Na_2S_2O_3} \cdot V_{Na_2S_2O_3} - 0.6\frac{m}{M}}{0.1\frac{m}{M}}\right). \quad (4.21)$$

In the $SrFe_{1-x}Co_xO_{3-\delta}$ material group, the B-site cations undergo reduction according to reactions (4.16) and (4.17). Since both cations follow the same redox reactions, the mean oxidation state of the B cation can be expressed as:

$$OS_B = 2 + \frac{C_{Na_2S_2O_3} \cdot V_{Na_2S_2O_3}}{\frac{m}{M}}. \quad (4.22)$$

The oxygen nonstoichiometry for these materials was determined as:

$$\delta_{SFC} = 1 - \frac{C_{Na_2S_2O_3} \cdot V_{Na_2S_2O_3}}{2 \cdot \frac{m}{M}}. \quad (4.23)$$

The uncertainties of the calculated parameters were estimated using the total-differential method, incorporating the individual uncertainties of all the measured values (summarised in **Table 4.3**).

Table 4.3. The individual uncertainties used for the calculation of the oxygen nonstoichiometry and mean oxidation states.

	Uncertainty
Concentration of $Na_2S_2O_3$	0.005 mol/dm^3
Volume of $Na_2S_2O_3$	0.05 ml
Mass of the sample	0.002 g

4.3.2. Thermogravimetry

Thermogravimetric (TG) analysis is a method used to investigate phenomena associated with mass changes, such as vaporisation, absorption/desorption, thermal decomposition, and solid-gas reactions. In this technique, the mass variations of the sample are measured as a function of time or temperature in a controlled atmosphere. The resulting thermogravimetric curve provides insight into the processes accompanied by mass changes.

In this study, solid-gas reactions occurring in the $BaCe_{0.6}Zr_{0.2}Y_{0.2-x}M_xO_{3-\delta}$ samples, specifically hydration and thermal reduction, were examined. To investigate the processes of water incorporation and oxygen release, thermogravimetric experiments were conducted using the Netzsch STA 449 Jupiter and Netzsch TG 401 Tarsus systems for water uptake and thermal reduction analyses, respectively. The diagram of the former device is shown in **Figure 4.7**. For the hydration experiment, the powder samples were initially annealed at 800 °C for 5 hours in dry air ($p_{H_2O} \sim 10^{-5}$ atm.) to remove water and surface carbon dioxide. After this step, the samples were cooled to 300 °C and maintained at this temperature for 2 hours. Subsequently, the gas flow was switched from dry air ($p_{H_2O} \sim 10^{-5}$ atm.) to humidified air ($p_{H_2O} \approx 0.023$ atm.) for approximately 2 hours. Afterwards, the gas was returned to dry air for an additional hour.

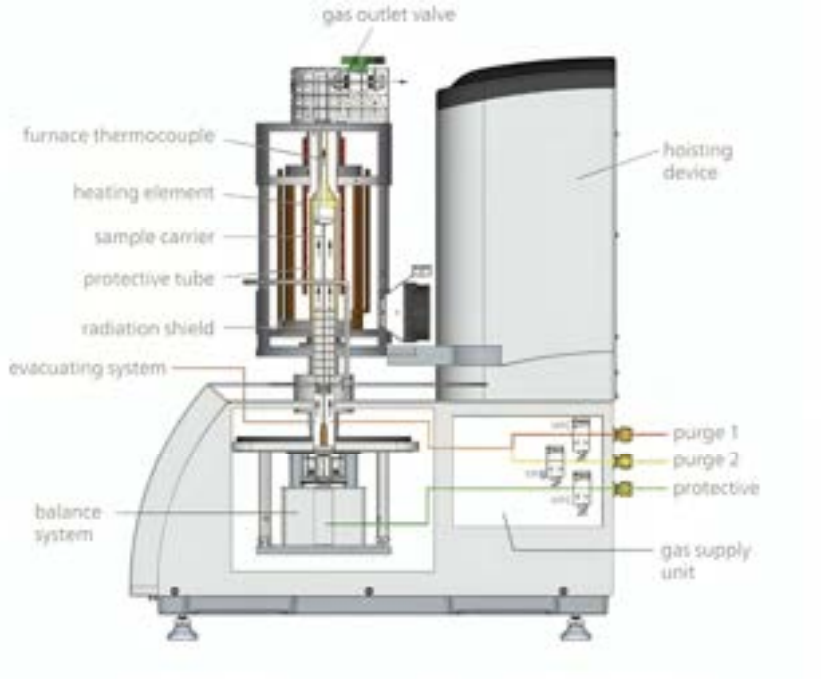

Figure 4.7. Diagram of the parts and functionalities of the Simultaneous Thermal Analyzer – STA 449 F1 Jupiter®.[145]

The difference in mass recorded in dry and wet atmospheres was used to estimate the relative mass change (%). Assuming hydration was the only process occurring during the measurement, the recorded mass change could be interpreted as the mass of water incorporated into the material. This value was then used to calculate the proton defect concentration according to the following equation:

$$[OH_O^{\bullet}] = \frac{2\Delta m \cdot M}{M_{H_2O} \cdot m}, \tag{4.24}$$

where M is the molar mass of the compound with the stoichiometric composition, M_{H_2O} is the molar mass of water, while m and Δm represent the mass and mass change of the analysed powder, respectively.

To assess the temperature evolution of oxygen nonstoichiometry in the analysed materials, the powder samples were heated up from room temperature to 800 °C and subsequently cooled down (with 2 °/min rates) in isobaric conditions. The recorded change of mass, attributed to the thermal reduction of samples, enabled the determination of oxygen nonstoichiometry changes according to equation:

$$\Delta\delta = \frac{\Delta m \cdot M}{\frac{1}{2} M_{O_2} \cdot m}, \tag{4.25}$$

where M_{O_2} is the molar mass of molecular oxygen. If the initial value of oxygen nonstoichiometry at room temperature is known (e.g. determined via iodometric titration), it is possible to assess the δ parameter at each analysed temperature. The $\Delta\delta$ values were determined from the data recorded during the cooling stage.

4.4. Electrical properties measurements

The temperature dependence of total conductivity and electrical conductivity relaxation (ECR) measurements were conducted on dense samples of the synthesised materials. The total electrical conductivity in dry and humidified air was assessed using electrochemical impedance spectroscopy (EIS) for the BCZYM group and the DC 4-wire (DC-4W) method for the SFC group. Additionally, the ECR method was employed to examine the kinetics of hydration/dehydration and oxidation/reduction.

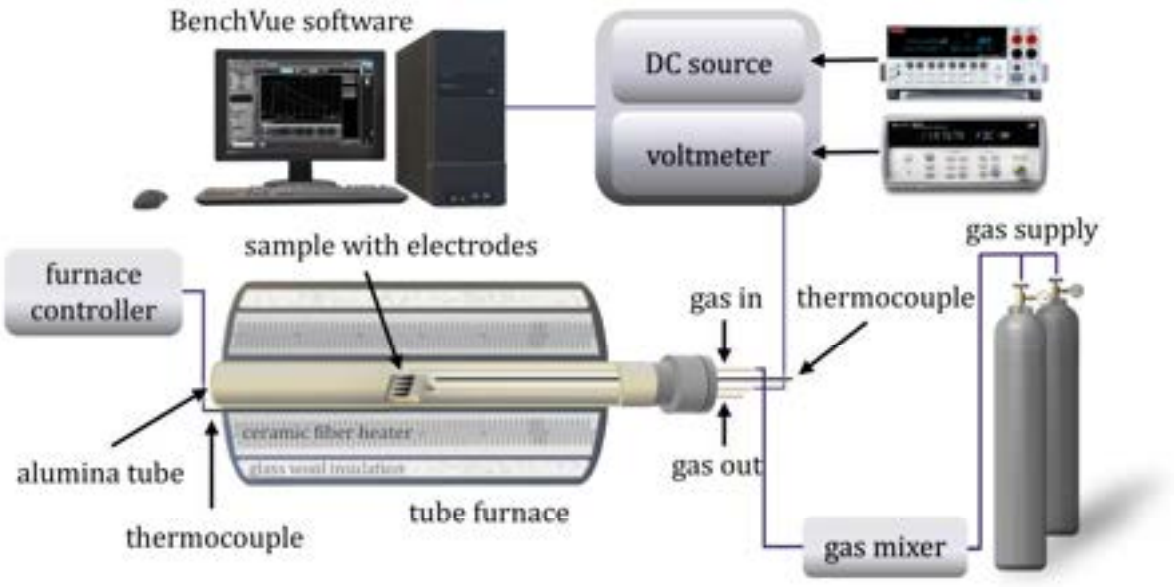

Figure 4.8. Schematic representation of the electrical properties measurement unit using the DC source and voltmeter.

The experimental setup used for the electrical studies is shown in **Figure 4.8**. The illustration presents an example of the system configured for the measurements

using the DC-4W method. For EIS measurements, the DC source and the voltmeter in the setup were replaced by a potentiostat/galvanostat.

4.4.1. DC 4-wire electrical measurements

The total electrical conductivity of the $SrFe_{1-x}Co_xO_{3-\delta}$ materials was measured using the DC-4W method. In this approach, two pairs of parallel electrodes are applied to the surface of the sample. The two outer electrodes at the opposite edges of the sample function as current electrodes, imposing a specific electrical current through the sample, while the two inner electrodes act as voltage electrodes. By knowing the dimensions of the sample, the current I_{DC} flowing through it, and the distance between the voltage electrodes L_{dist}, the conductivity of the sample can be calculated according to the equation:

$$\sigma = \frac{I_{DC}}{V} \cdot \frac{L_{dist}}{S_{area}}, \tag{4.26}$$

where V is the measured voltage and S_{area} is the cross-sectional area of the sample. Using four probes instead of two effectively eliminates the contribution from resistance of wires and contacts from the obtained results.

The samples were prepared as rectangular prisms. Four parallel platinum electrodes were applied using a platinum paste, after which platinum wires were attached to the electrodes. The wires were securely tied around the sample to ensure stability during handling and placement in the measurement cell and to prevent the detachment of the electrodes from the surface of the sample. The samples were subsequently sintered at 930 °C for 3 hours. The illustration depicting the sample with applied electrodes is shown in **Figure 4.9**.

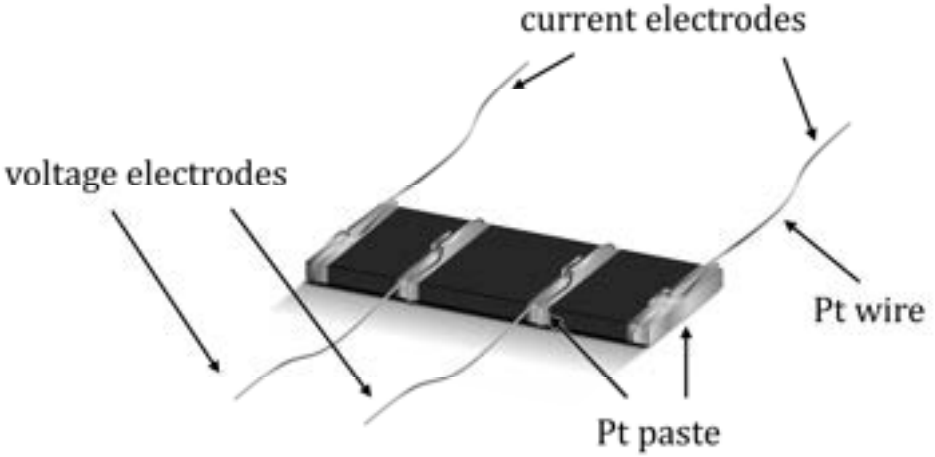

Figure 4.9. Sample with applied electrodes, prepared for the electrical measurement using the DC-4W method.

The measurements were performed under dry synthetic air conditions ($p_{O_2} = 0.2$ atm. and $p_{H_2O} \sim 10^{-5}$ atm.) in the $300 - 800$ °C temperature range. At each temperature,

the samples were stabilised for a minimum of one hour, although in the intermediate temperature range ($450 - 650$ °C), the stabilisation time was extended to $4 - 6$ hours. To assess the effect of water vapour on the electrical properties of the SFC materials, the total electrical conductivity of $SrFe_{0.6}Co_{0.4}O_{3-\delta}$ was also measured in wet synthetic air conditions ($p_{O_2} = 0.2$ atm. and $p_{H_2O} \approx 2.3 \times 10^{-2}$ atm.) within the same temperature range. A Keithley 2401 was used as a high-precision DC source, while a Keysight 34970A functioned as a voltmeter with integrated data acquisition.

4.4.2. Electrochemical impedance spectroscopy

The electrical properties of solids with total electrical conductivity below $\sim 10^{-2}$ S/cm can be characterised by measuring the impedance of the material. Electrochemical impedance spectroscopy (EIS) is particularly well-suited for analysing materials with ionic conductivity, since in DC measurements ions are blocked by most electrodes. A key advantage of this method lies in its ability to distinguish and characterise various electrochemical processes occurring within the material under the influence of an electric field. EIS enables the determination of both real and imaginary components of the impedance as a function of frequency.

The EIS method entails applying an alternating voltage U of variable frequency to the sample:

$$U = U_0 \, sin(\omega t), \tag{4.27}$$

where U_0 denotes the amplitude of the voltage signal, ω is the frequency of the signal, and t is time. The response is recorded as a phase-shifted current I in relation to the excitation signal:

$$I = I_0 \, sin(\omega t + \varphi), \tag{4.28}$$

where I_0 represents the amplitude of the current response, while φ is the phase shift. The measurement enables the determination of the impedance of the sample according to the equation:

$$Z = \frac{U}{I} = Z_0 \frac{sin(\omega t)}{sin(\omega t + \varphi)}, \tag{4.29}$$

A schematic representation of the two sinusoidal signals with a phase difference between them is shown in **Figure 4.10**, with examples of the influence of different electrical elements on the recorded signal.[146]

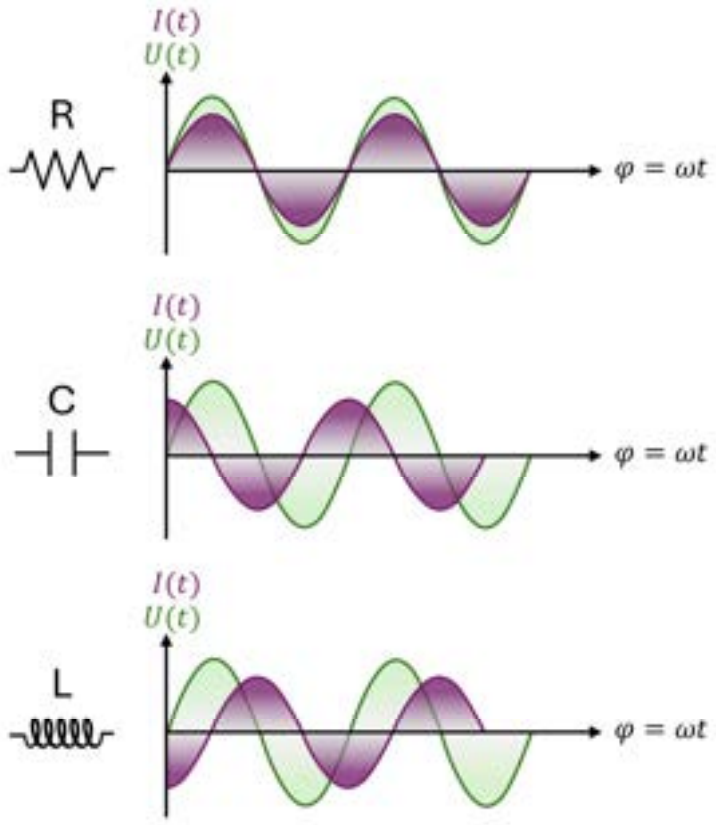

Figure 4.10. The sinusoidal signals of voltage and current presenting three different scenarios with a low amplitude alternating voltage applied to a resistor (R), a capacitor (C), and an inductor (L).

The impedance data is typically represented as Nyquist plots consisting of a series of semicircles, which can be modelled using equivalent electrical circuits, with each semicircle corresponding to distinct electrochemical processes governed by unique electrical parameters. The equivalent circuits can be constructed using electrical elements, such as resistors, inductors, and capacitors, denoted in the diagrams as R, L, and C, respectively. In solids, electrochemical processes characterised by capacitive behaviour, such as the ionic conductivity of grains, lead to a distortion of the observed semicircles. The permittivity of solids depends on the frequency of the alternating electric field. To accurately represent these processes, a constant phase element (CPE) can be introduced, of which the imaginary part of the impedance can be expressed as:

$$Z''_{CPE} = \frac{1}{Q(i\omega)^{\alpha_{CPE}}}, \tag{4.30}$$

where Q represents the admittance of the CPE, while α_{CPE} is a parameter reflecting the deviation of CPE from the ideal capacitor behaviour.[147] The influence of the α_{CPE} value on the shape of the semicircle is shown in **Figure 4.11**.

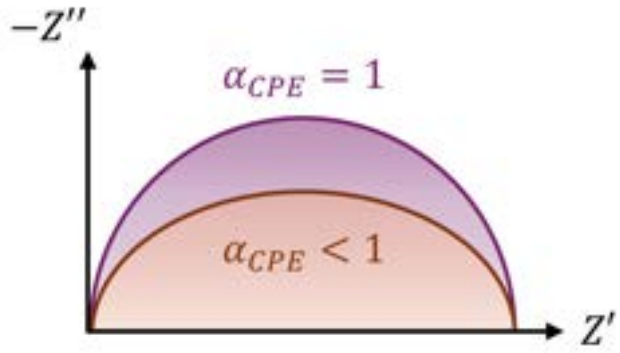

Figure 4.11. The Nyquist plot presenting two semicircles of different α_{CPE} parameter value. Z'' and Z' represent the imaginary and real parts of the impedance, respectively.

Electrochemical and physical processes in materials, such as charge transfer, adsorption, dissociation, diffusion, and conduction, are associated with specific characteristic time constants. However, when these time constants are similar, accurately attributing the observed phenomena to particular processes can be challenging or even impossible.

The fitting of each semicircle enables obtaining a set of parameters describing its shape. Based on their value, one can evaluate the capacitance corresponding to each semicircle according to the equation:

$$C_{semicircle} = Q^{1/\alpha_{CPE}} R^{\left(\frac{1}{\alpha_{CPE}}-1\right)}. \tag{4.31}$$

This parameter characterises the type of electrochemical process occurring in samples, enabling categorisation based on capacitance. The ranges of $C_{semicircle}$ corresponding to different types of processes taking place in solids are summarised in **Table 4.4**.[148]

Table 4.4. Possible interpretations of different capacitance values.[148]

Capacitance (F)	**Process/Phenomenon responsible**
10^{-12}	conductivity of the grains
$10^{-11} - 10^{-8}$	conductivity of the grain boundaries
$10^{-9} - 10^{-7}$	processes related to the surface charge layer
$10^{-7} - 10^{-5}$	processes occurring on the sample-electrode interface
10^{-4}	electrochemical reactions

After the fitting of the impedance data and the evaluation of the obtained fitting parameters, the conductivity of the material can be determined using the formula:

$$\sigma = \frac{1}{R_{tot}} \cdot \frac{x_t}{S_{electrode}}, \tag{4.32}$$

where x_t is the thickness of the sample (distance between the electrodes), $S_{\text{electrode}}$ is the area of the parallel platinum electrodes, and R_{tot} represents the total resistance of the material, calculated as the sum of resistances corresponding to the processes related only to the material itself (classified based on the capacitance obtained for each semicircle).

In this study, the electrical properties of the BCZYM material group were analysed using EIS within the temperature range of $300 - 800$ °C under both dry ($p_{H_2O} \sim 10^{-5}$ atm.) and wet ($p_{H_2O} \approx 2.3 \times 10^{-2}$ atm.) synthetic air conditions ($p_{O_2} = 0.2$ atm.). Impedance measurements were performed using a Gamry Reference 600+ device across a frequency range of 10 Hz to 3 MHz in potentiostatic mode. The samples, prepared as flat cylindrical pellets, were coated with platinum electrodes applied to both flat faces and sintered at 930 °C for 3 hours. The wires on opposite sides of the pellet were positioned at right angles to each other in order to reduce the risk of a short circuit. The illustration depicting the sample with applied electrodes is shown in **Figure 4.12**.

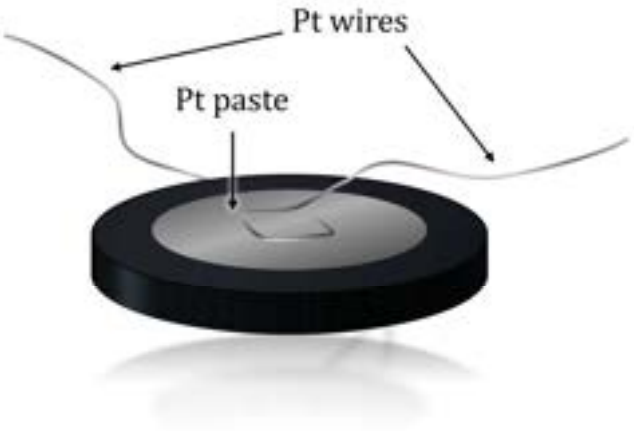

Figure 4.12. Sample with applied electrodes, prepared for the electrical measurement using the 2-point EIS.

4.4.3. Electrical conductivity relaxation

Understanding various electrochemical phenomena in mixed-conducting materials often requires a detailed analysis of oxygen or water surface exchange rates. For instance, the long-term degradation of intermediate-temperature solid oxide fuel cell (IT-SOFC) cathode materials has been previously investigated in relation to the kinetics of the oxygen reduction reaction (ORR).[149,150] However, the rate of oxygen surface exchange in mixed conductors in the presence of water vapour remains poorly understood.

The electrical conductivity relaxation (ECR) method is a technique used to derive surface exchange coefficients and diffusivities of species such as water, protons, or oxygen. This method involves monitoring the change in material conductivity following an abrupt change in the partial pressure of oxygen or water at a constant temperature. The incorporation and release of oxygen or water changes the concentrations of charge carriers within

the material, resulting from establishing a new equilibrium. The electrical conductivity of the material, therefore, changes. The rate at which these changes occur depends on the chemical diffusion coefficient and the chemical surface exchange coefficient of the incorporated species. The relationship between the concentration and the conductivity of the material in constant external conditions can be expressed through the equation:

$$\frac{c(t)-c(0)}{c(\infty)-c(0)}=\frac{\sigma(t)-\sigma(0)}{\sigma(\infty)-\sigma(0)}, \tag{4.33}$$

where $c(0)$, $c(t)$, and $c(\infty)$ represent the initial, time-dependent, and equilibrium concentrations of the considered species, respectively. Similarly, $\sigma(0)$, $\sigma(t)$, and $\sigma(\infty)$ denote the initial, time-dependent, and equilibrium electrical conductivities of the material.

The surface exchange and bulk diffusion fluxes at equilibrium follow the equation:

$$-D_{chem}\frac{\partial c}{\partial x}\Big|_{x=\pm a}=k_{chem}[c(\infty)-c(t)], \tag{4.34}$$

where a is the relevant dimension of the sample. Solving this partial differential equation yields a fitting function, which depends on the geometry of the sample. For this study, a 3D bar sample model was used, described by equation (4.35), using solutions of Fick's second law with appropriate boundary conditions:[151]

$$\frac{\sigma(t)-\sigma(0)}{\sigma(\infty)-\sigma(0)}= \\ =1-\sum_{m=1}^{\infty}\sum_{n=1}^{\infty}\sum_{p=1}^{\infty}\left\{\frac{2L_x^2\,exp\left(-\frac{\alpha_m^2 D_{chem}t}{x^2}\right)}{\alpha_m^2(\alpha_m^2+L_x^2+L_x)}\times\frac{2L_y^2\,exp\left(-\frac{\beta_n^2 D_{chem}t}{y^2}\right)}{\beta_n^2(\beta_n^2+L_y^2+L_y)}\times\frac{2L_z^2\,exp\left(-\frac{\gamma_p^2 D_{chem}t}{z^2}\right)}{\gamma_p^2(\gamma_p^2+L_z^2+L_z)}\right\}, \tag{4.35}$$

where L_x, L_y, and L_z are the Biot numbers defined as:

$$L_x=x\cdot\frac{k_{chem}}{D_{chem}}, L_y=y\cdot\frac{k_{chem}}{D_{chem}}, L_z=z\cdot\frac{k_{chem}}{D_{chem}}, \tag{4.36}$$

with x, y, and z representing half the sample's length, width, and thickness, respectively. The terms α_m, β_n, and γ_p are the positive roots of the equations:

$$\alpha_m tan\,(\alpha_m)=L_x, \beta_n tan\,(\beta_n)=L_y, \gamma_p tan\left(\gamma_p\right)=L_z. \tag{4.37}$$

In this study, the L_z parameter (subsequently referred to as L) was utilised to identify the slower, limiting process during the relaxation measurements.[152] If L fell below 0.03, the limiting process was surface exchange; conversely, if it exceeded 30, the limiting process was bulk diffusion. In both cases, it would be possible to determine only one coefficient, corresponding to the limiting process. If the L value was between 0.03 and 30, both coefficients could be established.

The ECR method was applied to analyse the BCZYM and SFC materials. For these diffusion studies, platinum reversible electrodes were arranged in a four-probe configuration (**Figure 4.9**). The conductivity evolution of the samples was measured using a ProboStat™ measurement system (NorECs, Norway) integrated with a current source and a voltmeter.

The time-dependent conductivity changes after altering the oxygen or water partial pressures were used to study oxygen and water diffusion, respectively. For the BCZYM materials, oxygen diffusion was investigated by switching the oxygen partial pressure between $p_{O_2} = 0.1$ atm. and $p_{O_2} = 10^{-3}$ atm. under both dry and wet gas mixtures at $500 - 800$ °C. Water diffusion studies were conducted in synthetic air over a temperature range of $450 - 800$ °C, with the water partial pressure toggled between $p_{H_2O} \sim 10^{-5}$ atm. and $p_{H_2O} \approx 0.023$ atm. For $SrFe_{0.6}Co_{0.4}O_{3-\delta}$, oxygen diffusion was studied by alternating the oxygen partial pressure between $p_{O_2} = 0.1$ atm. and $p_{O_2} = 1$ atm. under both dry and wet conditions.

The results of the ECR measurements on $BaCe_{0.6}Zr_{0.2}Y_{0.2-x}Fe_xO_{3-\delta}$ and $SrFe_{0.6}Co_{0.4}O_{3-\delta}$ samples were analysed using the NETL SOFC ECR Analysis software, developed by the National Energy Technology Laboratory (NETL), U.S. Department of Energy (DOE)[153], while the ECR data collected for $BaCe_{0.6}Zr_{0.2}Y_{0.1}Tb_{0.1}O_{3-\delta}$ was analysed using ECRTOOLS MATLAB toolbox, developed by Francesco Ciucci.[151] These tools enabled the determination of D_{chem} and/or k_{chem} for oxygen, hydrogen, or water by fitting experimental data to the proposed models using the nonlinear least squares method.

4.5. Thermoelectric measurements

The Seebeck effect is the phenomenon in which a thermovoltage is generated in the presence of a temperature gradient in the material. The Seebeck coefficient (S) is one of the measures of the thermoelectric properties of a material described by the formula:

$$S = \frac{\Delta V}{\Delta T}. \tag{4.38}$$

where ΔV is the thermovoltage, and ΔT is the temperature difference between the electrodes measuring the thermovoltage.

Thermoelectric measurements can be of great use in the investigation of the transport properties and defect chemistry of mixed ionic-electronic conductors. In the case of oxides with a hopping conduction mechanism, the Seebeck coefficient can be expressed using the Heikes formula:[154,155]

$$S = \pm\frac{k_B}{e}\left(ln\beta\frac{1-c}{c} + \frac{S_T^*}{k_B}\right), \tag{4.39}$$

where c signifies the concentration of the predominant electronic carriers, S_T^* represents the vibrational entropy, and β indicates a degeneracy factor that accounts for the local spin-orbit degeneracies of ions in various oxidation states.[156] To simplify equation (4.39), the β factor may be approximated as 1, which is valid for the materials examined in this study at temperatures above 300 °C.[157] Further simplification of (4.39) was made by Hombo et al., who assumed that the vibrational entropy term in the Seebeck coefficient of SFO was negligible.[158] The sign of the Seebeck coefficient depends on the sign of the majority charge carrier facilitating the entropy transport. Since the materials investigated in this work exhibit predominantly p-type electronic conductivity, the S parameter is expected to take positive values and can be expressed as:

$$S = \frac{k_B}{e}\left(ln\frac{1-p}{p}\right), \tag{4.40}$$

where p is the concentration of electron holes. Therefore, based on the Seebeck coefficient of the material, the carrier concentration in that material can be estimated. The contribution of vibrational entropy to thermoelectric properties has not been sufficiently addressed in the literature. Since the majority of reports focus on the electronic and configurational terms, the lattice-related effects contributing to the Seebeck coefficient are generally considered minor. Recent reports on perovskite oxides with mobile ionic defects indicate that the vibrational entropy can affect the thermoelectric transport in such materials, particularly at higher temperatures. For example, Tsvetkov et al. reported that in $BaZr_{0.9}Y_{0.1}O_{3-\delta}$ vibrational entropy significantly influences the thermoelectric transport of protons and oxygen ions, while its effect on the thermoelectric transport of electron holes is minor.[159] In materials exhibiting a small-polaron hopping mechanism of conduction, the vibrational entropy term in equation (4.39) typically contributes less than 10 μV/K to the Seebeck coefficient, as was previously reported for vanadium-based spinels[160], manganese oxides[161], and ferrite-cobaltite perovskites[162].

In this work, the Seebeck coefficient measurements were conducted using a Linseis LSR-4 system, with a schematic representation of the experimental setup provided in **Figure 4.13**. The samples were prepared as rectangular prisms, with four porous platinum electrodes.

A pair of electrodes was placed on the top and bottom surfaces of the sample to serve as thermal contacts, facilitating the introduction of a temperature gradient. The remaining two electrodes, positioned near the middle of the sample, were used as sense electrodes to measure the temperature difference and the thermovoltage between them. These measurements enabled the calculation of the Seebeck coefficient S using the following equation:

$$S = \frac{\Delta V}{T_2 - T_1} = \frac{V_2 - V_1}{T_2 - T_1}, \tag{4.41}$$

where T_1 and T_2 represent the temperatures, while V_1 and V_2 indicate the electric potential at the respective sense electrode positions.

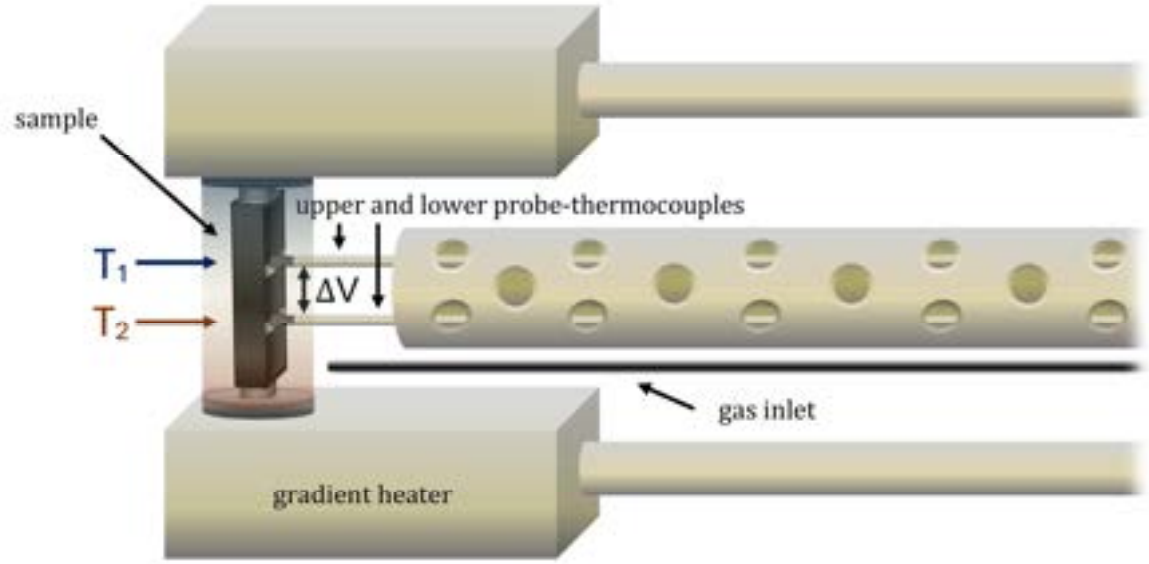

Figure 4.13. Schematic illustration of the central part of the Linseis LSR-4 setup used for the Seebeck coefficient measurements.

The distance between the electrodes was 6 mm or 4 mm. Data was collected during the cooling phase, ensuring temperature stabilisation at each measurement point. A cooling rate of 15 °C/min was applied between successive temperature points. The measurements were carried out in synthetic air ($p_{O_2} = 0.2$ atm.), under dry ($p_{H_2O} \sim 10^{-5}$ atm.) and humidified atmospheres ($p_{H_2O} \approx 0.023$ atm.). To eliminate the effect of the offset voltage on the obtained results, the voltage was measured at least 4 times at every temperature, each time using a different temperature gradient. The values of the Seebeck coefficient were calculated as the slope of the linear voltage dependence on the temperature difference between the two middle electrodes (T_1 and T_2).

5. Results and discussion

5.1. Properties of $BaCe_{0.6}Zr_{0.2}Y_{0.2-x}M_xO_{3-\delta}$ materials

5.1.1. Structural characterisation

Figure 5.1 shows the XRD patterns of $BaCe_{0.6}Zr_{0.2}Y_{0.2-x}Fe_xO_{3-\delta}$ (x = 0, 0.02, 0.05, 0.1) and $BaCe_{0.6}Zr_{0.2}Y_{0.1}M_{0.1}O_{3-\delta}$ (M = Tb, Pr). The reference sample BCZY622 exhibits the widest reflections, which is related to the wet-chemistry method of synthesis used for this material, producing smaller crystallites than the ones obtained by the SSRS method. All studied samples consisted of the main phase of perovskite oxide and a trace amount of other phase, giving rise to additional reflections (marked with a star sign), which most likely originated from the nickel oxide added during the second synthesis step.

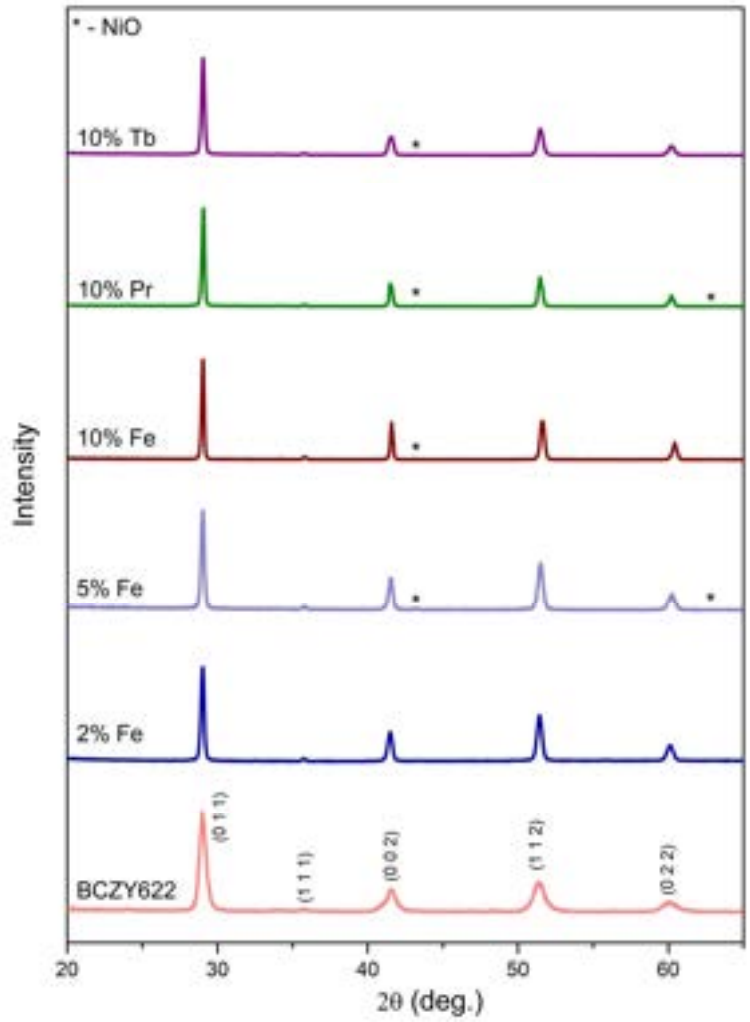

Figure 5.1. X-ray diffraction patterns of $BaCe_{0.6}Zr_{0.2}Y_{0.1}M_{0.1}O_{3-\delta}$ (M = Tb, Pr) and $BaCe_{0.6}Zr_{0.2}Y_{0.2-x}Fe_xO_{3-\delta}$ (x = 0, 0.02, 0.05, 0.1) collected at room temperature.

Adapted from J. Budnik, A. Mielewczyk-Gryń, M. Gazda and T. Miruszewski, "Water uptake kinetics and electrical transport in $BaCe_{0.6}Zr_{0.2}Y_{0.1}M_{0.1}O_{3-\delta}$ (M = Tb, Pr, Fe) protonic conductors", J. Mater. Chem. A, 2023, 11, 13389–13398, and from J. Budnik, A. Mielewczyk-Gryń, M. Gazda and T. Miruszewski, "Influence of iron content on water uptake and charge transport in $BaCe_{0.6}Zr_{0.2}Y_{0.2-x}Fe_xO_{3-\delta}$ triple-conducting oxides", J. Mater. Chem. A, 2024, 12, 14569–14582, with permission from the Royal Society of Chemistry.[163,164]

To appropriately establish the best-suited unit cell model for the Rietveld refinement, the XRD patterns of selected BCZYM have been refined using perovskite unit cells of three different symmetries: $Pm\bar{3}m$ (cubic), $R\bar{3}c$ (trigonal), and $Pmma$ (orthorhombic). The XRD diffraction patterns with the calculated and differential curves for $BaCe_{0.6}Zr_{0.2}Y_{0.2-x}Fe_xO_{3-\delta}$ (x = 0.02, 0.05, 0.1) and $BaCe_{0.6}Zr_{0.2}Y_{0.1}M_{0.1}O_{3-\delta}$ (M = Tb, Pr) are included in the **Appendix** (**Figures A1** and **A2**, respectively). The lowest R_{wp} attained for the cubic structure of BCZYFe2 indicates that it is the best model for this material, while for the $BaCe_{0.6}Zr_{0.2}Y_{0.1}M_{0.1}O_{3-\delta}$ (M = Tb, Pr) materials the lowest R_{wp} was obtained for the orthorhombic unit cell as the model structure. For BCZYFe5 and BCZYFe10, the quality of refinement metrics did not yield the best possible model determination. In the literature, similar materials, such as Fe-doped BCZY, Pr-doped BCY, and Pr-doped BCZY, have been reported as noncubic at room temperature.[165–167] The diverse symmetries observed in the BCZY-related perovskites could arise from tilting of the $(Ce,Zr,Y)O_6$ octahedra, which are difficult to detect by XRD. Moreover, the structural distortions, that may arise from the incorporation of the transition-metal substituent into the BCZY host material could be localised and undetectable by XRD analysis. Thus, the precise determination of the crystal symmetry for this group of materials might not be achievable using this method. Therefore, the symmetry of the materials investigated in this study will be regarded as pseudocubic.

The pseudocubic unit cell parameters obtained via Rietveld refinement of the collected patterns, along with the calculated Goldschmidt tolerance factors for each material, are summarised in **Table 5.1**. A tolerance factor is close to 1 for all investigated materials. The pseudocubic unit cell parameters for $BaCe_{0.6}Zr_{0.2}Y_{0.1}M_{0.1}O_{3-\delta}$ (where M = Tb, Pr, Fe) increase in the following order: Fe < Tb < Pr, consistent with the increasing radius of these cations.[168] Furthermore, the size of the unit cell increases as the iron content decreases in the $BaCe_{0.6}Zr_{0.2}Y_{0.2-x}Fe_xO_{3-\delta}$ series, which stems from the larger ionic radius of yttrium compared to that of iron.[168] BCZY622 exhibits the largest unit cell parameter of 4.3522(1) Å,[169] which agrees with the fact that the yttrium ion is present in a 3+ oxidation state, while ions of terbium, praseodymium and iron are expected to exist in an intermediate oxidation state between 3+ and 4+ (as confirmed by the XAS evaluation, see **Figure A5** in the **Appendix**), which can be associated with a lower ionic radius for the same coordination number.

The relative density of the studied samples is shown in **Table 5.1**. All obtained samples exhibit densities above 90%. This indicates that the nickel oxide used during the second step of synthesis leads to an effective densification of the samples. BCZYTb10 exhibits the highest relative density – 99.9%, while BCZYFe10 exhibits the lowest – 90.2%. Moreover, the decreased iron content positively influenced the densification of samples, with BCZYFe2

reaching 99.1% of theoretical density. This points to the detrimental effect of iron on the sintering properties of BCZYM materials.

Table 5.1. Goldschmidt tolerance factors, pseudocubic unit cell parameters with the respective GOF parameters and relative density determined for the samples of $BaCe_{0.6}Zr_{0.2}Y_{0.1}M_{0.1}O_{3-\delta}$ (M = Tb, Pr) and $BaCe_{0.6}Zr_{0.2}Y_{0.2-x}Fe_xO_{3-\delta}$ (x = 0, 0.02, 0.05, 0.1).

	t	$a = b = c$ (Å)	GOF	Relative density (%)
BCZY**Tb10** [163]	0.954	4.3470(2)	1.97	99.9
BCZY**Pr10** [163]	0.950	4.3487(2)	3.31	94.5
BCZY**Fe10** [163]	0.963	4.3205(2)	2.33	90.2
BCZY**Fe5** [164]	0.955	4.3307(2)	1.63	98.6
BCZY**Fe2** [164]	0.951	4.3515(1)	1.84	99.1
BCZY**622** [169]	0.948	4.3522(1)	1.94	97.5

Adapted from J. Budnik, A. Mielewczyk-Gryń, M. Gazda and T. Miruszewski, "Water uptake kinetics and electrical transport in $BaCe_{0.6}Zr_{0.2}Y_{0.1}M_{0.1}O_{3-\delta}$ (M = Tb, Pr, Fe) protonic conductors", J. Mater. Chem. A, 2023, 11, 13389–13398, and from J. Budnik, A. Mielewczyk-Gryń, M. Gazda and T. Miruszewski, "Influence of iron content on water uptake and charge transport in $BaCe_{0.6}Zr_{0.2}Y_{0.2-x}Fe_xO_{3-\delta}$ triple-conducting oxides", J. Mater. Chem. A, 2024, 12, 14569–14582, with permission from the Royal Society of Chemistry.[163,164]

To further investigate the effect of nickel oxide on the BCZYM samples, the representative of this group exhibiting the highest density, BCZYTb10, was synthesised without NiO. The XRD patterns of BCZYTb10 synthesised with and without the sintering aid are shown in **Figure 5.2**. The former sample was not single-phase. Therefore, nickel oxide can function not only as a sintering agent but may also lead to the formation of the single-phase cubic perovskite materials using only a two-step SSRS route. This effect may be related to the formation of a BaY_2NiO_5 phase during the second step of synthesis, which can promote grain growth and, after its decomposition, increase the concentrations of cation and oxygen vacancies, leading to the enhanced diffusion properties for those ions.[137] Since a comparison of the density of samples should involve only samples containing the same phase, the sample obtained without NiO was not subjected to the density evaluation.

To sum up, all synthesised BCZYM materials formed perovskite structures. The unit cell parameters reflected the ionic radii of the incorporated substituents. The relative density exceeded 90% for all samples, indicating effective sintering. The addition of nickel oxide was found to be crucial for phase purity, suggesting its dual role as a sintering aid and promoter of single-phase formation in BCZYM ceramics.

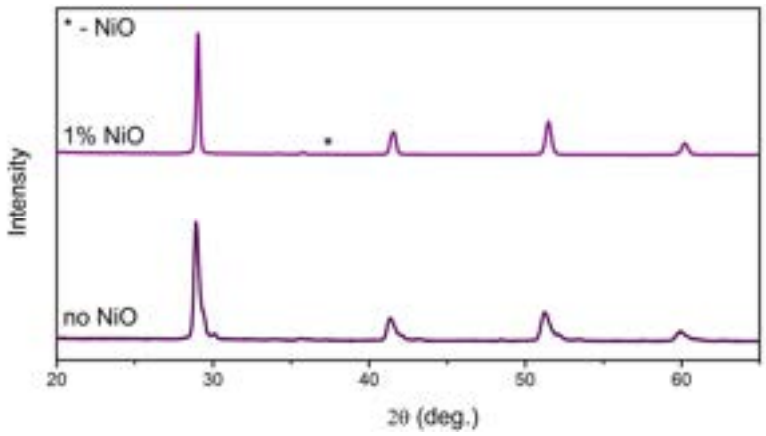

Figure 5.2. X-ray diffraction patterns of $BaCe_{0.6}Zr_{0.2}Y_{0.1}Tb_{0.1}O_{3-\delta}$ samples with 1 wt% of NiO[163] and no NiO added during the second step of synthesis.

5.1.2. Defect chemistry

To investigate the defect chemistry in the BCZYM material group, the concentrations of oxygen vacancies and proton defects have been evaluated. The concentration of oxygen vacancies has been determined by iodometric titration, yielding oxygen nonstoichiometry values for all analysed materials at room temperature. It was assumed that the concentration of oxygen atoms in the interstitial positions is negligible compared to the concentration of oxygen vacancies. Therefore, the oxygen nonstoichiometry has been interpreted directly as the concentration of oxygen vacancies. The obtained values of oxygen nonstoichiometry (δ) are shown in **Table 5.2**.

Table 5.2. Oxygen nonstoichiometry, proton concentration in air at 300 °C, as well as the average electronegativity of B and A cations and their difference, determined for and $BaCe_{0.6}Zr_{0.2}Y_{0.2-x}Fe_xO_{3-\delta}$ (x = 0, 0.02, 0.05, 0.1) and $BaCe_{0.6}Zr_{0.2}Y_{0.1}M_{0.1}O_{3-\delta}$ (M = Tb, Pr).

	δ (mol/mol)	$[OH_O^{\bullet}]$ (mol/mol)	$\frac{[OH_O^{\bullet}]}{2[v_O^{\bullet\bullet}]} \cdot 100\%$	$\frac{\chi_A + \chi_B}{2}$	$\chi_B - \chi_A$
BCZY622 [169]	0.103(2)	0.095	47%	1.321	0.468
BCZY**Fe2** [164]	0.104(3)	0.054	26%	1.323	0.472
BCZY**Tb10** [163]	0.094(2)	0.028	15%	1.326	0.479
BCZY**Fe5** [164]	0.086(4)	0.017	10%	1.326	0.479
BCZY**Pr10** [163]	0.073(2)	0.010	7%	1.330	0.487
BCZY**Fe10** [163,164]	0.066(5)	0.007	6%	1.332	0.489

Adapted from J. Budnik, A. Mielewczyk-Gryń, M. Gazda and T. Miruszewski, "Water uptake kinetics and electrical transport in $BaCe_{0.6}Zr_{0.2}Y_{0.1}M_{0.1}O_{3-\delta}$ (M = Tb, Pr, Fe) protonic conductors", J. Mater. Chem. A, 2023, 11, 13389–13398, and from J. Budnik, A. Mielewczyk-Gryń, M. Gazda and T. Miruszewski, "Influence of iron content on water uptake and charge transport in $BaCe_{0.6}Zr_{0.2}Y_{0.2-x}Fe_xO_{3-\delta}$ triple-conducting oxides", J. Mater. Chem. A, 2024, 12, 14569–14582, with permission from the Royal Society of Chemistry.[163,164]

The δ parameter assumes the highest and similar values for the materials with the lowest amount of transition-metal substituent – BCZY622 and BCZYFe2. The value above 0.1 mol/mol indicates either a small amount of Ce^{3+} present (consistent with the XAS results, see **Figure A7** in the **Appendix**) or, in the case of BCZYFe2, that the average oxidation state of the iron ion might assume a value lower than 3+ (XAS studies indicate that all iron-containing BCZYM materials possess Fe in oxidation state ≈ 3+, see **Figure A6** in the **Appendix**). In the $BaCe_{0.6}Zr_{0.2}Y_{0.1}M_{0.1}O_{3-\delta}$ and $BaCe_{0.6}Zr_{0.2}Y_{0.2-x}Fe_xO_{3-\delta}$ series, two tendencies have been observed. The oxygen nonstoichiometry of BCZYM depends on the M element and decreases in the following order: Tb > Pr > Fe. The second tendency is that the values of the δ parameter increase with the lowering of the amount of iron in the $BaCe_{0.6}Zr_{0.2}Y_{0.2-x}Fe_xO_{3-\delta}$ series. The unit cell parameter and oxygen nonstoichiometry as a function of iron content in $BaCe_{0.6}Zr_{0.2}Y_{0.2-x}Fe_xO_{3-\delta}$ materials are presented in **Figure 5.3**.

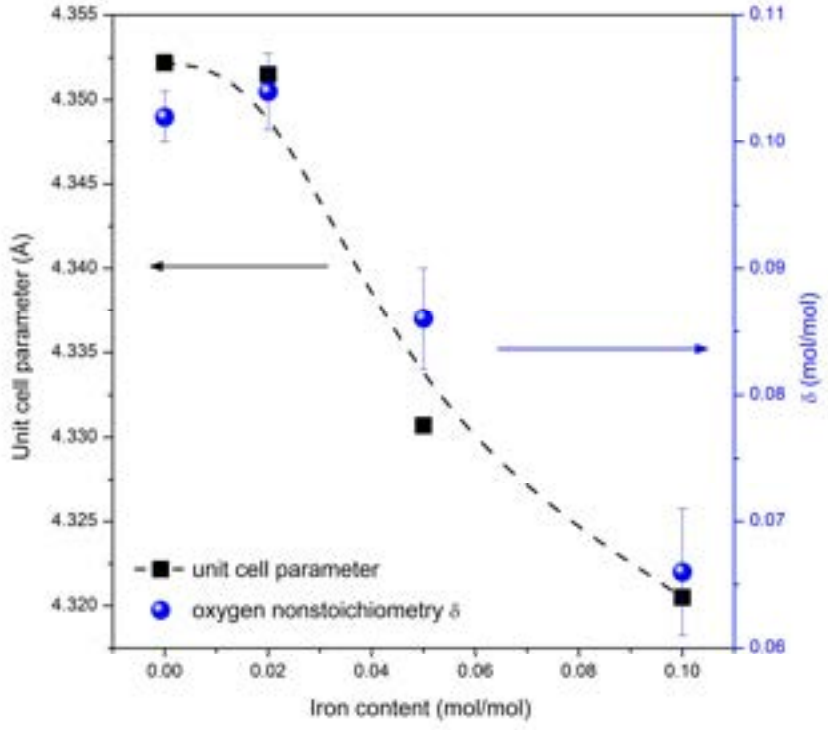

Figure 5.3. The pseudocubic unit cell parameter and the oxygen nonstoichiometry, determined via iodometric titration as a function of iron content in $BaCe_{0.6}Zr_{0.2}Y_{0.2-x}Fe_xO_{3-\delta}$ (x = 0, 0.02, 0.05, 0.1). The dashed line serves as a visual aid.

Adapted from J. Budnik, A. Mielewczyk-Gryń, M. Gazda and T. Miruszewski, "Influence of iron content on water uptake and charge transport in $BaCe_{0.6}Zr_{0.2}Y_{0.2-x}Fe_xO_{3-\delta}$ triple-conducting oxides", J. Mater. Chem. A, 2024, 12, 14569–14582, with permission from the Royal Society of Chemistry.[164]

The concentrations of proton defects in BCZYM samples at 300 °C were determined using thermogravimetric analysis. The mass changes recorded before and after the switches of atmospheres between dry and wet air and in the opposite direction are shown in **Figure 5.4**. Across all investigated samples, a visible mass increase was observed following the introduction of water vapour, signifying that all materials undergo water uptake at 300 °C.

The additional TG measurements at 450 °C and 600 °C are included in the **Appendix** in **Figure A3**.

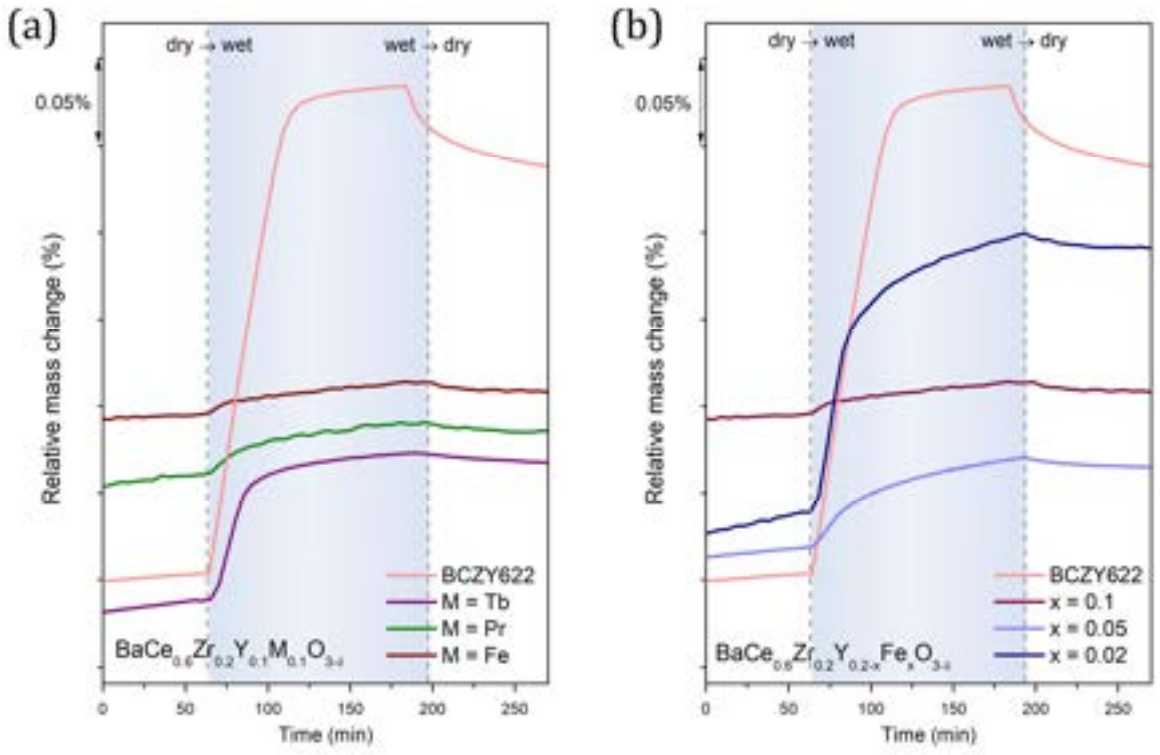

Figure 5.4. Time evolution of the mass change of $BaCe_{0.6}Zr_{0.2}Y_{0.1}M_{0.1}O_{3-\delta}$ (M = Tb, Pr, Fe) (a), and $BaCe_{0.6}Zr_{0.2}Y_{0.2-x}Fe_xO_{3-\delta}$ (x = 0.02, 0.05, 0.1) (b), recorded at 300 °C before and after switching the atmosphere from dry to wet and from wet to dry air. In both plots, the data for BCZY622 is shown as a reference.

Adapted from J. Budnik, A. Mielewczyk-Gryń, M. Gazda and T. Miruszewski, "Water uptake kinetics and electrical transport in $BaCe_{0.6}Zr_{0.2}Y_{0.1}M_{0.1}O_{3-\delta}$ (M = Tb, Pr, Fe) protonic conductors", J. Mater. Chem. A, 2023, 11, 13389–13398, and from J. Budnik, A. Mielewczyk-Gryń, M. Gazda and T. Miruszewski, "Influence of iron content on water uptake and charge transport in $BaCe_{0.6}Zr_{0.2}Y_{0.2-x}Fe_xO_{3-\delta}$ triple-conducting oxides", J. Mater. Chem. A, 2024, 12, 14569–14582, with permission from the Royal Society of Chemistry.[163,164]

Among the $BaCe_{0.6}Zr_{0.2}Y_{0.1}M_{0.1}O_{3-\delta}$ materials, the changes in relative masses were approximately 0.08%, 0.03%, and 0.02%, for the samples substituted with Tb, Pr, and Fe, respectively. The $BaCe_{0.6}Zr_{0.2}Y_{0.1}M_{0.1}O_{3-\delta}$ samples assumed a considerably lower hydration level than the reference sample BCZY622, of which the mass increased by almost 0.3%. Since the samples substituted with metal of varying valence can have an increased electron-hole concentrations in air compared to BCZY622 (exhibiting only hydration), the water uptake in the BCZYM materials could also proceed via hydrogenation. To identify the predominant water-uptake process in the studied materials in air, additional thermogravimetric measurements were conducted in a nitrogen atmosphere. The water uptake TG measurements conducted in nitrogen at 300 °C are included in the **Appendix** (**Figure A4**). The concentration of electron holes in the nitrogen atmosphere (low p_{O_2}) can be considered negligible. Consequently, the hydration process is responsible for the water uptake in such conditions. As the concentration of oxygen vacancies increases at lower oxygen partial pressures, the hydration levels for the investigated materials increased compared to those in air.

However, the mass relaxation curves remained similar. It can be assumed that the mechanism of the water-uptake process occurring in $BaCe_{0.6}Zr_{0.2}Y_{0.1}M_{0.1}O_{3-\delta}$ materials remains the same in both atmospheres; hence, the protons are most likely incorporated into the materials through the hydration reaction. Since the predominant water-uptake process established for BCZYFe10 was hydration, the samples with lower iron content, BCZYFe5 and BCZYFe2, are assumed to undergo hydration. Furthermore, based on the mass relaxation curves presented in **Figure 5.4b**, the materials with lower Fe content are more prone to hydration, which is related to the higher concentration of oxygen vacancies in those materials in comparison to BCZYFe10.

Equation (4.24) was employed to calculate the concentration of protons. The obtained values are included in **Table 5.2**. The material with no additional substituent, BCZY622, shows the highest proton concentration – 0.095 mol/mol. Among the $BaCe_{0.6}Zr_{0.2}Y_{0.1}M_{0.1}O_{3-\delta}$ samples, the concentration of protons shows a similar trend to that of the oxygen vacancies concentration – Tb > Pr > Fe. The same trend was observed in the case of $BaCe_{0.6}Zr_{0.2}Y_{0.2-x}Fe_xO_{3-\delta}$ materials, with decreasing values of proton concentrations as iron content increased. The concentration of proton defects as a function of the oxygen nonstoichiometry is shown in **Figure 5.5**. It can be seen that the proton concentration gradually increases with increasing oxygen-vacancy concentration, indicating a direct relationship between the two. This is expected for materials undergoing the hydration reaction.

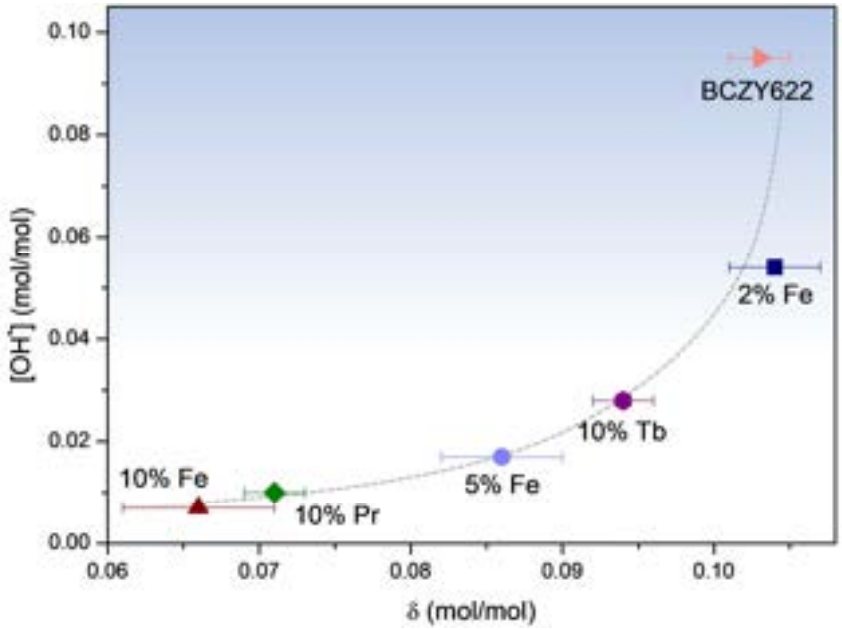

Figure 5.5. The proton concentration at 300 °C as a function of initial oxygen nonstoichiometry in $BaCe_{0.6}Zr_{0.2}Y_{0.2-x}M_xO_{3-\delta}$. The dashed line serves as a visual aid for the observed tendency.

Adapted from J. Budnik, A. Mielewczyk-Gryń, M. Gazda and T. Miruszewski, "Water uptake kinetics and electrical transport in $BaCe_{0.6}Zr_{0.2}Y_{0.1}M_{0.1}O_{3-\delta}$ (M = Tb, Pr, Fe) protonic conductors", J. Mater. Chem. A, 2023, 11, 13389–13398, and from J. Budnik, A. Mielewczyk-Gryń, M. Gazda and T. Miruszewski, "Influence of iron content on water uptake and charge transport in $BaCe_{0.6}Zr_{0.2}Y_{0.2-x}Fe_xO_{3-\delta}$ triple-conducting oxides", J. Mater. Chem. A, 2024, 12, 14569–14582, with permission from the Royal Society of Chemistry.[163,164]

To further investigate the influence of the type and amount of substituent on the water uptake properties of BCZYM materials, the proton concentration and the percentage amount of vacancies filled by proton defects were analysed. Both parameters, as a function of average cation electronegativity and the difference between the B and A cations' electronegativities, are shown in **Figure 5.6**. The details behind the determination of the obtained parameters are included in the **Appendix** (chapter **"Cation electronegativity evaluation"**). The increased iron content may lead to a partial delocalisation of electron holes on iron ions towards adjacent oxygen ions, diminishing the basicity of the oxygen. This leads to reduced proton-uptake efficiency, attributed to the higher electronegativity of iron, which decreases proton concentration.[56]

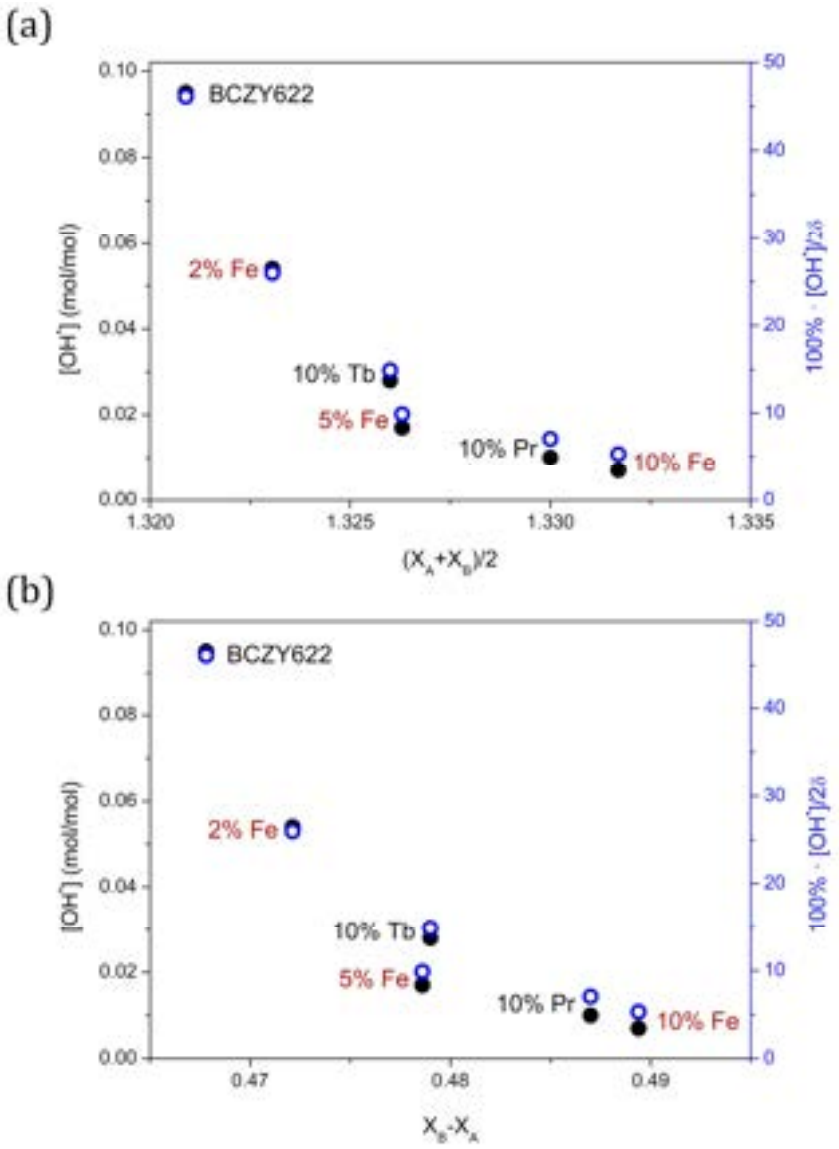

Figure 5.6. The proton concentration and the level of filling the oxygen vacancies by the proton defects in $BaCe_{0.6}Zr_{0.2}Y_{0.2-x}M_xO_{3-\delta}$ as a function of the mean electronegativity of A and B cations (a) and their difference (b).

Adapted from J. Budnik, A. Mielewczyk-Gryń, M. Gazda and T. Miruszewski, "Water uptake kinetics and electrical transport in $BaCe_{0.6}Zr_{0.2}Y_{0.1}M_{0.1}O_{3-\delta}$ (M = Tb, Pr, Fe) protonic conductors", J. Mater. Chem. A, 2023, 11, 13389–13398, and from J. Budnik, A. Mielewczyk-Gryń, M. Gazda and T. Miruszewski, "Influence of iron content on water uptake and charge transport in $BaCe_{0.6}Zr_{0.2}Y_{0.2-x}Fe_xO_{3-\delta}$ triple-conducting oxides", J. Mater. Chem. A, 2024, 12, 14569–14582, with permission from the Royal Society of Chemistry.[163,164]

According to the literature reports, the lower average A and B electronegativity[55] and their difference[45] lead to the higher water uptake. **Figure 5.6** presents that the data obtained in this work show a similar behaviour. There is a slight deviation from the monotonic changes shown by the samples containing 10 mol.% of Tb and 5 mol.% of Fe. Nonetheless, in both cases, the data follows the tendency of decreasing proton concentration with higher values of average cation electronegativity and their difference. The same observation applies to the level of vacancy filling by proton defects.

To analyse the kinetics of water uptake in the BCZYM materials, the time derivatives of mass changes were calculated. The relative mass change and its derivative for each investigated material are presented in **Figure 5.7**. The mass increase recorded following the switch from dry to humidified air occurs in two distinct stages across all samples. In the first stage, the mass increases rapidly, most likely due to the proton uptake. Subsequently, the time derivative flattens and remains stable, but does not diminish completely, indicating a slow, continuous change. The slower second step may originate from an additional process occurring in the materials, competing with hydration. Such behaviour was also recorded in other MIEC oxides, e.g. Sr(Ti, Fe)$O_{3-\delta}$ and double perovskite cobaltites, which, after the proton incorporation process, underwent oxidation during the second step of mass relaxation.[170–172]

In the case of $BaCe_{0.6}Zr_{0.2}Y_{0.2-x}Fe_xO_{3-\delta}$ (x = 0, 0.02, 0.05, 0.1) series, the rate of mass increase diminishes progressively with increasing iron content, while in the $BaCe_{0.6}Zr_{0.2}Y_{0.1}M_{0.1}O_{3-\delta}$ (M = Tb, Pr, Fe) group, the rate of water uptake shows a trend: Tb > Pr > Fe. For all the investigated samples, the transition from wet to dry air differs from the mass increase observed during the prior atmosphere switch. The mass is not restored to its initial pre-hydration level, indicating that a part of the introduced protons remains in the crystal structure after a one-hour dwell in dry air. Furthermore, the dehydration proceeds with a slower rate of mass change, indicating slower kinetics for proton release. Those results align with the high stability of proton defects in the ceramic materials at low temperatures, owing to the negative enthalpy of hydration that defines proton conductors.[5]

In summary, the defect chemistry of BCZYM materials was studied based on iodometric titration and thermogravimetric analysis. The oxygen-vacancy concentrations decreased with increasing Fe content in $BaCe_{0.6}Zr_{0.2}Y_{0.2-x}Fe_xO_{3-\delta}$ (x = 0, 0.02, 0.05, 0.1) series, while in the case of the $BaCe_{0.6}Zr_{0.2}Y_{0.1}M_{0.1}O_{3-\delta}$ (M = Tb, Pr, Fe) group, BCZYTb10 possessed the highest vacancy concentration. The proton concentrations at 300 °C increased with increasing oxygen nonstoichiometry values, confirming hydration as the dominant mechanism of proton incorporation in all studied materials. The concentration of protons and the percentage of oxygen vacancies filled by protons correlated with the average cation

electronegativity and the A-B site electronegativity difference. Water-uptake kinetics followed a two-stage process, with an initial fast hydration followed by a slower mass change, possibly related to oxidation. Thus, proton concentration and water uptake rate decreased with increasing Fe content in $BaCe_{0.6}Zr_{0.2}Y_{0.2-x}Fe_xO_{3-\delta}$, while in the case of the $BaCe_{0.6}Zr_{0.2}Y_{0.1}M_{0.1}O_{3-\delta}$ (M = Tb, Pr, Fe) materials, it followed the trend Tb > Pr > Fe. Dehydration proceeded more slowly than hydration.

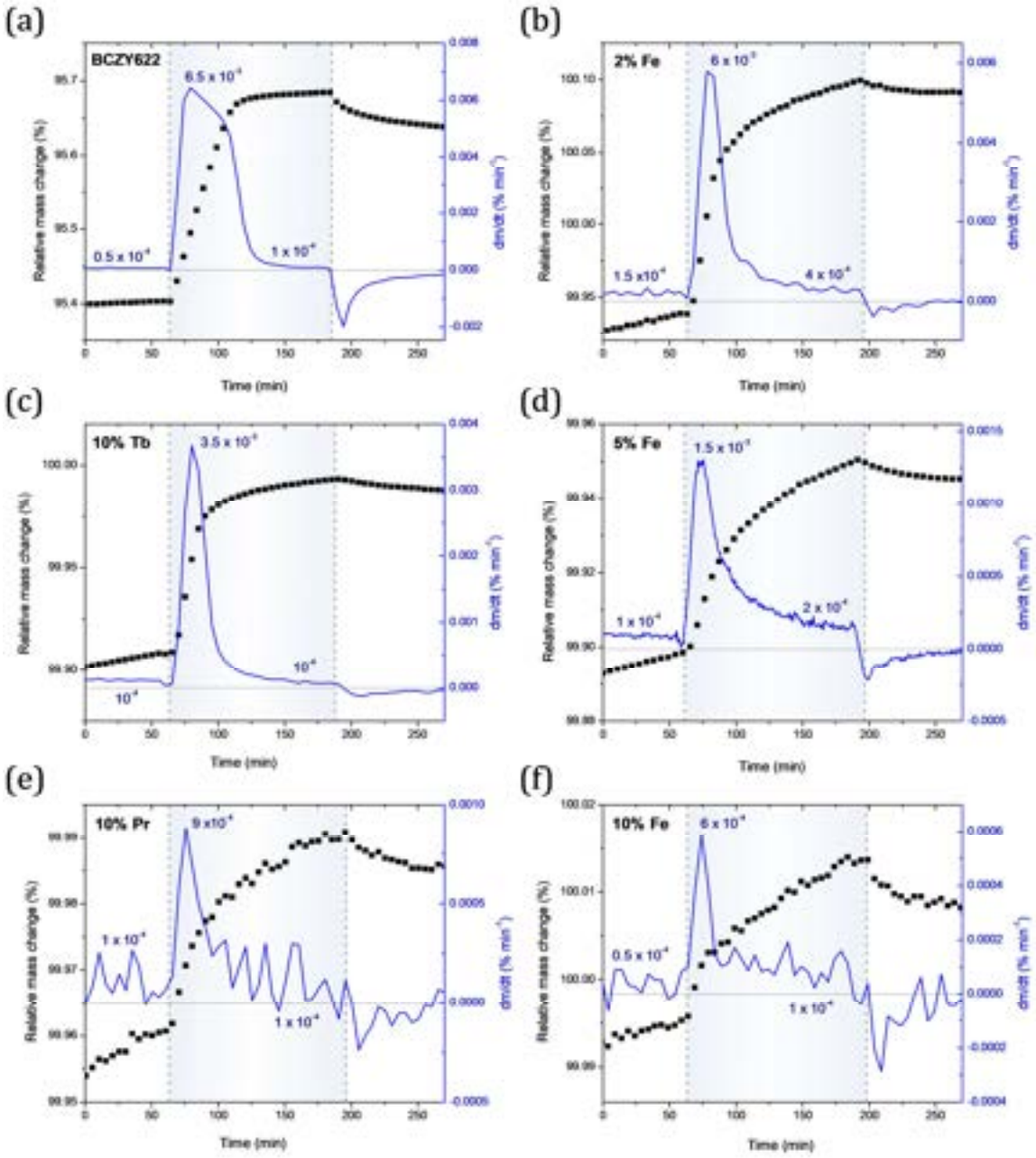

Figure 5.7. The relative mass change and its time derivative recorded during water uptake and release at 300 °C for $BaCe_{0.6}Zr_{0.2}Y_{0.2}O_{3-\delta}$[169] (a), $BaCe_{0.6}Zr_{0.2}Y_{0.18}Fe_{0.02}O_{3-\delta}$ (b), $BaCe_{0.6}Zr_{0.2}Y_{0.1}Tb_{0.1}O_{3-\delta}$ (c), $BaCe_{0.6}Zr_{0.2}Y_{0.15}Fe_{0.05}O_{3-\delta}$ (d), $BaCe_{0.6}Zr_{0.2}Y_{0.1}Pr_{0.1}O_{3-\delta}$ (e), and $BaCe_{0.6}Zr_{0.2}Y_{0.1}Fe_{0.1}O_{3-\delta}$ (f). The light-blue background signifies the humid atmosphere.

Adapted from J. Budnik, A. Mielewczyk-Gryń, M. Gazda and T. Miruszewski, "Water uptake kinetics and electrical transport in $BaCe_{0.6}Zr_{0.2}Y_{0.1}M_{0.1}O_{3-\delta}$ (M = Tb, Pr, Fe) protonic conductors", J. Mater. Chem. A, 2023, 11, 13389–13398, and from J. Budnik, A. Mielewczyk-Gryń, M. Gazda and T. Miruszewski, "Influence of iron content on water uptake and charge transport in $BaCe_{0.6}Zr_{0.2}Y_{0.2-x}Fe_xO_{3-\delta}$ triple-conducting oxides", J. Mater. Chem. A, 2024, 12, 14569–14582, with permission from the Royal Society of Chemistry.[163,164]

5.1.3. Electrical properties

The electrical conductivity of $BaCe_{0.6}Zr_{0.2}Y_{0.2-x}M_xO_{3-\delta}$ materials was measured using electrochemical impedance spectroscopy over a temperature range of 300 – 800 °C in dry and humidified synthetic air. The temperature dependence of the total electrical conductivity of all investigated samples is presented in **Figure 5.8**.

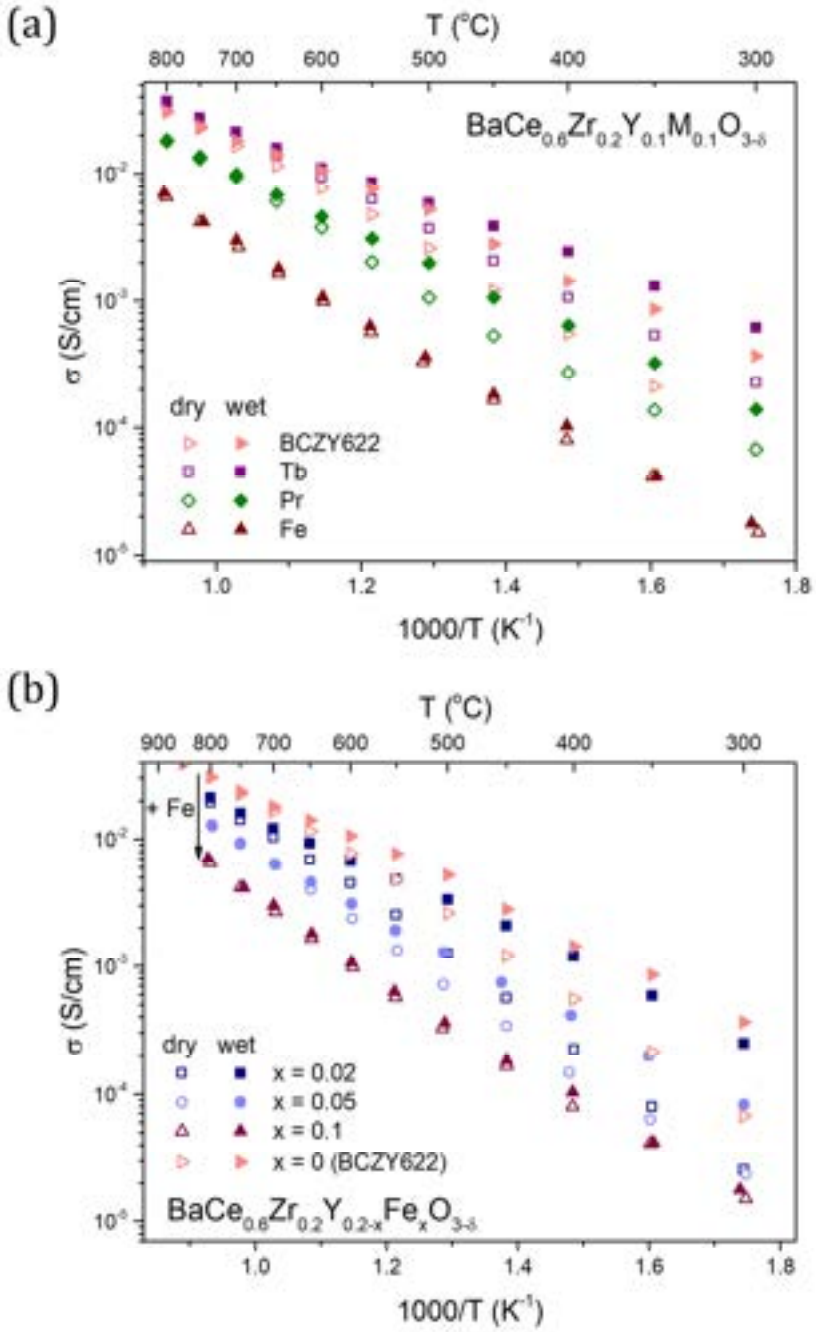

Figure 5.8. Total conductivity as a function of the inverse temperature in $BaCe_{0.6}Zr_{0.2}Y_{0.1}M_{0.1}O_{3-\delta}$ (M = Tb, Pr, Fe) series (a) and $BaCe_{0.6}Zr_{0.2}Y_{0.2-x}Fe_xO_{3-\delta}$ (x = 0.02, 0.05, 0.1) series (b), studied in dry and wet air. In both figures, the data for the reference sample $BaCe_{0.6}Zr_{0.2}Y_{0.2}O_{3-\delta}$ (BCZY622)[169] have been included.

Adapted from J. Budnik, A. Mielewczyk-Gryń, M. Gazda and T. Miruszewski, "Water uptake kinetics and electrical transport in $BaCe_{0.6}Zr_{0.2}Y_{0.1}M_{0.1}O_{3-\delta}$ (M = Tb, Pr, Fe) protonic conductors", J. Mater. Chem. A, 2023, 11, 13389–13398, and from J. Budnik, A. Mielewczyk-Gryń, M. Gazda and T. Miruszewski, "Influence of iron content on water uptake and charge transport in $BaCe_{0.6}Zr_{0.2}Y_{0.2-x}Fe_xO_{3-\delta}$ triple-conducting oxides", J. Mater. Chem. A, 2024, 12, 14569–14582, with permission from the Royal Society of Chemistry.[163,164]

All samples show higher total conductivity in wet ($p_{H_2O} \approx 2.3 \times 10^{-2}$ atm.) compared to dry ($p_{H_2O} \sim 10^{-5}$ atm.) atmosphere, with the difference becoming more pronounced at lower temperatures. This behaviour further confirms that hydration is the predominant proton-uptake mechanism, particularly below 750 °C where proton concentrations increase due to the exothermic nature of the hydration reaction. Since protons generally exhibit higher mobility than oxygen vacancies, their introduction increases total electrical conductivity at lower temperatures.[173]

In the $BaCe_{0.6}Zr_{0.2}Y_{0.1}M_{0.1}O_{3-\delta}$ (M = Tb, Pr, Fe) group (**Figure 5.8a**), the largest increase in the electrical conductivity upon hydration was recorded for the sample substituted with terbium. Moreover, the terbium substitution results in the highest total electrical conductivity at both dry and wet conditions. At 400 °C in wet atmosphere, BCZYTb10 reaches 2.4×10^{-3} S/cm compared to 1.4×10^{-3} S/cm for the reference BCZY622. The Pr-substituted sample shows total electrical conductivity values intermediate between those obtained for BCZYTb10 and BCZYFe10. BCZYFe10 exhibits the lowest total electrical conductivity among all BCZYM materials. BCZYPr10 shows a moderate increase in total conductivity in wet air, smaller than that observed for BCZYTb10 but still noticeable, suggesting that the water uptake takes place also in this material but to a lower extent, which agrees with the lower proton concentration determined for BCZYPr10 via TG.

In the $BaCe_{0.6}Zr_{0.2}Y_{0.2-x}Fe_xO_{3-\delta}$ (x = 0.02, 0.05, 0.1) series (**Figure 5.8b**), a decrease in the total electrical conductivity with increasing iron content was observed. BCZYFe2 and BCZYFe5 display a significant increase in the total electrical conductivity in humid conditions, indicating a proton incorporation. In contrast, the BCZYFe10 sample exhibits only slight differences between dry and wet air. This trend correlates with thermogravimetric analysis and iodometric titration results, which showed decreased oxygen-vacancy and proton concentrations with increasing Fe content (see **Table 5.2**).

All materials exhibit a thermally activated conduction mechanism. The linear fitting of the Arrhenius plot enabled the determination of activation energies for the conduction process, collected in **Table 5.3**. BCZYTb10 shows the lowest activation energies among the studied materials – (0.54 ± 0.01) eV in dry and (0.42 ± 0.01) eV in wet air. It also exhibits the highest difference between the activation energies associated with the conduction process in dry and wet conditions among the $BaCe_{0.6}Zr_{0.2}Y_{0.1}M_{0.1}O_{3-\delta}$ samples. Furthermore, in the case of BCZYTb10, the conductivity difference between wet and dry conditions at 300 °C surpasses the conductivity increase recorded for BCZY622 (3.9×10^{-4} S/cm vs 3.0×10^{-4} S/cm for BCZYTb10 and BCZY622, respectively). These results indicate significant proton transport in a wet atmosphere and support the thermogravimetric evidence of substantial water uptake in this sample. Considering that the proton concentration in BCZY622 was significantly higher

than that in BCZYTb10 (**Table 5.2**), this indicates an enhancing effect of terbium on the mobility of proton defects (further discussed in chapter **5.1.5**). Moreover, the activation energies in dry air for BCZY622 (below 500 °C) is (0.69 ± 0.02) eV, while for BCZYTb10 it is significantly lower. In contrast, BCZYFe10 demonstrates minimal differences between dry and wet conditions, with E_a values remaining relatively high (≈ 0.63 eV), suggesting a negligible contribution of proton defects to the total electrical conductivity. The Pr-substituted sample shows the highest activation energy in dry air among the $BaCe_{0.6}Zr_{0.2}Y_{0.1}M_{0.1}O_{3-\delta}$ samples – (0.68 ± 0.02) eV, while in the wet atmosphere below 500 °C, the activation energy is reduced and reaches (0.56 ± 0.02) eV.

Table 5.3. Activation energies for electrical conduction in dry and wet air of $BaCe_{0.6}Zr_{0.2}Y_{0.1}M_{0.1}O_{3-\delta}$ (M = Tb, Pr) and $BaCe_{0.6}Zr_{0.2}Y_{0.2-x}Fe_xO_{3-\delta}$ (x = 0, 0.02, 0.05, 0.1).

	Activation energy (eV)			
	Dry air		Wet air	
	300 − 500 °C	500 − 800 °C	300 − 500 °C	500 − 800 °C
BCZY**Tb10** [163]	0.54 ± 0.01		0.42 ± 0.01	
BCZY**Pr10**	0.68 ± 0.02		0.56 ± 0.02	0.64 ± 0.01
BCZY**Fe10** [164]	0.64 ± 0.02		0.63 ± 0.02	
BCZY**Fe5** [164]	0.68 ± 0.01		0.53 ± 0.01	
BCZY**Fe2** [164]	0.72 ± 0.02		0.46 ± 0.01	
BCZY622 [169]	0.69 ± 0.02	0.54 ± 0.01	0.50 ± 0.02	0.43 ± 0.02

Adapted from J. Budnik, A. Mielewczyk-Gryń, M. Gazda and T. Miruszewski, "Water uptake kinetics and electrical transport in $BaCe_{0.6}Zr_{0.2}Y_{0.1}M_{0.1}O_{3-\delta}$ (M = Tb, Pr, Fe) protonic conductors", J. Mater. Chem. A, 2023, 11, 13389–13398, and from J. Budnik, A. Mielewczyk-Gryń, M. Gazda and T. Miruszewski, "Influence of iron content on water uptake and charge transport in $BaCe_{0.6}Zr_{0.2}Y_{0.2-x}Fe_xO_{3-\delta}$ triple-conducting oxides", J. Mater. Chem. A, 2024, 12, 14569–14582, with permission from the Royal Society of Chemistry.[163,164]

The $BaCe_{0.6}Zr_{0.2}Y_{0.2-x}Fe_xO_{3-\delta}$ series also exhibits a thermally activated mechanism of conduction in the whole temperature range. Materials with lower iron content (BCZYFe2 and BCZYFe5) show higher electrical conductivities in wet compared to dry air. The electrical conductivity difference at 300 °C between wet and dry conditions is 2.2×10^{-4} S/cm for BCZYFe2 and 5.9×10^{-5} S/cm for BCZYFe5. The activation energies in dry air increase with decreasing iron content: (0.64 ± 0.02) eV, (0.68 ± 0.01) eV, and (0.72 ± 0.02) eV for BCZYFe10, BCZYFe5, and BCZYFe2, respectively. In wet conditions, the activation energies for BCZYFe2 and BCZYFe5 decrease to (0.46 ± 0.01) eV and (0.53 ± 0.01) eV, indicating significant proton conductivity contribution. Since, in the case of BCZYFe10, the activation

energy remains unchanged upon hydration, this confirms that proton transport is suppressed at high iron concentrations, possibly due to the relatively low concentration of oxygen vacancies, necessary for proton defect formation through the hydration reaction. However, the concentration of protons in BCZYFe10, equal to 0.007 mol/mol at 300 °C, is comparable to the value observed for the material substituted with Pr, which exhibits a significant increase in conductivity in a wet atmosphere. Therefore, other factors might be responsible for the negligible electrical conductivity increase in wet air in the case of BCZYFe10, such as proton trapping. This effect was also observed in acceptor-doped barium zirconates by Oikawa et al.[174] Another explanation for such behaviour might be the hydrogenation reaction being partly responsible for the introduction of protons into BCZYFe10, which lowers the concentration of electron holes and, in consequence, leads to a decrease in total conductivity of the material. The simultaneous occurrence of hydration and hydrogenation reactions in a specific proportion could result in a negligible electrical conductivity change after water uptake.

In conclusion, the $BaCe_{0.6}Zr_{0.2}Y_{0.2-x}Fe_xO_{3-\delta}$ compounds exhibit a clear composition-dependent shift in the total electrical conductivity. Lower iron content allows for more effective hydration and proton conduction, as indicated by the reduced activation energies under wet conditions. As the iron concentration increases, the defect structure becomes less favourable for proton incorporation, leading to diminished water uptake and higher activation energies for conduction.[175]

Figure 5.9 presents the total electrical conductivity of the investigated materials as a function of oxygen partial pressure at 800 °C and 600 °C for $BaCe_{0.6}Zr_{0.2}Y_{0.1}M_{0.1}O_{3-\delta}$ (M = Tb, Pr, Fe) and $BaCe_{0.6}Zr_{0.2}Y_{0.2-x}Fe_xO_{3-\delta}$ (x = 0.02, 0.05, 0.1) series. The differences in p_{O_2}- dependence between 800 °C and 600 °C are consistent with the thermally activated charge transport behaviour observed in **Figure 5.8**.

All BCZYM materials exhibit mixed ionic-electronic behaviour with predominantly p-type electronic conduction under oxidising conditions. At low p_{O_2} ($\leq 10^{-3}$ atm.), the total electrical conductivity is dominated by oxygen-ionic transport (σ_O), independent of oxygen partial pressure. At higher oxygen partial pressures ($> 10^{-3}$ atm.), p-type electronic conductivity (σ_h) becomes dominant in the total electrical conductivity (σ_{total}), following the relationship:

$$\sigma_{total} = \sigma_O + \sigma_h = \sigma_O + a_{h0} \cdot p_{O_2}^{\frac{1}{4}}, \tag{5.1}$$

where a_{h0} is a fitting parameter related to the partial electron-hole conductivity.[176] The electronic and oxygen-ionic partial conductivities were determined using equation (5.1) applied to the experimental data of $\sigma(p_{O_2})$.

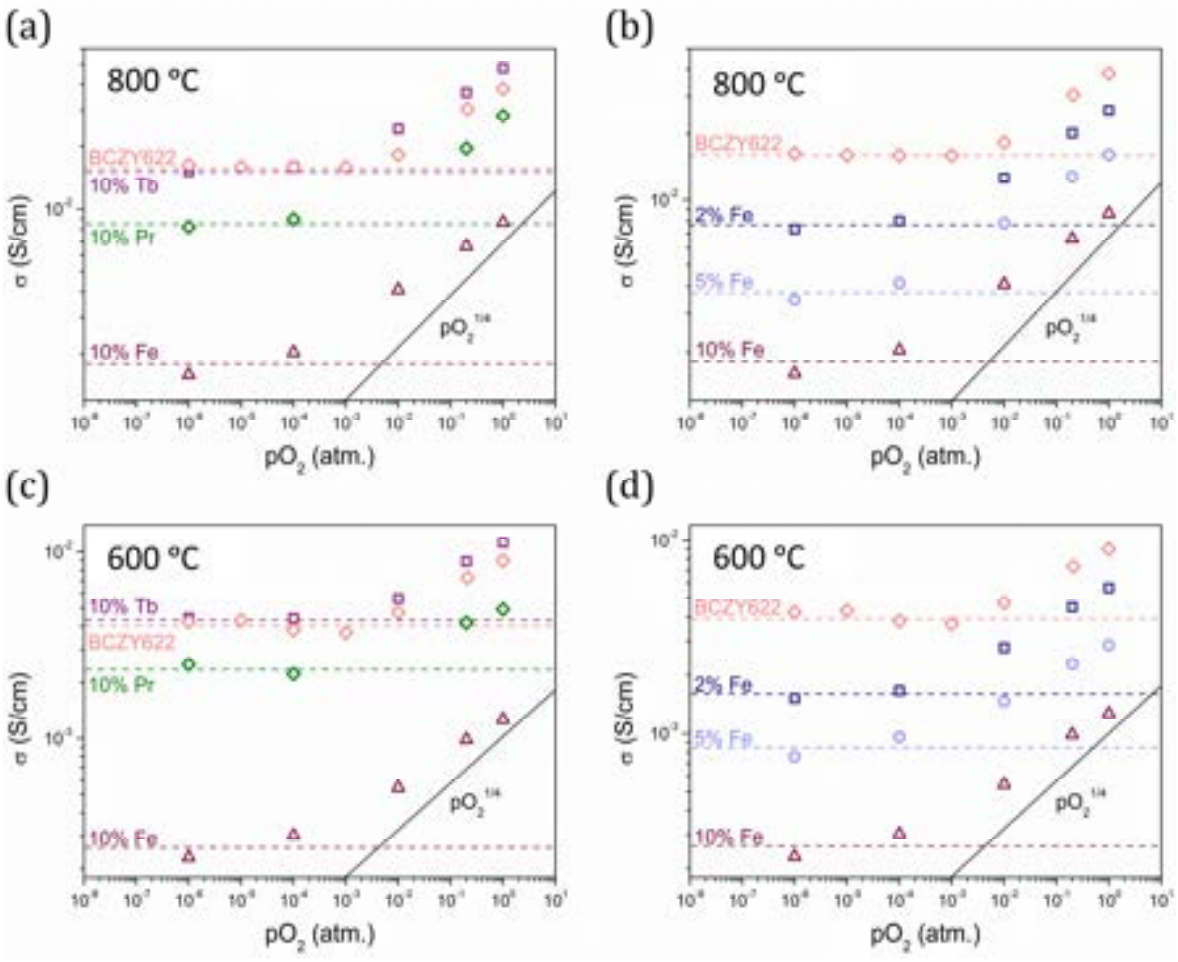

Figure 5.9. Oxygen partial pressure dependence of total electrical conductivity of $BaCe_{0.6}Zr_{0.2}Y_{0.1}M_{0.1}O_{3-\delta}$ (M = Tb, Pr, Fe) at 800 °C and 600 °C (a and c, respectively); and $BaCe_{0.6}Zr_{0.2}Y_{0.2-x}Fe_xO_{3-\delta}$ (x = 0, 0.02, 0.05, 0.1) at 800 °C and 600 °C (b and d, respectively). The data corresponding to $BaCe_{0.6}Zr_{0.2}Y_{0.2}O_{3-\delta}$ (BCZY622)[164,169] sample was included in all plots as a reference. All measurements were conducted in dry atmospheres.

Adapted from J. Budnik, A. Mielewczyk-Gryń, M. Gazda and T. Miruszewski, "Water uptake kinetics and electrical transport in $BaCe_{0.6}Zr_{0.2}Y_{0.1}M_{0.1}O_{3-\delta}$ (M = Tb, Pr, Fe) protonic conductors", J. Mater. Chem. A, 2023, 11, 13389–13398, and from J. Budnik, A. Mielewczyk-Gryń, M. Gazda and T. Miruszewski, "Influence of iron content on water uptake and charge transport in $BaCe_{0.6}Zr_{0.2}Y_{0.2-x}Fe_xO_{3-\delta}$ triple-conducting oxides", J. Mater. Chem. A, 2024, 12, 14569–14582, with permission from the Royal Society of Chemistry.[163,164]

Among the $BaCe_{0.6}Zr_{0.2}Y_{0.1}M_{0.1}O_{3-\delta}$ (M = Tb, Pr, Fe) compounds, BCZYTb10 and BCZY622 demonstrate comparable total electrical conductivity values across the studied p_{O_2} range. Their total conductivities are also the highest, followed by BCZYPr10 and BCZYFe10, consistent with the trends observed in **Figure 5.8**. The electronic contribution to total conductivity increases with temperature due to higher electron-hole concentrations. **Table 5.4** shows the transference numbers of electron holes ($t_h\cdot$) for all the studied materials in air. The values of $t_h\cdot$ indicate that the electronic conduction predominates in BCZYM materials. However, since oxygen-ionic conductivity remains significant even in oxidising conditions, the oxygen-vacancy concentrations must be relatively high, considering that their mobility is significantly lower than that of the electronic charge carriers.[85]

Table 5.4. Total conductivity of $BaCe_{0.6}Zr_{0.2}Y_{0.1}M_{0.1}O_{3-\delta}$ (M = Tb, Pr) and $BaCe_{0.6}Zr_{0.2}Y_{0.2-x}Fe_xO_{3-\delta}$ (x = 0, 0.02, 0.05, 0.1) determined in air at 800 °C and 600 °C with the corresponding ionic and electronic partial conductivities (related to conductance of oxygen ions and electron holes, respectively), as well as the resulting transference number of electron holes.

	T (°C)	σ_{total} (S/cm)	σ_O (S/cm)	σ_h (S/cm)	t_h·
BCZY**Tb10** [163]	800	3.7×10^{-2}	1.3×10^{-2}	2.3×10^{-2}	0.64
	600	8.9×10^{-3}	3.2×10^{-3}	5.5×10^{-3}	0.63
BCZY**Pr10** [163]	800	2.0×10^{-2}	$\approx 8.6 \times 10^{-3}$	$\approx 1.2 \times 10^{-2}$	≈ 0.60
	600	4.2×10^{-3}	$\approx 2.3 \times 10^{-3}$	$\approx 1.8 \times 10^{-3}$	≈ 0.43
BCZY**Fe10** [164]	800	6.6×10^{-3}	$\approx 2.1 \times 10^{-3}$	4.5×10^{-3}	0.67
	600	9.8×10^{-4}	$\approx 2.3 \times 10^{-4}$	7.1×10^{-4}	0.72
BCZY**Fe5** [164]	800	1.2×10^{-2}	$\approx 4.2 \times 10^{-3}$	8.1×10^{-3}	0.63
	600	2.3×10^{-3}	$\approx 8.5 \times 10^{-4}$	1.4×10^{-3}	0.60
BCZY**Fe2** [164]	800	2.0×10^{-2}	6.7×10^{-3}	1.3×10^{-2}	0.64
	600	4.5×10^{-3}	1.4×10^{-3}	3.0×10^{-3}	0.66
BCZY**622** [169]	800	2.9×10^{-2}	9.2×10^{-3}	2.0×10^{-2}	0.69
	600	7.0×10^{-3}	2.9×10^{-3}	4.1×10^{-3}	0.58

Adapted from J. Budnik, A. Mielewczyk-Gryń, M. Gazda and T. Miruszewski, "Water uptake kinetics and electrical transport in $BaCe_{0.6}Zr_{0.2}Y_{0.1}M_{0.1}O_{3-\delta}$ (M = Tb, Pr, Fe) protonic conductors", J. Mater. Chem. A, 2023, 11, 13389–13398, and from J. Budnik, A. Mielewczyk-Gryń, M. Gazda and T. Miruszewski, "Influence of iron content on water uptake and charge transport in $BaCe_{0.6}Zr_{0.2}Y_{0.2-x}Fe_xO_{3-\delta}$ triple-conducting oxides", J. Mater. Chem. A, 2024, 12, 14569–14582, with permission from the Royal Society of Chemistry.[163,164]

For the $BaCe_{0.6}Zr_{0.2}Y_{0.2-x}Fe_xO_{3-\delta}$ series, the total electrical conductivity decreases with increasing Fe content at 600 °C and 800 °C. Moreover, both ionic and electronic partial conductivities decrease with higher iron content (**Table 5.4**). This behaviour reflects a reduced concentration of oxygen vacancies and/or the associated changes in charge carrier mobility, reduced due to unit cell contraction.[168] BCZYFe2 exhibits the conductivity values closest to those of the reference BCZY622 sample, while BCZYFe10 demonstrates the lowest conductivity across the studied p_{O_2} range. The decrease in electronic partial conductivity of $BaCe_{0.6}Zr_{0.2}Y_{0.2-x}Fe_xO_{3-\delta}$ materials with higher iron content is consistent with the results reported by Tarutina et al.[175] This trend suggests that the iron reduces the electronic transport,

which may result from the electron hole trapping on iron ions[177] or the defect clustering effects[178].

The transference numbers of holes in the iron-substituted materials range from 0.60 to 0.72 at 600 °C and 800 °C. The transference numbers of holes corresponding to BCZYTb10 assume similar values, while in the case of BCZYPr10, the t_h• values are lower than those for other BCZYM materials. BCZY622 exhibits similar t_h• compared to BCZYTb10 and iron-containing materials. The transition-metal cation in the Ce/Zr/Y sublattice was expected to increase the electronic conductivity in the substituted samples by increasing the electron-hole concentration. However, apart from BCZYTb10, no increase in electronic conductivity was observed. On the other hand, all materials (except BCZYTb10) exhibited diminished ionic partial conductivity values in comparison to BCZY622. This likely stems from the lower concentration of oxygen vacancies, which is reduced by the incorporation of transition-metal cations with a higher average oxidation state than the host yttrium. The material substituted with terbium exhibits the highest electronic and oxygen-ionic partial conductivities, surpassing the BCZY622 reference. This suggests an enhanced mobility of oxygen vacancies in this material.

Overall, the substitution of Tb, Pr, or Fe into BCZY impacted the defect chemistry and the transport properties. All materials exhibited thermally activated conduction. The total electrical conductivity of all samples increased in wet conditions, which was attributed to proton incorporation via hydration. The highest conductivities in dry and wet air and the lowest activation energies were observed for the terbium-substituted sample. The total, ionic, and electronic conductivities decreased with increasing Fe content. Mixed ionic-electronic conduction with p-type electronic transport under oxidising conditions was confirmed for all BCZYM materials. Among the studied compositions, only Tb substitution enhanced oxygen-ionic and electronic transport.

5.1.4. Diffusion studies

5.1.4.1. Water diffusion

The diffusion of water in MIEC materials strongly depends on the contribution of mobile electron holes to the total electrical conductivity. The water incorporation and release that occur during hydration and dehydration, respectively, can exhibit either single- or two-fold behaviour.[179] The single-fold relaxation, observed in materials with low t_h•, corresponds to an ambipolar diffusion of hydrogen and oxygen. With higher t_h•, the presence of mobile electron holes allows for an independent diffusion of hydrogen and oxygen species, resulting in a two-fold relaxation process.[180] In the presence of water vapour in the atmosphere,

the water molecules first react with the surface of the material before incorporating into the bulk of the sample. The surface reaction begins with the dissociation of water:

$$H_2O \rightarrow 2H_{(ads)} + O_{(ads)}. \quad (5.2)$$

Subsequently, the adsorbed hydrogen and oxygen atoms participate in two reactions at different rates. The first, faster, process results in the formation of a proton defect at the expense of an electron hole:

$$H_{(ads)} + O_O^x + h^\bullet \rightarrow OH_O^\bullet. \quad (5.3)$$

This reaction results in a decrease in the total electrical conductivity due to the reduced concentration of electronic charge carriers, which have much higher mobility than ionic species, such as oxygen vacancies or protons.[181] In the second reaction, the adsorbed oxygen fills an oxygen vacancy, generating two electron holes:

$$O_{(ads)} + v_O^{\bullet\bullet} \rightarrow O_O^x + 2h^\bullet, \quad (5.4)$$

which leads to an increase in the total conductivity. Consequently, the curve recorded during the ECR experiment reflects the superposition of these two processes.

In this chapter, the water-uptake kinetics of $BaCe_{0.6}Zr_{0.2}Y_{0.1}Tb_{0.1}O_{3-\delta}$ and $BaCe_{0.6}Zr_{0.2}Y_{0.2-x}Fe_xO_{3-\delta}$ (x = 0.02, 0.05, 0.1) perovskite oxides were analysed using the ECR method. Since changes in water partial pressure do not significantly affect the oxygen partial pressure, the observed changes in the electrical conductivity of the studied materials were attributed to the water incorporation. Therefore, the determined surface exchange coefficients describe the steps of water adsorption, dissociation, and the incorporation of oxygen ions and protons into the structure of materials, as described by equations (5.2)-(5.4).

During water uptake, protons are incorporated into the structure, which leads to the relaxation curve ending in a plateau, associated with the sample reaching a new equilibrium. Typical relaxation profiles for hydration and dehydration of BCZYTb10 are presented in **Figure 5.10a**. In the case of this material, both processes proceed with two-fold, nonmonotonic kinetics, which is in agreement with the high values of $t_{h^\bullet}$ determined for this material (see **Table 5.4**). The electrical conductivity response depends on the direction of p_{H_2O} change: following a switch from wet to dry air, the conductivity does not return to its initial value before hydration. This is consistent with the TG water-uptake experiment (see **Figure 5.4**), where some of the proton defects did not leave the material after the atmosphere switched to dry air.

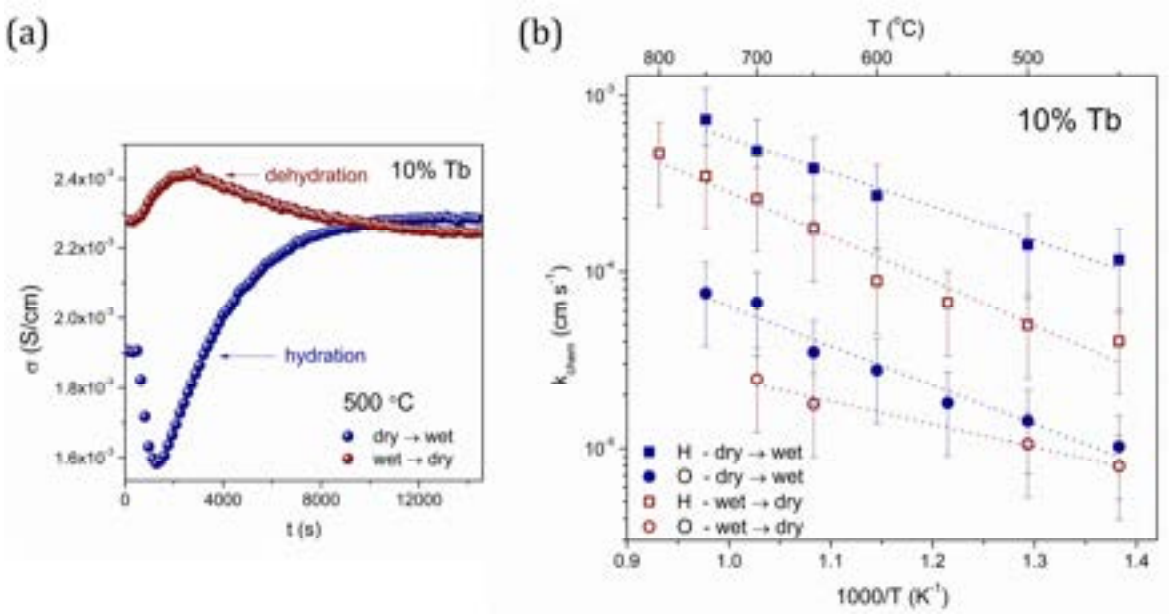

Figure 5.10. ECR curves recorded during the hydration and dehydration processes in $BaCe_{0.6}Zr_{0.2}Y_{0.1}Tb_{0.1}O_{3-\delta}$ at 500 °C (a) and the temperature dependence of chemical surface exchange coefficients obtained for the hydrogen and oxygen during hydration (dry → wet) and dehydration (wet → dry) in $BaCe_{0.6}Zr_{0.2}Y_{0.1}Tb_{0.1}O_{3-\delta}$ (b).

Adapted from J. Budnik, A. Mielewczyk-Gryń, M. Gazda and T. Miruszewski, "Water uptake kinetics and electrical transport in $BaCe_{0.6}Zr_{0.2}Y_{0.1}M_{0.1}O_{3-\delta}$ (M = Tb, Pr, Fe) protonic conductors", J. Mater. Chem. A, 2023, 11, 13389–13398, with permission from the Royal Society of Chemistry.[163]

The temperature dependence of the chemical surface exchange coefficients for hydrogen and oxygen during hydration and dehydration in BCZYTb10 is shown in **Figure 5.10b**. In the case of the k_{chem} corresponding to hydrogen, it ranges from 1.2×10^{-4} to 4.9×10^{-4} cm/s during hydration and from 4.0×10^{-5} to 2.4×10^{-4} cm/s during dehydration between 450 °C and 700 °C. The k_{chem} values observed for oxygen are lower, ranging from 1.0×10^{-5} to 6.6×10^{-5} cm/s during hydration and from 7.9×10^{-6} to 2.5×10^{-5} cm/s during dehydration. The rate of hydrogen surface reaction is higher than that of oxygen for hydration and dehydration. Moreover, the surface exchange coefficients corresponding to both species are higher in hydration than in dehydration, indicating that water adsorption is kinetically more favourable than desorption. The activation energies of surface exchange associated with hydration and dehydration of BCZYTb10 are shown in **Table 5.5**. In the case of hydrogen, the activation energies of surface exchange are (0.39 ± 0.03) eV and (0.50 ± 0.05) eV for hydration and dehydration, respectively. The values obtained in this study are comparable to those reported for other protonic conductors.[79,103,182] For oxygen ions, there is a more pronounced difference in the activation energies corresponding to hydration and dehydration (0.44 eV and 0.26 eV, respectively), indicating that proton defects also affect the process of oxygen chemisorption.

In the case of $BaCe_{0.6}Zr_{0.2}Y_{0.2-x}Fe_xO_{3-\delta}$ (x = 0.02, 0.05, 0.1) materials, the collected ECR data enabled the determination of not only the surface exchange coefficients, but also the diffusion coefficients associated with hydration and dehydration processes.

Representative ECR curves with the fitting data for all BCZYFe materials are included in the **Appendix** (**Figure A9**).

Table 5.5. Activation energies of surface exchange and diffusion related to hydration and dehydration, with a distinction between the processes related to the movement of protons and oxygen separately, in the case of the two-fold diffusion, or together, in the case of single-fold diffusion, for $BaCe_{0.6}Zr_{0.2}Y_{0.1}Tb_{0.1}O_{3-\delta}$ and $BaCe_{0.6}Zr_{0.2}Y_{0.2-x}Fe_xO_{3-\delta}$ (x = 0.02, 0.05, 0.1). The temperatures correspond to the ranges at which the activation energies have been determined.

		Activation energy (eV)				T (°C)
		Hydration		Dehydration		
		Hydrogen	Oxygen	Hydrogen	Oxygen	
BCZY**Tb**[163]	Surface exchange	0.39 ± 0.05 (450-750 °C)	0.44 ± 0.05 (450-750 °C)	0.50 ± 0.05 (450-800 °C)	0.26 ± 0.05 (450-700 °C)	–
BCZY**Fe10**[164]		0.50 ± 0.11		1.03 ± 0.13		500-800
BCZY**Fe5**[164]		0.20 ± 0.04		–		350-800
BCZY**Fe2**[164]		0.34 ± 0.04	0.60 ± 0.05	1.00 ± 0.13	1.14 ± 0.10	550-850
		0.24 ± 0.02		–		350-500
BCZY**Fe10**[164]	Diffusion	1.87 ± 0.05		–		500-750
BCZY**Fe5**[164]		0.13 ± 0.04		0.29 ± 0.03		300-800
BCZY**Fe2**[164]		–	1.27 ± 0.07	–	0.60 ± 0.05	550-850

Adapted from J. Budnik, A. Mielewczyk-Gryń, M. Gazda and T. Miruszewski, "Water uptake kinetics and electrical transport in $BaCe_{0.6}Zr_{0.2}Y_{0.1}M_{0.1}O_{3-\delta}$ (M = Tb, Pr, Fe) protonic conductors", J. Mater. Chem. A, 2023, 11, 13389–13398, and from J. Budnik, A. Mielewczyk-Gryń, M. Gazda and T. Miruszewski, "Influence of iron content on water uptake and charge transport in $BaCe_{0.6}Zr_{0.2}Y_{0.2-x}Fe_xO_{3-\delta}$ triple-conducting oxides", J. Mater. Chem. A, 2024, 12, 14569–14582, with permission from the Royal Society of Chemistry.[163,164]

The conductivity relaxation during water uptake observed for the iron-substituted samples varies depending on the composition and temperature. **Figure 5.11** presents the typical ECR curves recorded for BCZYFe2 during hydration and dehydration at 500 °C and at 800 °C. In the case of BCZYFe2, the water uptake in the 550 – 850 °C temperature range exhibits a two-fold, nonmonotonic behaviour, enabling the separate estimation of surface exchange and diffusion coefficients for hydrogen and oxygen (see **Figure 5.12a** and **b**). On the other hand, below 550 °C, the hydration and dehydration proceed with a single-fold relaxation, implying ambipolar diffusion of protons and oxygen vacancies, likely due to reduced electron-hole mobility at lower temperatures. In contrast, BCZYFe5 and BCZYFe10

exhibit single-fold hydration across the analysed temperature range. The occurrence of two-fold hydration in BCZYFe2 is consistent with its higher electronic partial conductivity, though the t_h• values determined for this material are not substantially higher in comparison to other iron-substituted materials. This suggests that not only the transference number but also the concentration of electron holes influence the nature of the hydration process. As a result, the direct comparison of water-uptake kinetics across the $BaCe_{0.6}Zr_{0.2}Y_{0.2-x}Fe_xO_{3-\delta}$ series is not straightforward.

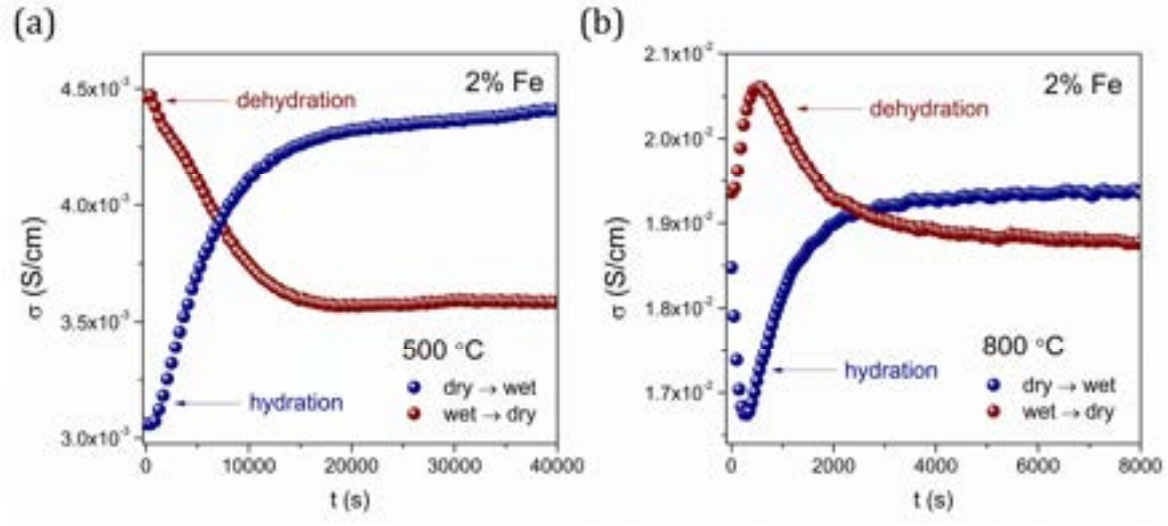

Figure 5.11. ECR curves collected during the hydration and dehydration processes in $BaCe_{0.6}Zr_{0.2}Y_{0.18}Fe_{0.02}O_{3-\delta}$ at 500 °C (a) and 800 °C (b). Below 550 °C, the hydration in BCZYFe2 occurs via ambipolar diffusion of protons and oxygen vacancies, whereas above this temperature, the process involves decoupled diffusion of protons and oxygen vacancies facilitated by mobile electron holes.

Adapted from J. Budnik, A. Mielewczyk-Gryń, M. Gazda and T. Miruszewski, "Influence of iron content on water uptake and charge transport in $BaCe_{0.6}Zr_{0.2}Y_{0.2-x}Fe_xO_{3-\delta}$ triple-conducting oxides", J. Mater. Chem. A, 2024, 12, 14569–14582, with permission from the Royal Society of Chemistry.[164]

The activation energies of surface exchange and diffusion related to hydration and dehydration of the analysed materials are collected in **Table 5.5**. The activation energies of surface exchange vary with material composition and atmospheric conditions. In all materials, the activation energies for hydration are lower than for dehydration, indicating that proton incorporation is more favourable than its release under the studied conditions. It aligns with the conclusions drawn from the TG data. In the case of BCZYFe2 in the $550 - 850$ °C range, the activation energies of surface exchange of oxygen are (0.60 ± 0.05) eV and (1.14 ± 0.10) eV for hydration and dehydration, respectively, while for the hydrogen – (0.34 ± 0.04) eV and (1.00 ± 0.13) eV for hydration and dehydration, respectively. This shows that the oxygen-related processes require more energy than proton-related ones, and that dehydration is energetically more demanding than hydration, suggesting that protons incorporated during the hydration are not easily released from the analysed materials even at elevated temperatures.

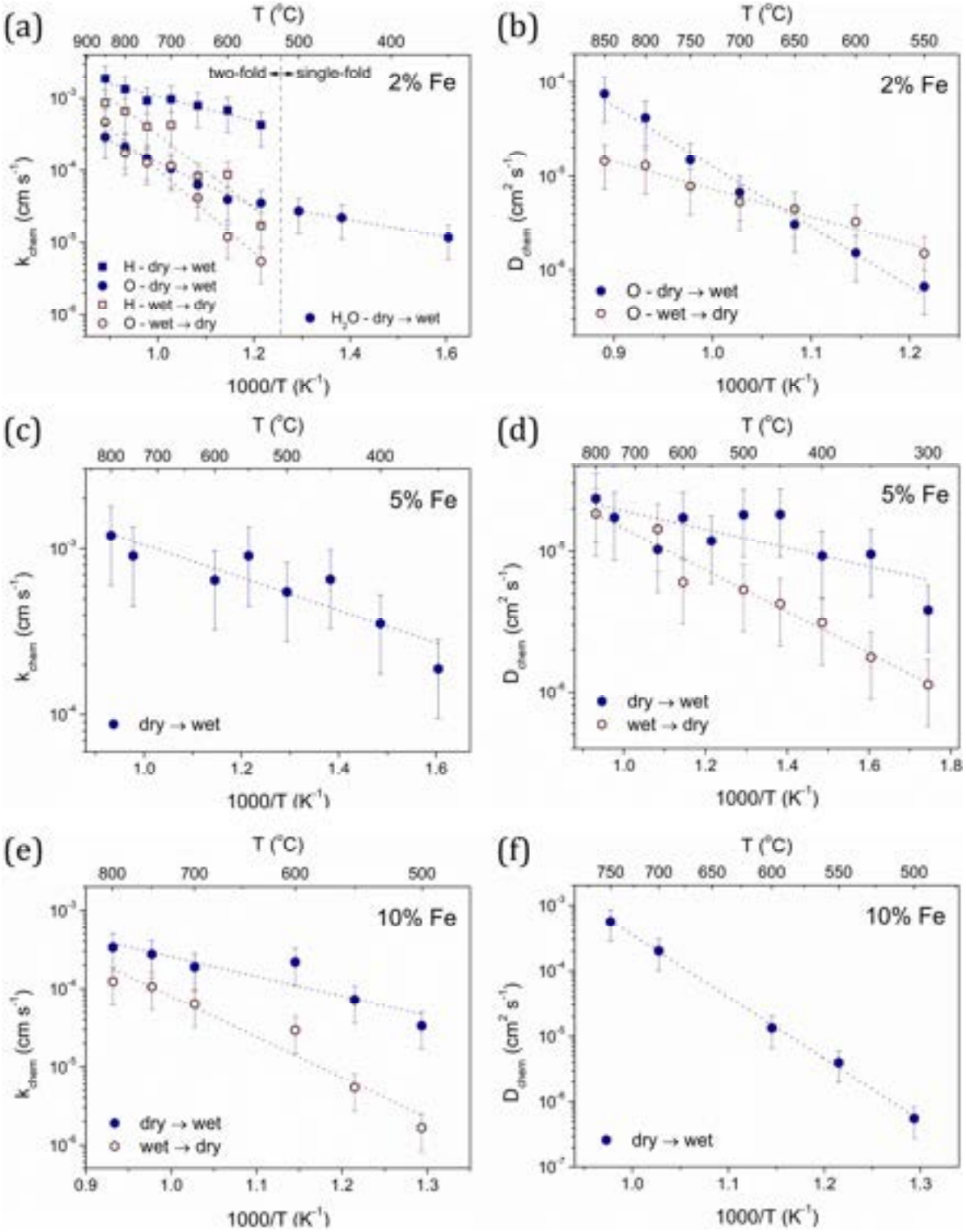

Figure 5.12. Temperature dependence of chemical surface exchange coefficients of hydrogen and oxygen or water in $BaCe_{0.6}Zr_{0.2}Y_{0.18}Fe_{0.02}O_{3-\delta}$ (a), $BaCe_{0.6}Zr_{0.2}Y_{0.15}Fe_{0.05}O_{3-\delta}$ (c), and $BaCe_{0.6}Zr_{0.2}Y_{0.1}Fe_{0.1}O_{3-\delta}$ (e); as well as the temperature dependence of chemical diffusion of oxygen or water in $BaCe_{0.6}Zr_{0.2}Y_{0.18}Fe_{0.02}O_{3-\delta}$ (b), $BaCe_{0.6}Zr_{0.2}Y_{0.15}Fe_{0.05}O_{3-\delta}$ (d), and $BaCe_{0.6}Zr_{0.2}Y_{0.1}Fe_{0.1}O_{3-\delta}$ (f); recorded during hydration (dry → wet) and/or dehydration (wet → dry).

Reproduced from J. Budnik, A. Mielewczyk-Gryń, M. Gazda and T. Miruszewski, "Influence of iron content on water uptake and charge transport in $BaCe_{0.6}Zr_{0.2}Y_{0.2-x}Fe_xO_{3-\delta}$ triple-conducting oxides", J. Mater. Chem. A, 2024, 12, 14569–14582, with permission from the Royal Society of Chemistry. [164]

The temperature dependencies of the chemical surface exchange coefficient and the diffusion coefficient related to water, or hydrogen and oxygen separately, determined for the $BaCe_{0.6}Zr_{0.2}Y_{0.2-x}Fe_xO_{3-\delta}$ series are presented in **Figure 5.12**. At $350 - 500$ °C, the water surface exchange coefficients of BCZYFe2 are similar to those for oxygen exchange at higher temperatures. This indicates that the slower processes related to oxygen-ion transport limit the water-uptake kinetics. The activation energy for water surface exchange during hydration is similar to that for hydrogen and much lower than that for oxygen at higher temperatures, which may be attributed to the "drag effect" of proton defects affecting the oxygen-vacancy mobility, as described by Hancke et al.[79] For BCZYFe5, the activation energy for water surface exchange during hydration is (0.20 ± 0.02) eV, which is significantly lower than the values obtained for BCZYFe10 ((0.50 ± 0.11) eV for hydration and (1.03 ± 0.13) eV for dehydration). Furthermore, the water incorporation in BCZYFe10 decreases the total electrical conductivity, possibly due to the lower mobility of protons compared to that of oxygen vacancies or the reduction in electronic conductivity. This may indicate that hydrogenation contributes to water uptake in addition to hydration in BCZYFe10. The observed decrease in conductivity may also be associated with oxidation enthalpy changes induced by the introduction of protons, potentially leading to a reduction in the wet atmosphere.[172]

Figure 5.12b, **d**, and **f** present the temperature dependencies of the chemical diffusion coefficient of oxygen in BCZYFe2, and the chemical diffusion coefficient of water in BCZYFe5 and BCZYFe10 during water uptake and release. At elevated temperatures, the chemical diffusion coefficient of water reaches the highest values for BCZYFe10, which is consistent with its highest activation energy (1.87 ± 0.05) eV. In contrast, BCZYFe5 exhibits surprisingly low activation energies for water diffusion – (0.13 ± 0.04) eV for hydration and (0.29 ± 0.03) eV for dehydration. This remains unexplained since the sample is dense, so it cannot be caused by the gas diffusion through the pores. In the case of BCZYFe5, the chemical diffusion coefficients for hydration are higher than those for dehydration, with the difference becoming negligible at the highest temperatures. For BCZYFe2, the oxygen diffusion during hydration has a much higher activation energy ((1.27 ± 0.07) eV) than during dehydration ((0.60 ± 0.05) eV). As a consequence, at lower temperatures, dehydration proceeds faster, while at higher temperatures, hydration becomes dominant. These differences highlight the asymmetric nature of water uptake and release in the studied materials. Oxygen diffusion in BCZYFe2 proceeds faster during dehydration, which may be related to the enhanced mobility of oxygen ions owing to the drag effect of protons, present in high concentration in the hydrated material.

To sum up, this chapter presented the hydration and dehydration studies of $BaCe_{0.6}Zr_{0.2}Y_{0.1}Tb_{0.1}O_{3-\delta}$ and $BaCe_{0.6}Zr_{0.2}Y_{0.2-x}Fe_xO_{3-\delta}$ (x = 0.02, 0.05, 0.1) materials,

investigated using the ECR method. Single-fold and two-fold stoichiometry relaxation behaviours during hydration/dehydration were observed. BCZYFe2 showed a two-fold kinetics in the high-temperature regime, which changed into a single-fold process below 550 °C. Hydration generally proceeded faster and required lower activation energy than dehydration. Iron in the $BaCe_{0.6}Zr_{0.2}Y_{0.2-x}Fe_xO_{3-\delta}$ materials influenced both the mechanism and kinetics of water transport. In BCZYFe10 hydration decreased the total electrical conductivity, likely due to reduced electronic charge carrier concentration.

5.1.4.2. Oxygen diffusion

Oxygen diffusion in solids is driven by the gradient in the chemical potential of oxygen. The process of molecular oxygen incorporation into the oxide lattice involves several stages, including chemisorption, reduction, electron transfer, oxygen species dissociation, and the eventual incorporation of an oxygen ion into the crystal lattice.[183] At the initial stage, molecular oxygen ($O_{2(g)}$) is chemisorbed at an unoccupied surface site, forming $O_{2(ads)}$:

$$O_{2(g)} \rightarrow O_{2(ads)}. \tag{5.5}$$

The adsorbed molecule diffuses on the surface and is reduced through a two-step mechanism:

1) $$O_{2(ads)} \rightarrow h^{\bullet} + O^{-}_{2(ads)}, \tag{5.6}$$

2) $$O^{-}_{2(ads)} \rightarrow h^{\bullet} + O^{2-}_{2(ads)}. \tag{5.7}$$

Here, $O^{-}_{2(ads)}$ signifies an adsorbed superoxide species, while $O^{2-}_{2(ads)}$ represents a peroxide species. The first reduction step is faster, while the electron transfer between the superoxide and peroxide species is relatively slow, thereby acting as a rate-limiting process.[109,184,185] Afterwards, the peroxide dissociates into single-ionised oxygen atoms:

$$O^{2-}_{2(ads)} \rightarrow 2O^{-}_{(ads)}, \tag{5.8}$$

and the oxygen ion is incorporated into the crystal lattice:

$$v_O^{\bullet\bullet} + O^{-}_{(ads)} \rightarrow h^{\bullet} + O_O^x, \tag{5.9}$$

where O_O^x represents an oxygen atom residing at an oxygen lattice site. The complete oxidation reaction can be expressed via a summarised reaction as:

$$v_O^{\bullet\bullet} + \frac{1}{2}O_{2(g)} \rightarrow 2h^{\bullet} + O_O^x. \tag{5.10}$$

The migration of the introduced oxygen ions follows the oxygen concentration gradient, thereby determining the diffusion relaxation profile. The resulting curve exhibits a monotonic character for oxidation and reduction.[186,187]

The oxidation and reduction kinetics of $BaCe_{0.6}Zr_{0.2}Y_{0.1}Tb_{0.1}O_{3-\delta}$ and $BaCe_{0.6}Zr_{0.2}Y_{0.2-x}Fe_xO_{3-\delta}$ (x = 0.02, 0.1) were analysed using ECR technique by monitoring the electrical conductivity response of the material to variations in oxygen partial pressure between $p_{O_2} = 0.1$ atm. and $p_{O_2} = 10^{-3}$ atm. under dry and humidified conditions. It was possible to determine the chemical diffusion coefficients for oxidation/reduction for both iron-substituted materials, the chemical diffusion coefficients for the reference material, and the chemical surface exchange coefficients for all analysed materials. For BCZY622 reference material, the chemical diffusion coefficient of oxygen in dry and wet conditions was determined using the modified Hebb-Wagner method. Those measurements were performed by our research group.[169]

Figure 5.13 demonstrate the typical relaxation curves recorded for BCZYTb10 at 650 °C in dry and wet conditions. The single-fold nature of oxidation and reduction processes irrespective of water vapour presence in the atmosphere was observed. These electrical conductivity changes correspond to the ambipolar diffusion of oxygen vacancies and electron holes, which was also observed for $BaZr_{0.8}Y_{0.2}O_{3-\delta}$ by Kim et al.[188] As can be seen in **Figure 5.13**, the oxidation and reduction of BCZYTb10 in dry and wet atmospheres follow different kinetics, indicating distinct surface exchange mechanisms in the presence of proton defects. The temperature dependence of the chemical surface exchange coefficient for both processes in BCZYTb10 is presented in **Figure 5.14**, with the corresponding activation energies listed in **Table 5.6**. The values of the surface exchange coefficients determined for BCZYTb10 range between 2×10^{-5} and 2×10^{-3} cm/s in the $550 - 700$ °C temperature range. Furthermore, the presence of water vapour leads to a decrease in activation energies, with the most pronounced effect observed for reduction – (1.63 ± 0.10) eV in dry and (1.13 ± 0.06) eV in wet conditions.

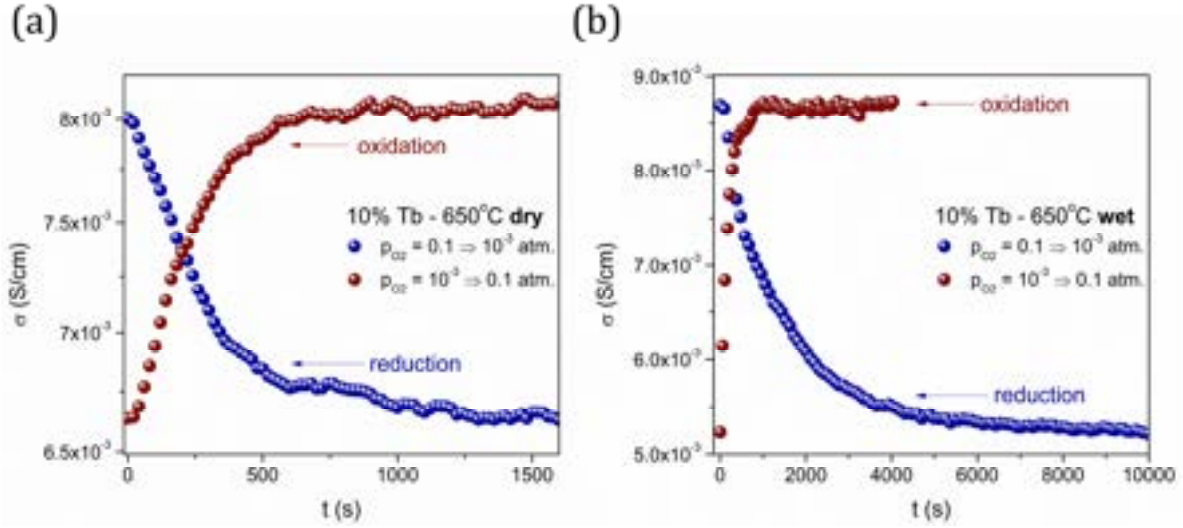

Figure 5.13. ECR curves recorded for $BaCe_{0.6}Zr_{0.2}Y_{0.1}Tb_{0.1}O_{3-\delta}$ during oxidation and reduction in dry (a) and wet (b) atmospheres at 650 °C.

Adapted from J. Budnik, A. Mielewczyk-Gryń, M. Gazda and T. Miruszewski, "Water uptake kinetics and electrical transport in $BaCe_{0.6}Zr_{0.2}Y_{0.1}M_{0.1}O_{3-\delta}$ (M = Tb, Pr, Fe) protonic conductors", J. Mater. Chem. A, 2023, 11, 13389–13398, with permission from the Royal Society of Chemistry.[163]

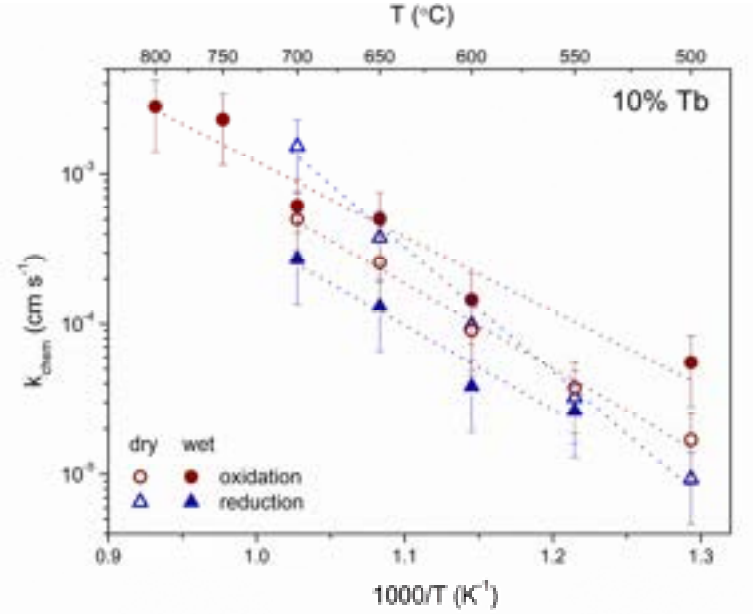

Figure 5.14. Temperature dependence of chemical surface exchange coefficients of oxygen corresponding to the oxidation and reduction processes in dry and wet conditions determined for $BaCe_{0.6}Zr_{0.2}Y_{0.1}Tb_{0.1}O_{3-\delta}$.

Adapted from J. Budnik, A. Mielewczyk-Gryń, M. Gazda and T. Miruszewski, "Water uptake kinetics and electrical transport in $BaCe_{0.6}Zr_{0.2}Y_{0.1}M_{0.1}O_{3-\delta}$ (M = Tb, Pr, Fe) protonic conductors", J. Mater. Chem. A, 2023, 11, 13389–13398, with permission from the Royal Society of Chemistry.[163]

Table 5.6. Activation energies of surface exchange and diffusion related to oxidation and reduction for $BaCe_{0.6}Zr_{0.2}Y_{0.1}Tb_{0.1}O_{3-\delta}$, $BaCe_{0.6}Zr_{0.2}Y_{0.2-x}Fe_xO_{3-\delta}$ (x = 0.02, 0.1), and $BaCe_{0.6}Zr_{0.2}Y_{0.2}O_{3-\delta}$. The temperatures included correspond to the ranges at which the activation energies have been determined.

			Activation energy (eV)	
			Dry	Wet
BCZY**Tb**[163]	Surface exchange	Oxidation	1.13 ± 0.06 (500-700 °C)	0.98 ± 0.11 (500-800 °C)
		Reduction	1.63 ± 0.10 (500-700 °C)	1.13 ± 0.18 (550-700 °C)
BCZY**Fe10**[164]		Oxidation	1.36 ± 0.31 (700-800 °C)	0.99 ± 0.12 (650-800 °C)
		Reduction	1.05 ± 0.02 (700-800 °C)	–
BCZY**Fe2**[164]		Oxidation	0.50 ± 0.07 (600-800 °C)	0.47 ± 0.20 (600-800 °C)
		Reduction	0.49 ± 0.13 (700-800 °C)	0.63 ± 0.07 (600-800 °C)
BCZY**Fe10**[164]	Diffusion	Oxidation	1.12 ± 0.17 (650-800 °C)	1.84 ± 0.27 (650-800 °C)
		Reduction	1.29 ± 0.17 (650-800 °C)	0.71 ± 0.02 (650-800 °C)
BCZY**Fe2**[164]		Oxidation	–	0.79 ± 0.19 (650-800 °C)
		Reduction	0.45 ± 0.06 (600-800 °C)	0.59 ± 0.04 (600-800 °C)
BCZY622[169]		–	1.23 ± 0.16 (700-850 °C)	0.92 ± 0.11 (700-850 °C)

Adapted from J. Budnik, A. Mielewczyk-Gryń, M. Gazda and T. Miruszewski, "Water uptake kinetics and electrical transport in $BaCe_{0.6}Zr_{0.2}Y_{0.1}M_{0.1}O_{3-\delta}$ (M = Tb, Pr, Fe) protonic conductors", J. Mater. Chem. A, 2023, 11, 13389–13398, and from J. Budnik, A. Mielewczyk-Gryń, M. Gazda and T. Miruszewski, "Influence of iron content on water uptake and charge transport in $BaCe_{0.6}Zr_{0.2}Y_{0.2-x}Fe_xO_{3-\delta}$ triple-conducting oxides", J. Mater. Chem. A, 2024, 12, 14569–14582, with permission from the Royal Society of Chemistry.[163,164]

The influence of water vapour on the oxygen incorporation and release processes in dry and humidified atmospheres was also investigated in BCZYFe2, BCZYFe10, and BCZY622. Representative ECR curves for oxidation and reduction with fitting data for both BCZYFe materials are included in the **Appendix** (**Figure A10**). The temperature dependencies of oxygen surface exchange and diffusion coefficients under dry and wet conditions determined for BCZYFe materials are presented in **Figure 5.15**, while the temperature dependencies of diffusion coefficients for BCZY622 are shown in **Figure 5.16**. The activation energies for surface exchange and diffusion related to oxidation/reduction are shown in **Table 5.6**.

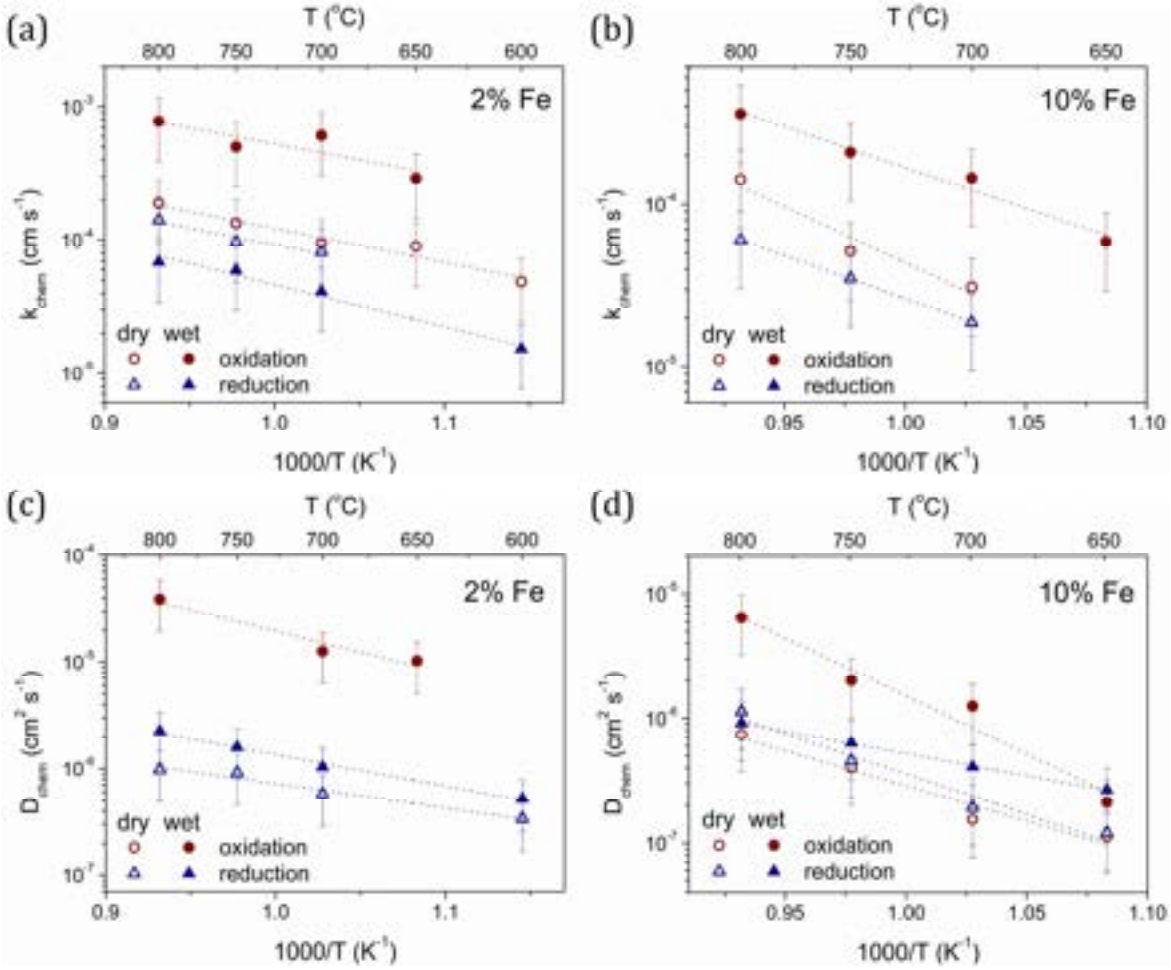

Figure 5.15. Temperature dependence of chemical surface exchange coefficients of oxygen in $BaCe_{0.6}Zr_{0.2}Y_{0.18}Fe_{0.02}O_{3-\delta}$ (a) and $BaCe_{0.6}Zr_{0.2}Y_{0.1}Fe_{0.1}O_{3-\delta}$ (b); as well as the temperature dependence of chemical diffusion of oxygen in $BaCe_{0.6}Zr_{0.2}Y_{0.18}Fe_{0.02}O_{3-\delta}$ (c) and $BaCe_{0.6}Zr_{0.2}Y_{0.1}Fe_{0.1}O_{3-\delta}$ (d); recorded during oxidation and reduction in dry and wet atmospheres.

Reproduced from J. Budnik, A. Mielewczyk-Gryń, M. Gazda and T. Miruszewski, "Influence of iron content on water uptake and charge transport in $BaCe_{0.6}Zr_{0.2}Y_{0.2-x}Fe_xO_{3-\delta}$ triple-conducting oxides", J. Mater. Chem. A, 2024, 12, 14569–14582, with permission from the Royal Society of Chemistry.[164]

Under dry conditions, BCZYFe2 shows minimal differences between chemical surface exchange coefficients corresponding to oxidation and reduction, whereas BCZYFe10

demonstrates slightly enhanced oxidation kinetics compared to reduction. Water vapour significantly increases surface exchange coefficients for oxidation in both compositions, indicating a significant impact on oxygen incorporation kinetics. Conversely, BCZYFe2 exhibits decreased surface exchange for reduction under humid conditions. These effects are similar to the influence of water vapour on the oxidation/reduction kinetics observed in BCZYTb.

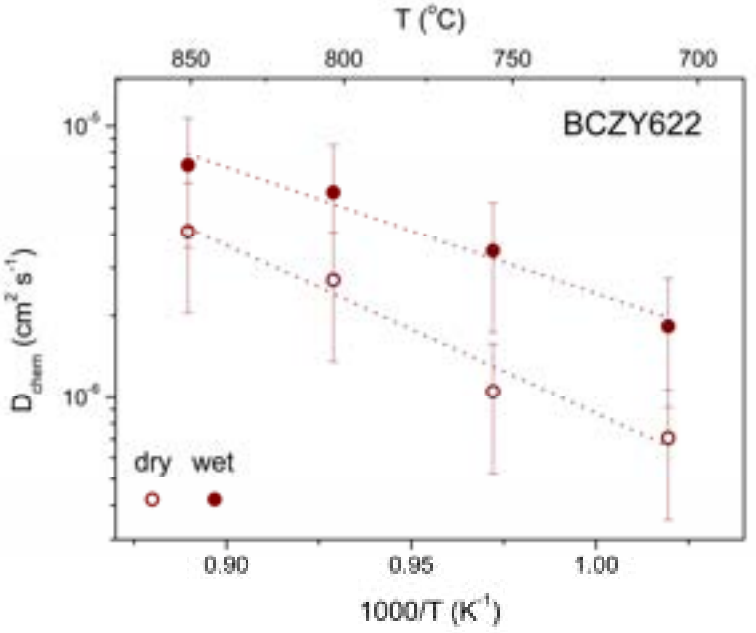

Figure 5.16. Temperature dependence of the chemical diffusion coefficient of oxygen in $BaCe_{0.6}Zr_{0.2}Y_{0.2}O_{3-\delta}$ recorded using the modified Hebb-Wagner method in dry and wet atmospheres.

For BCZYFe2, the activation energies of chemical diffusion and surface exchange are relatively low and weakly depend on the presence of water vapour or p_{O_2} switch direction. For BCZYFe10 under dry conditions, the diffusion activation energies for oxidation and reduction are comparable within experimental uncertainty. In humid conditions, the activation energy of reduction for BCZYFe10 is significantly lower ((0.71 ± 0.02) eV) compared to oxidation ((1.84 ± 0.27) eV). Furthermore, the energies obtained for oxygen diffusion of BCZYFe10 exhibit distinct values under different atmospheric conditions: (1.12 ± 0.17) eV and (1.84 ± 0.27) eV for dry and humid oxidation, respectively. The values for dry and wet reduction are (1.29 ± 0.17) eV and (0.71 ± 0.02) eV, respectively. The differences between activation energies in dry and wet atmospheres for both processes confirm the facilitating role of water vapour in the oxygen kinetics of BCZYFe10. The activation energies for both diffusion and surface exchange are significantly higher for BCZYFe10 compared to BCZYFe2, irrespective of the direction of the oxygen partial pressure change. Furthermore, the values of diffusion and surface exchange coefficients obtained for BCZYFe2 are significantly higher, which is consistent with the higher oxygen-ionic conductivity of this material than that of BCZYFe10 (see **Table 5.4**). Moreover, the D_{chem} values obtained in wet conditions for BCZY622 are lower than those corresponding to the oxidation

of BCZYFe2. Further discussion of the oxygen-vacancy transport, involving the mobility, will be performed in chapter **5.1.5**.

All studied materials show higher k_{chem} values for oxidation in the presence of water vapour. Furthermore, all materials for which the determination of the chemical oxygen diffusion coefficient was possible (BCZYFe2, BCZYFe10, and BCZY622) exhibit higher D_{chem} under wet conditions in the case of oxidation. The differences associated with the reduction (determined for the iron-substituted materials) are less pronounced. For BCZYFe10, the diffusion coefficients corresponding to reduction in wet atmospheres approach the values related to dry conditions at elevated temperatures.

The observed impact of water vapour on the oxygen kinetics may originate from the presence of proton defects residing near the surface of the materials. This effect might be related to the positive charge accumulated on the surface of oxides, associated with surface-segregated protons, which was demonstrated via first-principles calculations conducted for yttrium-doped barium cerate by Polfus et al.[189] The charge accumulation and defect segregation can substantially affect defect chemistry in the near-surface regions of a material. The enhanced oxidation kinetics and deteriorated reduction kinetics observed in this work suggest that the rates of surface reactions are predominantly controlled by the defect mobilities rather than their concentrations alone, indicating that the oxygen-vacancy mobility may be affected by the near-surface proton defects.

This chapter summarised the oxygen transport properties of $BaCe_{0.6}Zr_{0.2}Y_{0.1}Tb_{0.1}O_{3-\delta}$, $BaCe_{0.6}Zr_{0.2}Y_{0.2-x}Fe_xO_{3-\delta}$ (x = 0.02, 0.1), and $BaCe_{0.6}Zr_{0.2}Y_{0.2}O_{3-\delta}$. The oxidation and reduction kinetics were analysed under dry and wet atmospheres, allowing for the determination of chemical diffusion and/or surface exchange coefficients. The presence of water vapour generally enhanced oxygen incorporation and decreased the activation energies associated with this process, while its effect on reduction was more complex and material-dependent. The observed trends suggested that water vapour affects the surface defect chemistry, likely due to the accumulation of proton defects, while also influencing the oxygen-vacancy mobility.

5.1.4.3. Comparative analysis of the investigated materials

The diffusion of water and oxygen in BCZYTb10, BCZYFe2, BCZYFe5, BCZYFe10, and BCZY622 is governed by similar fundamental principles. Still, the substitution of iron introduced significant modifications to the water uptake and release kinetics compared to the kinetics observed for the terbium-substituted material. In BCZYTb10, hydration and dehydration proceed with two-fold, nonmonotonic kinetics in the studied temperature range, reflecting a substantial contribution of electron-hole conductivity. In BCZYFe2, a similar two-fold behaviour is observed only at higher temperatures, while at lower temperatures

and in more heavily substituted samples (BCZYFe5 and BCZYFe10), the behaviour becomes single-fold, indicating a transition to ambipolar diffusion as electron-hole conductivity decreases. This is consistent with partial electronic conductivity being the highest for BCZYFe2 among the Fe-substituted samples and the highest electronic conductivity of BCZYTb10 in comparison to all BCZYM materials studied in this work (see **Table 5.4**). The activation energies for surface exchange and diffusion processes were generally lower during hydration than during dehydration, indicating that the incorporation of protons is kinetically more favourable than their release.

In the case of the oxygen-related processes, BCZYTb10 demonstrated intermediate activation energies for chemical surface exchange, with values of (1.13 ± 0.06) eV for dry oxidation, and (1.63 ± 0.10) eV for dry reduction, as shown in **Table 5.6**. The iron-containing materials exhibited different behaviour patterns, with BCZYFe2 showing significantly lower activation energies for surface exchange ((0.50 ± 0.07) eV for dry oxidation and (0.49 ± 0.13) eV for dry reduction) compared to both BCZYTb10 and BCZYFe10. The higher iron content in BCZYFe10 resulted in elevated activation energies for both, surface exchange and diffusion in comparison with the values obtained for BCZYFe2. The surface exchange and diffusion coefficients were considerably higher in the case of BCZYFe2, which agrees with the determined oxygen-ionic conductivity values (**Table 5.4**), decreasing with increasing iron content in the material.

The ECR data indicate that among the Fe-substituted materials, BCZYFe2 showed enhanced oxygen kinetics in wet conditions, even though the oxygen-ionic conductivity of BCZY622 displayed higher values (**Table 5.4**). This might be due to different values of oxygen-vacancy concentration in the analysed materials. Another reason for these conflicting results might be due to deriving conclusions on the ionic transport based of D_{chem} data, which is not equivalent to the self-diffusion coefficients, directly related to the mobilities of the species. The next chapter aims to estimate the mobilities of oxygen vacancies based on the diffusion and partial conductivity data.

5.1.5. Mobility of ionic charge carriers

Given that the Wagner thermodynamic factor γ for the analysed material is known, the chemical diffusion coefficient of oxygen can be applied for the calculation of the mobility of oxygen ions. No reports of the thermodynamic enhancement factor γ for the BCZY family were found in the literature. However, another MIEC oxide of a perovskite structure has been studied by Wang et al., and the enhancement factor reported in their work was ≈ 100 at 800 °C.[190] This value was employed to estimate the self-diffusion coefficient of oxygen ions for the materials studied in this dissertation using equation (2.29). The self-

diffusion parameters of oxygen ions (D_O) and oxygen vacancies (D_{v_O}) can be related via equation:

$$D_{v_O} = \frac{3-\delta}{\delta} D_O, \tag{5.11}$$

where δ is the concentration of oxygen vacancies. The obtained oxygen vacancy diffusion parameters were then applied with formula (2.28), which enabled the calculation of the estimated mobility of oxygen vacancies ($u_{v_O^{\cdot\cdot},diff}$). **Table 5.7** presents the mobility values estimated based on the oxygen diffusion data of BCZY622, BCZYFe2 and BCZYFe10.

Table 5.7. The oxygen-vacancy concentration at 600 °C and 800 °C, the mobility of oxygen vacancies evaluated based on the electrical conductivity data ($u_{v_O^{\cdot\cdot},\sigma_O}$) and estimated from diffusion coefficient ($u_{v_O^{\cdot\cdot},diff}$) for $BaCe_{0.6}Zr_{0.2}Y_{0.2-x}Fe_xO_{3-\delta}$ (x =0, 0.02, 0.05, 0.1) and $BaCe_{0.6}Zr_{0.2}Y_{0.1}M_{0.1}O_{3-\delta}$ (Tb, Pr).

	$[v_O^{\cdot\cdot}]$ (cm^{-3})		Mobility $(cm^2/V \cdot s)$			
			$u_{v_O^{\cdot\cdot},\sigma_O}$		$u_{v_O^{\cdot\cdot},diff}$	
	600 °C	800 °C	600 °C	800 °C	600 °C	800 °C
BCZY622	2.08×10^{21}	2.25×10^{21}	4.3×10^{-6}	1.3×10^{-5}	–	8.9×10^{-6}
BCZY**Fe2**	1.73×10^{21}	1.83×10^{21}	2.5×10^{-6}	1.1×10^{-5}	1.8×10^{-6}	4.2×10^{-6}
BCZY**Fe5**	1.34×10^{21}	1.42×10^{21}	2.0×10^{-6}	9.2×10^{-6}	–	–
BCZY**Fe10**	1.00×10^{21}	1.13×10^{21}	7.1×10^{-7}	5.8×10^{-6}	–	5.1×10^{-6}
BCZY**Tb10**	1.44×10^{21}	1.49×10^{21}	6.9×10^{-6}	2.7×10^{-5}	–	–
BCZY**Pr10**	1.05×10^{21}	1.17×10^{21}	6.8×10^{-6}	2.3×10^{-5}	–	–

The self-diffusion coefficients for oxygen ions at 800 °C, determined for BCZY622, BCZYFe2, and BCZYFe10 via equation (2.29), are 2.7×10^{-8} cm²/V·s, 1.0×10^{-8} cm²/V·s, and 9.3×10^{-9} cm²/V·s, respectively. The oxygen vacancy self-diffusion D_{v_O} are 4.1×10^{-7} cm²/s, 1.9×10^{-7} cm²/V·s, and 2.4×10^{-7} cm²/V·s for BCZY622, BCZYFe2, and BCZYFe10, respectively. These values are comparable to the results obtained by Li et al. for 800 °C via molecular dynamics simulations for the barium zirconate substituted with 15 mol.% of Y, where D_O and D_{v_O} assumed values 1.2×10^{-8} cm²/V·s and 4.7×10^{-7} cm²/V·s, respectively.[191] This confirms that the thermodynamic factor utilised in this work for the calculation of D_O and D_{v_O} was a reasonable assumption for the BCZYM material group.

The mobility of a carrier can also be assessed based on the electrical conductivity data if the partial conductivity of the carrier and its concentration are known. The electrical conductivity measured as a function of oxygen partial pressure provided the information about the partial conductivities of electron holes and oxygen ions at 600 °C and 800 °C for all BCZYM materials (**Table 5.4**). The mobilities of oxygen vacancies established based on the partial conductivity data ($u_{v_O^{\cdot\cdot},\sigma_O}$) were calculated using the values of oxygen-vacancy concentration determined via thermogravimetry. The temperature dependence of oxygen nonstoichiometry for all analysed materials is shown in **Figure A11** in the **Appendix**. **Table 5.7** presents the mobility values evaluated from electrical conductivity measurement for all studied BCZYM materials. The oxygen-vacancy mobilities, estimated based on the oxygen diffusion data, adopt similar or slightly lower values to those determined from the partial oxygen-ionic conductivity data. The differences between the mobilities calculated by both methods are lower than an order of magnitude.

The $u_{v_O^{\cdot\cdot},\sigma_O}$ assume the highest values for BCZYTb10 with 6.9×10^{-6} cm²/V·s at 600 °C and 2.7×10^{-5} cm²/V·s at 800 °C. Moreover, the mobilities in both materials substituted with lanthanides (BCZYTb10 and BCZYPr10) surpass that in BCZY622. On the contrary, the substitution with iron leads to a decline in $u_{v_O^{\cdot\cdot},\sigma_O}$, where mobility values decrease with higher iron content, which indicates that not only lower concentrations, but also lower mobilities of oxygen vacancies are responsible for the significant decrease in oxygen-ionic and total electrical conductivity of $BaCe_{0.6}Zr_{0.2}Y_{0.2-x}Fe_xO_{3-\delta}$ materials.

The upper limit of the proton mobility can be assessed using established values of electrical transport parameters and the proton concentration at 300 °C. The total electrical conductivity can be written as a sum of two partial conductivities:

$$\sigma_{dry} = \sigma_{h,dry} + \sigma_{O,dry}, \tag{5.12}$$

where $\sigma_{h,dry}$ and $\sigma_{O,dry}$ denote the partial conductivity of electron holes and oxygen ions/vacancies in dry conditions, respectively. The total conductivity in wet air can be expressed as:

$$\sigma_{wet} = \sigma_{h,wet} + \sigma_{O,wet} + \sigma_{OH}, \tag{5.13}$$

where $\sigma_{h,wet}$ and $\sigma_{O,wet}$ represent the partial conductivity of electron holes and oxygen ions/vacancies in wet conditions, respectively, while σ_{OH} is the partial conductivity corresponding to protons. The difference between the total conductivity in wet and dry air can be expressed with the following equation:

$$\Delta\sigma = \sigma_{wet} - \sigma_{dry}. \tag{5.14}$$

The influence of water partial pressure on the partial conductivity of electron holes was assumed to be negligible. After transformations, presented in more detail in the **Appendix** (chapter "**The derivation of the maximum proton mobility formula**"), and assuming the invariance of oxygen-vacancy mobility in dry and wet conditions, it may be described by equation:

$$\Delta\sigma = e[OH_O^{\bullet}](u_{OH_O^{\bullet}} - u_{v_O^{\bullet\bullet}}). \tag{5.15}$$

Therefore, equation (5.15) allows for the determination of the proton mobility $u_{OH_O^{\bullet}}$ as:

$$u_{OH_O^{\bullet}} = \frac{\Delta\sigma}{e[OH_O^{\bullet}]} + u_{v_O^{\bullet\bullet}}. \tag{5.16}$$

The mobility of oxygen vacancies $u_{v_O^{\bullet\bullet},\sigma_O}$ at 600 °C can also be used as a higher limit at lower temperatures ($u_{v_O^{\bullet\bullet},max}$), such as 300 °C, at which the proton defect concentrations have been established using TG. Therefore, the upper limit of proton mobility at 300 °C can be expressed as:

$$u_{OH_O^{\bullet},max} = \frac{\Delta\sigma}{e[OH_O^{\bullet}]} + u_{v_O^{\bullet\bullet},max}. \tag{5.17}$$

Using the obtained value of proton mobility, it is also possible to calculate the upper limit for the partial conductivity associated with protons at 300 °C, by using the basic formula:

$$\sigma_{OH,max} = e[OH_O^{\bullet}]u_{OH_O^{\bullet},max}. \tag{5.18}$$

The obtained values of $u_{OH_O^{\bullet},max}$ and $\sigma_{OH,max}$ are shown in **Table 5.8**.

Table 5.8. The proton concentration ($[OH_O^{\bullet}]$) at 300 °C, as well as the upper limit of proton mobility ($u_{OH_O^{\bullet},max}$) and the upper limit of proton conductivity ($\sigma_{OH,max}$) determined for the same temperature for $BaCe_{0.6}Zr_{0.2}Y_{0.2-x}Fe_xO_{3-\delta}$ (x =0, 0.02, 0.05, 0.1) and $BaCe_{0.6}Zr_{0.2}Y_{0.1}M_{0.1}O_{3-\delta}$ (Tb, Pr).

	$[OH_O^{\bullet}]$ (cm^{-3})	$u_{OH_O^{\bullet},max}$ $(cm^2/V \cdot s)$	$\sigma_{OH,max}$ (S/cm)
BCZY622	1.25×10^{21}	6.0×10^{-6}	1.1×10^{-3}
BCZY**Fe2**	1.26×10^{21}	4.6×10^{-6}	4.9×10^{-4}
BCZY**Fe5**	1.06×10^{21}	3.8×10^{-6}	1.3×10^{-4}
BCZY**Fe10**	8.18×10^{20}	9.1×10^{-7}	1.3×10^{-5}
BCZY**Tb10**	1.14×10^{21}	1.4×10^{-5}	7.7×10^{-4}
BCZY**Pr10**	8.63×10^{20}	1.0×10^{-5}	2.0×10^{-4}

It should be noted that the assumption of unchanging oxygen-vacancy mobility in dry and wet atmospheres, given the higher chemical diffusion coefficients of oxygen in wet atmospheres observed in all studied samples, is crude. It may lead to overstating of $u_{OH_O^{\bullet},max}$ and $\sigma_{OH,max}$.

Although the upper limit of partial proton conductivity of the reference material BCZY622 assumes the highest value 1.1×10^{-3} S/cm, the BCZYTb10 material exhibits the highest mobility of protons among all studied materials (1.4×10^{-5} cm^2/V·s), with BCZYPr10 also surpassing $u_{OH_O^{\bullet},max}$ of BCZY622 (1.0×10^{-5} cm^2/V·s and 6.0×10^{-6} cm^2/V·s, respectively). The proton mobilities of BCZYFe2, BCZYFe5, and BCZYFe10 decrease with increasing iron content, pointing to the detrimental effect of iron substitution in BCZY622 on the mobilities of both ionic charge carriers – oxygen vacancies and protons. On the other hand, the substitution with terbium and praseodymium leads to the enhancement in the ionic carriers' mobilities compared to the unsubstituted material. These results are consistent with the conclusions stated in chapter **5.1.3**, based on total electrical conductivity measurements in dry and wet air.

In summary, the mobilities of oxygen vacancies in BCZYM were estimated using two complementary approaches: diffusion data and electrical conductivity measurements combined with iodometric titration. The results were comparable, validating the assumed enhancement thermodynamic factor of around 100. The substitution with iron resulted in a systematic decrease, while the introduction of Tb and Pr led to an increase in oxygen-vacancy mobility. The mobility of protons was estimated from proton concentrations and total conductivity in both dry and wet conditions. The highest proton mobilities were observed for BCZYTb10 and BCZYPr10, surpassing that of the reference BCZY622. A progressive decrease in proton mobility was observed with increasing iron content. These trends correspond to those obtained for oxygen-vacancy mobility, indicating a general impact of the employed substituents on the transport of both ionic charge carriers. Although the BCZY622 reference sample exhibited the highest partial proton conductivity, the results demonstrate the major role of lanthanide substitution in enhancing the transport of both oxygen vacancies and protons.

5.2. Properties of $SrFe_{1-x}Co_xO_{3-\delta}$ materials

5.2.1. Oxygen nonstoichiometry and B-cations oxidation state

When the oxidation state of the A-site cation of an $ABO_{3-\delta}$ oxide can be considered constant (+2), the oxygen nonstoichiometry can be related to the mean oxidation state of B-site cations (OS_B) via relationship:

$$\delta = \frac{4 - OS_B}{2}. \tag{5.19}$$

In this work, the oxygen nonstoichiometry in $SrFe_{1-x}Co_xO_{3-\delta}$ (x = 0, 0.2, 0.4, 0.6, 0.8) series was determined using iodometric titration and X-ray absorption spectroscopy at room temperature. The obtained values of δ were assumed to be equivalent to the concentration of oxygen vacancies in the materials.

Table 5.9 presents the oxygen nonstoichiometry values (δ_{titr}) and the average oxidation state of B cations (OS_{B-titr}) established via iodometric titration for all SFC materials. With increasing cobalt content, the oxygen nonstoichiometry in $SrFe_{1-x}Co_xO_{3-\delta}$ increases, which correlates with gradually decreasing values of OS_B. A similar tendency in $Sr(Fe,Co)O_{3-\delta}$, where the oxygen nonstoichiometry increased with higher substitution level of cobalt, was also reported by Kokhanovskii et al.[192] However, the δ values they obtained were notably lower (approximately 0.32 for the sample with 80 mol.% of Co on the B-site) in comparison to the values obtained in this work.

Table 5.9. The iron and cobalt oxidation states determined by the XAS method via the absorption edge analysis at K-edges of Fe and Co, as well as the average oxidation state of the B cation and oxygen nonstoichiometry values determined using XAS and iodometric titration for $SrFe_{1-x}Co_xO_{3-\delta}$ (x = 0, 0.2, 0.4, 0.6, 0.8).

Sample	OS_{Fe}	OS_{Co}	OS_B		δ (mol/mol)	
			XAS	titration	XAS	titration
$Sr\mathbf{Fe}O_{3-\delta}$	3.20 ± 0.09	–	3.20 ± 0.10	3.36 ± 0.05	0.40 ± 0.05	0.32 ± 0.03
$Sr\mathbf{Fe_{0.8}Co_{0.2}}O_{3-\delta}$	3.21 ± 0.09	2.94 ± 0.10	3.16 ± 0.10	3.29 ± 0.05	0.42 ± 0.05	0.36 ± 0.03
$Sr\mathbf{Fe_{0.6}Co_{0.4}}O_{3-\delta}$	3.22 ± 0.09	3.00 ± 0.10	3.14 ± 0.10	3.20 ± 0.05	0.43 ± 0.05	0.40 ± 0.02
$Sr\mathbf{Fe_{0.4}Co_{0.6}}O_{3-\delta}$	3.21 ± 0.09	3.03 ± 0.10	3.10 ± 0.10	3.10 ± 0.04	0.45 ± 0.05	0.45 ± 0.02
$Sr\mathbf{Fe_{0.2}Co_{0.8}}O_{3-\delta}$	3.21 ± 0.09	3.04 ± 0.10	3.08 ± 0.10	3.00 ± 0.04	0.47 ± 0.05	0.50 ± 0.02

Reproduced with permission from Jagoda Budnik, Maria Gazda, Alexey Maximenko, Aleksandra Mielewczyk-Gryń, Joanna Pośpiech, Sebastian Wachowski, Agnieszka Witkowska, and Tadeusz Miruszewski, "$Sr(Fe,Co)O_{3-\delta}$ Mixed Conductors: How Cobalt Drives Oxygen Vacancy Formation", Chemistry of Materials 2025, 37 (21), 8822–8834. Copyright 2025 American Chemical Society.[193]

Figure 5.17 presents the XANES spectra recorded for the $SrFe_{1-x}Co_xO_{3-\delta}$ series at the Fe and Co K-edges with their second derivatives. The first derivative spectra for both absorption edges are shown in the **Appendix** (**Figure A14**). The energy associated with the absorption edge (E_0) for an ion of a particular element is linearly dependent on its oxidation state. Therefore, the oxidation states of transition-metal (TM) cations were established by utilising reference data for materials containing iron and cobalt with well-defined oxidation states (Fe, FeO, Fe_2O_3 and Co, CoO, Co_3O_4, for the determination of the oxidation states of iron and cobalt respectively). The edge position in each spectrum was identified as the energy corresponding to half of the normalised edge-step intensity. Since the XAS data is acquired separately for each analysed element, this method enables the independent determination of average oxidation state associated with iron and cobalt, allowing for a more precise analysis of the influence of each TM ion in the investigated material series. Subsequently, to compare the results obtained using iodometric titration and those based on the XAS data, the values of OS_{B-XAS} were calculated for all studied materials. The average B-cation oxidation state can be calculated as a weighted average using the molar content of each element. Therefore, for the $SrFe_{1-x}Co_xO_{3-\delta}$ compounds, OS_B can be written as:

$$OS_B = x \cdot OS_{Co} + (1 - x) \cdot OS_{Fe}, \tag{5.20}$$

where OS_{Co} and OS_{Fe} represent the average oxidation states of cobalt and iron ions, respectively. By applying equation (5.19) to the determined values of OS_{B-XAS}, the oxygen nonstoichiometry (δ_{XAS}) was calculated.

Table 5.9 presents the average oxidation states of iron and cobalt, the average oxidation state of the B cation, and the oxygen nonstoichiometry derived from the XAS data. OS_{Fe} were found to be approximately 3.2(1), with no correlation with cobalt content, while OS_{Co} varies between 2.9(1) and 3.0(1). Since the oxidation states of iron and cobalt remain relatively stable across all investigated compositions, OS_{B-XAS} gradually decreases with increasing cobalt content, which corresponds to higher oxygen nonstoichiometry values. This trend is consistent with the iodometric titration results. The formal oxidation states used to calculate δ_{titr} reflect the overall charge balance and stoichiometry of a material. Conversely, the effective oxidation state of the B cation (determined from the XAS data) includes also additional influences from the local environment of the absorber, which depend on the covalency of the B–O bonds and charge-transfer effects. These effects are determined by the crystal structure and the electronegativities of the ions that constitute the oxide. In particular, the ability of cations to donate electrons to oxygen, determined by bond covalency, significantly affects the measured effective oxidation states.

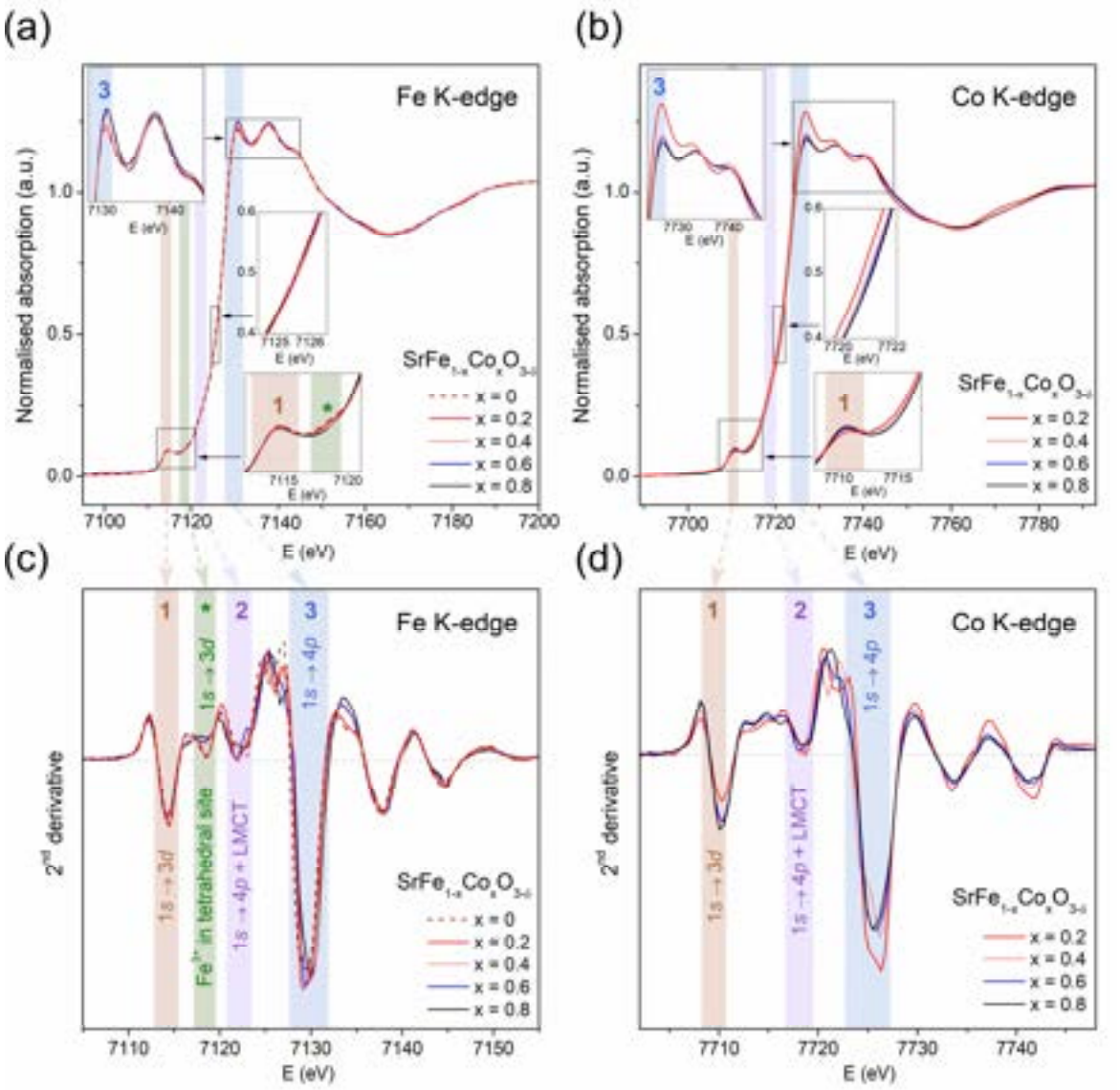

Figure 5.17. The XANES spectra and the second derivatives of the spectra corresponding to the iron K-edge (a, c, e) and to the cobalt K-edge (b, d, f), respectively, collected for $SrFe_{1-x}Co_xO_{3-\delta}$. The insets include close-ups of a pre-edge, white line, and half-height regions. The markers on the second derivative plots indicate the electron transitions that take place in a specific energy region.

Reproduced with permission from Jagoda Budnik, Maria Gazda, Alexey Maximenko, Aleksandra Mielewczyk-Gryń, Joanna Pośpiech, Sebastian Wachowski, Agnieszka Witkowska, and Tadeusz Miruszewski, "Sr(Fe,Co)$O_{3-\delta}$ Mixed Conductors: How Cobalt Drives Oxygen Vacancy Formation", Chemistry of Materials 2025, 37 (21), 8822–8834. Copyright 2025 American Chemical Society.[193]

The values of oxygen nonstoichiometry obtained by both methods are consistent for all SFC samples except $SrFeO_{3-\delta}$, where δ_{XAS} exceeds δ_{titr} slightly beyond experimental uncertainty. Considering that the bond between the transition metal and oxygen exhibits a partially covalent character, the observed differences between the oxygen nonstoichiometry determined by iodometric titration and by XAS might arise from charge-transfer effects, which influence the charge distribution and, in consequence, the energy levels associated with the transition metal. The charge transfer leads to a shifted E_0 of the K-edge of absorbing TM. As a result, the oxidation state of the transition metals appears to be lower than the formal oxidation state associated with the stoichiometry of the material. This "effective oxidation

state" leads to the overestimation of oxygen nonstoichiometry (δ_{XAS}). Such a scenario was also reported by Raimondi et al., who observed that charge-transfer effects shift the absorption edge of iron in reduced strontium ferrite.[60]

The observed increase in oxygen nonstoichiometry with higher cobalt content can be explained by differences in the electronic properties of Fe and Co cations. Iron and cobalt differ in their tendency to adopt higher oxidation states because of their different ionization potentials. Removing the fourth electron requires more energy for iron than for cobalt (54.8 eV and 51.3 eV, respectively), making Fe^{4+} relatively more stable than Co^{4+}.[194] Consequently, cobalt preferentially remains in a lower, while iron adopts a higher formal oxidation state. Charge compensation in the lattice occurs through the formation of oxygen vacancies, hence, the difference in the electronic configuration stability between the TM ions contributes to the higher oxygen nonstoichiometry observed in $SrFe_{1-x}Co_xO_{3-\delta}$ with increasing x.

Oxygen nonstoichiometry in $SrFe_{1-x}Co_xO_{3-\delta}$ can vary with temperature, which can directly affect the transport properties of the material. As the temperature increases, thermal reduction facilitates the formation of oxygen vacancies, increasing δ. This effect is typical of p-type perovskite conductors, and for materials containing Fe, Co, or Ti in the B-site it becomes particularly noticeable at temperatures above $200 - 300$ °C.[170,172,195] Consequently, both the concentration of charge carriers and their mobility may change with temperature due to variations in lattice oxygen content. This will be further discussed in chapter **5.2.3**.

In summary, the oxygen nonstoichiometry and the average oxidation state of transition-metal cations in the $SrFe_{1-x}Co_xO_{3-\delta}$ series were determined using two methods: iodometric titration and XAS. Increased cobalt content resulted in a monotonic increase in oxygen nonstoichiometry and a decrease in the average B-site cation oxidation state. The XAS analysis showed iron in a relatively stable ≈ 3.2 and cobalt in $2.9 - 3.0$ oxidation state. The oxygen nonstoichiometry calculated based on XAS data were consistent with iodometric titration results, except for $SrFeO_{3-\delta}$, where δ_{XAS} slightly exceeded δ_{titr}. This difference was attributed to the charge-transfer effects and the partial covalency of the TM–O bonds, which influence the apparent oxidation states derived from XAS.

5.2.2. Structural and electronic properties

The XRD diffraction patterns of the $SrFe_{1-x}Co_xO_{3-\delta}$ samples are presented in **Figure 5.18**. All diffractograms were analysed through Rietveld refinement, with a cubic perovskite structure ($Pm\bar{3}m$) assumed for each composition. The obtained lattice parameters are shown in **Table 5.10.** The diffractograms correspond to cubic perovskite phases, with minor additional peaks, denoted by asterisks in **Figure 5.18**.

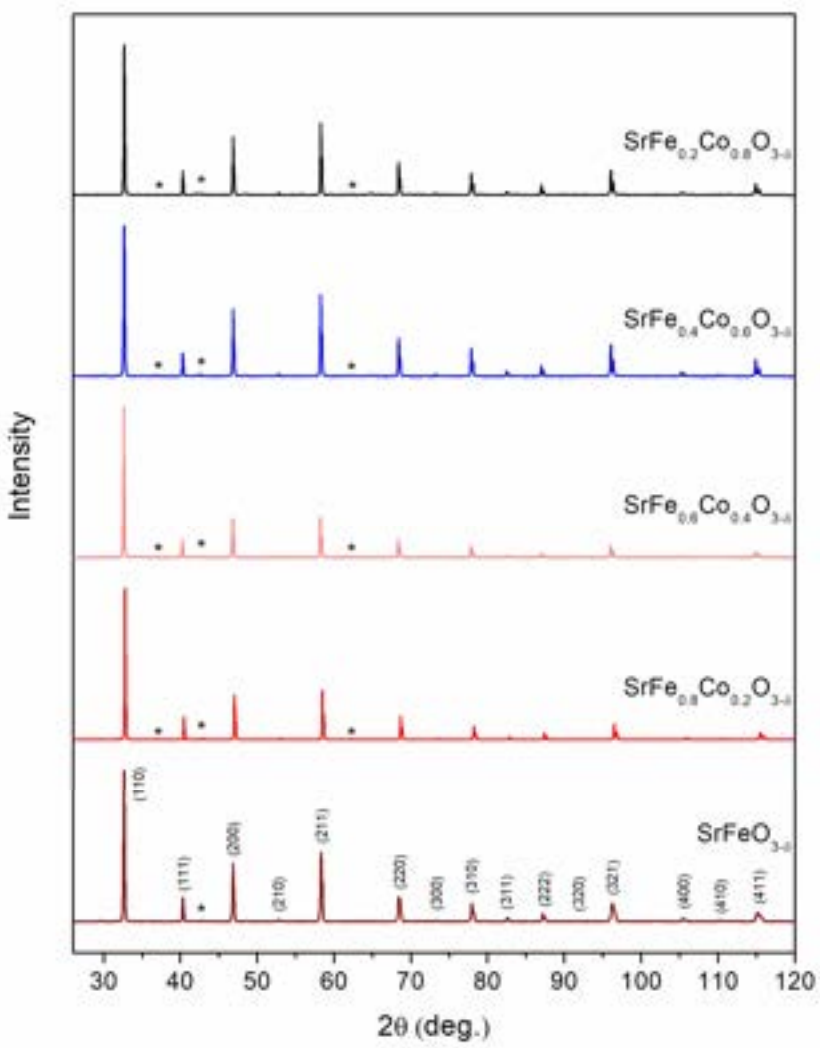

Figure 5.18. The XRD patterns collected at room temperature for $SrFe_{1-x}Co_xO_{3-\delta}$ samples under atmospheric air. The crystallographic planes corresponding to the cubic perovskite phase related to the visible reflections are labelled. The star signs indicate the minor reflections originating either from the small amounts of NiO or from the additional reflections related to the lowering of the crystal symmetry of the main SFC phase.

Reproduced with permission from Jagoda Budnik, Maria Gazda, Alexey Maximenko, Aleksandra Mielewczyk-Gryń, Joanna Pośpiech, Sebastian Wachowski, Agnieszka Witkowska, and Tadeusz Miruszewski, "Sr(Fe,Co)$O_{3-\delta}$ Mixed Conductors: How Cobalt Drives Oxygen Vacancy Formation", Chemistry of Materials 2025, 37 (21), 8822–8834. Copyright 2025 American Chemical Society.[193]

The secondary reflections most likely arise from nickel oxide, which was used as a sintering aid during the second synthesis stage. Alternatively, they may result from the symmetry reduction to lower symmetry structures, such as tetragonal or orthorhombic, since previous studies on strontium ferrite-cobaltites have indicated that some octahedral tilting may be possible in such systems.[196–198] Nevertheless, if any symmetry-lowering occurs, it likely involves minor distortions, given the low intensity of the additional peaks and the simple profile of the reflections observed at high 2θ angles. Therefore, to ensure the precision of the terminology used, the crystal structure of the SFC materials studied in this work is characterised as pseudocubic.[192]

Table 5.10 presents the crystal lattice parameters determined for the $SrFe_{1-x}Co_xO_{3-\delta}$ (x = 0, 0.2, 0.4, 0.6, 0.8). The values obtained in this work exceed those reported in the literature

(included in **Table 5.10** for comparison).[123,199] This observation is consistent with relatively high oxygen nonstoichiometry parameters found in this work, since in the referenced literature reports the oxygen nonstoichiometry was considered negligible. Furthermore, the crystal lattice parameters increase with higher x in $SrFe_{1-x}Co_xO_{3-\delta}$. As it will be shown below, the K-edge spectra of oxygen indicate that both Fe and Co ions adopt high-spin configurations in the bulk of SFC materials. Using the high-spin ionic radii for sixfold coordination from Shannon's database[168] together with the obtained oxidation states (approximately 3.0 for Co and 3.2 for Fe, see **Table 5.9**), the average ionic radius of cobalt is slightly smaller than that of iron – 0.61 Å vs 0.63 Å (the value for cobalt was taken directly as the high-spin radius of Co^{3+} (0.61 Å), while the value for iron was calculated as weighted average of the high-spin radii of Fe^{3+} (0.645 Å) and Fe^{4+} (0.585 Å)). The increase in unit-cell dimensions with higher Co content is likely driven by multiple factors, including local structural distortions and changes in oxygen nonstoichiometry. Higher concentrations of oxygen vacancies have been previously linked to lattice expansion.[200,201] Additionally, since cations with lower coordination numbers generally have smaller radii,[168] the reduction of the coordination geometry from the ideal octahedron can be related to a modified environment of the cation, further affecting the lattice parameters.

Table 5.10. The pseudocubic unit cell parameters with the corresponding Goodness of Fit (GOF) determined for $SrFe_{1-x}Co_xO_{3-\delta}$ (x = 0, 0.2, 0.4, 0.6, 0.8), as well as the parameters obtained by other researchers for the same compounds.

	$a = b = c$ (Å)	$\alpha = \beta = \gamma$ (°)	GOF
$SrFeO_{3-\delta}$	3.8708 (1)	90	1.08
	3.856[199]		-
$SrFe_{0.8}Co_{0.2}O_{3-\delta}$	3.8740 (1)		1.28
$SrFe_{0.6}Co_{0.4}O_{3-\delta}$	3.8751(1)		1.53
	3.866(2)[123]		-
$SrFe_{0.4}Co_{0.6}O_{3-\delta}$	3.8773(1)		1.47
	3.865(2)[123]		-
$SrFe_{0.2}Co_{0.8}O_{3-\delta}$	3.8778(1)		2.69
	3.861(1)[123]		-

Reproduced with permission from Jagoda Budnik, Maria Gazda, Alexey Maximenko, Aleksandra Mielewczyk-Gryń, Joanna Pośpiech, Sebastian Wachowski, Agnieszka Witkowska, and Tadeusz Miruszewski, "$Sr(Fe,Co)O_{3-\delta}$ Mixed Conductors: How Cobalt Drives Oxygen Vacancy Formation", Chemistry of Materials 2025, 37 (21), 8822–8834. Copyright 2025 American Chemical Society.[193]

The XANES spectra collected at the K-edges of iron and cobalt (**Figure 5.17**) were further analysed in order to examine the local environment around the TM ions of the SFC materials. The spectra of all materials recorded at both absorption edges display the following characteristic features: pre-edge shoulders (features 1 and 2) and post-edge peak (feature 3). The pre-edge peaks, evident at both edges, originate from the quadrupole transitions between the 1*s* orbital of TM and 3*d* orbitals of TM mixed with oxygen 2*p* orbitals of oxygen (feature 1) and from the dipolar transitions resulting from the $p-d$ orbital mixing of the transition metal (feature 2).[199] The features of the pre-edge region exhibit high sensitivity to the TMO_6 octahedra deformation, with the pre-peak intensity increasing when the centrosymmetry of the octahedron is reduced.[202] However, the features observed in the pre-edge region are also affected by 3*d* – 4*p* hybridisation, the spin state of the transition metal and its coordination environment. For this reason, the interpretation presented in this work should be regarded as preliminary, while its verification would require complex multiplet or crystal-field simulations.

Feature 2 arises from dipole transitions from the 1*s* level to 4*p* states hybridised with 2*p* oxygen states, with the subsequent ligand-to-metal charge transfer shakedown process (LMCT). With a decreasing number of available TM 4*p* – O 2*p* states, the intensity of this feature diminishes. Therefore, the characteristics of feature 2 are influenced by the transition metal coordination number and, consequently, depend on its oxidation state.[203] Feature 3 (white line) is associated with the main electron transition occurring during the K-edge absorption – the dipole-allowed transition from 1*s* core level to the 4*p* states of TM. Its probability depends on the 4*p* partial density of states (PDOS) of the transition metal. In perovskites, the intensity of this feature reflects the hybridisation degree between the transition metal 4*p* orbital and the 2*p* orbital of oxygen. With a higher covalency of the TM–O bond, the 4*p* orbital occupancy increases and reduces the $1s \rightarrow 4p$ transition probability. Therefore, with higher TM–O covalency, the intensity of the white line generally decreases.[204]

In the case of the SFC spectra collected at the K-edge of cobalt, the pre-edge peak 1, associated with electron transitions between the 1*s* core level and 3*d* state of TM, shifts slightly toward lower energies with higher cobalt content. There is a noticeable difference in the width of the pre-peak between $SrFe_{0.8}Co_{0.2}O_{3-\delta}$ (in which cobalt is in the lowest oxidation state, see **Table 5.9**) and other compositions with higher cobalt content. Raimondi et al. reported a contrasting result, where the oxidised strontium ferrite showed broader pre-edge features, while the reduced material displayed a sharp pre-edge peak in the K-edge spectra of iron.[60] The observed peak broadening may originate from a deviation from a fully symmetrical local geometry around cobalt ions. Nonetheless, there are no substantial changes in the pre-peak shape nor its intensity in the case of $SrFe_{1-x}Co_xO_{3-\delta}$ samples with $x \in \langle 0.4, 0.8 \rangle$, suggesting

that further cobalt addition into the B-site probably does not influence its position within the octahedron nor its local symmetry.

No significant differences in feature 2 in the K-edge spectra of both TM were observed between the SFC samples. However, there are visible variations in the feature 3 characteristics in the spectra of both TM K-edges. In the case of the Co K-edge spectra, the white line intensity is noticeably higher for the $SrFe_{0.8}Co_{0.2}O_{3-\delta}$ composition. Moreover, with increasing cobalt content, the intensity of this feature decreases. The opposite behaviour can be observed in the case of the K-edge spectra of iron, where the intensity of the white line decreases with higher cobalt content. This indicates that the Fe−O bond covalency decreases, while Co−O bonds become more covalent with increasing x in $SrFe_{1-x}Co_xO_{3-\delta}$. The TM−O bond covalency can be enhanced by increased concentration of oxygen vacancies or shorter interatomic distances between TM and oxygen.[205] According to the EXAFS results, provided and discussed in the **Appendix** (**Figure A15**), the lengths of the transition metal-oxygen bond display no substantial changes; hence, the variations in the intensity of feature 3 most likely correspond to differing oxygen-vacancy concentrations located around the TM. This indicates that oxygen vacancies tend to localise around cobalt ions, suggesting that cobalt serves as a stabilising centre for vacancies and influences the PDOS of the TM ions and the TM−O covalency in SFC materials.

Apart from the features 1-3 observed in all collected spectra, an additional feature * in the Fe K-edge spectra was identified at ≈ 7118 eV. This feature may be associated with Fe ions in a lower-coordination environment.[203] The ideal octahedral geometry can be disrupted by oxygen vacancies, giving rise to sites with lower coordination around TM ions. If a single oxygen is missing, the octahedron transforms into a square-pyramidal configuration, whereas the absence of two oxygens can create a tetrahedral one. While the formation of tetrahedral sites is less probable, both scenarios decrease the number of oxygen ligands around the transition metal. The changes in local coordination around iron ions can locally alter the electronic structure and lead to subtle variations in the pre-edge region observed in the Fe K-edge spectra.

Feature * is only visible for $SrFeO_{3-\delta}$ and $SrFe_{0.8}Co_{0.2}O_{3-\delta}$, which possess the lowest oxygen nonstoichiometry among the SFC series. This observation suggests that only when the amount of cobalt is low, the oxygen vacancies localise in the vicinity of Fe cations in numbers high enough to reduce their coordination number. This is consistent with the lower cobalt oxidation states observed for all investigated materials and the conclusion drawn from the white-line analysis, that oxygen vacancies preferentially localise around Co ions. Since feature * is not present in the Co K-edge spectra, the cobalt coordination polyhedra do not seem to be reduced to a tetrahedral geometry.

The shape and intensity of the pre-edge peaks can be further discussed via the analysis of their centroid, which can provide additional information about the coordination number and oxidation state of the absorbing atom. The integrated areas of the pre-edge peaks present in the K-edge spectra of iron plotted against their centroid positions are shown in **Figure 5.19**. The details behind the conducted analysis are provided in the **Appendix** (chapter **6.2.2**). The average oxidation state and coordination geometry of the B cations were analysed by comparing the data obtained for the investigated samples with the standard data for iron ions in defined oxidation states and coordination geometries. In the studied SFC materials, the centroid positions exceeded those typical of Fe^{3+}. This confirms that the iron oxidation state in the SFC series exceeds +3, as established by the absorption-edge analysis (**Table 5.9**).

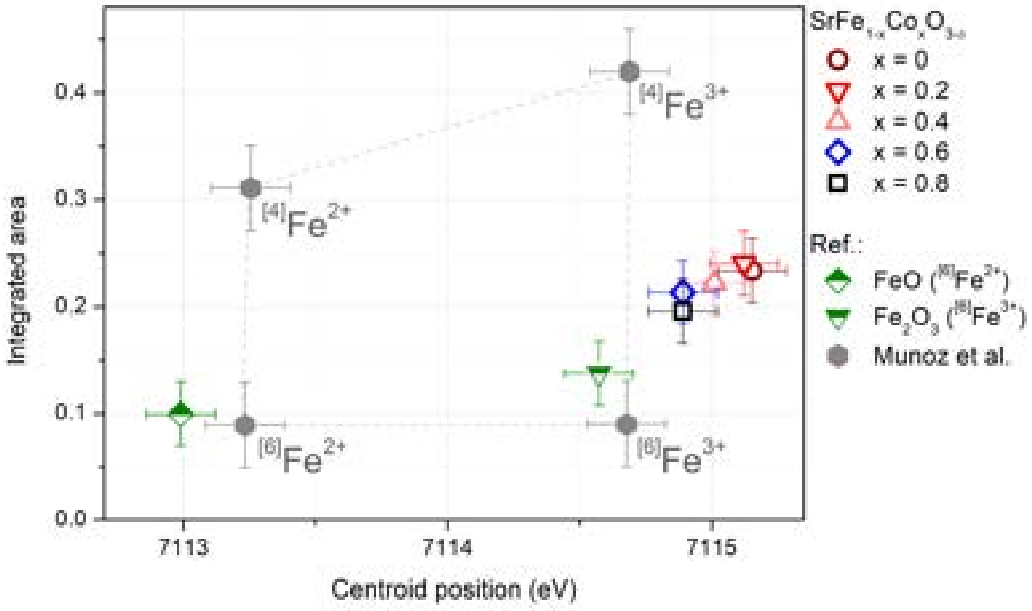

Figure 5.19. The integrated area of the pre-peaks observed in the K-edge spectra of iron for $SrFe_{1-x}Co_xO_{3-\delta}$ as a function of their centroid positions. The data corresponding to the standards of known valency and coordination are marked as grey hexagons.[206] The reference points obtained from FeO ($^{[6]}Fe^{2+}$) and Fe_2O_3 ($^{[6]}Fe^{3+}$) spectra are also included. The coordination number is indicated by numbers in square brackets, where [4] denotes tetrahedral and [6] octahedral geometry.

Reproduced with permission from Jagoda Budnik, Maria Gazda, Alexey Maximenko, Aleksandra Mielewczyk-Gryń, Joanna Pośpiech, Sebastian Wachowski, Agnieszka Witkowska, and Tadeusz Miruszewski, "$Sr(Fe,Co)O_{3-\delta}$ Mixed Conductors: How Cobalt Drives Oxygen Vacancy Formation", Chemistry of Materials 2025, 37 (21), 8822–8834. Copyright 2025 American Chemical Society.[193]

The integrated areas of the pre-peaks observed in the spectra of SFC are between those associated with perfectly tetrahedral and octahedral geometry, suggesting that the coordination of Fe in the studied materials represents a mixture of coordinations between 4 and 6. This is consistent with relatively high values of oxygen nonstoichiometry in these materials. Furthermore, the highest integrated areas are observed for the pre-peaks of the materials with the lowest cobalt content: $SrFeO_{3-\delta}$ and $SrFe_{0.8}Co_{0.2}O_{3-\delta}$. This suggests that the contribution of lower-coordinated iron in these materials is greater in comparison to SFC materials with higher cobalt content, which is consistent with the presence of feature *

in the spectra associated with lower coordination of iron observed for $SrFeO_{3-\delta}$ and $SrFe_{0.8}Co_{0.2}O_{3-\delta}$. With higher x in $SrFe_{1-x}Co_xO_{3-\delta}$, the coordination number of iron increases, despite the increase in oxygen-vacancy concentration. Therefore, oxygen vacancies do not occupy the positions in the vicinity of Fe, which further supports that the vacancies preferentially localise around cobalt.

To gain further insight into the local environment of TM ions, the EXAFS signals corresponding to the Fe and Co K-edge spectra were examined (see chapter **6.2.4**). The data confirm the mixed local geometry around TM cations. As indicated by the pre-edge region analysis, the coordination geometry of Fe ions in SFC varies between octahedral and tetrahedral.

In order to investigate the electronic properties of the $SrFe_{1-x}Co_xO_{3-\delta}$ series (x = 0.2, 0.4, 0.6, 0.8), the oxygen K-edge XANES spectra were collected and analysed. Since the spectra recorded at O K-edge reflect the electronic structure and density of states of TM, they can be very valuable for studying transition-metal oxides. **Figure 5.20** shows the O K-edge spectra recorded for SFC materials in total electron yield (TEY) and fluorescence yield (FY) detection modes. Since TEY probes only a few nanometres from the surface of the sample, while FY detection reaches tens to hundreds of nanometres, the combination of both detection modes provides both the surface-sensitive and bulk information about the studied material.[207] However, the fluorescence spectra may be influenced by self-absorption, occurring when the emitted photons are reabsorbed within the sample, and saturation. This can alter the shape and intensity of the spectral features, and should be considered when comparing surface and bulk electronic properties.

The pre-edge features observed in the O K-edge spectra originate from electron transitions from the oxygen 1*s* orbital to the unoccupied hybridised O 2*p* – TM 3*d* orbitals. Consequently, the local coordination environment and spin state of the transition metal, as well as the degree of centrosymmetry (for the octahedral coordination), significantly affect the shape, position and intensity of the features observed in this part of the spectrum. The utilisation of both TEY and FY detection modes enabled the comparison of the surface and bulk electronic properties of the studied materials.

The XANES spectra of the oxygen K-edge, acquired in TEY mode for the SFC series, are presented in **Figure 5.20a**. A distinct maximum between 532 and 534 eV (feature E) originates from the surface-adsorbed species, such as oxygen species or carbon-based impurities.[208,209] The intensity of this feature increases with cobalt content, suggesting enhanced surface adsorption. In contrast, feature E does not appear in the FY spectra (**Figure 5.20c**), which is consistent with the fact that fluorescence mode probes mostly the bulk of the material.

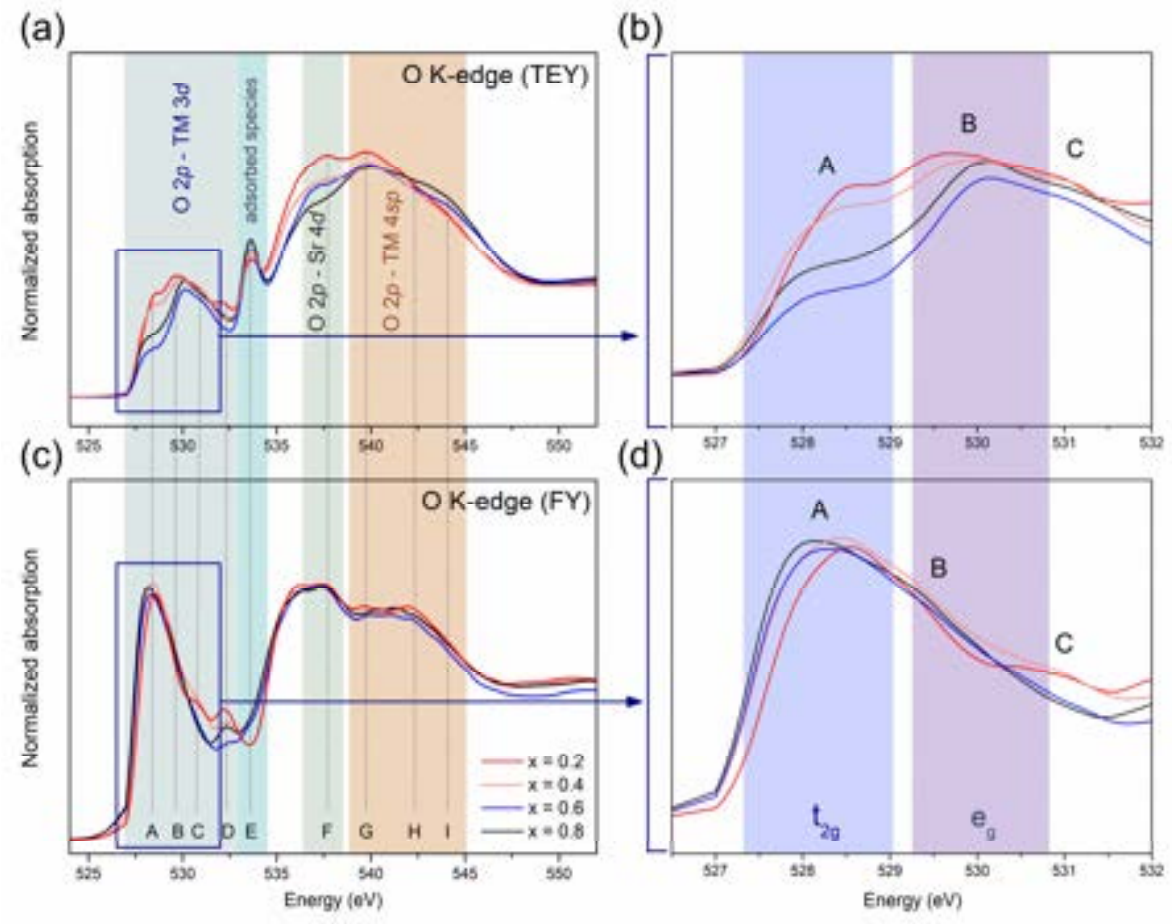

Figure 5.20. The XANES spectra corresponding to the K-edge of oxygen collected via TEY (a-b) and FY (c-d) detection modes for $SrFe_{1-x}Co_xO_{3-\delta}$. The observed peaks were assigned with letters A-I. The close-ups of the pre-edge for spectra recorded via both detection modes are shown in plots (b) and (d).

Reproduced with permission from Jagoda Budnik, Maria Gazda, Alexey Maximenko, Aleksandra Mielewczyk-Gryń, Joanna Pośpiech, Sebastian Wachowski, Agnieszka Witkowska, and Tadeusz Miruszewski, "$Sr(Fe,Co)O_{3-\delta}$ Mixed Conductors: How Cobalt Drives Oxygen Vacancy Formation", Chemistry of Materials 2025, 37 (21), 8822–8834. Copyright 2025 American Chemical Society.[193]

In the spectra recorded using both detection modes, there is a broad maximum above 535 eV, which comprises two distinct regions: one feature centred around ≈ 536 eV (feature F) and another set of features above 539 eV (features G-I). Feature F corresponds to the unoccupied O 2*p* states hybridised with Sr 4*d* orbitals, while peaks G-I can be attributed to 2*p* orbitals of oxygen hybridised with the 4*sp* states of TM.[210–212] Feature G can be associated with the hybridisation of 4*sp* states of TM with the O 2*p* states of O^{2-} species adsorbed on the surface of the material.[211] Features H and I can be assigned to the orbitals formed by the hybridisation of TM 4*sp* with O 2*p* states of monoxidic species.[212] As shown in the TEY spectra of SFC in **Figure 5.20a**, the relative intensity of the strontium-related feature F diminishes with increasing cobalt content. Although the origin of this change is unclear, it may be linked to a variation in the degree of hybridisation between the orbitals of O and Sr, potentially arising from structural or symmetry-related differences between the SFC compounds. Since no similar changes are present in the FY spectra (**Figure 5.20c**), this effect

can be solely ascribed to the surface of the material. Except for a slight increase in the intensity of feature I observed in the TEY spectra of $SrFe_{0.4}Co_{0.6}O_{3-\delta}$ and $SrFe_{0.2}Co_{0.8}O_{3-\delta}$ samples, no substantial differences between features H and I, associated with TM 4*sp* hybridisation, are evident across the studied materials in either TEY or FY spectra.

The most prominent differences between the O K-edge spectra of the investigated materials occur below 532 eV – in the pre-edge peak region (features A-C). **Figure 5.20b** and **d** show the close-ups of this part of the spectra collected in TEY and FY modes, respectively. The pre-edge region of O K-edge spectra may also reflect the electrical properties of the material, as its characteristics depend on the 3*d* states of TM. In perovskite-type oxides, the octahedral crystal field splits the 3*d* orbitals of transition metal into separate t_{2g} and e_g levels. The 1.5 — 2 eV energy separation between features A and B observed in the SFC spectra corresponds well with the orbital splitting values reported by Abbate et al. for $Sr(Fe,Co)O_{3-\delta}$.[133] The shape of the pre-edge peak is governed by the relative population of empty t_{2g} and e_g states and by the magnitude of the crystal-field splitting. When the relative number of empty states on a specific 3*d* level is higher, the probability of electrons transitioning to that level is greater, which results in higher absorption. The occupation of the e_g and t_{2g} states indicates the spin state of a transition-metal ion in an octahedral environment. Therefore, the intensity ratio of features A and B can serve as a qualitative indicator of the spin state of a B-site cation. It should be emphasised, that additional factors, such as the degree of TM–O covalency, local symmetry distortions, and the different probing depths of TEY and FY detection, may also influence the characteristics of these features.

In this work, the TEY and FY spectra were evaluated by comparing the observed trends with those reported for reference oxides of established spin states (Szpunar et al.[213]; Padilla-Pantoja[214]; Toulemonde et al.[215]; Sun and Zhou[216]), following the methodology commonly applied in earlier studies.[195,213] This comparative approach enabled evaluation of TM spin states in both the near-surface region and the bulk of the SFC materials.

As shown in **Figure 5.20b**, feature B displays greater intensity than feature A, which might indicate that, on the surface of the material, TM ions possess a higher density of unoccupied electronic states at e_g levels in comparison to t_{2g}. **Figure 5.21** illustrates how the occupation of the 3*d* states influences the spin state of cobalt and iron in the 3+ oxidation state. It can be seen that in this case, the expected ratios of unoccupied states at t_{2g} and e_g levels would be 2:3 and 1:3 for iron and cobalt in the intermediate spin state. Therefore, the observed difference between the A and B features suggests that the TMs are not in a high-spin (HS) state, which would typically yield a more intense peak A. Since the intensity difference between features A and B is not very pronounced, Fe and Co are likely not in the low-spin (LS) state, but rather exhibit a mixed or intermediate spin (IS) configuration.

This is consistent with the results reported for iron by Kawakami et al.[217] The difference between the intensities of features A and B increases with increasing cobalt content, which suggests that the number of unoccupied states at the higher energy level is also increasing.

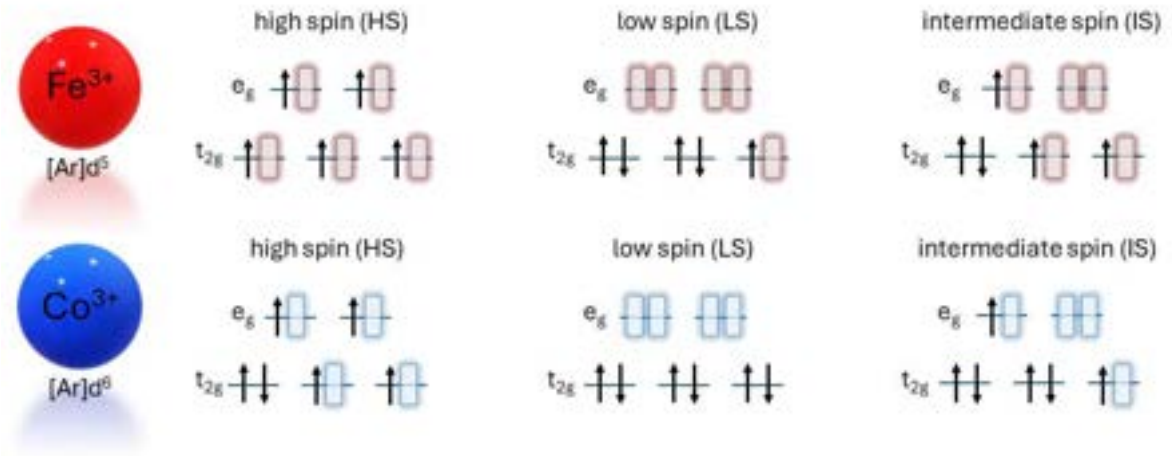

Figure 5.21. Diagram demonstrating possible occupations of 3*d* orbitals of Fe^{3+} and Co^{3+} ions in different spin states by valence electrons. Unoccupied states are indicated by empty frames.

Reproduced with permission from Jagoda Budnik, Maria Gazda, Alexey Maximenko, Aleksandra Mielewczyk-Gryń, Joanna Pośpiech, Sebastian Wachowski, Agnieszka Witkowska, and Tadeusz Miruszewski, "Sr(Fe,Co)$O_{3-\delta}$ Mixed Conductors: How Cobalt Drives Oxygen Vacancy Formation", Chemistry of Materials 2025, 37 (21), 8822–8834. Copyright 2025 American Chemical Society.[193]

The FY spectra (**Figure 5.20d**), which represent the volume information, show the opposite trend, with feature A exhibiting higher intensity than feature B, which may indicate a predominance of HS transition-metal cations in the volume of the material. This is in agreement with prior results of Bocquet et al. and Raimondi et al., who reported iron in the HS state in strontium ferrite.[60,117] The $SrFe_{1-x}Co_xO_{3-\delta}$ series was also investigated by Okazoe et al., who assumed that iron and cobalt were in HS and IS configurations, respectively, although they considered the oxidation state of both ions to be 4+.[196]

In the TEY spectra, the positions of features A and B, as well as the distance between them, change depending on the cobalt content in the SFC materials. In the case of $ABO_{3-\delta}$ oxides, the energy positions of the pre-edge peaks are determined by the ionic radius of cation A and the covalency of the B–O bond, governed by the valency of the B-site cation and the degree of overlap between B 3*d* and O 2*p* orbitals.[218] In the case of the SFC spectra collected in this work, a higher Co content in SFC materials leads to a larger energy difference between features A and B. This stems from the crystal field splitting dependence on TM cation type and its oxidation state, which can be described by the spectrochemical series of metals, according to which, Co^{3+} causes greater splitting than Fe^{3+}.[219] In contrast, the fluorescence spectra show only minor differences in the pre-edge region across the SFC series, with only

a slight shift of feature A toward lower energies with increasing Co content. This is consistent with the feature A shift observed in the TEY spectra.

Feature D, visible in **Figure 5.20a** and **c**, represents another absorption peak originating from the electron transitions to O 2*p* – TM 3*d* hybridised orbitals.[220] The presence of three distinct spectral features (A, B, and D), associated with the octahedral coordination of transition-metal ions, suggests that the TMO_6 octahedra are not ideal but distorted, further splitting the 3*d* states. Although no clear trend is observed in the intensity of feature D with varying cobalt content in SFC materials, all features related to octahedral coordination appear more pronounced in the FY mode. This suggests that the octahedral geometry is more likely in the bulk of the material compared to its surface which can be reduced, leading to a lower coordination of TM ions.

Feature C is associated with transition-metal ions in lower-coordination geometries, such as square-pyramidal[212] or tetrahedral[220]. For the $SrFe_{0.8}Co_{0.2}O_{3-\delta}$ and $SrFe_{0.6}Co_{0.4}O_{3-\delta}$ samples, the intensity of this feature in both TEY and FY spectra is comparable, which implies that the lower-coordination geometries are present not only at the surface but also in the bulk of these oxides. This is consistent with the relatively low oxidation states of the transition-metal cations (**Table 5.9**) observed in this study. In contrast, for the materials containing higher cobalt contents ($SrFe_{0.4}Co_{0.6}O_{3-\delta}$ and $SrFe_{0.2}Co_{0.8}O_{3-\delta}$), the diminished feature C in FY mode suggests that the reduced coordination geometry around the TM ions is not prevalent in the bulk of the material. This aligns with the findings from the second derivative analysis of the iron K-edge spectra (**Figure 5.17**).

In order to qualitatively evaluate the oxidation states of TM ions on the surface and in the bulk and explore the spin states of iron and cobalt ions separately, the X-ray absorption spectra for the SFC series were collected using TEY and FY detection modes at $L_{3,2}$ edges of Fe and Co. The TEY XANES spectra covering both $L_{3,2}$ edges for both TM ions are included in the **Appendix** (**Figure A17**). **Figure 5.22** presents the close-ups of the L_3 edge, which results from the electron excitation from the $2p_{3/2}$ core level of TM. In the case of iron TEY spectra, the differences in the L_3 shape between the analysed samples are not evident. In contrast, for the cobalt TEY spectra, there is a slight chemical shift of the L_3 maximum, where it appears at progressively higher energies as the cobalt content increases. This behaviour may reflect a subtle increase in the cobalt oxidation state with higher x in the near-surface regions of $SrFe_{1-x}Co_xO_{3-\delta}$, consistent with data collected in **Table 5.9**. A similar shift of the Co L_3 edge with increasing cobalt oxidation state was reported by Guan et al.[218] Moreover, with increasing cobalt content in the SFC samples, the relative intensity of the shoulder at ≈ 778.5 eV in the Co TEY spectra diminishes in comparison to the main maximum, which might suggest an increasing deviation from ideal cubic symmetry.[221]

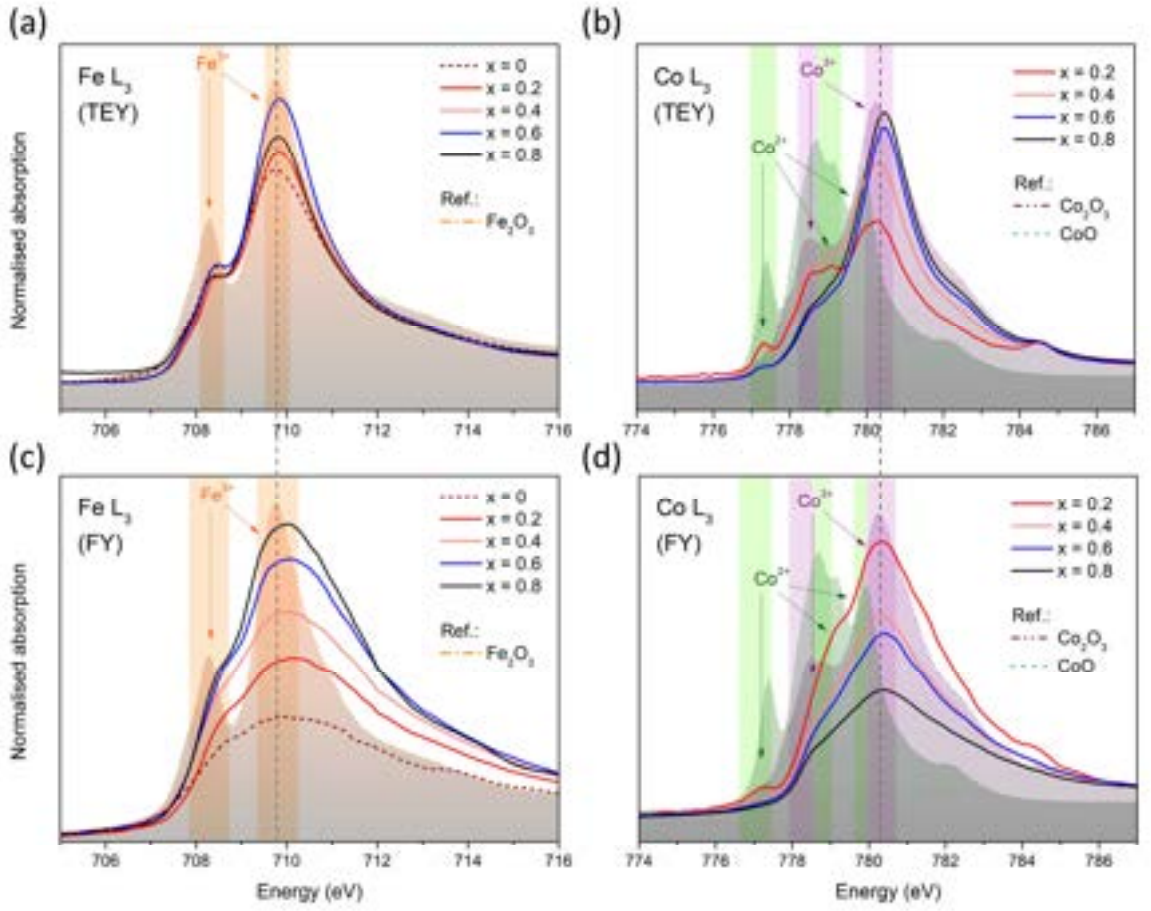

Figure 5.22. The XANES spectra corresponding to the L_3 edges of iron (a, c) and cobalt (b, d) collected via TEY and FY detection modes for $SrFe_{1-x}Co_xO_{3-\delta}$.

Reproduced with permission from Jagoda Budnik, Maria Gazda, Alexey Maximenko, Aleksandra Mielewczyk-Gryń, Joanna Pośpiech, Sebastian Wachowski, Agnieszka Witkowska, and Tadeusz Miruszewski, "$Sr(Fe,Co)O_{3-\delta}$ Mixed Conductors: How Cobalt Drives Oxygen Vacancy Formation", Chemistry of Materials 2025, 37 (21), 8822–8834. Copyright 2025 American Chemical Society.[193]

The local maxima observed in the Fe L_3 TEY spectra correspond well to those of Fe_2O_3, indicating that Fe^{3+} is the dominant oxidation state also on the surface of the studied materials. The local maxima of the Co L_3 edge in the TEY and FY spectra can be attributed to contributions from Co^{2+} and Co^{3+}, identified based on the spectra of reference compounds (CoO and Co_2O_3). The higher intensity of Co^{3+}-related features indicate that, even on the surface, it is the predominant valence of Co. Additionally, the feature at approximately 777.2 eV shows higher intensity in samples with lower cobalt content, which is in agreement with the lower average oxidation state of cobalt obtained for these compositions (**Table 5.9**).

There is a visible chemical shift of the main maximum between the iron ions on the surface and in the volume (TEY and FY spectra, respectively) of the SFC materials, confirming a lower average oxidation state of iron on the reduced surface. In the volume, the presence of Fe^{4+} is indicated by the broadening of the main maximum on the higher energy side. Similar broadening is also observed in the FY spectra of cobalt. Moreover, the features related to Co^{2+} are weaker for the volume data. This indicates a lower concentration of Co^{2+}

ions and a higher concentration of Co^{4+} ions in comparison to the surface regions. It should be noted that the effects of saturation and self-absorption can alter both the apparent intensities and shapes of features recorded in FY spectra.

Additional information can be obtained by analysing the branching ratio (BR), defined as the ratio of the intensity of peak L_3 to the sum of the intensities of peaks L_3 and L_2, corresponding to electron transitions from the TM core levels $2p_{3/2}$ and $2p_{1/2}$, respectively. This multiplet structure arises from spin-orbit coupling between the core-level and valence electrons, making the BR sensitive to the occupancy of *d* orbitals (valence) and the spin state of the transition metal.[222] The branching ratios calculated for $L_{3,2}$ of Fe and Co as a function of cobalt content in SFC materials are shown in **Figure 5.23**. The branching ratio values obtained from the volume data (FY) are lower than for the surface (TEY), especially in the case of Fe. This may be related to the reduced oxidation state of ions on the surface, as confirmed by the L_3-edge spectra analysis with a chemical shift of the main maximum between TEY and FY spectra.

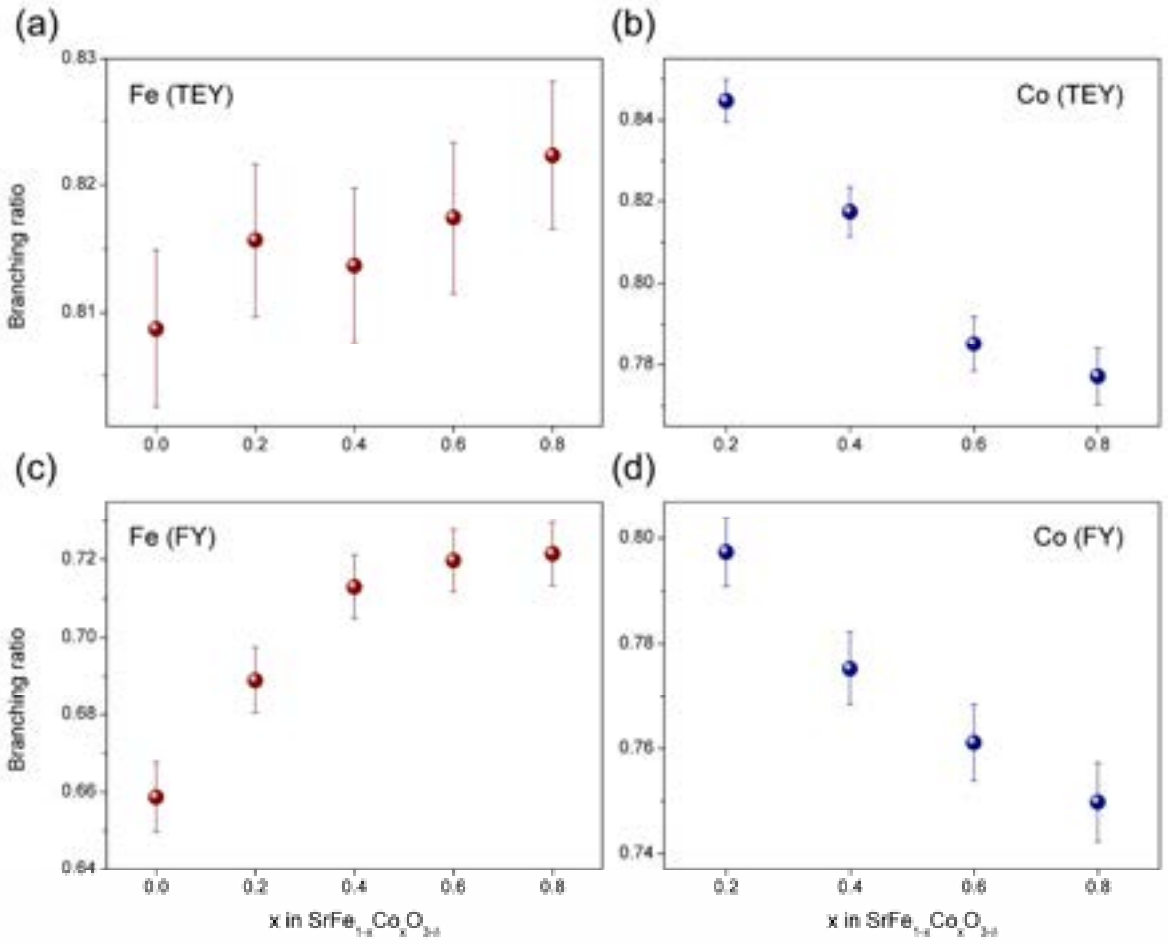

Figure 5.23. The $L_{3,2}$ branching ratios for iron (a, c) and cobalt (b, d) as a function of cobalt content (x) in $SrFe_{1-x}Co_xO_{3-\delta}$ calculated based on TEY and FY data.

Reproduced with permission from Jagoda Budnik, Maria Gazda, Alexey Maximenko, Aleksandra Mielewczyk-Gryń, Joanna Pośpiech, Sebastian Wachowski, Agnieszka Witkowska, and Tadeusz Miruszewski, "$Sr(Fe,Co)O_{3-\delta}$ Mixed Conductors: How Cobalt Drives Oxygen Vacancy Formation", Chemistry of Materials 2025, 37 (21), 8822–8834. Copyright 2025 American Chemical Society.[193]

The BR is sensitive to multiple factors, including the degree of TM–O covalency, the local coordination environment, as well as the oxidation and spin states of TM. Since the coordination number of iron did not show significant changes as a function of cobalt content (**Figure 5.19**) and the EXAFS analysis did not show significant variations in the Fe–O distances (see **Figure A15** in the **Appendix**), the covalency of the Fe–O can be expected to remain similar between different SFC compositions. Moreover, the oxidation state of iron for all SFC materials is essentially constant. Therefore, the variations of BR in this case can be attributed to the spin state changes. A higher BR for iron suggests enhanced spin-orbit coupling and a transition towards a higher spin state with increasing cobalt content. In the case of cobalt, the oxidation state slightly decreases in materials with higher cobalt content, which can be partially responsible for the observed decrease of BR, as reported by Shafeie et al.[222] However, the differences they observed in BR values were very modest, even with large changes in the formal oxidation state of cobalt. In our case, the oxidation state of cobalt showed only minor increases across the studied SFC materials, so the substantial decrease in the BR parameter may be attributed to a shift towards a lower spin state in materials with higher cobalt content. These findings align with the change in the intensities of pre-edge features A and B, observed in the TEY O K-edge spectra.

The relative intensities and shapes of features L_3 and L_2 recorded in FY mode can be distorted due to self-saturation effects. Therefore, an additional uncertainty in the BR values, determined based on the FY data, is introduced. Even when this limitation is taken into account, the compositional trends remain clear – increasing Co content in SFC results in higher BR for iron and lower BR for cobalt. This behaviour is observed in both TEY and FY measurements, indicating that the evolution of electronic structure with composition is reflected similarly in the near-surface and bulk regions of the materials.

In summary, the structural and electronic properties of the $SrFe_{1-x}Co_xO_{3-\delta}$ materials were found to be influenced by the cobalt content. Single-phase pseudocubic perovskite materials were obtained across the entire SFC series. The unit cell parameters were higher than reported in the literature and increased with cobalt content, consistent with the determined lower oxidation states of the transition-metal cations. Iron coordination varied between octahedral and tetrahedral. Cobalt was established as a stabilising centre for oxygen vacancies, governing the covalency of TM–O bonds of both transition metals. TM cations exhibited intermediate or mixed spin states near the surface, while in the bulk, they were in a high-spin state. Lower-coordination geometries were observed for iron in the volume of materials with low cobalt content, but they were predominantly located in the surface region of the materials with higher cobalt content. A dominant Fe^{3+} oxidation state and a mixed Co^{2+}/Co^{3+} oxidation state were confirmed in the near-surface region of all

SFC materials, with cobalt showing a gradual shift toward a higher oxidation state with increasing cobalt content. The spin states of the TM located near the surface varied with material composition: the iron spin state increased, whereas the cobalt spin state decreased with higher cobalt content.

5.2.3. Electrical transport properties

Figure 5.24 presents the total electrical conductivity of $SrFe_{1-x}Co_xO_{3-\delta}$ samples as a function of temperature in dry air. In this atmosphere, that is in oxidising conditions, all compositions demonstrate p-type conduction by a small-polaron hopping mechanism.[123,157,223,224] The conductivity varies depending on the chemical composition. $SrFeO_{3-\delta}$ shows substantially lower conductivity in comparison to the materials containing cobalt. The maximum electrical conductivity recorded for $SrFeO_{3-\delta}$ does not exceed 100 S/cm. Conversely, $SrFe_{0.6}Co_{0.4}O_{3-\delta}$ exhibits the highest total conductivity value, reaching 177 S/cm at approximately 500 °C. This value remains significantly lower than ≈ 275 S/cm at the same temperature that was reported by Wang et al.[119,123] In contrast to their work, which showed a monotonic increase in conductivity with increasing cobalt content, the results presented in this study exhibit a nonmonotonic relationship.

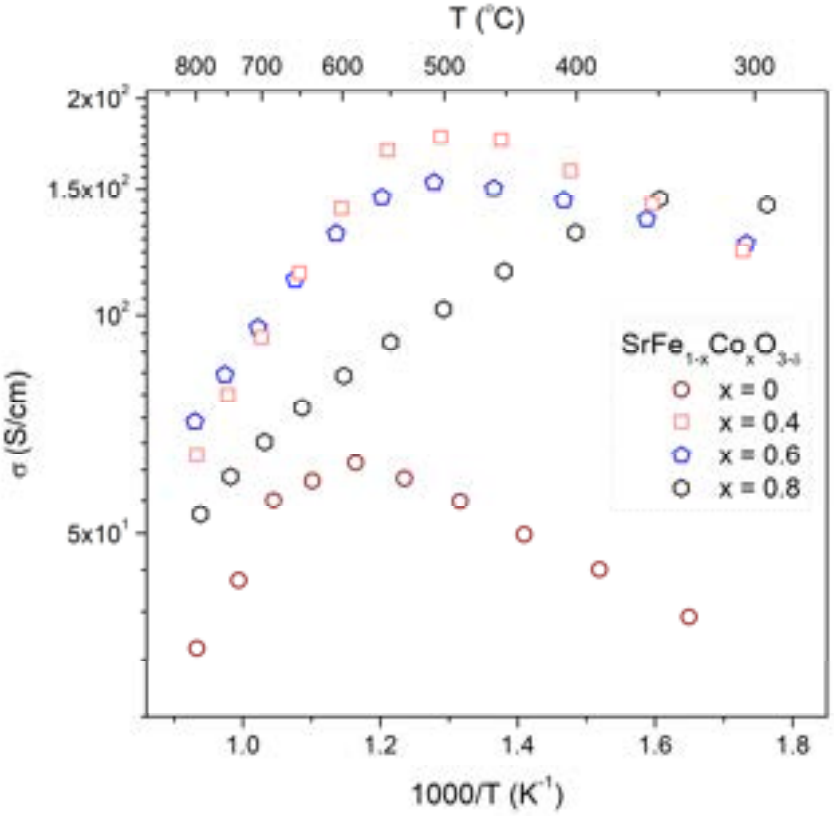

Figure 5.24. Total electrical conductivity as a function of temperature for $SrFe_{1-x}Co_xO_{3-\delta}$ (x = 0, 0.4, 0.6, 0.8) in dry air.

Reproduced from Jagoda Budnik, Maria Gazda, Tadeusz Miruszewski, "Electrical and thermoelectric transport of $SrFe_{1-x}Co_xO_{3-\delta}$ mixed-conducting perovskites", Solid State Sciences, 2026, 173, 108174. Copyright © 2026 Elsevier.[225]

All investigated compositions display a qualitatively similar temperature dependence of total electrical conductivity. At lower temperatures, conductivity increases with increasing temperature due to thermally activated small-polaron hopping of electron holes. Above a specific temperature, further heating results in a decrease in electrical conductivity. Since the charge neutrality is maintained mainly via compensation of oxygen vacancies by electron holes (ionic compensation), the observed conductivity decrease is likely the result of thermal reduction, which lowers the electron-hole concentration in accordance with the reaction:

$$2h^{\bullet} + O_O^X = v_O^{\bullet\bullet} + \frac{1}{2}\, O_2. \tag{5.21}$$

Moreover, thermal reduction may induce a phase transition to a lower-symmetry structure.[197,226] This transition may therefore influence the spatial distribution of the electronic density around the ions, significantly affecting the conduction of electronic charge carriers. When small-polaron conduction dominates, the temperature dependence of electrical conductivity can be described by an Arrhenius-type relation, given in the equation:

$$\sigma \cdot T = \sigma_0\, exp\left(\frac{-E_a}{k_B T}\right), \tag{5.22}$$

where σ denotes the total electrical conductivity, σ_0 the pre-exponential factor, and E_a the activation energy for conduction. The E_a values derived from this model are shown in **Table 5.11**. The activation energy values decrease with increasing cobalt content in $SrFe_{1-x}Co_xO_{3-\delta}$. Tai et al. also found a similar trend in E_a with increasing Co content in the related $La_{0.5}Sr_{0.5}Fe_{1-x}Co_xO_{3-\delta}$ system ($x \in \langle 0, 0.8\rangle$).[227] The same tendency was observed for the SFC material group by Wang et al.[123], yet the E_a values presented in their work were lower.

Table 5.11. Activation energies for conduction (E_a) and mobility (E_m), as well as the temperatures corresponding to the maximum of conductivity T_{max} for $SrFe_{1-x}Co_xO_{3-\delta}$ (x = 0, 0.4, 0.6, 0.8). The activation energies for conduction have been obtained using two methods: from the Arrhenius equation applied to the low-temperature conductivity data and based on T_{max}.

	T_{max} (°C)	E_a (eV)		E_m (eV)
		from Arrhenius equation (5.22)	from $k_B T_{max}$	
$Sr\mathbf{Fe}O_{3-\delta}$	600	0.16 ± 0.01	0.075	0.161 ± 0.004
$Sr\mathbf{Fe_{0.6}Co_{0.4}}O_{3-\delta}$	500	0.14 ± 0.01	0.066	0.147 ± 0.002
$Sr\mathbf{Fe_{0.4}Co_{0.6}}O_{3-\delta}$	500	0.10 ± 0.01	0.064	0.104 ± 0.003
$Sr\mathbf{Fe_{0.2}Co_{0.8}}O_{3-\delta}$	350	–	0.054	–

Adapted from Jagoda Budnik, Maria Gazda, Tadeusz Miruszewski, "Electrical and thermoelectric transport of $SrFe_{1-x}Co_xO_{3-\delta}$ mixed-conducting perovskites", Solid State Sciences, 2026, 173, 108174. Copyright © 2026 Elsevier.[225]

The observed lower total electrical conductivity and higher activation energy for conduction compared to previous literature reports[119,123] might be caused by a few reasons, with the usage of NiO as a sintering aid and a high oxygen nonstoichiometry being the most likely ones. The presence of NiO in the samples could have altered the resulting microstructure by segregating at grain boundaries, thereby affecting grain-boundary conductivity and, ultimately, the total conductivity of the ceramic samples. What is more, nickel can partially replace the B cations in the lattice:

$$2NiO \xrightarrow{Sr(Fe,Co)O_{3-\delta}} 2Ni'_{Fe,Co} + v_O^{\bullet\bullet} + 2O_O^x. \quad (5.23)$$

Therefore, nickel substitution of the B-cation can increase oxygen-vacancy concentration, resulting in improved grain sintering and oxygen-ionic conductivity. Such observations were made for $Ba(Zr,Ce)O_3$, in which nickel was partially incorporated into the crystal lattice as an acceptor dopant, forming a phase with reduced electronic but increased ionic conductivity.[228–230] Furthermore, Kharton et al. observed that adding Al_2O_3 to $SrFeO_3$-based electronic conductors improved densification but decreased oxygen permeability.[126] Previous studies on ferrite and cobaltite materials have shown how introducing nickel affects their physicochemical properties.[231–235] Most of these reports concern materials in the Sr-Fe-Co-O family containing relatively large amounts of nickel, typically above 7 mol.%, which is considerably higher than those applied in this work. For instance, Makhloufi et al. investigated $SrCo_{1-x}Ni_xO_3$ ceramics with nickel contents reaching 40 mol.%.[236] Their results demonstrated that such a high amount of Ni can still be incorporated into the cobalt sublattice, leading to the formation of a single-phase solid solution. They also observed that such a substitution led to an increased total electrical conductivity. In the case of materials studied in this dissertation, the decreased electrical conductivity may stem from the lower electrical conductivity of nickel oxide ($\sim 10^{-2}$ S/cm at 800 °C).[233] This value is more than three orders of magnitude lower than the total conductivity of the investigated SFC materials. Therefore, even small amounts of NiO aggregated at grain boundaries can reduce the overall electrical conductivity of the sample. Another reason for a low total electrical conductivity observed in this work may be a relatively high oxygen nonstoichiometry determined at room temperature (see **Table 5.9**). This suggests that even at the lowest temperatures, SFC oxides are reduced in comparison to the literature cases, which may lead to a decreased concentration of electron holes. Alternatively, the observed low conductivity may be attributed to diminished local symmetry around the transition-metal ions, which weakens the overlap between the transition metal *3d* and oxygen *2p* orbitals. However, no significant octahedra deformation, nor the reduction of the crystal symmetry, have been observed based on the XAS and XRD structural investigation. Therefore, the addition of 1 wt% NiO as well as a high oxygen

nonstoichiometry were most likely responsible for the electrical conductivity values being approximately 40% lower than those reported in the literature for NiO-free samples.[123]

In the systems, in which the conductivity is described by the Arrhenius relationship with a temperature-dependent pre-exponential factor (e.g. eq. (5.22)), two distinct temperature regions can be distinguished. When $k_BT < E_a$ (low-temperature region), the exponential term in equation (5.22) dominates the temperature dependence of electrical conductivity, while when $k_BT > E_a$ (high-temperature region), the temperature dependence is predominantly governed by the pre-exponential term $\frac{\sigma_0}{T}$. Provided no structural transitions, the temperature corresponding to maximum conductivity, T_{max}, can be estimated via equation:[227,237]

$$E_a \approx k_B T_{max}, \tag{5.24}$$

where T_{max} is the temperature at which conductivity peaks. The estimated T_{max} and the E_a values obtained from equation (5.22) (Arrhenius fitting) and equation (5.24) (T_{max} approximation) are included in **Table 5.11**. As the cobalt content in $SrFe_{1-x}Co_xO_{3-\delta}$ (x = 0, 0.4, 0.6, 0.8) increases, T_{max} decreases. For the Co-rich sample (x = 0.8), the measured conductivity profile indicates that the expected maximum should lie at lower temperatures, around 350 °C. As a result, the conductivity curve for this composition does not exhibit a well-defined maximum in the recorded temperature range. The T_{max} values obtained in this work are similar to those reported by Wang et al.[123]

Both sets of E_a values decline with increased cobalt content, but those derived from Arrhenius fitting are nearly twice as high, suggesting that either σ_0, E_a, or both are temperature-dependent. This might be due to structural distortions caused by the reduction of the materials at elevated temperatures, which could lead to a decreased crystal symmetry and lower electrical conductivity.[237] Such behaviour has also been reported for $SrFeO_{3-\delta}$ by Hombo et al.[110]

In order to further analyse the concentration and mobility of electron holes in the investigated materials, the Seebeck coefficient measurements have been conducted. **Figure 5.25**, **Figure 5.26**, and **Figure 5.27** show the temperature dependencies of the Seebeck coefficient, the electronic carrier concentration, and the mobility of electron holes, respectively. The electron-hole concentration (p) was estimated using equation (4.40)**.** The mobility of electron holes ($u_{h^\bullet}$) was calculated using equation:

$$u_{h^\bullet} = \frac{\sigma}{p \cdot e}, \tag{5.25}$$

where e denotes the elementary charge. In oxidising atmospheres, the total conductivity of the SFC materials is primarily electronic, as the oxygen-ionic conductivity is at least two

orders of magnitude lower and can be considered negligible.[124,125,238–240] Hence, the total conductivity effectively reflects the partial conductivity corresponding to electron holes with good approximation and the mobility values, calculated from equation (5.25), represent the transport of electronic charge carriers.

As can be seen in **Figure 5.25**, the Seebeck coefficient increases with temperature, displaying a plateau at the lowest temperatures. This behaviour is consistent with earlier reports on both undoped and cobalt-substituted $SrFeO_{3-\delta}$.[157,241] Moreover, increasing cobalt content leads to a gradual decrease in the Seebeck coefficient. The values of this parameter for strontium ferrate correspond well to the values obtained for the same material by Hombo et al.[110]

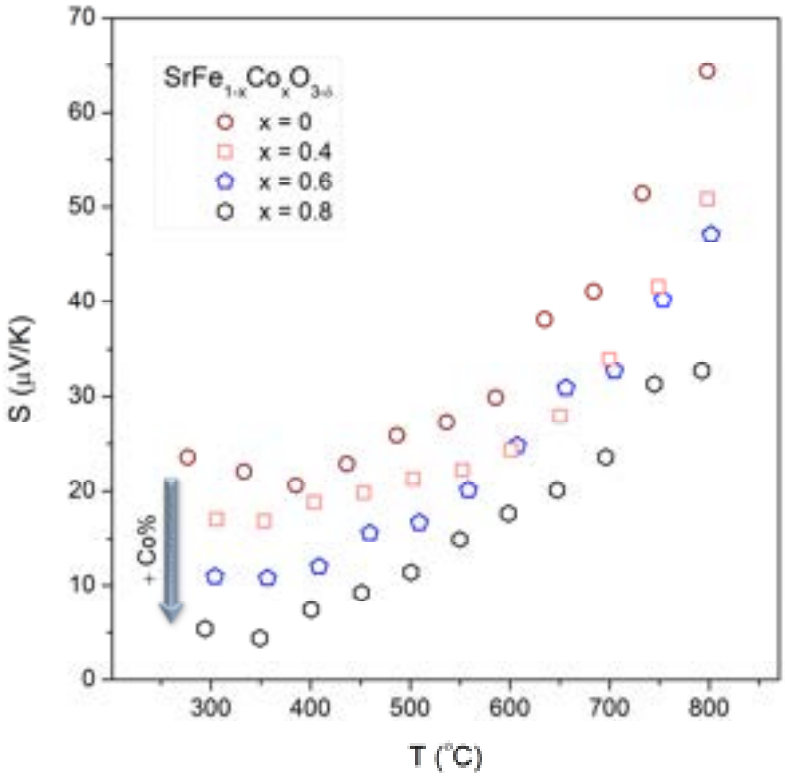

Figure 5.25. The Seebeck coefficient of $SrFe_{1-x}Co_xO_{3-\delta}$ (x = 0, 0.4, 0.6, 0.8) as a function of temperature, measured in dry air.

Adapted from Jagoda Budnik, Maria Gazda, Tadeusz Miruszewski, "Electrical and thermoelectric transport of $SrFe_{1-x}Co_xO_{3-\delta}$ mixed-conducting perovskites", Solid State Sciences, 2026, 173, 108174. Copyright © 2026 Elsevier.[225]

Figure 5.26 presents the electron-hole concentration as a function of temperature. To reflect the possible influence of vibrational entropy on the Seebeck coefficient (eq. (4.39)), error bars were introduced to all data points. Their lower limit corresponds to the value obtained directly from the simplified Heikes formula without the vibrational contribution (eq. (4.40)). The upper limit includes the additional term of about 10 μV/K, following the estimate proposed by Goodenough.[160] In this way, the range of values shown in the figure incorporates the potential effect of vibrational entropy in the examined materials.

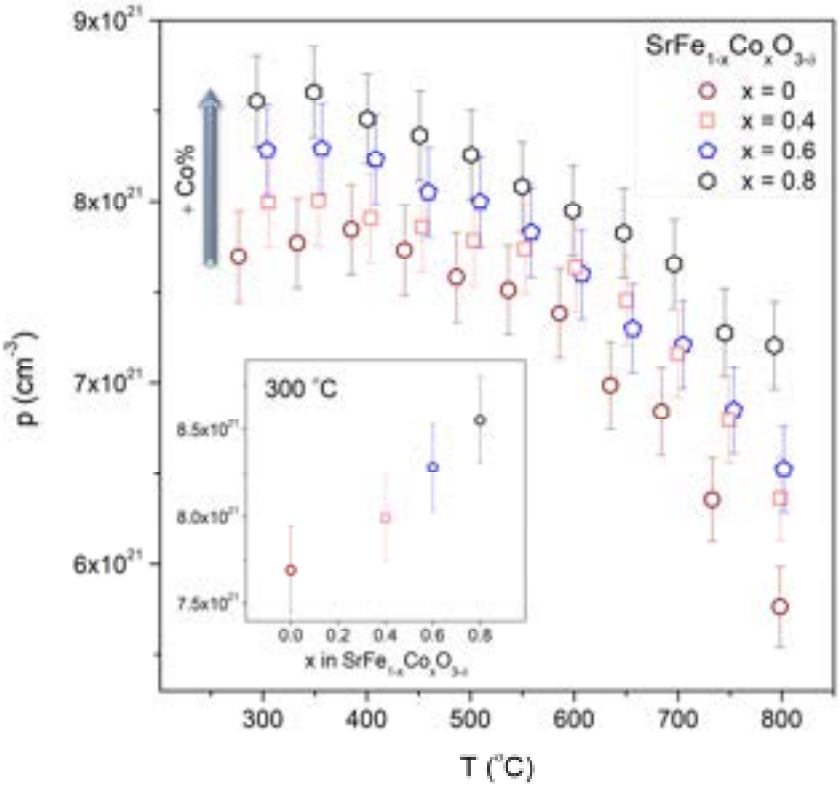

Figure 5.26. The electron-hole concentration as a function of temperature for $SrFe_{1-x}Co_xO_{3-\delta}$ (x = 0, 0.4, 0.6, 0.8). The electron-hole concentration at 300 °C as a function of cobalt content is shown in the inset.

Adapted from Jagoda Budnik, Maria Gazda, Tadeusz Miruszewski, "Electrical and thermoelectric transport of $SrFe_{1-x}Co_xO_{3-\delta}$ mixed-conducting perovskites", Solid State Sciences, 2026, 173, 108174. Copyright © 2026 Elsevier.[225]

For all compositions, p is relatively constant below approximately 400 °C and begins to decrease above this temperature, due to the thermal reduction and oxygen-vacancy concentration increase. This process leads to a lower electron-hole concentration, contributing to the electrical conductivity decrease observed in **Figure 5.24**, which was also observed in the literature reports.[110] The obtained concentrations of holes are lower than those reported for $SrFeO_{3-\delta}$ by Hombo et al.[110] However, the oxygen nonstoichiometry determined in their work was significantly lower than the values obtained in this study. This further suggests that the lower electrical conductivity in comparison to literature reports may originate from the materials being initially reduced at room temperature, with additional reduction likely occurring at higher temperatures. The inset in **Figure 5.26** reveals a linear correlation between the electron-hole concentration and cobalt content in $SrFe_{1-x}Co_xO_{3-\delta}$ at 300 °C. However, the increase in p does not directly correspond to conductivity trends in **Figure 5.24**. This indicates that the charge-carrier mobility might be the dominant factor governing the observed conductivity maxima in $SrFe_{1-x}Co_xO_{3-\delta}$ (x = 0, 0.4, 0.6, 0.8).

Based on the electrical conductivity data and electron-hole concentration derived from the thermoelectric data, the impact of cobalt content in the $SrFe_{1-x}Co_xO_{3-\delta}$ series on the mobility of electron holes was assessed (**Figure 5.27**). The calculated electron-hole

mobilities fall in the range of 10^{-2} to 10^{-1} cm²/V·s, which is in agreement with the mobility data reported for cobaltite-ferrite perovskites exhibiting small-polaron conduction.[111,162]

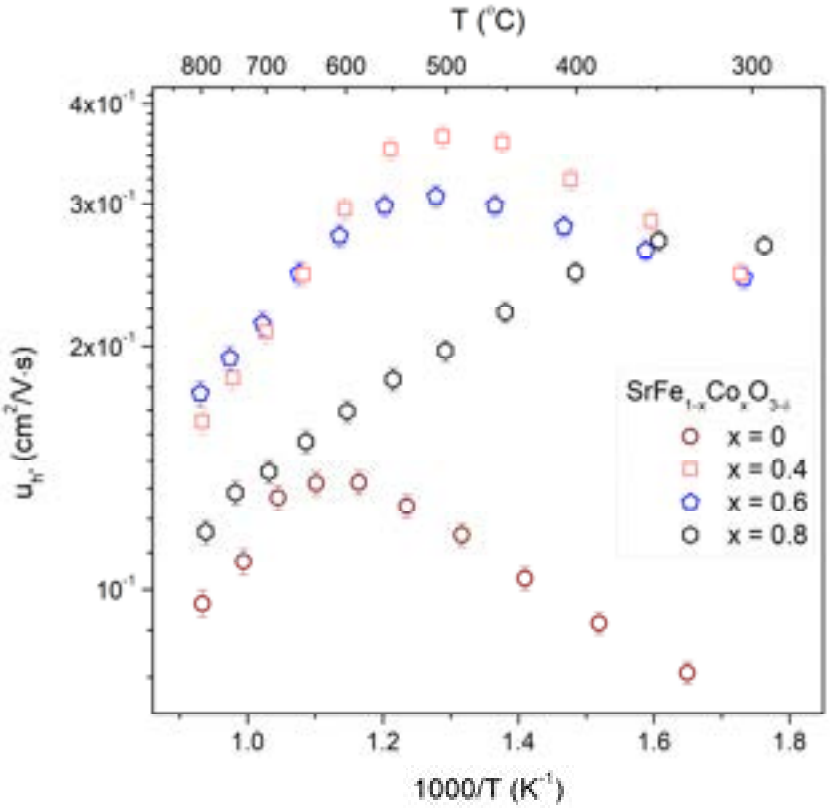

Figure 5.27. The mobility of electron holes as a function of inverted temperature for $SrFe_{1-x}Co_xO_{3-\delta}$ (x = 0, 0.4, 0.6, 0.8).

Adapted from Jagoda Budnik, Maria Gazda, Tadeusz Miruszewski, "Electrical and thermoelectric transport of $SrFe_{1-x}Co_xO_{3-\delta}$ mixed-conducting perovskites", Solid State Sciences, 2026, 173, 108174. Copyright © 2026 Elsevier.[225]

The electron-hole mobility maxima agree with the temperatures of maximum conductivity for each composition, suggesting that the drop of electrical conductivity above T_{max} is caused primarily by the reduced mobility of electronic charge carriers rather than decreased carrier concentration. The lowered mobility of electronic charge carriers may result from diminished TM $3d$ – O $2p$ orbital overlap caused by reduction-induced structural changes.

The small-polaron mobility, above half the Debye temperature, can be expressed as:[242]

$$u_h \cdot T = u_0 \, exp\left(\frac{-E_m}{k_B T}\right), \tag{5.26}$$

where E_m represents the activation energy of the carrier mobility and u_o is a pre-exponential factor.[48] **Table 5.11** includes the values of E_m derived from the data in the temperature ranges associated with the thermally activated conduction of electron holes. The values of E_m decrease with rising cobalt content and closely match the E_a values, suggesting that E_a mainly reflects the energy for carrier migration rather than their formation. This interpretation is consistent with the observed temperature-dependent decrease in electron-hole

concentration, indicating that the thermally induced excitation of holes is negligible compared to the effect of thermal reduction.

The mobility data for oxygen ions are rarely available. Nonetheless, the Nernst-Einstein relation can be employed along with the oxygen self-diffusion coefficient ($\approx 10^{-6}$ cm^2/V·s at 800 °C)[243] to calculate the mobility of oxygen ions. The resulting oxygen-ion mobility is approximately 10^{-5} cm^2/V·s. This value is around three orders of magnitude lower than the mobility of small polarons. Consequently, the contribution of oxygen ions to the total electrical conductivity can be considered negligible and the total electrical conductivity reflects primarily the behaviour of electronic carriers.

In summary, all $SrFe_{1-x}Co_xO_{3-\delta}$ (x = 0, 0.4, 0.6, 0.8) materials exhibited p-type conduction via a small-polaron hopping mechanism. The highest conductivity was recorded for $SrFe_{0.6}Co_{0.4}O_{3-\delta}$, while $SrFeO_{3-\delta}$ showed significantly lower conductivity values. At elevated temperatures, the total electrical conductivity decreased due to the thermal reduction. The activation energies for conduction decreased with increasing cobalt content. Seebeck coefficient measurements provided information about the electron-hole concentration, confirming that the observed conductivity trends were primarily governed by the changes in carrier mobility. The use of NiO as a sintering aid, as well as the high oxygen nonstoichiometry observed in the studied samples, likely contributed to the lower conductivity values relative to literature data.

5.2.4. Influence of water

The transport properties of mixed ionic-electronic conductors depend on the surrounding atmosphere. However, the influence of water vapour on the MIEC oxides that do not exhibit water uptake (or the effect is negligible) has not been thoroughly investigated. In this work, the influence of water vapour on the transport properties of $SrFe_{0.6}Co_{0.4}O_{3-\delta}$ as a representative of the $SrFe_{1-x}Co_xO_{3-\delta}$ (x = 0, 0.2, 0.4, 0.6, 0.8) series was studied. The electrical and thermoelectric measurements, as well as the oxidation/reduction experiments using the ECR method, were conducted in dry and wet conditions.

Figure 5.28 presents the temperature dependencies of chemical surface exchange and chemical diffusion coefficients of oxygen determined for the oxidation and reduction of $SrFe_{0.6}Co_{0.4}O_{3-\delta}$ in dry and wet conditions. The chemical surface exchange coefficients for oxidation are higher than for reduction, regardless of the presence of water vapour. However, the values of k_{chem} in humidified atmospheres are lower than those obtained in dry gases. This shows the detrimental effect of water vapour on the rates of oxygen-related reactions occurring at the material surface. The lower values of k_{chem} during the oxidation

step in wet conditions may be related to a lower number of available adsorption sites. The adsorbed water on the surface of the material prevents the adsorption and the dissociation of oxygen molecules, restricting incorporation of oxygen ions into the crystal lattice. Similarly, during the reduction step in wet atmospheres, the adsorbed water molecules hinder the surface exchange process, limiting the release of oxygen from the material to the surrounding low-p_{O_2} environment. On the other hand, the chemical diffusion coefficients determined for the oxidation step are higher in wet than in dry conditions. This suggests that water enhances the oxygen-ionic transport in the material.

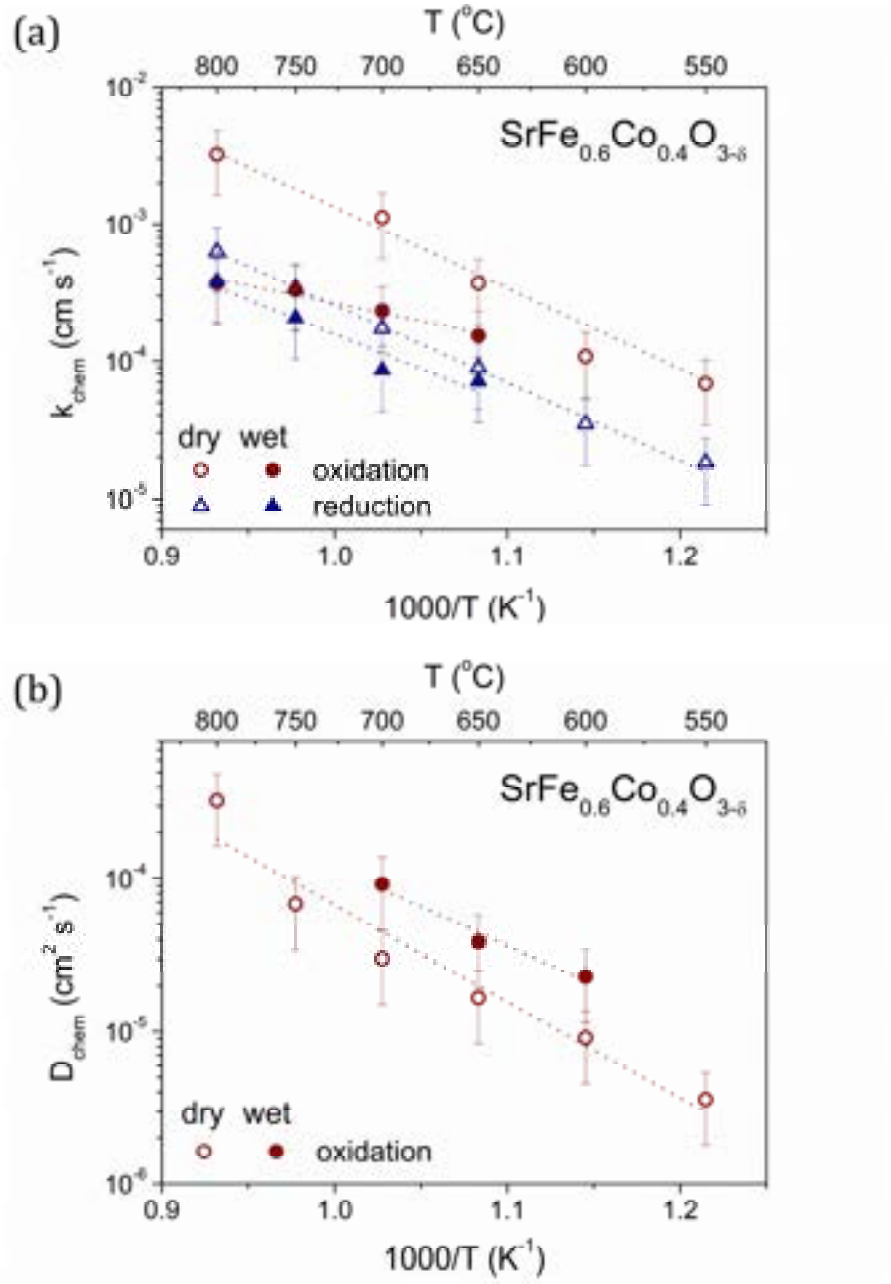

Figure 5.28. The parameters obtained from the ECR data collected for the oxidation and reduction of $SrFe_{0.6}Co_{0.4}O_{3-\delta}$ in dry and wet conditions: chemical surface exchange coefficients (a) and chemical diffusion coefficients (b).

The activation energies of surface exchange and diffusion of oxygen are presented in **Table 5.12**. The activation energies for both processes during the oxidation decreased in wet conditions. This effect is the most pronounced in the case of the surface exchange recorded during oxidation, where it changes form (1.17 ± 0.10) eV to (0.51 ± 0.07) eV in dry and wet conditions, respectively.

Table 5.12. The activation energies of surface exchange and diffusion of oxygen corresponding to oxidation and reduction of $SrFe_{0.6}Co_{0.4}O_{3-\delta}$ in dry and wet conditions.

		Activation energy (eV)	
		Dry	Wet
Surface exchange	Oxidation	1.17 ± 0.10 (550 − 800 °C)	0.51 ± 0.07 (650 − 800 °C)
	Reduction	1.12 ± 0.03 (550 − 800 °C)	1.00 ± 0.19 (650 − 800 °C)
Diffusion	Oxidation	1.25 ± 0.15 (550 − 800 °C)	$\approx 1.00 \pm 0.18$ (600 − 700 °C)

The temperature dependencies of the Seebeck coefficient and total electrical conductivity of $SrFe_{0.6}Co_{0.4}O_{3-\delta}$ measured in dry and wet air are presented in **Figure 5.29a** and **b**. The temperature dependencies of the Seebeck coefficient follow the same trend for dry and wet air, but below 650 °C the values of *S* in wet air start to be lower than that in dry air. The difference between them increases with decreasing temperature.

The total electrical conductivity in wet air exhibits a similar tendency to that observed in dry air. In both cases, electrical conductivity increases in the low-temperature region, indicating a thermally activated small-polaron hopping mechanism. Above a certain temperature, the conductivity gradually decreases with further temperature increase. Regardless of similar temperature dependencies, the values observed in dry and wet air differ. The conductivity of $SrFe_{0.6}Co_{0.4}O_{3-\delta}$ recorded in wet air is lower than that in the dry air in the whole temperature range. The maximum electrical conductivity in dry and wet air are 168 S/cm and 120 S/cm, respectively. The most significant differences are observed at the lowest temperatures, specifically below the temperature corresponding to the conductivity maximum (T_{max}), with differences becoming systematically lower as the temperature increases.

Figure 5.29c shows the temperature dependence of electron-hole concentrations in $SrFe_{0.6}Co_{0.4}O_{3-\delta}$ in dry and wet air. Below 650 °C the concentrations in wet air are higher, while above that temperature, they are slightly lower. The observed increase in the concentration of electron holes in the wet atmosphere could be associated with oxidation, due to the water vapour influencing the oxidation enthalpy

of the material.[172,244] It could be also responsible for the enhanced oxygen diffusion in humidified atmospheres, observed in the ECR data (see **Figure 5.28b**).

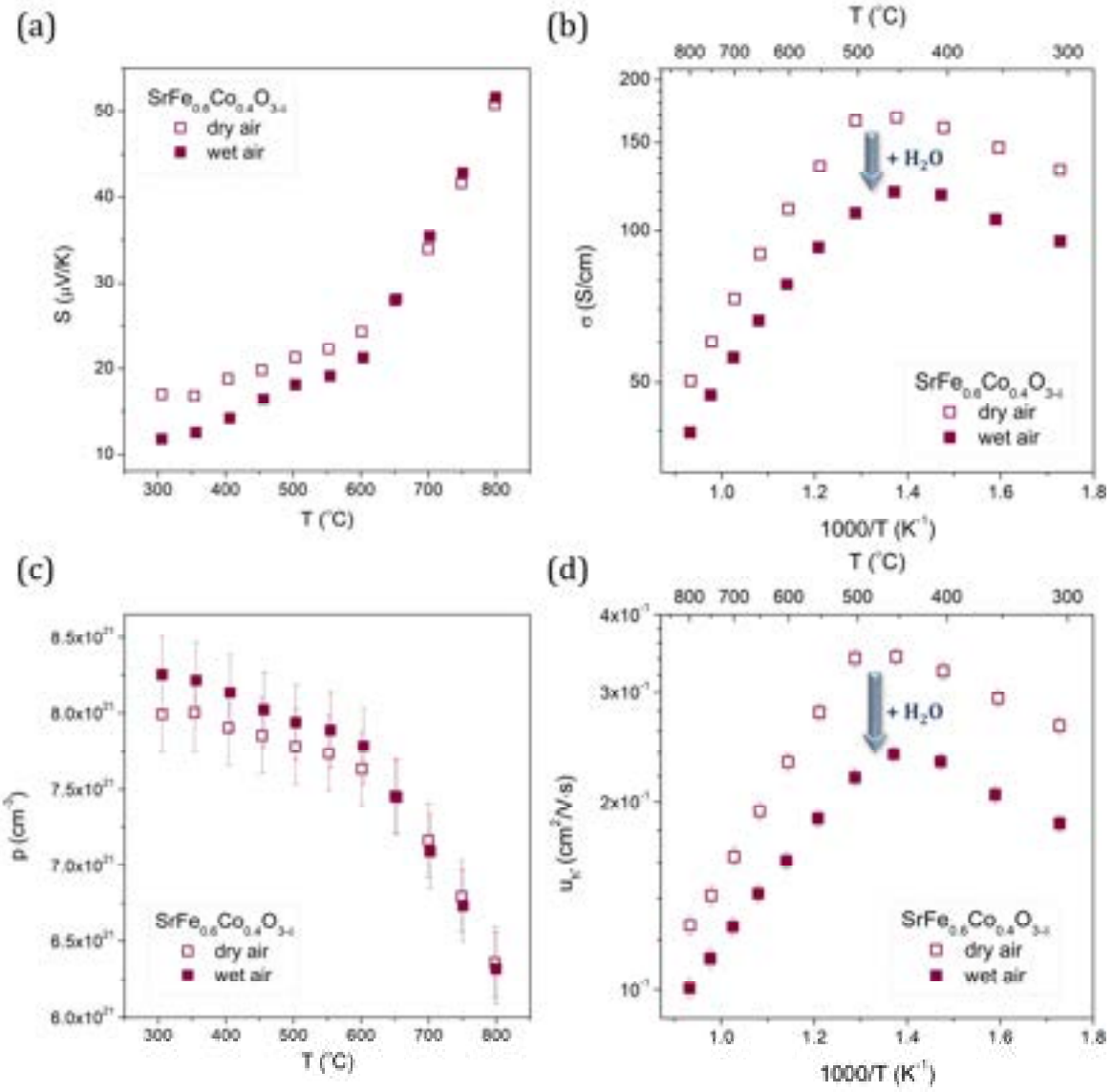

Figure 5.29. The temperature dependencies of the Seebeck coefficient (a), total electrical conductivity (b), electron-hole concentration (c), and mobility of electron holes (d) of $SrFe_{0.6}Co_{0.4}O_{3-\delta}$ in dry and wet air.

Figure 5.29d presents the temperature dependence of electron-hole mobility in $SrFe_{0.6}Co_{0.4}O_{3-\delta}$ in dry and wet air, which follows a similar trend to that observed for total conductivity. The values of electron-hole mobilities increase with increasing temperature in the low-temperature region, signifying the thermally activated conduction mechanism of electronic charge carriers, and decline after reaching T_{max}. The mobility values in a wet atmosphere fall below those determined for a dry atmosphere, with the difference between them being the most pronounced below T_{max}. These results support the previously proposed hypothesis that the decrease in the electron-hole mobilities is predominantly responsible for the reduction of electrical conductivity of $SrFe_{0.6}Co_{0.4}O_{3-\delta}$ in the presence of water vapour. The change in the mobilities of electron holes caused by the presence of proton defects may

suggest some reduction in the crystal symmetry, weakening the TM 3*d* − O 2*p* orbitals overlap. The deformation of the unit cell due to the presence of protons was also reported by Hoedl et al. for $BaFeO_{3-\delta}$.[245] These structural changes could also be responsible for the observed enhancement of the chemical diffusion of oxygen. This would be consistent with the observation made for the BCZYM material group, where the highest mobilities of ionic charge carriers were observed in the materials exhibiting an orthorhombic crystal structure.

In summary, the influence of water vapour on the transport properties of $SrFe_{0.6}Co_{0.4}O_{3-\delta}$ was investigated. The chemical surface exchange coefficients for both oxidation and reduction decreased in the wet conditions, suggesting a limiting effect of water vapour on the surface reactions involving oxygen. In contrast, the chemical diffusion coefficients for oxidation increased in wet conditions, indicating enhanced oxygen transport in the bulk of the material. The total electrical conductivity in wet air was lower than that in dry air across the entire temperature range. This was primarily attributed to a decrease in electron-hole mobility. The reduced values of electron-hole mobilities in water vapour suggest a possible distortion of the crystal structure due to the presence of proton defects. These structural changes may also be responsible for the increased chemical diffusion coefficient of oxygen.

Conclusions

This dissertation presents studies of defect chemistry, structure, and charge-transport properties of two groups of mixed-conducting perovskite oxides, $BaCe_{0.6}Zr_{0.2}Y_{0.2-x}M_xO_{3-\delta}$ (BCZYM) and $SrFe_{1-x}Co_xO_{3-\delta}$ (SFC). The aim of this study was to understand how chemical composition, water uptake, and local structural changes influence the mobility and concentration of charge carriers. This work enabled a direct evaluation of the formulated theses and provided an interpretation of how oxygen vacancies, proton defects, and electronic carriers interact within these materials.

Firstly, the possibility of improving transport properties of BCZYM by substituting yttrium with mixed-valence elements, i.e. terbium, praseodymium and iron, was explored. The results demonstrated that such enhancement can be achieved, but it is strongly dependent on the specific substituent, which can affect both electronic and ionic transport. The substitution of terbium led to the highest total electrical conductivity, reaching 2.4×10^{-3} S/cm at 400 °C, and the lowest activation energies for conduction in wet air. It also increased the partial electronic conductivity in comparison to the reference material BCZY622. Terbium also increased proton mobility to 1.4×10^{-5} $cm^2/V{\cdot}s$ at 300 °C and oxygen-vacancy mobility to 6.9×10^{-6} $cm^2/V{\cdot}s$ at 600 °C, surpassing the mobility values obtained for BCZY622. Praseodymium substitution moderately improved the mobilities of oxygen vacancies and protons relative to BCZY622, while significantly reducing water uptake. Iron substitution decreased the mobility of both ionic carriers and limited water uptake. Both Pr and Fe substitution decreased the partial electronic conductivity. Therefore, only the substitution of Tb increased electronic partial conductivity, while also enhancing oxygen-vacancy and proton mobility, supporting the idea that mixed-valence cations can facilitate transport properties even beyond electronic charge carriers. The proton concentration in BCZYM materials correlated directly with the oxygen-vacancy concentration, confirming that proton incorporation occurs via hydration reaction. It also depended on the electronegativities of the cations. Concluding, all of these observations highlight the importance of the proper choice of substituent, rather than its mixed-valency alone, for achieving desired electrical properties.

The second group of materials, $SrFe_{1-x}Co_xO_{3-\delta}$, was investigated to analyse whether cobalt substitution stabilises oxygen vacancies while preserving the high symmetry of the crystal lattice. The pseudocubic lattice parameters of SFC ranged from 3.871 Å for $SrFeO_{3-\delta}$ to 3.878 Å for $SrFe_{0.2}Co_{0.8}O_{3-\delta}$, reflecting the influence of cobalt on lattice expansion. The results confirmed that Co increase the concentration of oxygen vacancies and also served as a stabilising centre for these species. The transport behaviour of electron

holes in SFC was found to be controlled mainly by changes in mobility rather than by carrier concentration. $SrFe_{0.6}Co_{0.4}O_{3-\delta}$ exhibited the highest electrical conductivity in dry air across the studied SFC compositions, reaching a maximum of 177 S/cm at 500 °C.

The role of proton defects in bulk and surface ionic transport in both material groups was investigated. In $BaCe_{0.6}Zr_{0.2}Y_{0.2-x}M_xO_{3-\delta}$, hydration had a pronounced effect: proton incorporation not only enabled proton conduction but also enhanced oxygen transport by reducing the activation energies for oxygen surface exchange and increasing the oxygen diffusion coefficients during oxidation. This demonstrated that interactions between protons and oxygen vacancies can significantly influence the mobility of oxygen vacancies and the overall oxidation kinetics in mixed ionic-electronic conductors. Moreover, although $SrFe_{0.6}Co_{0.4}O_{3-\delta}$ incorporates only small amounts of protons, water vapour still affected the transport behaviour in this material, lowering the mobility of electron holes and modifying surface oxygen exchange rates. For instance, the activation energy for chemical surface exchange during oxidation decreased from 1.17 eV in dry to 0.51 eV in wet conditions. In conclusion, across both material groups, water vapour played a significant role in transport properties. In $BaCe_{0.6}Zr_{0.2}Y_{0.2-x}M_xO_{3-\delta}$, the presence of proton defects enhanced oxygen diffusion. In SFC, even small amounts of protons influenced electron-hole mobility and oxygen diffusion, indicating that protons can impact electrical transport properties beyond protonic conduction. Concluding, proton defects play a broader role than commonly assumed, affecting not only protonic but also oxygen-ionic and electronic transport.

The results presented in this dissertation also confirmed the effectiveness of NiO as a sintering aid. Nickel oxide enabled the obtaining of dense, phase-pure ceramics in only two steps of solid-state synthesis. In SFC, the presence of NiO was likely responsible for a significant decrease in electrical conductivity, indicating that the addition of sintering aid interfered with the transport process of SFC materials. However, despite relatively high oxygen nonstoichiometry levels, it did not prevent the formation of high-symmetry perovskite phases.

The results presented in this dissertation confirm the formulated theses pointing to the correlations between composition, proton uptake, and charge transport in both BCZYM and SFC materials: mixed-valence substitutions in $BaCe_{0.6}Zr_{0.2}Y_{0.2-x}M_xO_{3-\delta}$ improve electronic and ionic transport when chosen appropriately; cobalt stabilises oxygen vacancies in $SrFe_{1-x}Co_xO_{3-\delta}$ without reducing lattice symmetry; NiO facilitates synthesis of dense, single-phase materials; and proton defects influence the transport of other charge carriers. Moreover, the mobility of charge carriers, rather than their absolute concentration, is often the decisive factor governing electrical conductivity in these materials. The findings obtained in this work contribute to the deeper understanding of mixed ionic-electronic perovskite oxides.

In summary, this work explored the charge-transport mechanisms in perovskite ceramics by investigating how specific substituents and water vapour influence the concentration and mobilities of oxygen vacancies, proton defects, and electronic carriers.

This dissertation was based on the research supported by the National Science Centre Poland under grant number 2021/41/N/ST5/03437.

Literature

(1) Samsudin, A. M.; Bodner, M.; Hacker, V. A Brief Review of Poly(Vinyl Alcohol)-Based Anion Exchange Membranes for Alkaline Fuel Cells. *Polymers*. MDPI September 1, **2022**. https://doi.org/10.3390/polym14173565.

(2) Zhang, W.; Zhang, X.; Song, Y.; Wang, G. Recent Progress on Cathode Materials for Protonic Ceramic Fuel Cells. *Next Sustainability* **2024**, *3*, 100028. https://doi.org/10.1016/j.nxsust.2024.100028.

(3) Bae, K.; Jang, D. Y.; Choi, H. J.; Kim, D.; Hong, J.; Kim, B. K.; Lee, J. H.; Son, J. W.; Shim, J. H. Demonstrating the Potential of Yttrium-Doped Barium Zirconate Electrolyte for High-Performance Fuel Cells. *Nat. Commun.* **2017**, *8*. https://doi.org/10.1038/ncomms14553.

(4) Coors, W. G. Protonic Ceramic Fuel Cells for High-Efficiency Operation with Methane. In *Journal of Power Sources*; **2003**; Vol. 118, pp 150–156. https://doi.org/10.1016/S0378-7753(03)00072-7.

(5) Duan, C.; Huang, J.; Sullivan, N.; O'Hayre, R. Proton-Conducting Oxides for Energy Conversion and Storage. *Appl. Phys. Rev.* **2020**, *7* (1), 1–40. https://doi.org/10.1063/1.5135319.

(6) Nasani, N.; Dias, P. A. N.; Saraiva, J. A.; Fagg, D. P. Synthesis and Conductivity of $Ba(Ce,Zr,Y)O_{3-\delta}$ Electrolytes for PCFCs by New Nitrate-Free Combustion Method. *Int. J. Hydrogen Energy* **2013**, *38* (20), 8461–8470. https://doi.org/10.1016/j.ijhydene.2013.04.078.

(7) Duan, C.; Kee, R.; Zhu, H.; Sullivan, N.; Zhu, L.; Bian, L.; Jennings, D.; O'Hayre, R. Highly Efficient Reversible Protonic Ceramic Electrochemical Cells for Power Generation and Fuel Production. *Nat. Energy* **2019**, *4* (3), 230–240. https://doi.org/10.1038/s41560-019-0333-2.

(8) Ranran, P.; Yan, W.; Lizhai, Y.; Zongqiang, M. Electrochemical Properties of Intermediate-Temperature SOFCs Based on Proton Conducting Sm-Doped $BaCeO_3$ Electrolyte Thin Film. *Solid State Ion.* **2006**, *177* (3–4), 389–393. https://doi.org/10.1016/j.ssi.2005.11.020.

(9) Choi, S.; Kucharczyk, C. J.; Liang, Y.; Zhang, X.; Takeuchi, I.; Ji, H. il; Haile, S. M. Exceptional Power Density and Stability at Intermediate Temperatures in Protonic Ceramic Fuel Cells. *Nat. Energy* **2018**, *3* (3), 202–210. https://doi.org/10.1038/s41560-017-0085-9.

(10) Reihaneh Zohourian Aboutorabi. Mixed-Conducting Perovskites as Cathodes in Protonic Ceramic Fuel Cells: Defect Chemistry and Transport Properties. *Universität Stuttgart* **2018**, 78–80.

(11) Risch, M. Perovskite Electrocatalysts for the Oxygen Reduction Reaction in Alkaline Media. *Catalysts* **2017**, *7* (5), 154. https://doi.org/10.3390/catal7050154.

(12) Qian, Y.; Ruan, Q.; Xue, M.; Chen, L. Emerging Perovskite Materials for Supercapacitors: Structure, Synthesis, Modification, Advanced Characterization, Theoretical Calculation and Electrochemical Performance. *Journal of Energy Chemistry* **2024**, *89*, 41–70. https://doi.org/10.1016/J.JECHEM.2023.10.028.

(13) Park, H.; Ha, C.; Lee, J. H. Advances in Piezoelectric Halide Perovskites for Energy Harvesting Applications. *J. Mater. Chem. A Mater.* **2020**, *8* (46), 24353–24367. https://doi.org/10.1039/D0TA08780G.

(14) Cao, J.; Ji, Y.; Shao, Z. Perovskites for Protonic Ceramic Fuel Cells: A Review. *Energy Environ. Sci.* **2022**, *15* (6), 2200–2232. https://doi.org/10.1039/D2EE00132B.

(15) Richter, J.; Holtappels, P.; Graule, T.; Nakamura, T.; Gauckler, L. J. Materials Design for Perovskite SOFC Cathodes. *Monatsh. Chem.* **2009**, *140* (9), 985–999. https://doi.org/10.1007/s00706-009-0153-3.

(16) Brittman, S.; Adhyaksa, G. W. P.; Garnett, E. C. The Expanding World of Hybrid Perovskites: Materials Properties and Emerging Applications. *MRS Commun.* **2015**, *5* (1), 7. https://doi.org/10.1557/MRC.2015.6.

(17) Tao, Q.; Xu, P.; Li, M.; Lu, W. Machine Learning for Perovskite Materials Design and Discovery. *npj Computational Materials 2021 7:1* **2021**, *7* (1), 1–18. https://doi.org/10.1038/s41524-021-00495-8.

(18) Alhashmi, A.; Kanoun, M. B.; Goumri-Said, S. Machine Learning for Halide Perovskite Materials ABX_3 (B = Pb, X = I, Br, Cl) Assessment of Structural Properties and Band Gap Engineering for Solar Energy. *Materials* **2023**, *16* (7), 2657. https://doi.org/10.3390/ma16072657.

(19) George, G.; Rao Ede, S.; Luo, Z. *Fundamentals of Perovskite Oxides; Synthesis, Structure, Properties and Applications*; CRC Press, **2021**.

(20) Bhalla, A. S.; Guo, R.; Roy, R. The Perovskite Structure — a Review of Its Role in Ceramic Science and Technology. *Materials Research Innovations* **2000**, *4* (1), 3–26. https://doi.org/10.1007/s100190000062.

(21) Aïssa, B.; Ali, A.; El-Mellouhi, F. Oxide and Organic–Inorganic Halide Perovskites with Plasmonics for Optoelectronic and Energy Applications: A Contributive Review. *Catalysts* **2021**, *11* (9), 1057. https://doi.org/10.3390/catal11091057.

(22) Goldschmidt, V. M. Die Gesetze Der Krystallochemie. *Naturwissenschaften* **1926**, *14*, 477–485. https://doi.org/10.1177/089686089501500104.

(23) Labhasetwar, N.; Saravanan, G.; Kumar Megarajan, S.; Manwar, N.; Khobragade, R.; Doggali, P.; Grasset, F. Perovskite-Type Catalytic Materials for Environmental Applications. *Sci. Technol. Adv. Mater.* **2015**, *16* (3), 1–13. https://doi.org/10.1088/1468-6996/16/3/036002.

(24) Chakraborty, T.; Yadav, R.; Elizabeth, S.; Bhat, H. L. Evolution of Jahn–Teller Distortion, Transport and Dielectric Properties with Doping in Perovskite $NdFe_{1-x}Mn_xO_3$ ($0 \le x \le 1$) Compounds. *Physical Chemistry Chemical Physics* **2016**, *18* (7), 5316–5323. https://doi.org/10.1039/C5CP07083J.

(25) Varignon, J.; Bibes, M.; Zunger, A. Origins versus Fingerprints of the Jahn-Teller Effect in d-Electron ABX_3 Perovskites. *Phys. Rev. Res.* **2019**, *1* (3), 033131. https://doi.org/10.1103/PhysRevResearch.1.033131.

(26) Ortiz-Vitoriano, N.; Ruiz de Larramendi, I.; Gil de Muro, I.; Larrañaga, A.; Ruiz de Larramendi, J. I.; Rojo, T. A Novel One Step Synthesized Co-Free Perovskite/Brownmillerite Nanocomposite for Solid Oxide Fuel Cells. *J. Mater. Chem.* **2011**, *21* (26), 9682. https://doi.org/10.1039/c1jm10911a.

(27) Fuller, C. A.; Berrod, Q.; Frick, B.; Johnson, M. R.; Clark, S. J.; Evans, J. S. O.; Evans, I. R. Brownmillerite-Type Sr_2ScGaO_5 Oxide Ion Conductor: Local Structure, Phase Transition, and Dynamics. *Chemistry of Materials* **2019**, *31* (18), 7395–7404. https://doi.org/10.1021/acs.chemmater.9b02051.

(28) Singh, A. K.; Kumar, A.; Singh, B. P. A Review on the Magnetic Behaviour of Ni and Mn Based Double Perovskites. *Prabha Materials Science Letters* **2024**, *3* (2), 218–241. https://doi.org/10.33889//PMSL.2024.3.2.014.

(29) Obada, D. O.; Akinpelu, S. B.; Abolade, S. A.; Okafor, E.; Ukpong, A. M.; Kumar R, S.; Akande, A. Lead-Free Double Perovskites: A Review of the Structural, Optoelectronic, Mechanical, and Thermoelectric Properties Derived from First-Principles Calculations, and Materials Design Applicable for Pedagogical Purposes. *Crystals (Basel).* **2024**, *14* (1), 86. https://doi.org/10.3390/cryst14010086.

(30) Kumar, V.; Kathiravan, A.; Jhonsi, M. A. Beyond Lead Halide Perovskites: Crystal Structure, Bandgaps, Photovoltaic Properties and Future Stance of Lead-Free Halide Double Perovskites. *Nano Energy* **2024**, *125*, 109523. https://doi.org/10.1016/j.nanoen.2024.109523.

(31) Banerjee, A.; Awasthi, M. K.; Maji, P.; Pal, M.; Aziz, S. T.; Lahiri, G. K.; Dutta, A. Double Perovskite Oxides Bringing a Revelation in Oxygen Evolution Reaction Electrocatalyst Design. *ChemElectroChem* **2023**, *10* (4). https://doi.org/10.1002/celc.202201098.

(32) Momma, K.; Izumi, F. *VESTA 3* for Three-Dimensional Visualization of Crystal, Volumetric and Morphology Data. *J. Appl. Crystallogr.* **2011**, *44* (6), 1272–1276. https://doi.org/10.1107/S0021889811038970.

(33) Brittman, S.; Adhyaksa, G. W. P.; Garnett, E. C. The Expanding World of Hybrid Perovskites: Materials Properties and Emerging Applications. *MRS Commun.* **2015**, *5* (1), 7–26. https://doi.org/10.1557/mrc.2015.6.

(34) Schmitt, R.; Nenning, A.; Kraynis, O.; Korobko, R.; Frenkel, A. I.; Lubomirsky, I.; Haile, S. M.; Rupp, J. L. M. A Review of Defect Structure and Chemistry in Ceria and Its Solid Solutions. *Chem. Soc. Rev.* **2020**, *49* (2), 554–592. https://doi.org/10.1039/C9CS00588A.

(35) Browning, N. D.; Klie, R. F.; Lei, Y. Vacancy Segregation at Grain Boundaries in Ceramic Oxides. In *Mixed Ionic Electronic Conducting Perovskites for Advanced Energy Systems*; Springer Netherlands: Dordrecht, **2004**; Vol. PV 2003-29, pp 15–25. https://doi.org/10.1007/978-1-4020-2349-1_2.

(36) Evans, D. M.; Holstad, T. S.; Mosberg, A. B.; Småbråten, D. R.; Vullum, P. E.; Dadlani, A. L.; Shapovalov, K.; Yan, Z.; Bourret, E.; Gao, D.; Akola, J.; Torgersen, J.; van Helvoort, A. T. J.; Selbach, S. M.; Meier, D. Conductivity Control via Minimally Invasive Anti-Frenkel Defects in a Functional Oxide. *Nat. Mater.* **2020**, *19* (11), 1195–1200. https://doi.org/10.1038/s41563-020-0765-x.

(37) Smith, T.; Moxon, S.; Tse, J. S.; Skelton, J. M.; Cooke, D. J.; Gillie, L. J.; da Silva, E. L.; Harker, R. M.; Storr, M. T.; Parker, S. C.; Molinari, M. Structural Dynamics of Schottky and Frenkel Defects in CeO_2: A Density-Functional Theory Study. *Journal of Physics: Energy* **2023**, *5* (2), 025004. https://doi.org/10.1088/2515-7655/acbb29.

(38) Mahmoud, S.; Carrez, P.; Landeiro Dos Reis, M.; Mousseau, N.; Cordier, P. Diffusion Mechanism of Bound Schottky Defect in Magnesium Oxide. *Phys. Rev. Mater.* **2021**, *5* (3), 033609. https://doi.org/10.1103/PhysRevMaterials.5.033609.

(39) Hamed Mashhadzadeh, A.; Salmankhani, A.; Zarghami Dehghani, M.; Spitas, C.; Saeb, M. R. Influence of Defects upon Mechanical Properties of Oxide Materials. In *Metal Oxide Defects*; Elsevier, **2023**; pp 253–280. https://doi.org/10.1016/B978-0-323-85588-4.00017-9.

(40) Mabuchi, T. Revealing the Anticorrelation Behavior Mechanism between the Grotthuss and Vehicular Diffusions for Proton Transport in Concentrated Acid Solutions. *J. Phys. Chem. B* **2022**, *126* (17), 3319–3326. https://doi.org/10.1021/acs.jpcb.1c09742.

(41) Kreuer, K.-D.; Dippel, T.; Meyer, W.; Maier, J. Nafion ® Membranes: Molecular Diffusion, Proton Conductivity and Proton Conduction Mechanism. *MRS Proceedings* **1992**, *293* (1), 273. https://doi.org/10.1557/PROC-293-273.

(42) Agmon, N. The Grotthuss Mechanism. *Chem. Phys. Lett.* **1995**, *244* (5–6), 456–462. https://doi.org/10.1016/0009-2614(95)00905-J.

(43) Münch, W.; Kreuer, K. D.; Adams; Seifert, G.; Maier, J. The Relation between Crystal Structure and the Formation and Mobility of Protonic Charge Carriers in Perovskite-Type Oxides: A Case Study of Y-Doped $BaCeO_3$ and $SrCeO_3$. *Phase Transitions* **1999**, *68* (3), 567–586. https://doi.org/10.1080/01411599908224535.

(44) Kreuer, K. D. Aspects of the Formation and Mobility of Protonic Charge Carriers and the Stability of Perovskite-Type Oxides. *Solid State Ion.* **1999**, *125* (1–4), 285–302. https://doi.org/10.1016/S0167-2738(99)00188-5.

(45) Norby, T. Proton Conductivity in Perovskite Oxides. In *Perovskite Oxide for Solid Oxide Fuel Cells*; Ishihara, T., Ed.; Fuel Cells and Hydrogen Energy; Springer US: Boston, MA, **2009**; pp 217–241. https://doi.org/10.1007/978-0-387-77708-5.

(46) Ishihara, T. *Perovskite Oxide for Solid Oxide Fuel Cells*; Ishihara, T., Ed.; Fuel Cells and Hydrogen Energy; Springer US: Boston, MA, **2009**. https://doi.org/10.1007/978-0-387-77708-5.

(47) Kofstad, P.; Norby, T. *Defects and Transport in Crystalline Solids*; University of Oslo, **2007**.

(48) Bosman, A. J.; van Daal, H. J. Small-Polaron versus Band Conduction in Some Transition-Metal Oxides. *Adv. Phys.* **1970**, *19* (77), 1–117. https://doi.org/10.1080/00018737000101071.

(49) Huang, K.; Goodenough, J. B. *Solid Oxide Fuel Cell Technology. Principles, Performance and Operations*; CRC Press ; Woodhead Publishing Ltd., **2009**.

(50) Nakayama, M.; Ohshima, H.; Nogami, M.; Martin, M. A Concerted Migration Mechanism of Mixed Oxide Ion and Electron Conduction in Reduced Ceria Studied by First-

Principles Density Functional Theory. *Physical Chemistry Chemical Physics* **2012**, *14* (17), 6079. https://doi.org/10.1039/c2cp00020b.

(51) Kim, J.; Sengodan, S.; Kwon, G.; Ding, D.; Shin, J.; Liu, M.; Kim, G. Triple-Conducting Layered Perovskites as Cathode Materials for Proton-Conducting Solid Oxide Fuel Cells. *ChemSusChem* **2014**, *7* (10), 2811–2815. https://doi.org/10.1002/cssc.201402351.

(52) Duan, C.; Tong, J.; Shang, M.; Nikodemski, S.; Sanders, M.; Ricote, S.; Almansoori, A.; O'Hayre, R. Readily Processed Protonic Ceramic Fuel Cells with High Performance at Low Temperatures. *Science (1979).* **2015**, *349* (6254), 1321–1326. https://doi.org/10.1126/science.aab3987.

(53) Ding, H.; Wu, W.; Jiang, C.; Ding, Y.; Bian, W.; Hu, B.; Singh, P.; Orme, C. J.; Wang, L.; Zhang, Y.; Ding, D. Self-Sustainable Protonic Ceramic Electrochemical Cells Using a Triple Conducting Electrode for Hydrogen and Power Production. *Nat. Commun.* **2020**, *11* (1), 1907. https://doi.org/10.1038/s41467-020-15677-z.

(54) Papac, M.; Stevanović, V.; Zakutayev, A.; O'Hayre, R. Triple Ionic–Electronic Conducting Oxides for next-Generation Electrochemical Devices. *Nat. Mater.* **2021**, *20* (3), 301–313. https://doi.org/10.1038/s41563-020-00854-8.

(55) Zohourian, R.; Merkle, R.; Maier, J. Proton Uptake into the Protonic Cathode Material $BaCo_{0.4}Fe_{0.4}Zr_{0.2}O_{3-\delta}$ and Comparison to Protonic Electrolyte Materials. *Solid State Ion.* **2017**, *299*, 64–69. https://doi.org/10.1016/j.ssi.2016.09.012.

(56) Zohourian, R.; Merkle, R.; Raimondi, G.; Maier, J. Mixed-Conducting Perovskites as Cathode Materials for Protonic Ceramic Fuel Cells: Understanding the Trends in Proton Uptake. *Adv. Funct. Mater.* **2018**, *28* (35), 1–10. https://doi.org/10.1002/adfm.201801241.

(57) Münch, W. Proton Diffusion in Perovskites: Comparison between $BaCeO_3$, $BaZrO_3$, $SrTiO_3$, and $CaTiO_3$ Using Quantum Molecular Dynamics. *Solid State Ion.* **2000**, *136–137* (1–2), 183–189. https://doi.org/10.1016/S0167-2738(00)00304-0.

(58) Medarde, M.; Mesot, J.; Lacorre, P.; Rosenkranz, S.; Fischer, P.; Gobrecht, K. High-Pressure Neutron-Diffraction Study of the Metallization Process in $PrNiO_3$. *Phys. Rev. B* **1995**, *52* (13), 9248–9258. https://doi.org/10.1103/PhysRevB.52.9248.

(59) Salamon, M. B.; Jaime, M. The Physics of Manganites: Structure and Transport. *Rev. Mod. Phys.* **2001**, *73* (3), 583–628. https://doi.org/10.1103/RevModPhys.73.583.

(60) Raimondi, G.; Giannici, F.; Longo, A.; Merkle, R.; Chiara, A.; Hoedl, M. F.; Martorana, A.; Maier, J. X-Ray Spectroscopy of $(Ba,Sr,La)(Fe,Zn,Y)O_{3-\delta}$ Identifies Structural and

Electronic Features Favoring Proton Uptake. *Chemistry of Materials* **2020**, *32* (19), 8502–8511. https://doi.org/10.1021/acs.chemmater.0c02655.

(61) Raimondi, G.; Longo, A.; Giannici, F.; Merkle, R.; Hoedl, M. F.; Chiara, A.; Sahle, C. J.; Maier, J. Electronic Modifications in (Ba,La)(Fe,Zn,Y)$O_{3-\delta}$ Unveiled by Oxygen K-Edge X-Ray Raman Scattering. *J. Mater. Chem. A Mater.* **2022**, *10* (16), 8866–8876. https://doi.org/10.1039/D1TA10211G.

(62) Miruszewski, T. Zbadanie właściwości strukturalnych i elektrycznych niestechiometrycznych, domieszkowanych związków typu Sr_x(Ti,Fe)$O_{3-\delta}$, Gdańsk University of Technology, **2016**.

(63) Raimondi, G. Defect Chemistry of Mixed Conducting Perovskites: Interplay of Protonic Defects, Oxygen Vacancies and Electron Holes, Max Planck Institute, **2022**.

(64) Poetzsch, D.; Merkle, R.; Maier, J. Stoichiometry Variation in Materials with Three Mobile Carriers — Thermodynamics and Transport Kinetics Exemplified for Protons, Oxygen Vacancies, and Holes. *Adv. Funct. Mater.* **2015**, *25* (10), 1542–1557. https://doi.org/10.1002/adfm.201402212.

(65) Poetzsch, D.; Merkle, R.; Maier, J. Proton Conductivity in Mixed-Conducting BSFZ Perovskite from Thermogravimetric Relaxation. *Physical Chemistry Chemical Physics* **2014**, *16* (31), 16446. https://doi.org/10.1039/C4CP00459K.

(66) Sánchez de Bustamante, L.; Santos Silva, R.; Martínez, J. L.; Fernández-Díaz, M. T.; Aguadero, A.; Alonso, J. A. Valence Variability Induced in $SrMoO_3$ Perovskite by Mn Doping: Evaluation of a New Family of Anodes for Solid-Oxide Fuel Cells. *Materials* **2025**, *18* (3), 542. https://doi.org/10.3390/ma18030542.

(67) Yang, C.; Grimaud, A. Factors Controlling the Redox Activity of Oxygen in Perovskites: From Theory to Application for Catalytic Reactions. *Catalysts* **2017**, *7* (5), 149. https://doi.org/10.3390/catal7050149.

(68) Yamanaka, S.; Fujikane, M.; Hamaguchi, T.; Muta, H.; Oyama, T.; Matsuda, T.; Kobayashi, S.; Kurosaki, K. Thermophysical Properties of $BaZrO_3$ and $BaCeO_3$. *J. Alloys Compd.* **2003**, *359* (1–2), 109–113. https://doi.org/10.1016/S0925-8388(03)00214-7.

(69) Genet, F.; Loridant, S.; Ritter, C.; Lucazeau, G. Phase Transitions in $BaCeO_3$: Neutron Diffraction and Raman Studies. *Journal of Physics and Chemistry of Solids* **1999**, *60* (12), 2009–2021. https://doi.org/10.1016/S0022-3697(99)00031-1.

(70) Bhide, S. V.; Virkar, A. V. Stability of $BaCeO_3$-Based Proton Conductors in Water-Containing Atmospheres. *J. Electrochem. Soc.* **1999**, *146* (6), 2038–2044. https://doi.org/10.1149/1.1391888.

(71) Zakowsky, N.; Williamson, S.; Irvine, J. Elaboration of CO_2 Tolerance Limits of $BaCe_{0.9}Y_{0.1}O_{3-\delta}$ Electrolytes for Fuel Cells and Other Applications. *Solid State Ion.* **2005**, *176* (39–40), 3019–3026. https://doi.org/10.1016/j.ssi.2005.09.040.

(72) Medvedev, D.; Lyagaeva, J.; Plaksin, S.; Demin, A.; Tsiakaras, P. Sulfur and Carbon Tolerance of $BaCeO_3$–$BaZrO_3$ Proton-Conducting Materials. *J. Power Sources* **2015**, *273*, 716–723. https://doi.org/10.1016/j.jpowsour.2014.09.116.

(73) Chi, X.; Zhang, J.; Wen, Z.; Liu, Y.; Wu, M.; Wu, X. Influence of In Doping on the Structure, Stability and Electrical Conduction Behavior of $Ba(Ce,Ti)O_3$ Solid Solution. *J. Alloys Compd.* **2013**, *554*, 378–384. https://doi.org/10.1016/j.jallcom.2012.11.197.

(74) Xie, K.; Yan, R.; Chen, X.; Dong, D.; Wang, S.; Liu, X.; Meng, G. A New Stable $BaCeO_3$-Based Proton Conductor for Intermediate-Temperature Solid Oxide Fuel Cells. *J. Alloys Compd.* **2009**, *472* (1–2), 551–555. https://doi.org/10.1016/j.jallcom.2008.05.036.

(75) Medvedev, D.; Murashkina, A.; Pikalova, E.; Demin, A.; Podias, A.; Tsiakaras, P. $BaCeO_3$: Materials Development, Properties and Application. *Prog. Mater. Sci.* **2014**, *60* (1), 72–129. https://doi.org/10.1016/j.pmatsci.2013.08.001.

(76) Schober, T. Water Vapor Solubility and Electrochemical Characterization of the High Temperature Proton Conductor $BaZr_{0.9}Y_{0.1}O_{2.95}$. *Solid State Ion.* **2000**, *127* (3–4), 351–360. https://doi.org/10.1016/S0167-2738(99)00283-0.

(77) Loureiro, F. J. A.; Ramasamy, D.; Ribeiro, A. F. G.; Mendes, A.; Fagg, D. P. Underscoring the Transport Properties of Yttrium-Doped Barium Cerate in Nominally Dry Oxidising Conditions. *Electrochim. Acta* **2020**, *334*, 135625. https://doi.org/10.1016/j.electacta.2020.135625.

(78) Malavasi, L.; Ritter, C.; Chiodelli, G. Correlation between Thermal Properties, Electrical Conductivity, and Crystal Structure in the $BaCe_{0.80}Y_{0.20}O_{2.9}$ Proton Conductor. *Chemistry of Materials* **2008**, *20* (6), 2343–2351. https://doi.org/10.1021/cm7033917.

(79) Hancke, R.; Li, Z.; Haugsrud, R. The Kinetics of Hydration and H/D Isotope Exchange of Y-Doped Barium Cerate and Lanthanum Tungstate Studied by Transient Thermogravimetry. *J. Electrochem. Soc.* **2013**, *160* (8), F757–F763. https://doi.org/10.1149/2.020308jes.

(80) Yoo, H.-I.; Kim, J.-K.; Lee, C.-E. Electrical Conductivity Relaxations and Chemical Diffusivities of $BaCe_{0.95}Yb_{0.05}O_{2.975}$ upon Hydration and Oxidation. *J. Electrochem. Soc.* **2009**, *156* (1), B66. https://doi.org/10.1149/1.3005981.

(81) Bohn, H. G.; Schober, T. Electrical Conductivity of the High-Temperature Proton Conductor $BaZr_{0.9}Y_{0.1}O_{2.95}$. *Journal of the American Ceramic Society* **2000**, *83* (4), 768–772. https://doi.org/10.1111/j.1151-2916.2000.tb01272.x.

(82) Fluri, A.; Marcolongo, A.; Roddatis, V.; Wokaun, A.; Pergolesi, D.; Marzari, N.; Lippert, T. Enhanced Proton Conductivity in Y-Doped $BaZrO_3$ via Strain Engineering. *Advanced Science* **2017**, *4* (12). https://doi.org/10.1002/advs.201700467.

(83) Gaikwad, P. S.; Pawar, G.; Shin, Y. K.; Hossain, Md. J.; van Duin, A. Modeling Dynamic Evolution of Oxygen Vacancies in Solid Oxide Materials. *J. Electrochem. Soc.* **2023**, *170* (11), 113501. https://doi.org/10.1149/1945-7111/ad0722.

(84) Jing, Y.; Aluru, N. R. The Role of A-Site Ion on Proton Diffusion in Perovskite Oxides (ABO_3). *J. Power Sources* **2020**, *445*, 227327. https://doi.org/10.1016/j.jpowsour.2019.227327.

(85) Lim, D.-K.; Park, C.-J.; Choi, M.-B.; Park, C.-N.; Song, S.-J. Partial Conductivities of Mixed Conducting $BaCe_{0.65}Zr_{0.2}Y_{0.15}O_{3-\delta}$. *Int. J. Hydrogen Energy* **2010**, *35* (19), 10624–10629. https://doi.org/10.1016/j.ijhydene.2010.07.122.

(86) Han, D.; Liu, X.; Bjørheim, T. S.; Uda, T. Yttrium-Doped Barium Zirconate-Cerate Solid Solution as Proton Conducting Electrolyte: Why Higher Cerium Concentration Leads to Better Performance for Fuel Cells and Electrolysis Cells. *Adv. Energy Mater.* **2021**, *11* (8), 1–11. https://doi.org/10.1002/aenm.202003149.

(87) Okuyama, Y.; Ebihara, N.; Okuyama, K.; Mizutani, Y. Improvement of Protonic Ceramic Fuel Cells with Thin Film BCZY Electrolyte. *ECS Meeting Abstracts* **2015**, *MA2015-03* (1), 364–364. https://doi.org/10.1149/MA2015-03/1/364.

(88) Sawant, P.; Varma, S.; Wani, B. N.; Bharadwaj, S. R. Synthesis, Stability and Conductivity of $BaCe_{0.8-x}Zr_xY_{0.2}O_{3-\delta}$ as Electrolyte for Proton Conducting SOFC. *Int. J. Hydrogen Energy* **2012**, *37* (4), 3848–3856. https://doi.org/10.1016/j.ijhydene.2011.04.106.

(89) Liu, Y.; Yang, L.; Liu, M.; Tang, Z.; Liu, M. Enhanced Sinterability of $BaZr_{0.1}Ce_{0.7}Y_{0.1}Yb_{0.1}O_{3-\delta}$ by Addition of Nickel Oxide. *J. Power Sources* **2011**, *196* (23), 9980–9984. https://doi.org/10.1016/j.jpowsour.2011.08.047.

(90) Lee, S.; Park, I.; Lee, H.; Shin, D. Continuously Gradient Anode Functional Layer for BCZY Based Proton-Conducting Fuel Cells. *Int. J. Hydrogen Energy* **2014**, *39* (26), 14342–14348. https://doi.org/10.1016/j.ijhydene.2014.03.135.

(91) Lee, K.-R.; Tseng, C.-J.; Jang, S.-C.; Lin, J.-C.; Wang, K.-W.; Chang, J.-K.; Chen, T.-C.; Lee, S.-W. Fabrication of Anode-Supported Thin BCZY Electrolyte Protonic Fuel Cells Using NiO Sintering Aid. *Int. J. Hydrogen Energy* **2019**, *44* (42), 23784–23792. https://doi.org/10.1016/j.ijhydene.2019.07.097.

(92) Norby, T. Solid-State Protonic Conductors: Principles, Properties, Progress and Prospects. *Solid State Ion.* **1999**, *125* (1–4), 1–11. https://doi.org/10.1016/S0167-2738(99)00152-6.

(93) Melnik, J.; Luo, J.; Chuang, K. T.; Sanger, A. R. Stability and Electric Conductivity of Barium Cerate Perovskites Co- Doped with Praseodymium. *The Open Fuels & Energy Science Journal* **2008**, *1* (1), 7–10. https://doi.org/10.2174/1876973X00801010007.

(94) Mukundan, R.; Davies, P. K.; Worrell, W. L. Electrochemical Characterization of Mixed Conducting $Ba(Ce_{0.8-y}Pr_yGd_{0.2})O_{2.9}$ Cathodes. *J. Electrochem. Soc.* **2001**, *148* (1), A82. https://doi.org/10.1149/1.1344520.

(95) Shimura, T.; Tanaka, H.; Matsumoto, H.; Yogo, T. Influence of the Transition-Metal Doping on Conductivity of a $BaCeO_3$-Based Protonic Conductor. *Solid State Ion.* **2005**, *176* (39–40), 2945–2950. https://doi.org/10.1016/j.ssi.2005.09.027.

(96) Azimova, M. A.; McIntosh, S. Transport Properties and Stability of Cobalt Doped Proton Conducting Oxides. *Solid State Ion.* **2009**, *180* (2–3), 160–167. https://doi.org/10.1016/j.ssi.2008.12.013.

(97) Matsumoto, H.; Shimura, T.; Higuchi, T.; Tanaka, H.; Katahira, K.; Otake, T.; Kudo, T.; Yashiro, K.; Kaimai, A.; Kawada, T.; Mizusaki, J. Protonic-Electronic Mixed Conduction and Hydrogen Permeation in $BaCe_{0.9-x}Y_{0.1}Ru_xO_{3-\alpha}$. *J. Electrochem. Soc.* **2005**, *152* (3), A488. https://doi.org/10.1149/1.1852442.

(98) Kim, D.-Y.; Miyoshi, S.; Tsuchiya, T.; Yamaguchi, S. Electronic Defect Formation in Fe-Doped $BaZrO_3$ Studied by X-Ray Absorption Spectroscopy. *Chemistry of Materials* **2014**, *26* (2), 927–934. https://doi.org/10.1021/cm402369v.

(99) Kim, D.; Miyoshi, S.; Tsuchiya, T.; Yamaguchi, S. Percolation Conductivity in $BaZrO_3$–$BaFeO_3$ Solid Solutions. *Solid State Ion.* **2014**, *262*, 875–878. https://doi.org/10.1016/j.ssi.2014.01.007.

(100) Fabbri, E.; Markus, I.; Bi, L.; Pergolesi, D.; Traversa, E. Tailoring Mixed Proton-Electronic Conductivity of $BaZrO_3$ by Y and Pr Co-Doping for Cathode Application in Protonic SOFCs. *Solid State Ion.* **2011**, *202* (1), 30–35. https://doi.org/10.1016/J.SSI.2011.08.019.

(101) Kasyanova, A. V.; Tarutina, L. R.; Rudenko, A. O.; Lyagaeva, J. G.; Medvedev, D. A. $Ba(Ce,Zr)O_3$-Based Electrodes for Protonic Ceramic Electrochemical Cells: Towards Highly Compatible Functionality and Triple-Conducting Behaviour. *Russian Chemical Reviews* **2020**, *89* (6), 667–692. https://doi.org/10.1070/RCR4928.

(102) Bucher, E.; Sitte, W. Long-Term Stability of the Oxygen Exchange Properties of $(La,Sr)_{1-z}(Co,Fe)O_{3-\delta}$ in Dry and Wet Atmospheres. *Solid State Ion.* **2011**, *192* (1), 480–482. https://doi.org/10.1016/j.ssi.2010.01.006.

(103) Solís, C.; Escolastico, S.; Haugsrud, R.; Serra, J. M. $La_{5.5}WO_{12-\delta}$ Characterization of Transport Properties under Oxidizing Conditions: A Conductivity Relaxation Study. *The Journal of Physical Chemistry C* **2011**, *115* (22), 11124–11131. https://doi.org/10.1021/jp2015066.

(104) Vashuk, V. V.; Kokhanovskii, L. V.; Yushkevich, I. I. Electrical Conductivity and Oxygen Stoichiometry of $SrFeO_{3-\delta}$. *Inorganic Materials* **2000**, *36* (1), 79–83. https://doi.org/10.1007/BF02758386.

(105) Takeda, Y.; Kanno, K.; Takada, T.; Yamamoto, O.; Takano, M.; Nakayama, N.; Bando, Y. Phase Relation in the Oxygen Nonstoichiometric System, $SrFeO_x$ ($2.5 \leq x \leq 3.0$). *J. Solid State Chem.* **1986**, *63* (2), 237–249. https://doi.org/10.1016/0022-4596(86)90174-X.

(106) Hodges, J. P.; Short, S.; Jorgensen, J. D.; Xiong, X.; Dabrowski, B.; Mini, S. M.; Kimball, C. W. Evolution of Oxygen-Vacancy Ordered Crystal Structures in the Perovskite Series $SrnFenO_{3n-1}$ (n = 2, 4, 8, and ∞), and the Relationship to Electronic and Magnetic Properties. *J. Solid State Chem.* **2000**, *151* (2), 190–209. https://doi.org/10.1006/jssc.1999.8640.

(107) Fernández-Ropero, A. J.; Porras-Vázquez, J. M.; Cabeza, A.; Slater, P. R.; Marrero-López, D.; Losilla, E. R. High Valence Transition Metal Doped Strontium Ferrites for Electrode Materials in Symmetrical SOFCs. *J. Power Sources* **2014**, *249*, 405–413. https://doi.org/10.1016/j.jpowsour.2013.10.118.

(108) Rothschild, A.; Menesklou, W.; Tuller, H. L.; Ivers-Tiffée, E. Electronic Structure, Defect Chemistry, and Transport Properties of $SrTi_{1-x}Fe_xO_{3-y}$ Solid Solutions. *Chemistry of Materials* **2006**, *18* (16), 3651–3659. https://doi.org/10.1021/cm052803x.

(109) Merkle, R.; Maier, J. How Is Oxygen Incorporated into Oxides? A Comprehensive Kinetic Study of a Simple Solid-State Reaction with $SrTiO_3$ as a Model Material. *Angewandte Chemie International Edition* **2008**, *47* (21), 3874–3894. https://doi.org/10.1002/anie.200700987.

(110) Hombo, J.; Matsumoto, Y.; Kawano, T. Electrical Conductivities of $SrFeO_{3-\delta}$ and $BaFeO_{3-\delta}$ Perovskites. *J. Solid State Chem.* **1990**, *84* (1), 138–143. https://doi.org/10.1016/0022-4596(90)90192-Z.

(111) Patrakeev, M. V.; Leonidov, I. A.; Kozhevnikov, V. L.; Kharton, V. V. Ion–Electron Transport in Strontium Ferrites: Relationships with Structural Features and Stability. *Solid State Sci.* **2004**, *6* (9), 907–913. https://doi.org/10.1016/j.solidstatesciences.2004.05.002.

(112) Liu, L.; Liu, G.; Wu, S.; He, J.; Zhou, Y.; Demir, M.; Huang, R.; Ruan, Z.; Jiang, G.; Ma, P. Fe-Substituted $SrCoO_3$ Perovskites as Electrode Materials for Wide Temperature-Tolerant Supercapacitors. *Ceram. Int.* **2024**, *50* (1), 1970–1980. https://doi.org/10.1016/j.ceramint.2023.10.301.

(113) Nagai, T.; Ito, W.; Sakon, T. Relationship between Cation Substitution and Stability of Perovskite Structure in $SrCoO_{3-\delta}$ - Based Mixed Conductors. *Solid State Ion.* **2007**, *177* (39–40), 3433–3444. https://doi.org/10.1016/j.ssi.2006.10.022.

(114) Grenier, J.-C.; Fournès, L.; Pouchard, M.; Hagenmuller, P. A Mössbauer Resonance Investigation of ^{57}Fe Doped $Sr_2Co_2O_5$. *Mater. Res. Bull.* **1986**, *21* (4), 441–449. https://doi.org/10.1016/0025-5408(86)90009-7.

(115) Deng, Z. Q.; Yang, W. S.; Liu, W.; Chen, C. S. Relationship between Transport Properties and Phase Transformations in Mixed-Conducting Oxides. *J. Solid State Chem.* **2006**, *179* (2), 362–369. https://doi.org/10.1016/J.JSSC.2005.10.027.

(116) de la Calle, C.; Aguadero, A.; Alonso, J. A.; Fernández-Díaz, M. T. Correlation between Reconstructive Phase Transitions and Transport Properties from $SrCoO_{2.5}$ Brownmillerite: A Neutron Diffraction Study. *Solid State Sci.* **2008**, *10* (12), 1924–1935. https://doi.org/10.1016/j.solidstatesciences.2008.03.015.

(117) Bocquet, A. E.; Fujimori, A.; Mizokawa, T.; Saitoh, T.; Namatame, H.; Suga, S.; Kimizuka, N.; Takeda, Y.; Takano, M. Electronic Structure of $SrFe^{4+}O_3$ and Related Fe Perovskite Oxides. *Phys. Rev. B* **1992**, *45* (4), 1561–1570. https://doi.org/10.1103/PhysRevB.45.1561.

(118) Cascos, V.; Martínez-Coronado, R.; Alonso, J. A. New Nb-Doped $SrCo_{1-x}Nb_xO_{3-\delta}$ Perovskites Performing as Cathodes in Solid-Oxide Fuel Cells. *Int. J. Hydrogen Energy* **2014**, *39* (26), 14349–14354. https://doi.org/10.1016/j.ijhydene.2014.03.100.

(119) Yi, J.; Feng, S.; Zeng, Q.; Chen, C. Structure, Electrical and Oxygen Transport Properties of Fe-Doped $SrCoO_{3-\delta}$ Perovskites. *Chinese Journal of Chemical Physics* **2015**, *28* (2), 189–192. https://doi.org/10.1063/1674-0068/28/cjcp1411192.

(120) Vashook, V. V.; Zinkevich, M. V.; Ullmann, H.; Paulsen, J.; Trofimenko, N.; Teske, K. Oxygen Non-Stoichiometry and Electrical Conductivity of the Binary Strontium Cobalt Oxide $SrCoO_x$. *Solid State Ion.* **1997**, *99* (1–2), 23–32. https://doi.org/10.1016/S0167-2738(97)00192-6.

(121) Kleveland, K.; Einarsrud, M.; Grande, T. Sintering Behavior, Microstructure, and Phase Composition of $Sr(Fe,Co)O_{3-\delta}$ Ceramics. *Journal of the American Ceramic Society* **2000**, *83* (12), 3158–3164. https://doi.org/10.1111/j.1151-2916.2000.tb01698.x.

(122) Prado, F.; Armstrong, T.; Caneiro, A.; Manthiram, A. Structural Stability and Oxygen Permeation Properties of $Sr_{3-x}La_xFe_{2-y}Co_yO_{7-\delta}$ ($0 \le x \le 0.3$ and $0 \le y \le 1.0$). *J. Electrochem. Soc.* **2001**, *148* (4), J7. https://doi.org/10.1149/1.1354605.

(123) Wang, Z.; Zhao, H.; Xu, N.; Shen, Y.; Ding, W.; Lu, X.; Li, F. Electrical Conductivity and Structural Stability of $SrCo_{1-x}Fe_xO_{3-\delta}$. *Journal of Physics and Chemistry of Solids* **2011**, *72* (1), 50–55. https://doi.org/10.1016/j.jpcs.2010.10.084.

(124) Aasland, S. Oxygen Permeation of $SrFe_{0.67}Co_{0.33}O_{3-d}$. *Solid State Ion.* **2000**, *135* (1–4), 713–717. https://doi.org/10.1016/S0167-2738(00)00389-1.

(125) Shaula, A. L.; Kharton, V. V.; Vyshatko, N. P.; Tsipis, E. V.; Patrakeev, M. V.; Marques, F. M. B.; Frade, J. R. Oxygen Ionic Transport in $SrFe_{1-y}Al_yO_{3-\delta}$ and $Sr_{1-x}Ca_xFe_{0.5}Al_{0.5}O_{3-\delta}$ Ceramics. *J. Eur. Ceram. Soc.* **2005**, *25* (4), 489–499. https://doi.org/10.1016/j.jeurceramsoc.2004.03.011.

(126) Kharton, V. V.; Shaula, A. L.; Snijkers, F. M. M.; Cooymans, J. F. C.; Luyten, J. J.; Marozau, I. P.; Viskup, A. P.; Marques, F. M. B.; Frade, J. R. Oxygen Transport in Ferrite-Based Ceramic Membranes: Effects of Alumina Sintering Aid. *J. Eur. Ceram. Soc.* **2006**, *26* (16), 3695–3704. https://doi.org/10.1016/j.jeurceramsoc.2005.10.013.

(127) Teraoka, Y.; Zhang, H.-M.; Furukawa, S.; Yamazoe, N. Oxygen Permeation through Perovskite-Type Oxides. *Chem. Lett.* **1985**, *14* (11), 1743–1746. https://doi.org/10.1246/cl.1985.1743.

(128) Silva, R. S.; Gainza, J.; dos Santos, C.; Rodrigues, J. E. F. S.; Dejoie, C.; Huttel, Y.; Biskup, N.; Nemes, N. M.; Martínez, J. L.; Ferreira, N. S.; Alonso, J. A. Magnetoelastic Coupling and Cryogenic Magnetocaloric Effect in Two-Site Disordered $GdSrCoFeO_6$ Double Perovskite. *Chemistry of Materials* **2023**, *35* (6), 2439–2455. https://doi.org/10.1021/acs.chemmater.2c03574.

(129) Pal, A.; Ghosh, S.; Joshi, A. G.; Kumar, S.; Patil, S.; Gupta, P. K.; Singh, P.; Gangwar, V. K.; Prakash, P.; Singh, R. K.; Schwier, E. F.; Sawada, M.; Shimada, K.; Ghosh, A. K.; Das, A.; Chatterjee, S. Investigation of Multi-Mode Spin–Phonon Coupling and Local B-Site Disorder in Pr_2CoFeO_6 by Raman Spectroscopy and Correlation with Its Electronic Structure by XPS and XAS Studies. *Journal of Physics: Condensed Matter* **2019**, *31* (27), 275802. https://doi.org/10.1088/1361-648X/ab144f.

(130) Silva, R. S.; Rodrigues, J. E.; Gainza, J.; Serrano-Sánchez, F.; Martínez, L.; Huttel, Y.; Martínez, J. L.; Alonso, J. A. Magnetoelastic Coupling Evidence by Anisotropic Crossed Thermal Expansion in Magnetocaloric $RSrCoFeO_6$ (R = Sm, Eu) Double Perovskites. *Inorg. Chem.* **2024**, *63* (15), 7007–7018. https://doi.org/10.1021/acs.inorgchem.4c00594.

(131) Silva, R. S.; Santos, C.; Escote, M. T.; Costa, B. F. O.; Moreno, N. O.; Paz, S. P. A.; Angélica, R. S.; Ferreira, N. S. Griffiths-like Phase, Large Magnetocaloric Effect, and Unconventional Critical Behavior in the $NdSrCoFeO_6$ Disordered Double Perovskite. *Phys. Rev. B* **2022**, *106* (13), 134439. https://doi.org/10.1103/PhysRevB.106.134439.

(132) Silva, R. S.; Serrano-Sánchez, F.; Rodrigues, J. E.; Santos, C.; Attah-Baah, J. M.; dos Reis, R. D.; Martínez, J. L.; Alonso, J. A.; Ferreira, N. S. Magnetostructural Coupling, Kondo-like Behavior, and Magnetocaloric Performance in Fe-Doped $Nd_{0.5}(Sr_{0.4}Ba_{0.1})CoO_3$ Perovskites. *J. Mater. Chem. C Mater.* **2025**, *13* (28), 14608–14623. https://doi.org/10.1039/D5TC00977D.

(133) Abbate, M.; Zampieri, G.; Okamoto, J.; Fujimori, A.; Kawasaki, S.; Takano, M. X-Ray Absorption of the Negative Charge-Transfer Material $SrFe_{1-x}Co_xO_3$. *Phys. Rev. B* **2002**, *65* (16), 165120. https://doi.org/10.1103/PhysRevB.65.165120.

(134) Stein, A.; Keller, S. W.; Mallouk, T. E. Turning Down the Heat: Design and Mechanism in Solid-State Synthesis. *Science (1979).* **1993**, *259* (5101), 1558–1564. https://doi.org/10.1126/science.259.5101.1558.

(135) Merkle, R.; Maier, J. On the Tammann-Rule. *Z. Anorg. Allg. Chem.* **2005**, *631* (6–7), 1163–1166. https://doi.org/10.1002/zaac.200400540.

(136) Nikodemski, S.; Tong, J.; O'Hayre, R. Solid-State Reactive Sintering Mechanism for Proton Conducting Ceramics. *Solid State Ion.* **2013**, *253*, 201–210. https://doi.org/10.1016/j.ssi.2013.09.025.

(137) Tong, J.; Clark, D.; Bernau, L.; Sanders, M.; O'Hayre, R. Solid-State Reactive Sintering Mechanism for Large-Grained Yttrium-Doped Barium Zirconate Proton Conducting Ceramics. *J. Mater. Chem.* **2010**, *20* (30), 6333–6341. https://doi.org/10.1039/c0jm00381f.

(138) Degen, T.; Sadki, M.; Bron, E.; König, U.; Nénert, G. The HighScore Suite. *Powder Diffr.* **2014**, *29* (S2), S13–S18. https://doi.org/10.1017/S0885715614000840.

(139) Toby, B. H. A Simple Solution to the Rietveld Refinement Recipe Problem. *J. Appl. Crystallogr.* **2024**, *57* (1), 175–180. https://doi.org/10.1107/S1600576723011032.

(140) Toby, B. H. *R* Factors in Rietveld Analysis: How Good Is Good Enough? *Powder Diffr.* **2006**, *21* (1), 67–70. https://doi.org/10.1154/1.2179804.

(141) Newville, M. Fundamentals of XAFS. *Rev. Mineral. Geochem.* **2014**, *78* (1), 33–74. https://doi.org/10.2138/rmg.2014.78.2.

(142) Calvin, S. *XAFS for Everyone*; CRC Press, **2013**.

(143) Ravel, B.; Newville, M. *ATHENA*, *ARTEMIS*, *HEPHAESTUS*: Data Analysis for X-Ray Absorption Spectroscopy Using *IFEFFIT*. *J. Synchrotron Radiat.* **2005**, *12* (4), 537–541. https://doi.org/10.1107/S0909049505012719.

(144) Solé, V. A.; Papillon, E.; Cotte, M.; Walter, Ph.; Susini, J. A Multiplatform Code for the Analysis of Energy-Dispersive X-Ray Fluorescence Spectra. *Spectrochim. Acta Part B At. Spectrosc.* **2007**, *62* (1), 63–68. https://doi.org/10.1016/j.sab.2006.12.002.

(145) Simultaneous Thermal Analyzer – STA 449 F1 Jupiter® (Brochure). Netzsch. https://analyzing-testing.netzsch.com/en-US/products/simultaneous-thermogravimetry-differential-scanning-calorimetry-sta-tg-dsc/sta-449-f1-jupiter (accessed 2024-12-03).

(146) Lazanas, A. Ch.; Prodromidis, M. I. Electrochemical Impedance Spectroscopy — A Tutorial. *ACS Measurement Science Au* **2023**, *3* (3), 162–193. https://doi.org/10.1021/acsmeasuresciau.2c00070.

(147) Jorcin, J.-B.; Orazem, M. E.; Pébère, N.; Tribollet, B. CPE Analysis by Local Electrochemical Impedance Spectroscopy. *Electrochim. Acta* **2006**, *51* (8–9), 1473–1479. https://doi.org/10.1016/j.electacta.2005.02.128.

(148) Irvine, J. T. S.; Sinclair, D. C.; West, A. R. Electroceramics: Characterization by Impedance Spectroscopy. *Advanced Materials* **1990**, *2* (3), 132–138. https://doi.org/10.1002/adma.19900020304.

(149) Simner, S. P.; Anderson, M. D.; Engelhard, M. H.; Stevenson, J. W. Degradation Mechanisms of La–Sr–Co–Fe–O_3 SOFC Cathodes. *Electrochemical and Solid-State Letters* **2006**, *9* (10), A478. https://doi.org/10.1149/1.2266160.

(150) Backhaus-Ricoult, M. SOFC - A Playground for Solid State Chemistry. *Solid State Sci.* **2008**, *10* (6), 670–688. https://doi.org/10.1016/j.solidstatesciences.2007.11.021.

(151) Ciucci, F. Electrical Conductivity Relaxation Measurements: Statistical Investigations Using Sensitivity Analysis, Optimal Experimental Design and ECRTOOLS. *Solid State Ion.* **2013**, *239*, 28–40. https://doi.org/10.1016/j.ssi.2013.03.020.

(152) Shin, C.; Yoo, H. Al-Doped $SrTiO_3$: Part II, Unusual Thermodynamic Factor and Chemical Diffusivity. *Solid State Ion.* **2007**, *178* (15–18), 1089–1094. https://doi.org/10.1016/j.ssi.2007.05.009.

(153) Abernathy, H.; Yang, T.; Liu, J.; Na, B. NETL Electrical Conductivity Relaxation(ECR) Analysis Tool. January **2021**. https://doi.org/10.18141/1762415.

(154) Tuller, H. L.; Nowick, A. S. Small Polaron Electron Transport in Reduced CeO_2 Single Crystals. *Journal of Physics and Chemistry of Solids* **1977**, *38* (8), 859–867. https://doi.org/10.1016/0022-3697(77)90124-X.

(155) Heikes, R. R.; Ure, R. W. *Thermoelectricity. Science and Engineering. [By] R.R. Heikes and R.W. Ure, Jr. ... With the Collaboration of Stephen J. Angello [and Others], Etc*; New York, London: Interscience Publishers, **1961**.

(156) Koshibae, W.; Tsutsui, K.; Maekawa, S. Thermopower in Cobalt Oxides. *Phys. Rev. B* **2000**, *62* (11), 6869–6872. https://doi.org/10.1103/PhysRevB.62.6869.

(157) Poulsen, F. W.; Lauvstad, G.; Tunold, R. Conductivity and Seebeck Measurements on Strontium Ferrates. *Solid State Ion.* **1994**, *72*, 47–53. https://doi.org/10.1016/0167-2738(94)90123-6.

(158) Taguchi, H.; Sonoda, M.; Nagao, M. Relationship between Angles for Mn–O–Mn and Electrical Properties of Orthorhombic Perovskite-Type $(Ca_{1-x}Sr_x)MnO_3$. *J. Solid State Chem.* **1998**, *137* (1), 82–86. https://doi.org/10.1006/jssc.1997.7701.

(159) Tsvetkov, D.; Ivanov, I.; Malyshkin, D.; Sereda, V.; Zuev, A. Thermoelectric Behavior of $BaZr_{0.9}Y_{0.1}O_{3-d}$ Proton Conducting Electrolyte. *Membranes (Basel).* **2019**, *9* (9), 120. https://doi.org/10.3390/membranes9090120.

(160) Goodenough, J. B. Seebeck Coefficients in Vanadium Spinels. *Mater. Res. Bull.* **1970**, *5* (8), 621–629. https://doi.org/10.1016/0025-5408(70)90103-0.

(161) Dorris, S. E.; Mason, T. O. Electrical Properties and Cation Valencies in Mn_3O_4. *Journal of the American Ceramic Society* **1988**, *71* (5), 379–385. https://doi.org/10.1111/j.1151-2916.1988.tb05057.x.

(162) Jung, J.-I.; Misture, S. T.; Edwards, D. D. Oxygen Stoichiometry, Electrical Conductivity, and Thermopower Measurements of BSCF ($Ba_{0.5}Sr_{0.5}Co_xFe_{1-x}O_{3-\delta}$, $0 \leq x \leq 0.8$) in Air. *Solid State Ion.* **2010**, *181* (27–28), 1287–1293. https://doi.org/10.1016/j.ssi.2010.06.033.

(163) Budnik, J.; Mielewczyk-Gryń, A.; Gazda, M.; Miruszewski, T. Water Uptake Kinetics and Electrical Transport in $BaCe_{0.6}Zr_{0.2}Y_{0.1}M_{0.1}O_{3-\delta}$ (M = Tb, Pr, Fe) Protonic Conductors. *J. Mater. Chem. A Mater.* **2023**, *11* (25), 13389–13398. https://doi.org/10.1039/D2TA07236J.

(164) Budnik, J.; Mielewczyk-Gryń, A.; Gazda, M.; Miruszewski, T. Influence of Iron Content on Water Uptake and Charge Transport in $BaCe_{0.6}Zr_{0.2}Y_{0.2-x}Fe_xO_{3-\delta}$ Triple-Conducting Oxides. *J. Mater. Chem. A Mater.* **2024**, *12* (24), 14569–14582. https://doi.org/10.1039/D3TA06917F.

(165) Mirfakhraei, B.; Ramezanipour, F.; Paulson, S.; Birss, V.; Thangadurai, V. Effect of Sintering Temperature on Microstructure, Chemical Stability, and Electrical Properties of Transition Metal or Yb-Doped $BaZr_{0.1}Ce_{0.7}Y_{0.1}M_{0.1}O_{3-\delta}$ (M=Fe, Ni, Co, and Yb). *Front. Energy Res.* **2014**, *2* (9), 1–10. https://doi.org/10.3389/fenrg.2014.00009.

(166) Petit, C. T. G.; Tao, S. Structure and Conductivity of Praseodymium and Yttrium Co-Doped Barium Cerates. *Solid State Sci.* **2013**, *17*, 115–121. https://doi.org/10.1016/j.solidstatesciences.2012.12.004.

(167) Heras-Juaristi, G.; Amador, U.; Fuentes, R. O.; Chinelatto, A. L.; Romero de Paz, J.; Ritter, C.; Fagg, D. P.; Pérez-Coll, D.; Mather, G. C. Thermal Evolution of Structures and Conductivity of Pr-Substituted $BaZr_{0.7}Ce_{0.2}Y_{0.1}O_{3-\delta}$: Potential Cathode Components for Protonic Ceramic Fuel Cells. *J. Mater. Chem. A Mater.* **2018**, *6* (13), 5324–5334. https://doi.org/10.1039/C7TA09570H.

(168) Shannon, R. D. Revised Effective Ionic Radii and Systematic Studies of Interatomic Distances in Halides and Chalcogenides. *Acta Crystallographica Section A* **1976**, *32* (5), 751–767. https://doi.org/10.1107/S0567739476001551.

(169) Miruszewski, T.; Dzierzgowski, K.; Winiarz, P.; Wachowski, S.; Mielewczyk-Gryń, A.; Gazda, M. Hebb–Wagner Polarization Method for Determining the Oxygen Ion

Conductivity in Barium Cerate-Zirconate. *J. Mater. Chem. A Mater.* **2022**, *10* (13), 7218–7227. https://doi.org/10.1039/D1TA10916B.

(170) Wachowski, S. L.; Szpunar, I.; Sørby, M. H.; Mielewczyk–Gryń, A.; Balaguer, M.; Ghica, C.; Istrate, M. C.; Gazda, M.; Gunnæs, A. E.; Serra, J. M.; Norby, T.; Strandbakke, R. Structure and Water Uptake in $BaLnCo_2O_{6-\delta}$ (Ln = La, Pr, Nd, Sm, Gd, Tb and Dy). *Acta Mater.* **2020**, *199*, 297–310. https://doi.org/10.1016/j.actamat.2020.08.018.

(171) Miruszewski, T.; Dzierzgowski, K.; Winiarz, P.; Wachowski, S.; Mielewczyk-Gryń, A.; Gazda, M. Structural Properties and Water Uptake of $STi_{1-x}Fe_xO_{3-x/2-\delta}$. *Materials* **2020**, *13* (4). https://doi.org/10.3390/ma13040965.

(172) Miruszewski, T.; Dzierzgowski, K.; Winiarz, P.; Jaworski, D.; Wiciak-Pawłowska, K.; Skubida, W.; Wachowski, S.; Mielewczyk-Gryń, A.; Gazda, M. Structure and Transport Properties of Triple-Conducting $Ba_xSr_{1-x}Ti_{1-y}Fe_yO_{3-\delta}$ Oxides. *RSC Adv.* **2021**, *11* (32), 19570–19578. https://doi.org/10.1039/D0RA10048J.

(173) Huse, M.; Norby, T.; Haugsrud, R. Effects of A and B Site Acceptor Doping on Hydration and Proton Mobility of $LaNbO_4$. In *International Journal of Hydrogen Energy*; **2012**; Vol. 37, pp 8004–8016. https://doi.org/10.1016/j.ijhydene.2011.10.020.

(174) Oikawa, I.; Takamura, H. Correlation among Oxygen Vacancies, Protonic Defects, and the Acceptor Dopant in Sc-Doped $BaZrO_3$ Studied by ^{45}Sc Nuclear Magnetic Resonance. *Chemistry of Materials* **2015**, *27* (19), 6660–6667. https://doi.org/10.1021/acs.chemmater.5b02441.

(175) Tarutina, L. R.; Vdovin, G. K.; Lyagaeva, J. G.; Medvedev, D. A. $BaCe_{0.7-x}Zr_{0.2}Y_{0.1}Fe_xO_{3-\delta}$ Derived from Proton-Conducting Electrolytes: A Way of Designing Chemically Compatible Cathodes for Solid Oxide Fuel Cells. *J. Alloys Compd.* **2020**, *831*, 154895. https://doi.org/10.1016/j.jallcom.2020.154895.

(176) Song, C. R.; Yoo, H. I. Chemical Diffusivity of $BaTiO_{3-\delta}$: IV, Acceptor-Doped Case. *Journal of the American Ceramic Society* **2000**, *83* (4), 773–779. https://doi.org/10.1111/j.1151-2916.2000.tb01273.x.

(177) Merkle, R.; Sitte, W.; Maier, J. Water Incorporation into Materials with Three Mobile Carriers: Two-Fold Relaxation of the Electromotive Force in Fe-Doped $SrTiO_3$ and Importance of Hole Trapping. *Solid State Ion.* **2020**, *347* (December 2019), 115174. https://doi.org/10.1016/j.ssi.2019.115174.

(178) Jiang, K.; He, Z.; Meng, J.; Ren, Y.; Su, Q. Low Temperature Preparation and Fuel Cell Properties of Rare Earth Doped Barium Cerate Solid Electrolytes. *Sci. China B Chem.* **1999**, *42* (3), 298–304. https://doi.org/10.1007/BF02874246.

(179) Poetzsch, D.; Merkle, R.; Maier, J. Proton Uptake in the H+-SOFC Cathode Material $Ba_{0.5}Sr_{0.5}Fe_{0.8}Zn_{0.2}O_{3-\delta}$: Transition from Hydration to Hydrogenation with Increasing Oxygen Partial Pressure. *Faraday Discuss.* **2015**, *182*, 129–143. https://doi.org/10.1039/c5fd00013k.

(180) Yoo, H.-I.; Yoon, J.-Y.; Ha, J.-S.; Lee, C.-E. Hydration and Oxidation Kinetics of a Proton Conductor Oxide, $SrCe_{0.95}Yb_{0.05}O_{2.975}$. *Phys. Chem. Chem. Phys.* **2008**, *10* (7), 974–982. https://doi.org/10.1039/B709371C.

(181) Lim, D.-K.; Park, C.-J.; Choi, M.-B.; Park, C.-N.; Song, S.-J. Partial Conductivities of Mixed Conducting $BaCe_{0.65}Zr_{0.2}Y_{0.15}O_{3-\delta}$. *Int. J. Hydrogen Energy* **2010**, *35* (19), 10624–10629. https://doi.org/10.1016/j.ijhydene.2010.07.122.

(182) Riess, I. Point Defect Concentrations in Surface Layers of Binary Oxides. *Solid State Ion.* **2019**, *329* (August 2018), 95–109. https://doi.org/10.1016/j.ssi.2018.10.007.

(183) Merkle, R.; Maier, J. Oxygen Incorporation into Fe-Doped $SrTiO_3$: Mechanistic Interpretation of the Surface Reaction. *Physical Chemistry Chemical Physics* **2002**, *4* (17), 4140–4148. https://doi.org/10.1039/b204032h.

(184) Maier, J. Interaction of Oxygen with Oxides: How to Interpret Measured Effective Rate Constants? *Solid State Ion.* **2000**, *135* (1–4), 575–588. https://doi.org/10.1016/S0167-2738(00)00438-0.

(185) Lim, D.-K.; Im, H.-N.; Jeon, S.-Y.; Park, J.-Y.; Song, S.-J. Experimental Evidence of Hydrogen–Oxygen Decoupled Diffusion into $BaZr_{0.6}Ce_{0.25}Y_{0.15}O_{3-\delta}$. *Acta Mater.* **2013**, *61* (4), 1274–1283. https://doi.org/10.1016/j.actamat.2012.11.003.

(186) Yoo, H.; Lee, C. Two-Fold Diffusion Kinetics of Oxygen Re-Equilibration in Donor-Doped $BaTiO_3$. *Journal of the American Ceramic Society* **2005**, *88* (3), 617–623. https://doi.org/10.1111/j.1551-2916.2005.00123.x.

(187) Kim, E.; Yoo, H. I. Two-Fold -to-Single-Fold Transition of the Conductivity Relaxation Patterns of Proton-Conducting Oxides upon Hydration/Dehydration. *Solid State Ion.* **2013**, *252*, 132–139. https://doi.org/10.1016/j.ssi.2013.04.005.

(188) Polfus, J. M.; Bjørheim, T. S.; Norby, T.; Bredesen, R. Surface Defect Chemistry of Y-Substituted and Hydrated $BaZrO_3$ with Subsurface Space-Charge Regions. *J. Mater. Chem. A Mater.* **2016**, *4* (19), 7437–7444. https://doi.org/10.1039/C6TA02067D.

(189) Wang, S.; van der Heide, P. A. W.; Chavez, C.; Jacobson, A. J.; Adler, S. B. An Electrical Conductivity Relaxation Study of $La_{0.6}Sr_{0.4}Fe_{0.8}Co_{0.2}O_{3-\delta}$. *Solid State Ion.* **2003**, *156* (1–2), 201–208. https://doi.org/10.1016/S0167-2738(02)00178-9.

(190) Li, X.; Tang, Z.; Zhang, L. Molecular Dynamics Simulations of Point/Line Defect Structures and Oxygen Diffusion Mechanism in Yttrium-Doped Barium Zirconate. *SCIENTIA SINICA Chimica* **2019**, *49* (8), 1104–1113. https://doi.org/10.1360/SSC-2019-0044.

(191) Kokhanovskii, L. V.; Vashuk, V. V.; Ol'shevskaya, O. P.; Kirilenko, O. I. Oxygen Stoichiometry and Phase Transitions of $SrCo_{1-x}Fe_xO_{3-\delta}$. *Inorganic Materials* **2001**, *37* (7), 730–736. https://doi.org/10.1023/A:1017642610832.

(192) Budnik, J.; Gazda, M.; Maximenko, A.; Mielewczyk-Gryń, A.; Pośpiech, J.; Wachowski, S.; Witkowska, A.; Miruszewski, T. $Sr(Fe,Co)O_{3-\delta}$ Mixed Conductors: How Cobalt Drives Oxygen Vacancy Formation. *Chemistry of Materials* **2025**, *37* (21), 8822–8834. https://doi.org/10.1021/acs.chemmater.5c01904.

(193) Lide, D. R.; *CRC Handbook of Chemistry and Physics, 84th Edition, 2003-2004*; CRC Press, **2004**.

(194) Wachowski, S. L.; Szpunar, I.; Pośpiech, J.; Balcerzak, D.; Mielewczyk-Gryń, A.; Nadolska, M.; Balaguer, M.; Serra, J. M.; Vøllestad, E.; Gazda, M.; Strandbakke, R.; Norby, T. Physicochemical Properties of $La_{0.5}Ba_{0.5}Co_{1-x}Fe_xO_{3-\delta}$ ($0 \leq x \leq 1$) as Positrode for Proton Ceramic Electrochemical Cells. *Acta Mater.* **2025**, *284*, 120585. https://doi.org/10.1016/j.actamat.2024.120585.

(195) Okazoe, C. Oxygen Doping in $SrFe_{1-x}Co_xO_3$ Perovskite Oxides by the Electrochemical Method. *Solid State Ion.* **1996**, *86–88*, 1431–1435. https://doi.org/10.1016/0167-2738(96)00325-6.

(196) Tikhonovich, V.; Naumovich, E.; Logvinovich, D.; Kharton, V.; Vecher, A. Oxygen Deficiency and Phase Transitions in $SrCo_{1-x-y}Fe_xCr_yO_{3-\delta}$ (x=0.10–0.40, y=0–0.05). *Journal of Solid State Electrochemistry* **2003**, *7* (2), 77–82. https://doi.org/10.1007/s10008-002-0321-4.

(197) Hodges, J. P.; Jorgensen, J. D.; Miller, D. J.; Ma, B.; Balachandran, U.; Richardson, J. W. Crystal Structures of Mixed-Conducting Oxides Present in The Sr-Fe-Co-O System. *MRS Proceedings* **1997**, *496*, 173. https://doi.org/10.1557/PROC-496-173.

(198) Haas, O.; Vogt, U. F.; Soltmann, C.; Braun, A.; Yoon, W.-S.; Yang, X. Q.; Graule, T. The Fe K-Edge X-Ray Absorption Characteristics of $La_{1-x}Sr_xFeO_{3-\delta}$ Prepared by Solid State

Reaction. *Mater. Res. Bull.* **2009**, *44* (6), 1397–1404. https://doi.org/10.1016/j.materresbull.2008.11.026.

(199) Zamani, S. M. M.; Behdinan, K. The Effect of Oxygen Vacancy and Temperature on the Lattice Parameters of Mullite Using a Novel Bridging Cell Multiscale Method. *Ceram. Int.* **2017**, *43* (15), 12239–12248. https://doi.org/10.1016/j.ceramint.2017.06.085.

(200) Tyunina, M.; Pacherova, O.; Kocourek, T.; Dejneka, A. Anisotropic Chemical Expansion Due to Oxygen Vacancies in Perovskite Films. *Sci. Rep.* **2021**, *11* (1), 15247. https://doi.org/10.1038/s41598-021-93968-1.

(201) Kotomin, E. A.; Kuzmin, A.; Purans, J.; Timoshenko, J.; Piskunov, S.; Merkle, R.; Maier, J. Theoretical and Experimental Studies of Charge Ordering in $CaFeO_3$ and $SrFeO_3$ Crystals. *physica status solidi (b)* **2022**, *259* (1). https://doi.org/10.1002/pssb.202100238.

(202) Gyu Kim, M.; Sang Cho, H.; Hyun Yo, C. Fe K-Edge X-Ray Absorption (XANES/EXAFS) Spectroscopic Study of the Nonstoichiometric $SrFe_{1-x}Sn_xO_{3-y}$ System. *Journal of Physics and Chemistry of Solids* **1998**, *59* (9), 1369–1381. https://doi.org/10.1016/S0022-3697(98)00246-7.

(203) Che, Q.; van den Bosch, I. C. G.; Le, P. T. P.; Lazemi, M.; van der Minne, E.; Birkhölzer, Y. A.; Nunnenkamp, M.; Peerlings, M. L. J.; Safonova, O. V.; Nachtegaal, M.; Koster, G.; Baeumer, C.; de Jongh, P.; de Groot, F. M. F. In Situ X-Ray Absorption Spectroscopy of $LaFeO_3$ and $LaFeO_3/LaNiO_3$ Thin Films in the Electrocatalytic Oxygen Evolution Reaction. *The Journal of Physical Chemistry C* **2024**, *128* (13), 5515–5523. https://doi.org/10.1021/acs.jpcc.3c07864.

(204) Li, Z.; Mao, X.; Feng, D.; Li, M.; Xu, X.; Luo, Y.; Zhuang, L.; Lin, R.; Zhu, T.; Liang, F.; Huang, Z.; Liu, D.; Yan, Z.; Du, A.; Shao, Z.; Zhu, Z. Prediction of Perovskite Oxygen Vacancies for Oxygen Electrocatalysis at Different Temperatures. *Nat. Commun.* **2024**, *15* (1), 9318. https://doi.org/10.1038/s41467-024-53578-7.

(205) Munoz, M.; Vidal, O.; Marcaillou, C.; Pascarelli, S.; Mathon, O.; Farges, F. Iron Oxidation State in Phyllosilicate Single Crystals Using Fe-K Pre-Edge and XANES Spectroscopy: Effects of the Linear Polarization of the Synchrotron X-Ray Beam. *American Mineralogist* **2013**, *98* (7), 1187–1197. https://doi.org/10.2138/am.2013.4289.

(206) Asakura, D.; Hosono, E.; Nanba, Y.; Zhou, H.; Okabayashi, J.; Ban, C.; Glans, P.-A.; Guo, J.; Mizokawa, T.; Chen, G.; Achkar, A. J.; Hawthron, D. G.; Regier, T. Z.; Wadati, H. Material/Element-Dependent Fluorescence-Yield Modes on Soft X-Ray Absorption

Spectroscopy of Cathode Materials for Li-Ion Batteries. *AIP Adv.* **2016**, *6* (3). https://doi.org/10.1063/1.4943673.

(207) Butorin, S. M.; Guo, J.-H.; Wassdahl, N.; Bray, G.; Glans, P.; Wiell, T.; Duda, L.-C.; Nordgren, J.; Lundstrom, T.; Klauda, M.; Markl, J.; Fink, C.; Saemann-Ischenko, G. Tunable Excitation X-Ray Fluorescence Spectroscopy in Phase Analysis of High-T_c Superconductors. *Journal of Physics: Condensed Matter* **1994**, *6* (43), 9267–9274. https://doi.org/10.1088/0953-8984/6/43/024.

(208) Imamura, M.; Matsubayashi, N.; Shimada, H. Catalytically Active Oxygen Species in $La_{1-x}Sr_xCoO_{3-\delta}$ Studied by XPS and XAFS Spectroscopy. *J. Phys. Chem. B* **2000**, *104* (31), 7348–7353. https://doi.org/10.1021/jp994148k.

(209) Harvey, A. S.; Yang, Z.; Infortuna, A.; Beckel, D.; Purton, J. A.; Gauckler, L. J. Development of Electron Holes across the Temperature-Induced Semiconductor–Metal Transition in $Ba_{1-x}Sr_xCo_{1-y}Fe_yO_{3-\delta}$ (x, y = 0.2–0.8): A Soft X-Ray Absorption Spectroscopy Study. *Journal of Physics: Condensed Matter* **2009**, *21* (1), 015801. https://doi.org/10.1088/0953-8984/21/1/015801.

(210) Ruckman, M. W.; Chen, J.; Qiu, S. L.; Kuiper, P.; Strongin, M.; Dunlap, B. I. Interpreting the near Edges of O_2 and O_2^- in Alkali-Metal Superoxides. *Phys. Rev. Lett.* **1991**, *67* (18), 2533–2536. https://doi.org/10.1103/PhysRevLett.67.2533.

(211) Karvonen, L.; Valkeapää, M.; Liu, R.-S.; Chen, J.-M.; Yamauchi, H.; Karppinen, M. O-*K* and Co-*L* XANES Study on Oxygen Intercalation in Perovskite $SrCoO_{3-\delta}$. *Chemistry of Materials* **2010**, *22* (1), 70–76. https://doi.org/10.1021/cm9021563.

(212) Szpunar, I.; Strandbakke, R.; Sørby, M. H.; Wachowski, S. L.; Balaguer, M.; Tarach, M.; Serra, J. M.; Witkowska, A.; Dzik, E.; Norby, T.; Gazda, M.; Mielewczyk-Gryń, A. High-Temperature Structural and Electrical Properties of $BaLnCo_2O_6$ Positrodes. *Materials* **2020**, *13* (18). https://doi.org/10.3390/ma13184044.

(213) Padilla-Pantoja, J. Spin-Lattice Coupling in Strongly Correlated Cobalt Oxides Investigated by Synchrotron and Neutron Techniques, **2016**. https://ddd.uab.cat/record/165980 (accessed 2025-10-01).

(214) Toulemonde, O.; N'Guyen, N.; Studer, F.; Traverse, A. Spin State Transition in $LaCoO_3$ with Temperature or Strontium Doping as Seen by XAS. *J. Solid State Chem.* **2001**, *158* (2), 208–217. https://doi.org/10.1006/jssc.2001.9094.

(215) Sun, H.; Zhou, W. Progress on X-Ray Absorption Spectroscopy for the Characterization of Perovskite-Type Oxide Electrocatalysts. *Energy & Fuels* **2021**, *35* (7), 5716–5737. https://doi.org/10.1021/ACS.ENERGYFUELS.1C00534.

(216) Kawakami, T.; Tsujimoto, Y.; Kageyama, H.; Chen, X.-Q.; Fu, C. L.; Tassel, C.; Kitada, A.; Suto, S.; Hirama, K.; Sekiya, Y.; Makino, Y.; Okada, T.; Yagi, T.; Hayashi, N.; Yoshimura, K.; Nasu, S.; Podloucky, R.; Takano, M. Spin Transition in a Four-Coordinate Iron Oxide. *Nat. Chem.* **2009**, *1* (5), 371–376. https://doi.org/10.1038/nchem.289.

(217) Guan, D.; Zhou, J.; Hu, Z.; Zhou, W.; Xu, X.; Zhong, Y.; Liu, B.; Chen, Y.; Xu, M.; Lin, H.; Chen, C.; Wang, J.; Shao, Z. Searching General Sufficient-and-Necessary Conditions for Ultrafast Hydrogen-Evolving Electrocatalysis. *Adv. Funct. Mater.* **2019**, *29* (20). https://doi.org/10.1002/adfm.201900704.

(218) Ishii, T.; Tsuboi, S.; Sakane, G.; Yamashita, M.; Breedlove, B. K. Universal Spectrochemical Series of Six-Coordinate Octahedral Metal Complexes for Modifying the Ligand Field Splitting. *Dalton Trans.* **2009**, No. 4, 680–687. https://doi.org/10.1039/B810590A.

(219) Pardo, V.; Botta, P. M.; Baldomir, D.; Rivas, J.; Piñeiro, A.; de la Calle, C.; Alonso, J. A.; Arias, J. E. Electronic Structure of the Antiferromagnetic Phase of $Sr_2Co_2O_5$. *Physica B Condens. Matter* **2008**, *403* (5–9), 1636–1638. https://doi.org/10.1016/j.physb.2007.10.207.

(220) Szpunar, I. The Lanthanide Influence on Selected Properties of $BaLnCo_2O_{6-\delta}$, Gdańsk University of Technology, Gdańsk, **2022**. https://mostwiedzy.pl/en/publication/the-lanthanide-influence-on-selected-properties-of-balnco2o6-d,162935-1 (accessed 2025-10-16).

(221) Shafeie, S.; Grins, J.; Istomin, S. Ya.; Karvonen, L.; Chen, S. A.; Chen, T. H.; Chen, J. M.; Weidenkaff, A.; Karppinen, M.; Sirtl, T.; Svensson, G. Phase Formation, Crystal Structures and Magnetic Properties of Perovskite-Type Phases in the System $La_2Co_{1+z}(Mg_xTi_{1-x})_{1-z}O_6$. *J. Solid State Chem.* **2011**, *184* (1), 177–190. https://doi.org/10.1016/j.jssc.2010.11.002.

(222) Tsipis, E. V.; Naumovich, E. N.; Patrakeev, M. V.; Yaremchenko, A. A.; Marozau, I. P.; Kovalevsky, A. V.; Waerenborgh, J. C.; Kharton, V. V. Oxygen Deficiency, Vacancy Clustering and Ionic Transport in $(La,Sr)CoO_{3-\delta}$. *Solid State Ion.* **2011**, *192* (1), 42–48. https://doi.org/10.1016/j.ssi.2010.03.029.

(223) Huang, K.; Lee, H. Y.; Goodenough, J. B. Sr- and Ni-Doped $LaCoO_3$ and $LaFeO_3$ Perovskites: New Cathode Materials for Solid-Oxide Fuel Cells. *J. Electrochem. Soc.* **1998**, *145* (9), 3220–3227. https://doi.org/10.1149/1.1838789.

(224) Budnik, J.; Gazda, M.; Miruszewski, T. Electrical and Thermoelectric Transport of $SrFe_{1-x}Co_xO_{3-\delta}$ Mixed-Conducting Perovskites. *Solid State Sci.* **2026**, *173*, 108174. https://doi.org/10.1016/j.solidstatesciences.2025.108174.

(225) Kokhanovskii, L. V.; Zonov, Yu. G.; Ol'shevskaya, O. P.; Pan'kov, V. V. Structural Stability of $SrCo_{1-x}Fe_xO_{3-\delta}$ Solid Solutions. *Inorganic Materials* **2005**, *41* (8), 876–881. https://doi.org/10.1007/s10789-005-0229-3.

(226) Tai, L. Structure and Electrical Properties of $La_{1-x}Sr_xCo_{1-y}Fe_yO_3$. Part 1. The System $La_{0.8}Sr_{0.2}Co_{1-y}Fe_yO_3$. *Solid State Ion.* **1995**, *76* (3–4), 259–271. https://doi.org/10.1016/0167-2738(94)00244-M.

(227) Shimada, H.; Yamaguchi, T.; Sumi, H.; Yamaguchi, Y.; Nomura, K. Additive Effect of NiO on Electrochemical Properties of Mixed Ion Conductor $BaZr_{0.1}Ce_{0.7}Y_{0.1}Yb_{0.1}O_{3-\delta}$. *Journal of the Ceramic Society of Japan* **2017**, *125* (4), P4-1-P4-4. https://doi.org/10.2109/jcersj2.125.P4-1.

(228) Han, D.; Uemura, S.; Hiraiwa, C.; Majima, M.; Uda, T. Detrimental Effect of Sintering Additives on Conducting Ceramics: Yttrium-Doped Barium Zirconate. *ChemSusChem* **2018**, *11* (23), 4102–4113. https://doi.org/10.1002/cssc.201801837.

(229) Bu, J.; Jönsson, P. G.; Zhao, Z. The Effect of NiO on the Conductivity of $BaZr_{0.5}Ce_{0.3}Y_{0.2}O_{3-\delta}$ Based Electrolytes. *RSC Adv.* **2016**, *6* (67), 62368–62377. https://doi.org/10.1039/C6RA09936J.

(230) Kiselev, E. A.; Proskurnina, N. V.; Voronin, V. I.; Cherepanov, V. A. Phase Equilibria and Crystal Structures of Solid Solutions in the Sr-Fe-Ni-O System at 1100°C in Air. *Inorganic Materials* **2009**, *45* (3), 271–277. https://doi.org/10.1134/S0020168509030108.

(231) Kiselev, E. A.; Proskurnina, N. V.; Voronin, V. I.; Cherepanov, V. A. Phase Equilibria and Crystal Structures of Phases in the La-Fe-Ni-O System at 1370 K in Air. *Inorganic Materials* **2007**, *43* (2), 167–175. https://doi.org/10.1134/S0020168507020148.

(232) Moore, R. J.; White, J. Equilibrium Relationships in the System NiO-CoO-O_2. *J. Mater. Sci.* **1974**, *9* (9), 1393–1400. https://doi.org/10.1007/BF00552924.

(233) Kuboon, S.; Hu, Y. H. Study of NiO–CoO and Co_3O_4–Ni_3O_4 Solid Solutions in Multiphase Ni–Co–O Systems. *Ind. Eng. Chem. Res.* **2011**, *50* (4), 2015–2020. https://doi.org/10.1021/ie101249r.

(234) Melkozerova, M.; Aksenova, T.; Gavrilova, L.; Cherepanov, V. Phase Equilibria and the Structure of Individual Phases in the Sr–Co–Ni–O System at 1100°C in Air. *Russian Journal of Physical Chemistry* **2005**, *79*, 1197–1202.

(235) Makhloufi, S.; Omari, M. Structural, Electrical and Electrochemical Characterizations of Perovskite Ni-Doped $SrCoO_{3-\delta}$. *J. Inorg. Organomet. Polym. Mater.* **2016**, *26* (1), 32–40. https://doi.org/10.1007/s10904-015-0295-1.

(236) Li, X.; Zhao, H.; Zhou, X.; Xu, N.; Xie, Z.; Chen, N. Electrical Conductivity and Structural Stability of La-Doped $SrTiO_3$ with A-Site Deficiency as Anode Materials for Solid Oxide Fuel Cells. *Int. J. Hydrogen Energy* **2010**, *35* (15), 7913–7918. https://doi.org/10.1016/j.ijhydene.2010.05.043.

(237) Katsuki, M. High Temperature Properties of $La_{0.6}Sr_{0.4}Co_{0.8}Fe_{0.2}O_{3-\delta}$ Oxygen Nonstoichiometry and Chemical Diffusion Constant. *Solid State Ion.* **2003**, *156* (3–4), 453–461. https://doi.org/10.1016/S0167-2738(02)00733-6.

(238) Teraoka, Y.; Zhang, H. M.; Okamoto, K.; Yamazoe, N. Mixed Ionic-Electronic Conductivity of $La_{1-x}Sr_xCo_{1-y}Fe_yO_{3-\delta}$ Perovskite-Type Oxides. *Mater. Res. Bull.* **1988**, *23* (1), 51–58. https://doi.org/10.1016/0025-5408(88)90224-3.

(239) Orikasa, Y.; Ina, T.; Nakao, T.; Mineshige, A.; Amezawa, K.; Oishi, M.; Arai, H.; Ogumi, Z.; Uchimoto, Y. An X-Ray Absorption Spectroscopic Study on Mixed Conductive $La_{0.6}Sr_{0.4}Co_{0.8}Fe_{0.2}O_{3-\delta}$ Cathodes. I. Electrical Conductivity and Electronic Structure. *Physical Chemistry Chemical Physics* **2011**, *13* (37), 16637. https://doi.org/10.1039/c1cp20982e.

(240) Nishiyama, S.; Nagaoka, J.; Hattori, T. Thermoelectric Properties of Several Strontium Ferrites, $SrFe_{12}O_{19}$, $SrFeO_{3-x}$ and $Sr_4Fe_6O_{13+x}$. *Transactions of the Materials Research Society of Japan* **2004**, *29*, 2825–2828.

(241) Zdiri, F.; Alonso, J. M.; Mnasri, T.; de la Presa, P.; Morales, I.; Martínez, J. L.; Ben Younes, R.; Marin, P. Effects of Partial Manganese Substitution by Cobalt on the Physical Properties of $Pr_{0.7}Sr_{0.3}Mn_{(1-x)}CoxO_3$ ($0 \leq x \leq 0.15$) Manganites. *Materials 2023, Vol. 16, Page 1573* **2023**, *16* (4), 1573. https://doi.org/10.3390/MA16041573.

(242) Wang, L.; Merkle, R.; Maier, J. Surface Kinetics and Mechanism of Oxygen Incorporation Into $Ba_{1-x}Sr_xCo_yFe_{1-y}O_{3-\delta}$ SOFC Microelectrodes. *J. Electrochem. Soc.* **2010**, *157* (12), B1802. https://doi.org/10.1149/1.3494224.

(243) Hoedl, M. F.; Gryaznov, D.; Merkle, R.; Kotomin, E. A.; Maier, J. Interdependence of Oxygenation and Hydration in Mixed-Conducting $(Ba,Sr)FeO_{3-\delta}$ Perovskites Studied by Density Functional Theory. *The Journal of Physical Chemistry C* **2020**, *124* (22), 11780–11789. https://doi.org/10.1021/ACS.JPCC.0C01924.

(244) Hoedl, M. F.; Ertural, C.; Merkle, R.; Dronskowski, R.; Maier, J. The Orbital Nature of Electron Holes in $BaFeO_3$ and Implications for Defect Chemistry. *The Journal of Physical Chemistry C* **2022**, *126* (30), 12809–12819. https://doi.org/10.1021/ACS.JPCC.2C02545.

(245) Li, K.; Xue, D. Estimation of Electronegativity Values of Elements in Different Valence States. *J. Phys. Chem. A* **2006**, *110* (39), 11332–11337. https://doi.org/10.1021/jp062886k.

(246) Vračar, M.; Kuzmin, A.; Merkle, R.; Purans, J.; Kotomin, E. A.; Maier, J.; Mathon, O. Jahn-Teller Distortion around Fe^{4+} in $Sr(Fe_xTi_{1-x})O_{3-\delta}$ from x-Ray Absorption Spectroscopy, X-Ray Diffraction, and Vibrational Spectroscopy. *Phys. Rev. B Condens. Matter Mater. Phys.* **2007**, *76* (17), 1–12. https://doi.org/10.1103/PhysRevB.76.174107.

(247) Kuzmin, A.; Purans, J.; Benfatto, M.; Natoli, C. R. X-Ray-Absorption Study of Rhenium L_3 and L_1 Edges in ReO_3: Multiple-Scattering Approach. *Phys. Rev. B* **1993**, *47* (5), 2480–2486. https://doi.org/10.1103/PhysRevB.47.2480.

List of figures

List of tables

Appendix

6.1. BCZYM group

6.1.1. Additional details of Rietveld refinement

To ascertain whether alternative space group structures more accurately represent the symmetry of the $BaCe_{0.6}Zr_{0.2}Y_{0.2-x}Fe_xO_{3-\delta}$ compounds, the crystal data of lower symmetry perovskite structures (orthorhombic and trigonal) were employed for the Rietveld refinement of the diffractograms. The structural parameters and the refinement quality indices obtained with the cubic ($Pm\bar{3}m$), orthorhombic ($Imma$), and trigonal ($R\bar{3}c$) crystal data are shown in **Tables A1** and **A2**, for $BaCe_{0.6}Zr_{0.2}Y_{0.2-x}Fe_xO_{3-\delta}$ (x = 0.02, 0.05, 0.1) and $BaCe_{0.6}Zr_{0.2}Y_{0.1}M_{0.1}O_{3-\delta}$ (M = Tb, Pr), respectively. The XRD patterns, along with the associated fitting and differential curves, are presented in **Figures A1** and **A2**.

In the case of the $BaCe_{0.6}Zr_{0.2}Y_{0.2-x}Fe_xO_{3-\delta}$ (x = 0.02, 0.05, 0.1) series, the orthorhombic and trigonal patterns should contain low-intensity reflections, which could be hidden in the background. For $BaCe_{0.6}Zr_{0.2}Y_{0.1}Tb_{0.1}O_{3-\delta}$ and $BaCe_{0.6}Zr_{0.2}Y_{0.1}Pr_{0.1}O_{3-\delta}$, the best fitting was obtained using the orthorhombic unit cell. To compare unit cell parameters of these oxides to those with cubic structures, they were recalculated according to $abc = a^3_{pseudocubic}$ and named as "pseudocubic" in the text.

Table A1. The structural parameters of cubic, orthorhombic, and trigonal $BaCe_{0.6}Zr_{0.2}Y_{0.2-x}Fe_xO_{3-\delta}$ (x = 0.02, 0.05, 0.1) unit cells obtained using Rietveld refinement, the profile function used, and the refinement quality indices (expected residual, profile residual, weighted profile residual, and goodness of fit).

		BCZYFe2			BCZYFe5			BCZYFe10		
		Cubic	Ortho-rhombic	Trigonal	Cubic	Ortho-rhombic	Trigonal	Cubic	Ortho-rhombic	Trigonal
Unit cell	a (Å)	4.3515(1)	6.1493(4)	6.1471(2)	4.3307(1)	6.1158(2)	6.1200(2)	4.3205(2)	6.0980(4)	6.1026(2)
	b (Å)		8.6849(6)			8.6508(3)			8.6321(7)	
	c (Å)		6.1743(3)	15.1259(7)		6.1437(2)	15.0348(5)		6.1294(3)	15.0101(7)
	α (°)	90	90	90	90	90	90	90	90	90
	β (°)									
	γ (°)			120			120			120
Profile function		Pseudo Voigt								
Agreement indices	R_{exp}	4.26	4.26	4.25	5.55	5.54	5.54	12.82	12.82	12.82
	R_p	4.03	4.18	4.10	4.44	4.29	4.38	13.85	15.53	16.28
	R_{wp}	5.85	6.20	6.15	6.56	6.32	6.55	18.38	20.00	20.40
	GOF	1.89	2.12	2.09	1.40	1.30	1.39	2.06	2.44	2.53

Table A2. The structural parameters of cubic, orthorhombic, and trigonal $BaCe_{0.6}Zr_{0.2}Y_{0.1}M_{0.1}O_{3-\delta}$ (M = Tb, Pr) unit cells obtained using Rietveld refinement, the profile function used, and the refinement quality indices (expected residual, profile residual, weighted profile residual, and goodness of fit).

		BCZYTb			BCZYPr		
		Cubic	Ortho-rhombic	Trigonal	Cubic	Ortho-rhombic	Trigonal
Unit cell	a (Å)	4.3470(1)	6.1425(2)	6.1463(4)	4.3487(1)	6.1434(1)	6.1439(1)
	b (Å)		8.6663(2)			8.6801(2)	
	c (Å)		6.1698(2)	15.045(2)		6.1700(1)	15.1043(3)
	α (°)	90	90	90	90	90	90
	β (°)						
	γ (°)			120			120
Profile function		Pseudo Voigt					
Agreement indices	R_{exp}	1.06	1.06	1.06	1.05	1.05	1.05
	R_p	1.00	0.87	0.98	1.19	0.97	1.17
	R_{wp}	1.48	1.21	1.42	1.91	1.43	1.95
	GOF	1.97	1.32	1.79	3.31	1.85	3.45

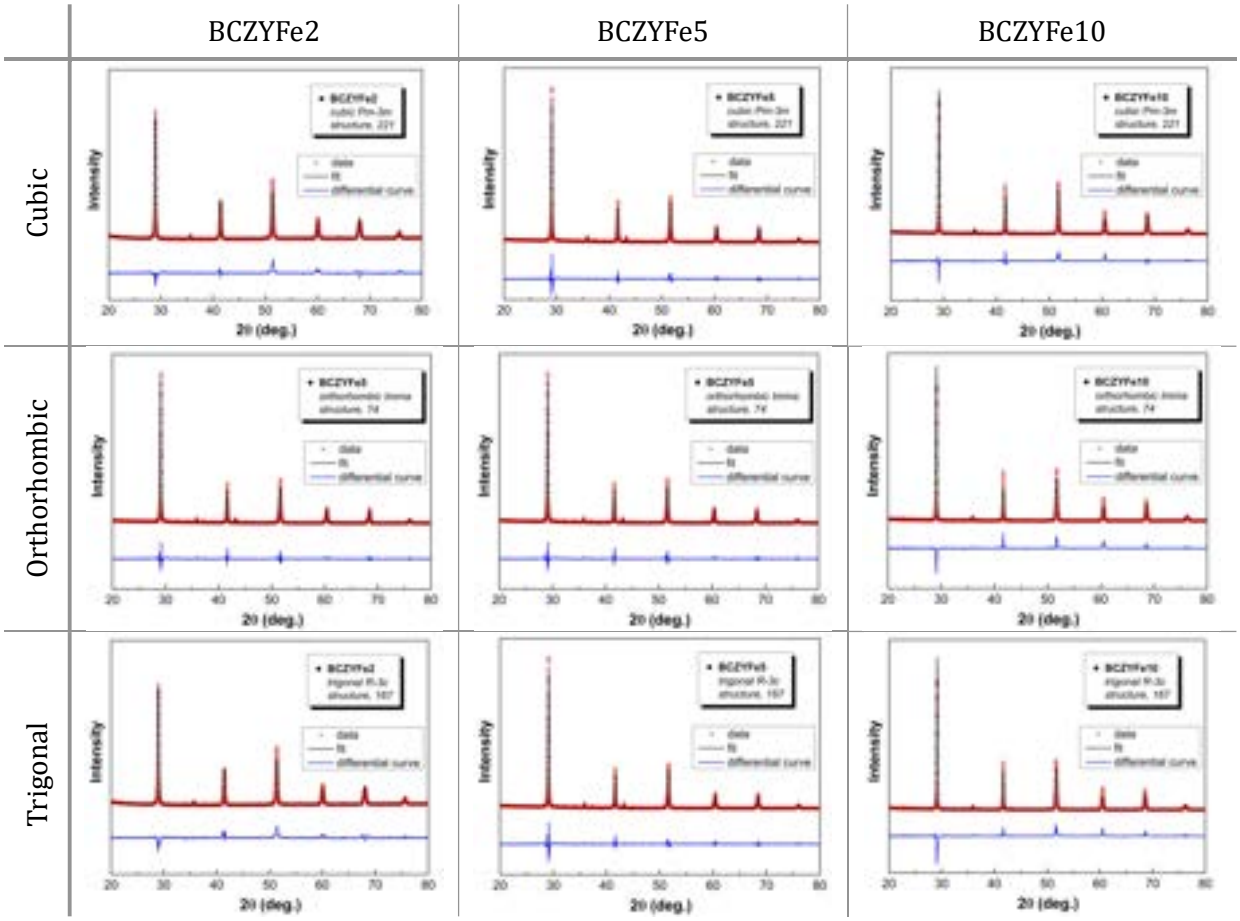

Figure A1. Diffractograms with fitting and differential curves for $BaCe_{0.6}Zr_{0.2}Y_{0.18}Fe_{0.02}O_{3-\delta}$ (BCZYFe2), $BaCe_{0.6}Zr_{0.2}Y_{0.15}Fe_{0.05}O_{3-\delta}$ (BCZYFe5), and $BaCe_{0.6}Zr_{0.2}Y_{0.1}Fe_{0.1}O_{3-\delta}$ (BCZYFe10), refined with the crystal data corresponding to cubic, orthorhombic and trigonal unit cells.

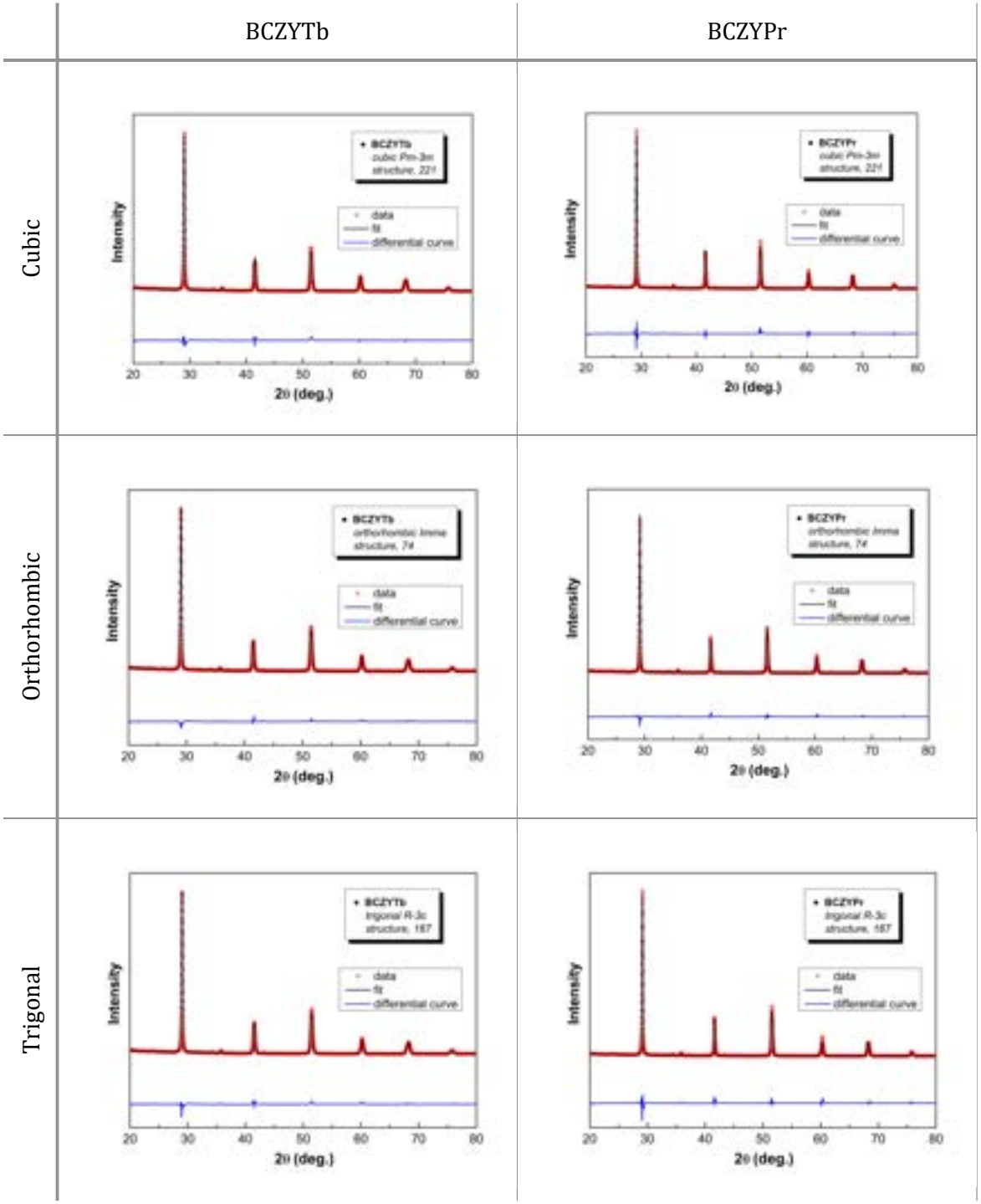

Figure A2. Diffractograms with fitting and differential curves for $BaCe_{0.6}Zr_{0.2}Y_{0.1}Tb_{0.1}O_{3-\delta}$ (BCZYTb10) and $BaCe_{0.6}Zr_{0.2}Y_{0.1}Pr_{0.1}O_{3-\delta}$ (BCZYPr10), refined with the crystal data corresponding to cubic, orthorhombic and trigonal unit cells.

6.1.2. Additional thermogravimetric measurements

Figure A3 shows the relative mass change of $BaCe_{0.6}Zr_{0.2}Y_{0.2-x}Fe_xO_{3-\delta}$ (x = 0.02, 0.05, 0.1) samples collected at 300 °C, 450 °C, and 600 °C during the atmosphere switches: from dry to wet and from wet to dry air.

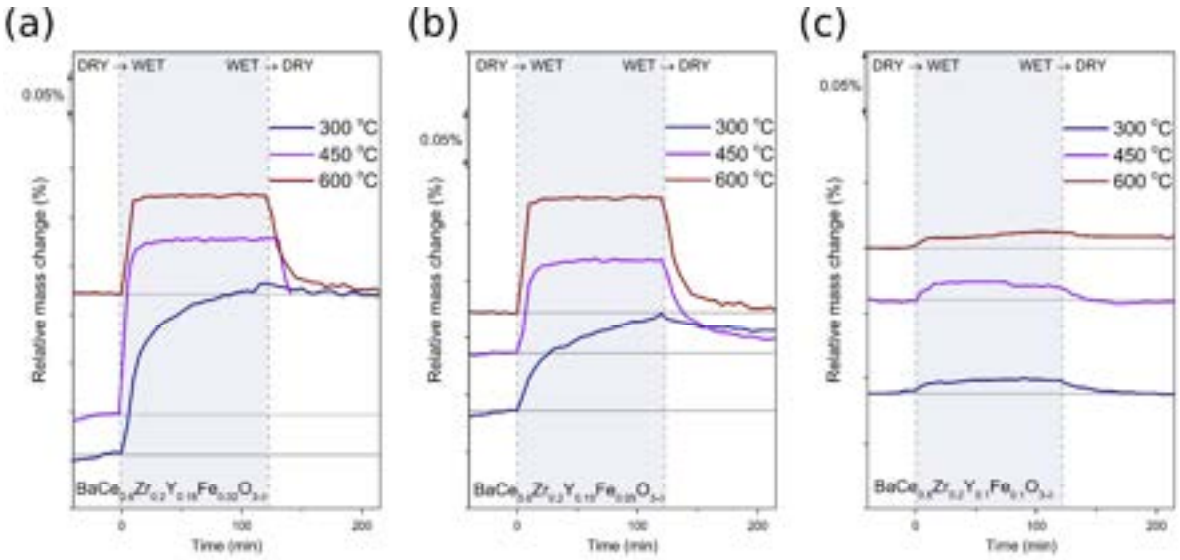

Figure A3. The relative change of mass collected for $BaCe_{0.6}Zr_{0.2}Y_{0.2-x}Fe_xO_{3-\delta}$ (x = 0.02, 0.05, 0.1) following an isothermal switch from dry to wet and from wet to dry air at 300 °C, 450 °C, and 600 °C.

The hydration analysis via thermogravimetry was additionally conducted in nitrogen at 300 °C, in order to investigate if the nature of the water-uptake process changes from hydration (in pure nitrogen) to hydrogenation or some mixed process in higher oxygen partial pressures (synthetic air). The comparison of the thermograms obtained in N_2 and air at 300 °C is shown in **Figure A4**.

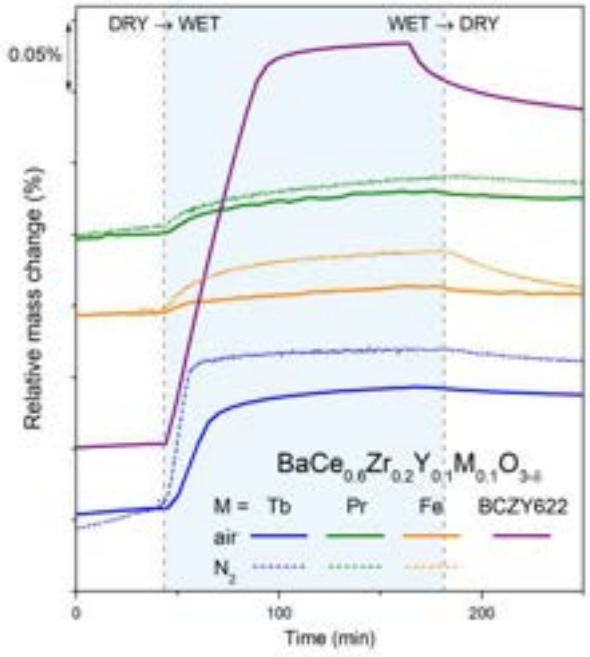

Figure A4. The relative change of mass following an isothermal switch at 300 °C between dry and wet nitrogen or air obtained for $BaCe_{0.6}Zr_{0.2}Y_{0.1}M_{0.1}O_{3-\delta}$ (M = Tb, Pr, Fe) and $BaCe_{0.6}Zr_{0.2}Y_{0.2}O_{3-\delta}$.

Reproduced from J. Budnik, A. Mielewczyk-Gryń, M. Gazda and T. Miruszewski, "Water uptake kinetics and electrical transport in $BaCe_{0.6}Zr_{0.2}Y_{0.1}M_{0.1}O_{3-\delta}$ (M = Tb, Pr, Fe) protonic conductors", J. Mater. Chem. A, 2023, 11, 13389–13398.

6.1.3. XANES spectra

The XANES spectra of hydrated and dried samples of BCZYTb10 and BCZYPr10 recorded at the L_3-edge of terbium and praseodymium are presented in **Figure A5**. The spectra of Tb_4O_7 and Pr_6O_{11} were included as references. The differences between dried and hydrated samples are not apparent in the spectra of both materials. However, based on change in the spectral features in comparison to reference data, the average oxidation states of Tb in both BCZYTb10 samples most likely exceed those present in the reference oxide Tb_4O_7 (which corresponds to $Tb^{3.5+}$). The shape of the Pr L_3-edge is close to the one observed in Pr_6O_{11}, indicating an average oxidation state of praseodymium in BCZYPr10 samples close to the reference (3.67+), but the main maximum is located at higher energy, which suggest that the oxidation state of praseodymium is slightly higher.

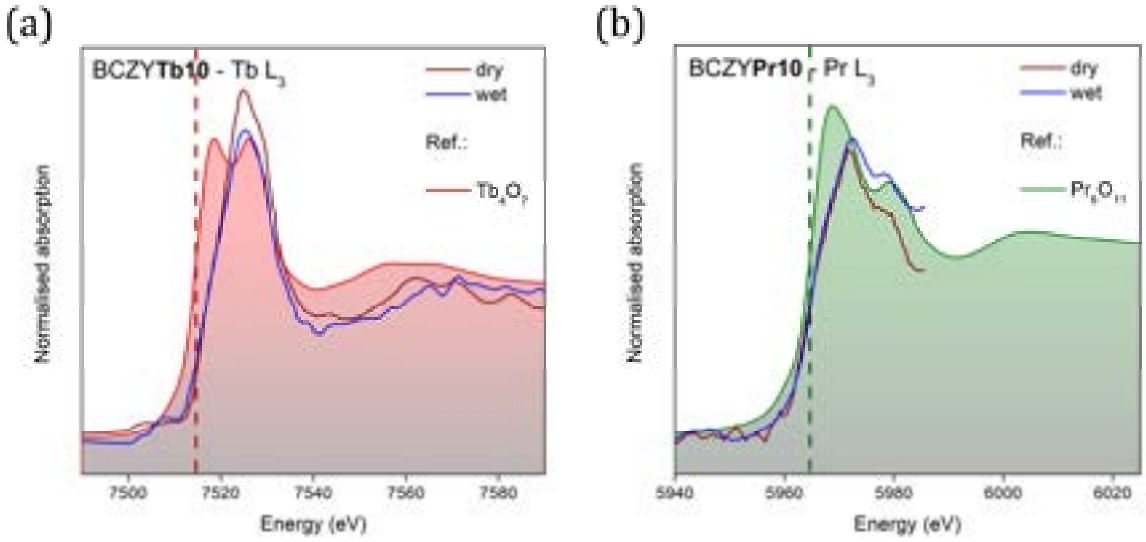

Figure A5. The XANES spectra recorded in transmission mode for dried and hydrated samples of BCZYTb10 at the L_3-edge of terbium (a) and BCZYPr10 at the L_3 edge of praseodymium (b).

Figure A6 shows the XANES spectra recorded in fluorescence mode for dried and hydrated BCZYFe2, BCZYFe5, and BCZYFe10 at the K-edge of iron. The spectra of iron in varying oxidation states (metallic foil and oxides measured in transmission mode) were added as references. The dashed lines indicate the absorption edges for each reference, corresponding to iron in oxidation states 0, 2+, and 3+, respectively. The precise determination of the average oxidation state of iron in the studied BCZYM materials was not feasible due to the low quality of the collected spectra, caused by the low iron content in the studied compounds. Nevertheless, the position of absorption edges corresponding to BCZYFe2, BCZYFe5, and BCZYFe10 is very close to the Fe_2O_3 edge, indicating that the average oxidation state of iron in those compounds is close to 3+. The hydration of samples does not affect the shape of the spectra, nor the position of E_0, which suggests that the introduction of protons do not change the local environment around Fe ions substantially.

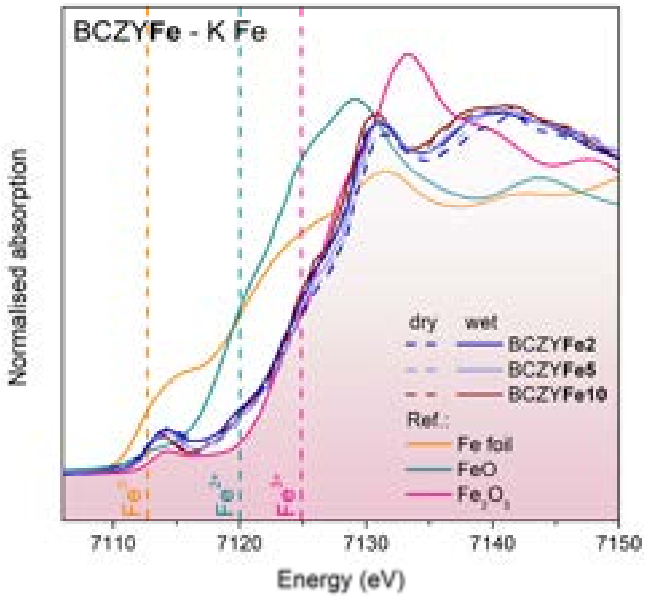

Figure A6. The XANES spectra of dried and hydrated samples of BCZYFe2, BCZYFe5, and BCZYFe10 recorded at the K-edge of iron in fluorescence mode, as well as the spectra for reference compounds measured in transmission mode. The dashed lines indicate the position of the absorption edge for each reference.

Figure A7 presents the XANES spectra recorded in transmission mode for dried and hydrated samples of $BaCe_{0.6}Zr_{0.2}Y_{0.2-x}M_xO_{3-\delta}$ at the L_3-edge of cerium. The spectrum of CeO_2 has been included in every plot as a reference. CeO_2 powder was subjected to thermal treatment in an oxygen atmosphere prior to the measurement, in order to ensure high oxidation state of cerium (≈ 100% of 4+). The shape of the BCZYM spectra differ from the reference CeO_2, which indicates different electronic structure and coordination geometry around cerium ion in the perovskites. The shape of the spectrum is similar to that of CeO_2, but the additional feature C at ≈ 5724 eV suggests some Ce^{3+} in BCZYM materials. Nevertheless, cerium assumes an average oxidation state close to 4+. The biggest difference between dried and hydrated samples was observed for BCZYFe2 and BCZYFe5, which might be connected to a significant proton concentration detected in those samples (see **Table 5.2**). The spectra of iron did not change significantly between dried and hydrated states. This suggests that protons might preferentially localise on oxygen atoms around other B-site ions, e.g. cerium, which might be observed as a change in the characteristics of the spectra measured at Ce L_3-edge. There is no significant change in the spectra of BCZYFe10, BCZYPr10, and BCZYTb10. This may be caused by either a low proton concentration (BCZYFe10) or by preferential localisation of protons around praseodymium and terbium (BCZYPr10, and BCZYTb10). To support this hypothesis, it should be noted that the spectra at Tb and Pr L_3-edges (**Figures A5a, b**) show a visible difference between dried and hydrated sample, which indicate that protons might preferentially localise on oxygen atoms surrounding terbium and praseodymium.

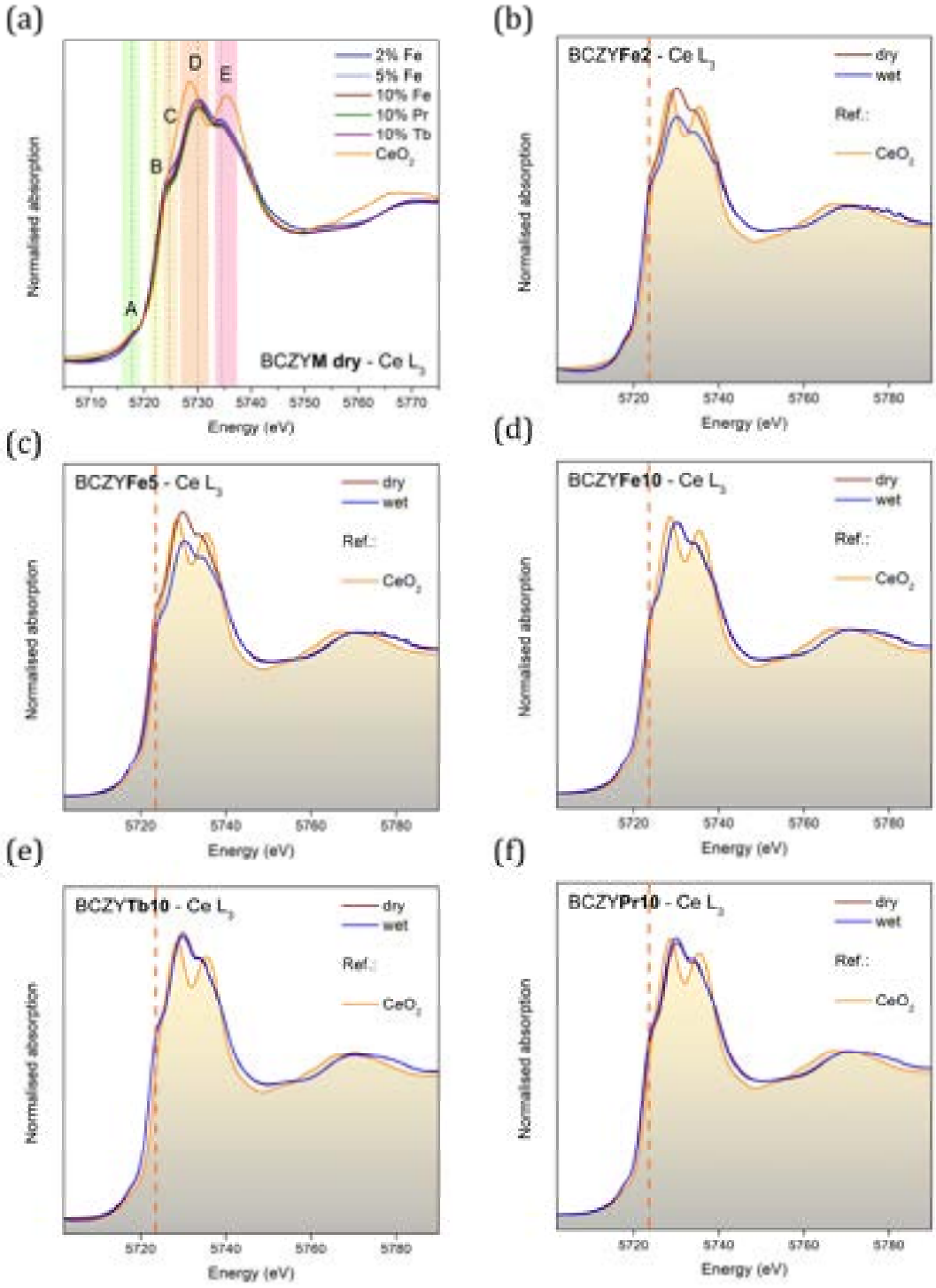

Figure A7. The XANES spectra recorded in transmission mode for dried and hydrated samples of $BaCe_{0.6}Zr_{0.2}Y_{0.2-x}M_xO_{3-\delta}$ at the L_3-edge of cerium: (a) all dried BCZYM compositions, (b) $BaCe_{0.6}Zr_{0.2}Y_{0.18}Fe_{0.02}O_{3-\delta}$, (c) $BaCe_{0.6}Zr_{0.2}Y_{0.15}Fe_{0.05}O_{3-\delta}$, (d) $BaCe_{0.6}Zr_{0.2}Y_{0.1}Fe_{0.1}O_{3-\delta}$, (e) $BaCe_{0.6}Zr_{0.2}Y_{0.1}Tb_{0.1}O_{3-\delta}$, (f) $BaCe_{0.6}Zr_{0.2}Y_{0.1}Pr_{0.1}O_{3-\delta}$. The letters in (a) mark the positions corresponding to electron transitions occurring at those energies.

6.1.4. Cation electronegativity evaluation

The electronegativities of A and B cations within $BaCe_{0.6}Zr_{0.2}Y_{0.2-x}M_xO_{3-\delta}$ (M = Fe, Tb, Pr) materials were calculated based on the values provided by Li et al.[246], which take into account the valence state and coordination number of each ion. The electronegativity of B has been

established as a weighted average of the electronegativities corresponding to Ce, Zr, Y, and M with the application of their molar content in each compound:

$$\chi_B = 0.6 \cdot \chi_{Ce} + 0.2 \cdot \chi_{Zr} + (0.2 - x) \cdot \chi_Y + x \cdot \chi_M \quad (6.1)$$

To properly estimate the electronegativity of M cations, which generally possess a variable valence, the oxidation state of M cation (OS_M) in each BCZYM material has been estimated based on the values of oxygen nonstoichiometry δ obtained using the iodometric titration:

$$OS_M = \frac{0.2 - 2\delta + 3x}{x} \quad (6.2)$$

The oxidation state of cerium, in view of the Ce L-edge spectra of the BCZYM compounds (see **Figure A7**), was assumed to be 100% 4+. The electronegativity of iron was assumed to be equal to the value corresponding to Fe^{3+}, based on the XAS analysis of the K-edge spectra of iron (**Figure A6**).

6.1.5. Impedance data analysis

Figure A8 presents Nyquist plots obtained for $BaCe_{0.6}Zr_{0.2}Y_{0.2-x}Fe_xO_{3-\delta}$ (x = 0.02, 0.05, 0.1) samples, along with the fitted curves and corresponding equivalent circuits. Each plot represents measurements performed in dry and wet air atmospheres at 300 °C and 800 °C.

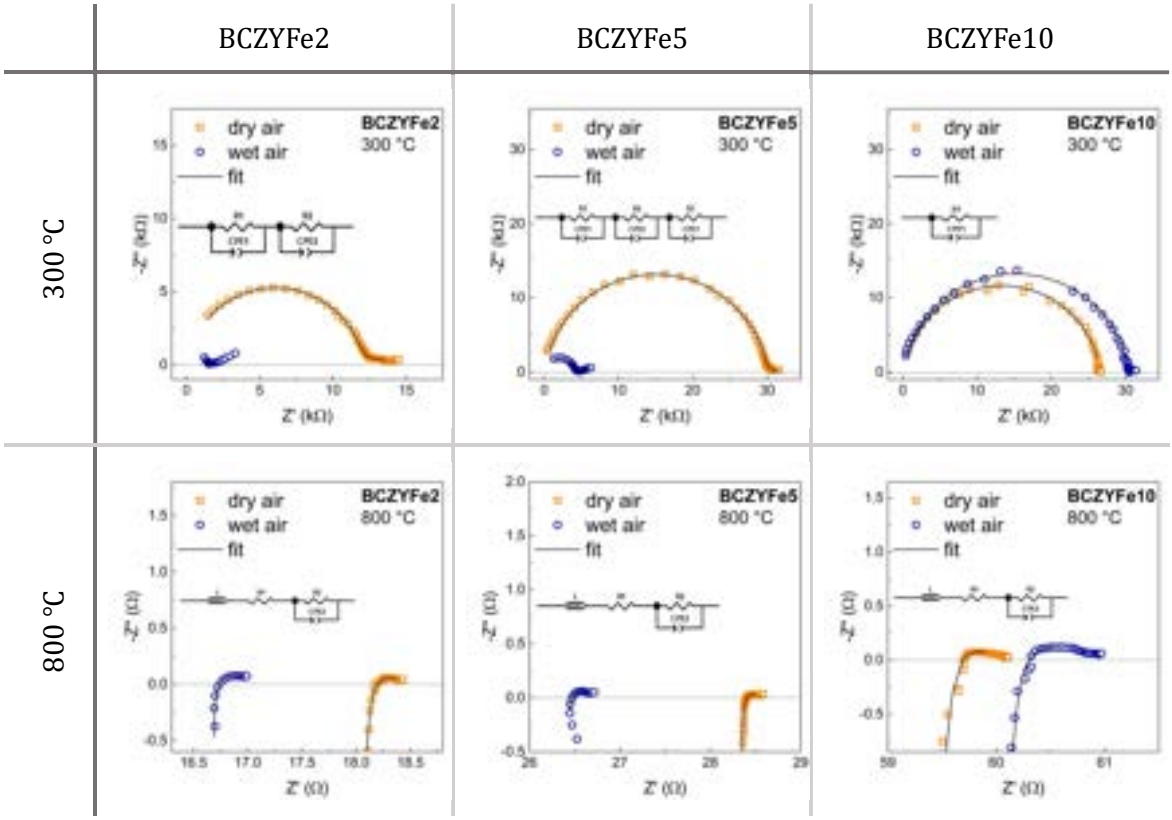

Figure A8. Nyquist plots obtained for $BaCe_{0.6}Zr_{0.2}Y_{0.18}Fe_{0.02}O_{3-\delta}$ (BCZYFe2), $BaCe_{0.6}Zr_{0.2}Y_{0.15}Fe_{0.05}O_{3-\delta}$ (BCZYFe5), and $BaCe_{0.6}Zr_{0.2}Y_{0.1}Fe_{0.1}O_{3-\delta}$ (BCZYFe10), with the curves fitted using the equivalent circuits shown in each plot.

6.1.6. Additional ECR data and details about the fitting procedure

The dimensions of BCZYFe samples examined during hydration/dehydration and oxidation/reduction via the ECR method, along with the values of the L parameter and the coefficients obtained by fitting for each procedure and temperature, are provided in **Tables A2** and **A3**. An evaluation of electrical conductivity response was conducted utilising the nonlinear least squares method. The fitting ranges for k_{chem} and D_{chem} were set to $10^{-6} - 10^{-4}$ cm/s and $10^{-8} - 10^{-4}$ cm^2/s, respectively. **Figure A9** and **A10** present the representative ECR data with fitted curves for hydration and oxidation in $BaCe_{0.6}Zr_{0.2}Y_{0.2-x}Fe_xO_{3-\delta}$ (x = 0.02, 0.05, 0.1). The analysis of two-fold relaxation of water involved dividing the data into regions dominated by H and O, which were then fitted independently, as illustrated in **Figure A9a.**

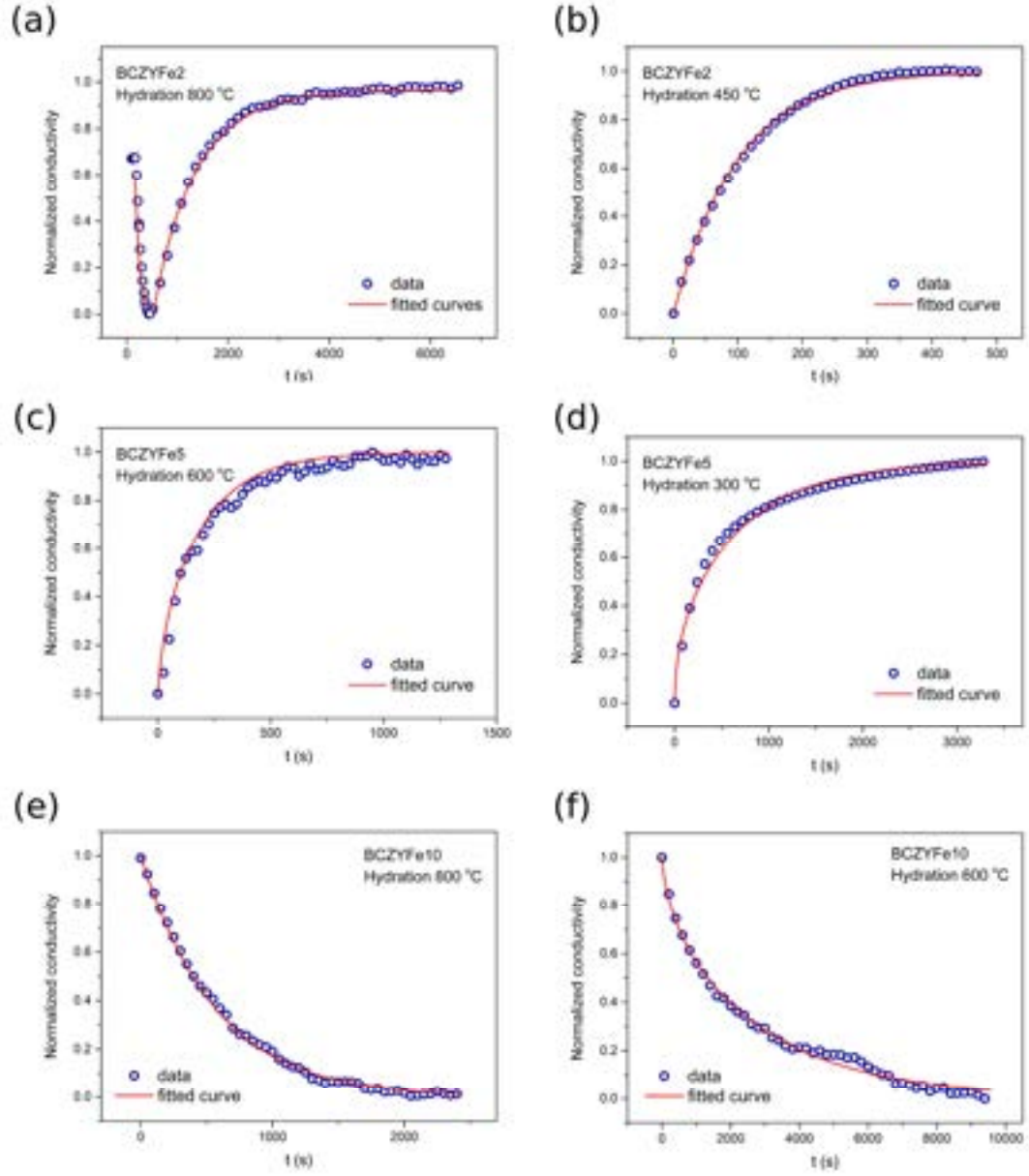

Figure A9. The representative ECR data with the fitted curves obtained for hydration of $BaCe_{0.6}Zr_{0.2}Y_{0.18}Fe_{0.02}O_{3-\delta}$ (a-b), $BaCe_{0.6}Zr_{0.2}Y_{0.15}Fe_{0.05}O_{3-\delta}$ (c-d), and $BaCe_{0.6}Zr_{0.2}Y_{0.1}Fe_{0.1}O_{3-\delta}$ (e-f).

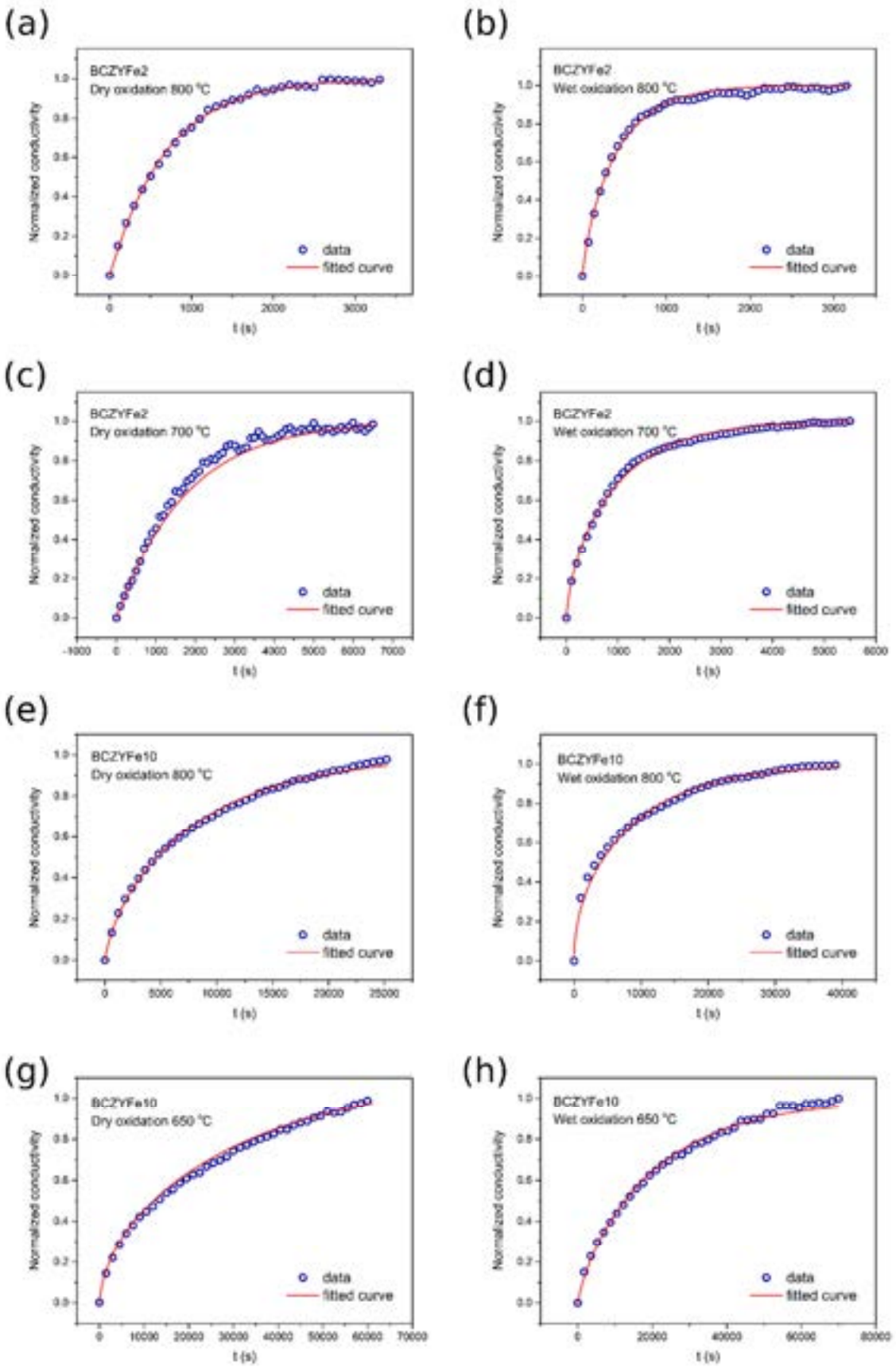

Figure A10. The representative ECR data with the fitted curves obtained for oxidation of $BaCe_{0.6}Zr_{0.2}Y_{0.18}Fe_{0.02}O_{3-\delta}$ (a -d), and $BaCe_{0.6}Zr_{0.2}Y_{0.1}Fe_{0.1}O_{3-\delta}$ (e-h) measured at dry and wet conditions.

Table A3. The dimensions of samples examined during hydration and dehydration using the ECR method, along with the values of *L* parameter and the coefficients established through fitting for each process and temperature.

Material	Dimensions of sample	Process	T (°C)		L	Determined
BCZYFe2	14.9 mm × 8.1 mm × 1.75 mm	Hydration	850	H	2.3×10^{-5}	k
				O	0.34	D and k
			800	H	1.7×10^{-5}	k
				O	0.45	D and k
			750	H	1.4×10^{-5}	k
				O	0.86	D and k
			700	H	1.7×10^{-5}	k
				O	1.4	D and k
			650	H	1.1×10^{-5}	k
				O	1.8	D and k
			600	H	2.7×10^{-5}	k
				O	2.3	D and k
			550	H	1.9×10^{-5}	k
				O	4.6	D and k
			500	Single-fold	1.9×10^{-5}	k
			450		1.4×10^{-4}	k
			350		1.0	D and k
		Dehydration	850	H	1.4×10^{-5}	k
				O	2.8	D and k
			800	H	2.4×10^{-5}	k
				O	1.2	D and k
			750	H	2.0×10^{-5}	k
				O	1.4	D and k

			700	H	2.5×10^{-5}	k
				O	1.9	D and k
			650	H	9.9×10^{-5}	k
				O	0.8	D and k
			600	H	3.0×10^{-5}	k
				O	0.32	D and k
			550	H	1.9×10^{-5}	k
				O	0.32	D and k
BCZYFe5	15.4 mm × 8.55 mm × 2.0 mm	Hydration	800	Single-fold	5.1	D and k
			750		5.2	D and k
			650		7.4×10^{7}	D
			600		3.8	D and k
			550		7.7	D and k
			500		3.0	D and k
			450		3.3	D and k
			400		3.8	D and k
			350		2.0	D and k
			300		1.2×10^{7}	D
		Dehydration	800		11.4	D and k
			750		22.2	D and k
			650		7.6×10^{6}	D
			600		8.4×10^{6}	D
			500		65	D
			450		80	D
			400		80	D and k
			350		2.3×10^{5}	D
			300		4.1×10^{5}	D

BCZYFe10	15.7 mm × 8.65 mm × 2.75 mm	Hydration	800		2.4×10^{5}	k
			750		6.8×10^{-2}	D and k
			700		9.7×10^{-2}	D and k
			600		2.3	D and k
			550		2.5	D and k
			500		8.3	D and k
		Dehydration	800		0.42	k
			750		12	D and k
			700		1.9×10^{-5}	k
			600		3.1×10^{-5}	k
			550		9.4×10^{-5}	k
			500		4.0×10^{-4}	k

Table A4. The dimensions of samples examined during oxidation/reduction using the ECR method, along with the *L* parameter values and the coefficients established through fitting for each process and temperature.

Material	Dimensions of sample	Process		T (°C)	L	Determined
BCZYFe2	14.9 mm × 8.1 mm × 1.75 mm	Dry	Oxidation	800	1.5×10^{-5}	k
				750	3.5×10^{-6}	k
				700	1.5×10^{-5}	k
				650	8.1×10^{-6}	k
				600	2.3×10^{-6}	k
			Reduction	800	12	D and k
				750	9.3	D and k
				700	12	D and k
				600	1.1×10^{6}	D

		Wet	Oxidation	800	1.8	D and k
				750	0.27	k
				700	4.2	D and k
				650	2.5	D and k
			Reduction	800	2.7	D and k
				750	3.3	D and k
				700	3.5	D and k
				600	2.6	D and k
BCZYFe10	14.2 mm × 7.9 mm × 1.6 mm	Dry	Oxidation	800	15	D and k
				750	10	D and k
				700	16	D and k
				650	38	D
			Reduction	800	4.2	D and k
				750	6.2	D and k
				700	7.8	D and k
				650	1.0×10^3	D
		Wet	Oxidation	800	4.5	D and k
				750	8.3	D and k
				700	9.3	D and k
				650	22	D and k
			Reduction	800	1.1×10^5	D
				750	3.1×10^5	D
				700	8.3×10^6	D
				650	6.8	D and k

6.1.7. The derivation of the maximum proton mobility formula

The upper limit of proton mobility can be evaluated using the electrical conductivity values and the proton concentrations at 300 °C. The sum of two partial conductivities represents the total electrical conductivity in dry atmospheres:

$$\sigma_{dry} = \sigma_{h,dry} + \sigma_{O,dry}, \tag{6.3}$$

where $\sigma_{h,dry}$ and $\sigma_{\mathrm{O},dry}$ are the partial conductivity of electron holes and oxygen ions in dry conditions, respectively. The total electrical conductivity in humid air can be described as:

$$\sigma_{wet} = \sigma_{h,wet} + \sigma_{O,wet} + \sigma_{OH}, \tag{6.4}$$

where $\sigma_{h,\mathrm{wet}}$ and $\sigma_{\mathrm{O,wet}}$ represent the partial conductivity of electron holes and oxygen ions in wet conditions, respectively, while σ_{OH} is the partial conductivity of protons. The difference between the total conductivity in wet and dry air equals:

$$\Delta\sigma = \sigma_{wet} - \sigma_{dry}. \tag{6.5}$$

Assuming a constant oxygen-ion mobility in both dry and humid atmospheres, we obtain:

$$\Delta\sigma = \sigma_{h,wet} + \sigma_{O,wet} + \sigma_{OH} - \sigma_{h,dry} - \sigma_{O,dry}. \tag{6.6}$$

Assuming that $\sigma_{h,wet} \approx \sigma_{h,dry}$, $\delta \approx [v_O^{\bullet\bullet}]_{300℃}$, and $u_{v_O^{\bullet\bullet},wet} \approx u_{v_O^{\bullet\bullet},dry} \rightarrow u_{v_O^{\bullet\bullet}}$, the difference between the total conductivity in wet and dry air may be expressed as:

$$\Delta\sigma = \sigma_{O,wet} + \sigma_{OH} - \sigma_{O,dry} = \tag{6.7}$$

$$= 2e[v_O^{\bullet\bullet}]_{wet}u_{v_O^{\bullet\bullet},wet} - 2e[v_O^{\bullet\bullet}]_{dry}u_{v_O^{\bullet\bullet},dry} + e[OH_O^{\bullet}]u_{OH_O^{\bullet}} = \tag{6.8}$$

$$= 2e(\delta - \tfrac{[OH_O^{\bullet}]}{2})u_{v_O^{\bullet\bullet}} - 2e\delta u_{v_O^{\bullet\bullet}} + e[OH_O^{\bullet}]u_{OH_O^{\bullet}} = \tag{6.9}$$

$$= e[OH_O^{\bullet}]u_{OH_O^{\bullet}} - 2e\frac{[OH_O^{\bullet}]}{2}u_{v_O^{\bullet\bullet}} \tag{6.10}$$

Therefore:

$$\Delta\sigma = e[OH_O^{\bullet}](u_{OH_O^{\bullet}} - u_{v_O^{\bullet\bullet}}), \tag{6.11}$$

which allows the determination of the proton mobility $u_{OH_O^{\bullet}}$ as:

$$u_{OH_O^{\bullet}} = \frac{\Delta\sigma}{e[OH_O^{\bullet}]} + u_{v_O^{\bullet\bullet}}. \tag{6.12}$$

Since the mobility of oxygen vacancies $u_{v_O^{\bullet\bullet},\sigma_O}$ is known only at 600 °C, it will be used as upper limit ($u_{v_O^{\bullet\bullet},max}$) also at lower temperatures. Consequently, the upper threshold of proton mobility at 300 °C can be defined as:

$$u_{OH_O^{\bullet},max} = \frac{\Delta\sigma}{e[OH_O^{\bullet}]} + u_{v_O^{\bullet\bullet},max}. \quad (6.13)$$

6.1.8. Temperature dependence of oxygen nonstoichiometry

Figure A11 shows the temperature dependence of oxygen nonstoichiometry for $BaCe_{0.6}Zr_{0.2}Y_{0.2-x}M_xO_{3-\delta}$. The values correspond to the change in relation to the values obtain at room temperature via iodometric titration and were obtained using TG during cooling (with cooling rate 2 °/min).

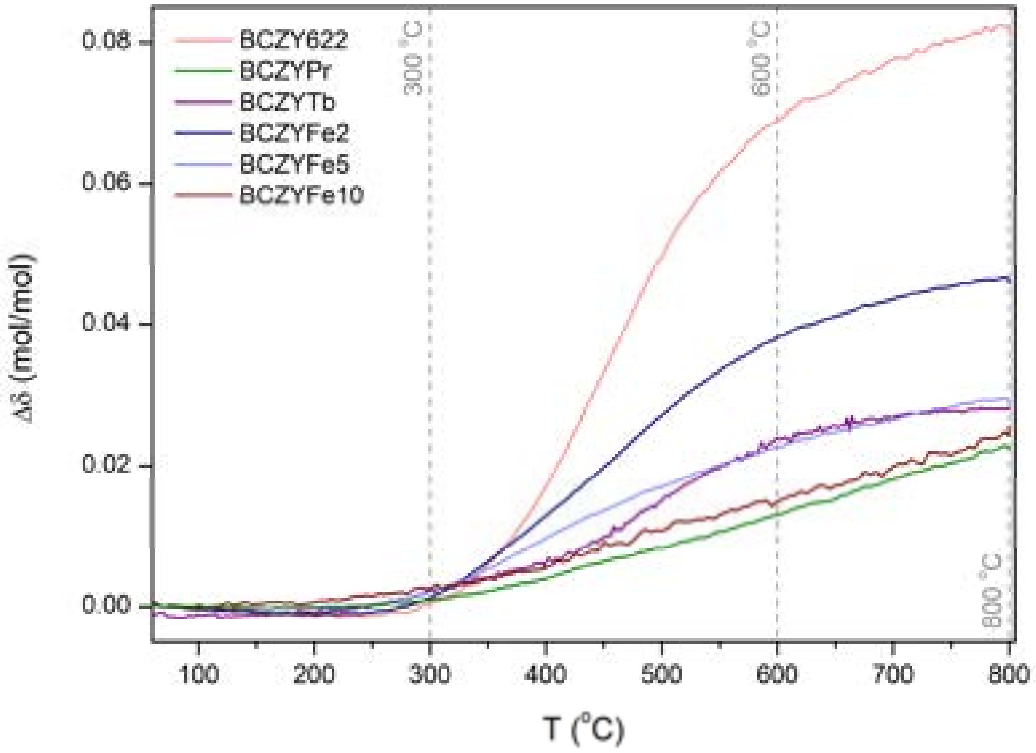

Figure A11. Temperature dependence of oxygen nonstoichiometry change (relative to the values obtain at room temperature) for $BaCe_{0.6}Zr_{0.2}Y_{0.2-x}M_xO_{3-\delta}$.

6.2. SFC group

6.2.1. The samples obtained without NiO

The XRD diffraction patterns of $Sr(Fe,Co)_{3-\delta}$ samples obtained using the multiple-step SSRS synthesis without the usage of NiO are shown in **Figure A12**. The samples of $SrFe_{1-x}Co_xO_{3-\delta}$, where $x \leq 0.8$, were single-phase and exhibited a cubic crystal structure, while for the two samples with higher cobalt content ($x = 0.9$ and 1), a single-phase composition was not achieved.

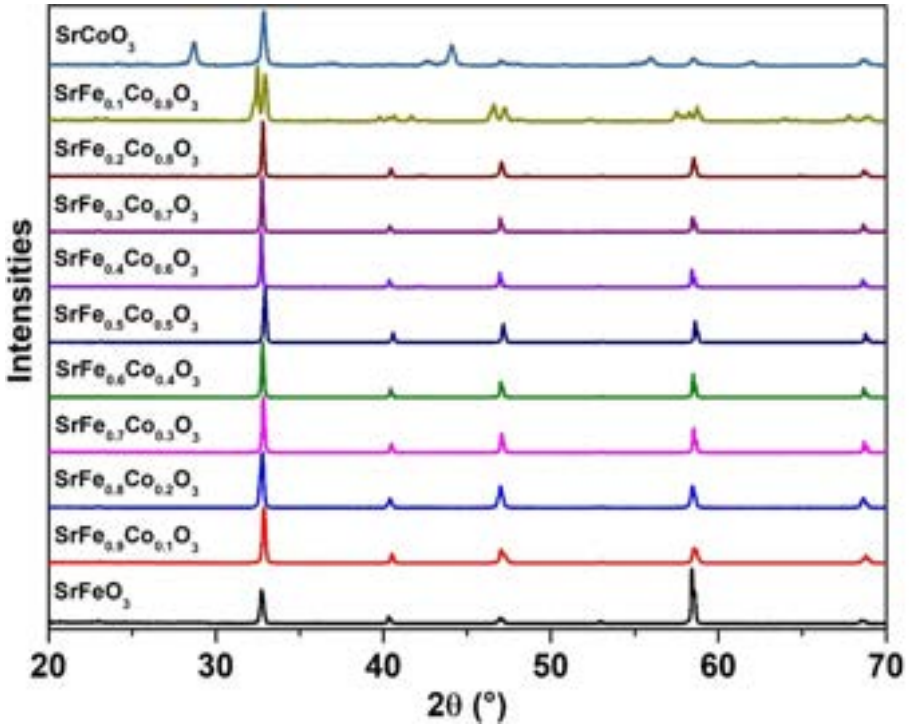

Figure A12. The XRD patterns collected at room temperature for $SrFe_{1-x}Co_xO_{3-\delta}$ (x = 0, 0.2, 0.4, 0.6, 0.8) samples, synthesised without any sintering aid.

6.2.2. The derivation of the centroid and integration area of pre-edge peaks

The pre-edge peak curve was fitted to the spectrum with the pre-peak shape isolated from the stronger signals arising from more intense electron transitions (treated here as a background and removed). The centroid position and the area under the resulting curve were subsequently examined. The integration limits were set at the points where the pre-edge peak intensity diminished, as illustrated in **Figure A13**.

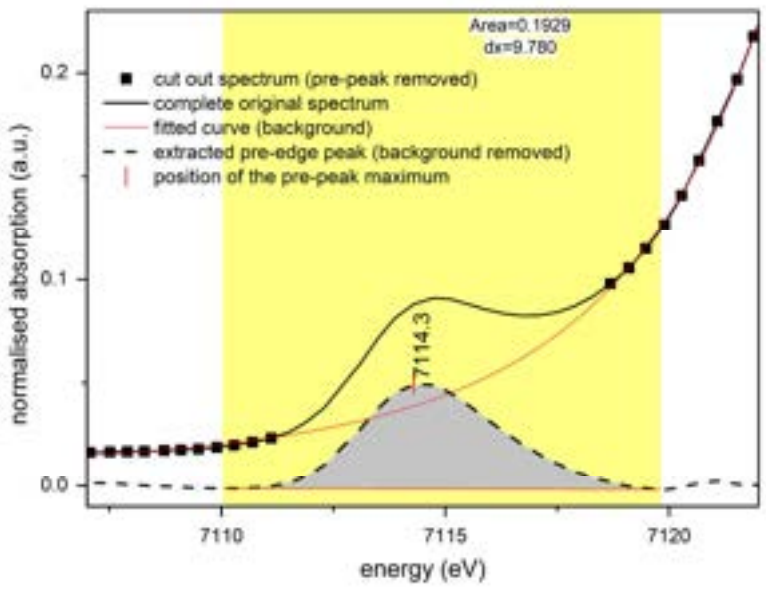

Figure A13. The pre-edge peak extraction and centroid determination performed for the iron K-edge spectrum of $SrFe_{0.2}Co_{0.8}O_{3-\delta}$.

6.2.3. The first derivatives of XANES spectra at iron and cobalt K-edges

Figure A14 presents the first derivatives of XANES spectra collected for $SrFe_{1-x}Co_xO_{3-\delta}$ (x = 0, 0.2, 0.4, 0.6, 0.8) at the K-edges of iron and cobalt. The electron transitions occurring in the marked energy regions are labelled on the plots.

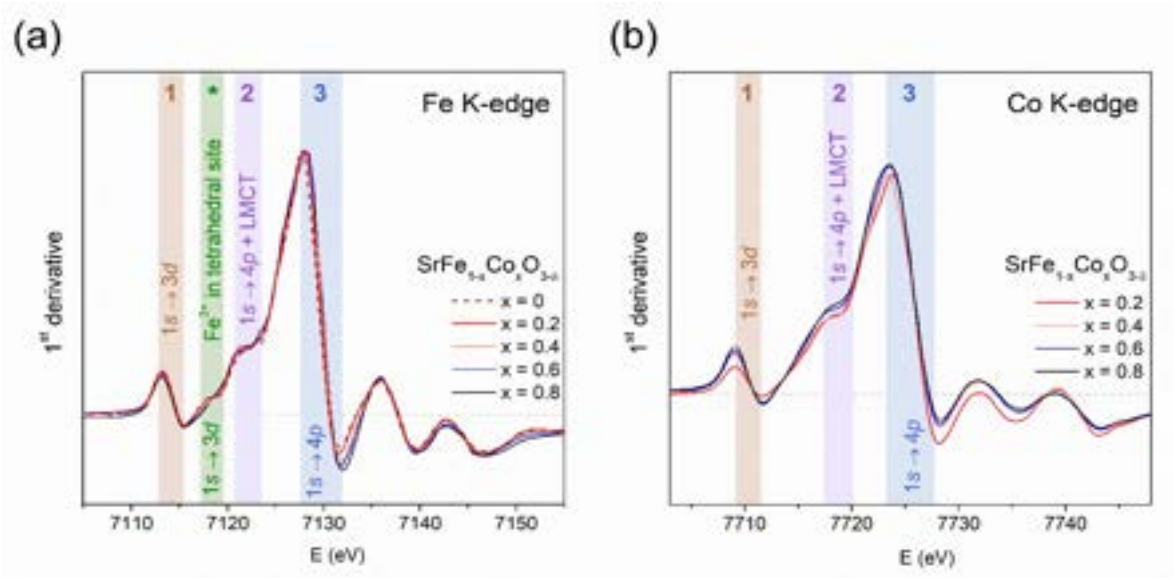

Figure A14. The first derivatives of the $SrFe_{1-x}Co_xO_{3-\delta}$ (x = 0, 0.2, 0.4, 0.6, 0.8) XANES absorption spectra recorded at the K-edge of iron (a) and cobalt (b), respectively. The markers represent the electron transitions taking place in the specified energy regions.

6.2.4. EXAFS analysis

The K-edge spectra of Fe and Co were analysed in the EXAFS range to investigate the local structure of the transition-metal cations in more detail. **Figure A15** shows the Fourier transforms (FT) of EXAFS signals at the K-edges of Fe and Co for $SrFe_{1-x}Co_xO_{3-\delta}$. The shown FT curves were shifted, in accordance with the applied phase correction. The labels of the main maxima correspond to the coordination shells responsible for their occurrence. The first maximum corresponds to the bonds between the central (absorbing transition metal) atom and the neighbouring oxygen atoms, the second is associated with the bond with strontium atoms, whereas the third maximum is related to the next closest transition metal (Fe or Co), located in the adjacent unit cells.

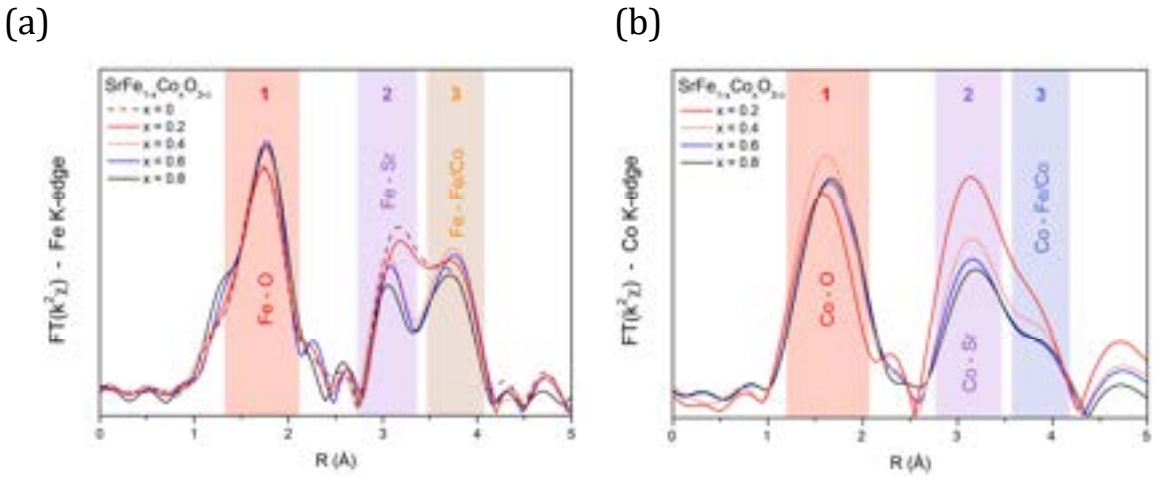

Figure A15. The Fourier transforms of EXAFS of $SrFe_{1-x}Co_xO_{3-\delta}$ (x = 0, 0.2, 0.4, 0.6, 0.8) samples recorded at the K-edge of iron (a) and cobalt (b).

In comparison to the Fe–O bond length observed in samples with a higher concentration of Co, the distance between iron and oxygen in $SrFeO_{3-\delta}$ and $SrFe_{0.8}Co_{0.2}O_{3-\delta}$ is reduced. This aligns with the pre-edge feature *, associated with lower coordination around the Fe ion, observed in the XANES spectra of these materials. This feature can be related to a lower ionic radius for this coordination compared to the octahedral one.[168] Moreover, the first maximum is shifted towards higher values of R, and the intensity for this coordination shell shows a slight increase with the rising amount of cobalt in the materials. This aligns with the findings from the pre-peak centroid analysis, suggesting a moderate rise in coordination number as the Co amount increases. The observed trend of elongating TM–O bond lengths is evident in the case of cobalt, with the first maximum shifted towards greater R values. Nonetheless, the Co–O bond lengths, as shown by the position of the first maximum in **Figure A15b**, are notably shorter than those recorded for Fe–O, despite the average oxidation states of Co being lower than those of iron across all examined materials. The reduced Co–O bond length may be attributed, in part, to the smaller ionic radius of Co^{3+}.

Even in a high-spin state, Co^{3+} exhibits a radius that is less than that of Fe^{3+} (0.61 Å compared to 0.645 Å, for HS $^{[6]}Co^{3+}$ and HS $^{[6]}Fe^{3+}$, respectively).[168] Additionally, there could be alternative explanations for the reduction in the ionic radius, including a decrease in the spin state or a lower average cation coordination.[210] The lower spin state of cobalt corresponds to a reduced ionic radius of 0.545 Å compared to 0.61 Å for $^{[6]}Co^{3+}$ in the high-spin state.[168]

The third maximum primarily results from multiple scattering (TM–O–TM path). The proximity of the TM–O–TM angle to 180° results in a more distinct maximum associated with the third coordination shell in the Fourier transforms of EXAFS. This can be explained by the "lens effect" of the atom in the middle (oxygen), whose increased forward-scattering amplitude amplifies the obtained signal.[247,248] Moreover, Haas et al. noted that the first maximum increasingly dominated the second and third maxima as the unit cell symmetry of $La_{1-x}Sr_xFeO_{3-\delta}$ lowered from cubic to rhombohedral, and orthorhombic, accompanied by an increase in the octahedra distortion.[199]

Figure A16 illustrates the ratios between the intensity corresponding to the first and second main peaks. There is a trend of increasing intensity of the first main maximum in comparison to the second maximum with increasing cobalt content, which can be observed for the K-edge of both Fe and Co. Nonetheless, no similar tendency was observed regarding the third maximum, which is also ascribed to the multiple scattering paths of linear TM–O–TM configurations within the perovskite structure. Consequently, it remains unclear whether the BO_6 undergo rotation or if the transition metal displaces within the octahedron.

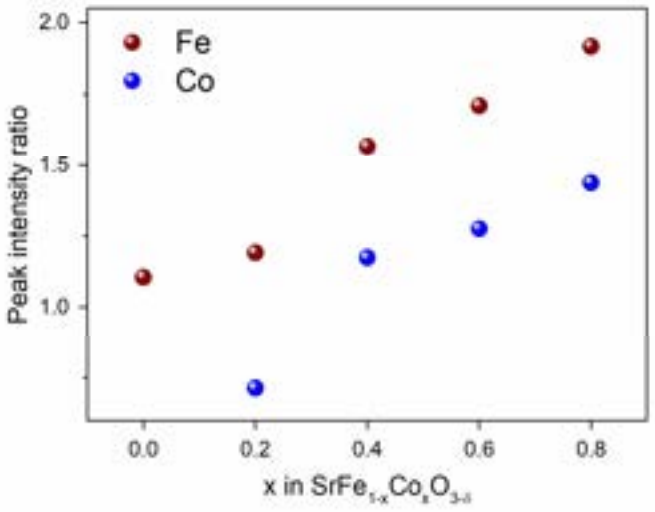

Figure A16. The ratio between the intensities of the maxima associated with the first and second coordination shells of the central atom in the Fourier transform of EXAFS (see **Figure A15**).

6.2.5. XANES spectra – $L_{3,2}$ edges of iron and cobalt

The XANES spectra of all investigated SFC materials recorded at both edges are presented in **Figure A17**. The first maximum (L_3) results from the excitation of the $2p_{3/2}$ core

electrons of the absorbing transition metal. The second maximum (L_2) is associated with the excitation of the $2p_{1/2}$ core electrons. The variations in the shape of the Fe $L_{3,2}$ spectra among the examined materials are not evident. The energy corresponding to the Co L_3 maximum progressively shifts to higher energies with increasing Co content.

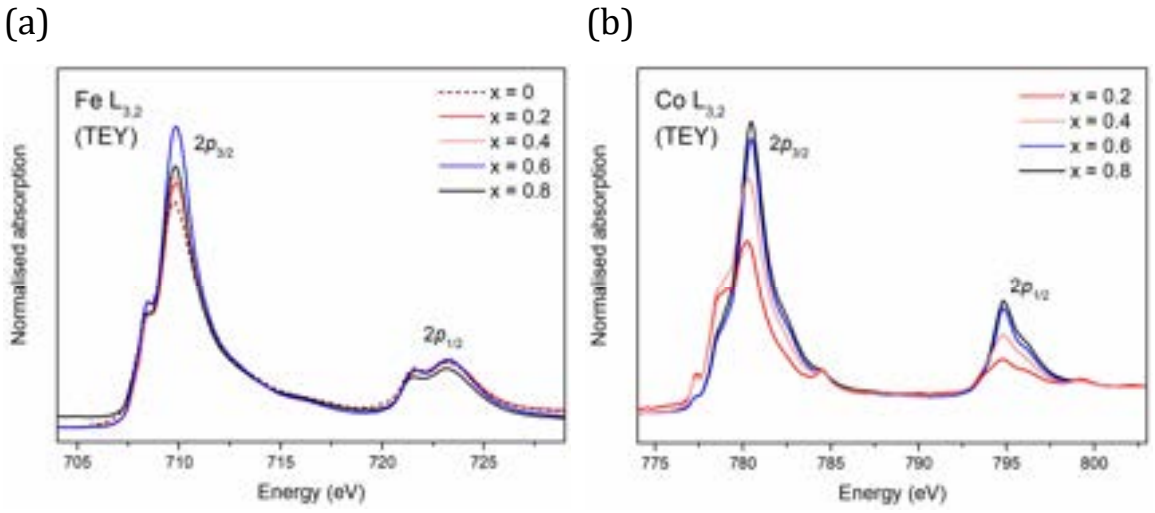

Figure A17. The XANES spectra recorded in TEY detection mode for $SrFe_{1-x}Co_xO_{3-\delta}$ (x = 0, 0.2, 0.4, 0.6, 0.8) at $L_{3,2}$ edges of iron (a) and cobalt (b).